Therapeutic and Environmental Stress in Central Nervous System Disease Models: Stress-Associated Cellular Plasticity in Glioblastoma and Myelomeningocele

Dissertation

Zur Erlangung des akademischen Grades

Doktor der Naturwissenschaften

(Dr.rer.nat.)

der Mathematisch-Naturwissenschaftlichen Fakultät

der Christian-Albrechts-Universität zu Kiel

Vorgelegt von

Jacqueline Clüver

Kiel, Juni 2026

Erste Gutachterin:	Professor Dr. Dr. Janka Held-Feindt
Zweiter Gutachter:	Professor Dr. Axel Scheidig
Tag der mündlichen Prüfung:	13.Oktober 2026

Preface

This dissertation consists partly of previously published work. Parts of this dissertation have already been published in the following two publications:

Hellmold, D.*, Johanning, L.*, **Clüver, J.***, Holler, J., Schröder, N.O., Bayler, F., Ahmeti, H., Kubelt-Kwamin, C., Wieker, S., Helmers, A., Synowitz, M., Held-Feindt, J., Effect of focused ultrasound-induced mechanical ablation on stemness and dormancy properties of residual/peri-focally localized glioblastoma cells, *Neuro-Oncology Advances*, Vol. 7,1 (2025), doi:10.1093/noajnl/vdaf184

Knerlich-Lukoschus, F.*, **Clüver, J.*,** Manczuk, I., Bayler, F., Hellmold, D., Synowitz, M., Held-Feindt, J., Neuroprotective properties of erythropoietin (Epo) and its receptor (EpoR) in open spinal dysraphism (OSD): an investigation of EpoR expression in a rat OSD model, along with *in vitro* studies on the neuroprotective effects of Epo on rat spinal cord-derived neural progenitor cells. *Childs Nerv Syst,* Vol. 41,1 358 (2025), doi: 10.1007/s00381-025-07032-8

* these authors contributed in equal measure

In this dissertation, data, which are parts of the mentioned publications, are briefly described, whereas, additional, unpublished data are explained in more detail.

Abstract

Stress within the central nervous system (CNS) can profoundly alter cellular states. However, it remains unclear whether stress-associated conditions within the CNS influence stemness-associated changes in cellular properties, and whether these effects are stressor-specific or represent a broader principle of cellular response in the CNS. Therefore, this thesis investigated how distinct CNS stressors influence stremness- dormancy-, or progenitor-associated cellular properties in two different CNS disease models. In a glioblastoma model, mechanical focused ultrasound (mFUS) was used to induce therapeutic stress. Furthermore, amniotic fluid-associated environmental stress was induced in a myelomeningocele (MMC) model.

In the glioblastoma model, mFUS generated focal cytotoxic damage and induced a heterogeneous dormancy- and stemness-associated marker profile in surviving focal and peri-focal tumor cell populations. An increased capacity for stem cell-associated spheroid formation, along with reduced cytotoxicity to subsequent chemotherapy, suggests that mFUS-induced stress can shift residual tumor cells into a stemness- and dormancy-associated state that is more resistant to therapeutic measures.

In the MMC model, adult rat spinal cord-derived neural progenitor cells were exposed to human-based artificial amniotic fluid (aAF). This aAF reduced cell proliferation, increased cytotoxicity, and influenced the expression of stemness- and progenitor-associated cellular markers in a time-specific manner. Thus, this model suggests stress-associated impairment of progenitor maintenance and cellular differentiation, which could be partially counteracted by neuroprotective erythropoietin treatment.

Both models yielded results suggesting that stress influences stemness- and progenitor-associated cell states, thereby supporting the overarching hypothesis that stemness-associated changes may represent a broader CNS response mechanism to stress. However, the stress response is highly context-dependent, and its biological significance appears to depend on both cell type and the disease under study.

Zusammenfassung

Stress im zentralen Nervensystem (ZNS) kann Zellzustände tiefgreifend beeinflussen. Ob dabei Stress im ZNS Stammzell-assoziierte Veränderungen beeinflusst und ob diese stressorspezifisch sind oder möglicherweise ein übergeordnetes zelluläres Prinzip im ZNS darstellen, ist bislang nicht vollständig geklärt. Ziel dieser Arbeit war es daher, den Einfluss unterschiedlicher Stressoren auf Stammzell-, Ruhezustand- und Vorläuferzell-assoziierte Zellzustände in zwei unterschiedlichen ZNS-Modellen zu untersuchen. In einem Glioblastom-Modell wurde mechanisch fokussierter Ultraschall (mFUS) verwendet, um therapeutisch-assoziierten Stress auszulösen. Zusätzlich wurde amnionflüssigkeitsassoziierter Umweltstress in einem Myelomeningocele-Modell (MMC) induziert.

Im Glioblastom-Modell führte mFUS zu einer fokalen zytotoxischen Schädigung und zeigte eine heterogene Induktion von Ruhezustand- und Stammzell-assoziierten Markern in überlebenden residualen und perifokalen Tumorzellpopulationen. Eine erhöhte Kapazität zur stammzell-assoziierten Sphärenbildung sowie verminderte Zytotoxizität gegenüber nachfolgender Chemotherapeutika-Behandlung deuten insgesamt darauf hin, dass mFUS-induzierter Stress residuale Tumorzellen in einen Stammzell- und Ruhezustand-assoziierten therapietoleranten Zustand verschieben kann.

Im MMC-Modell wurden adulte, aus dem Rückenmark gewonnene neurale Vorläuferzellen von Ratten humanbasierter künstlicher Amnionflüssigkeit (aAF) ausgesetzt. Diese aAF reduzierte die Zellproliferation, erhöhte die Zytotoxizität und veränderte die Expression von Stammzell- und Vorläufer-assoziierten Zellmarkern. Damit weist dieses Modell auf eine stressassoziierte Beeinträchtigung des Erhalts von Vorläuferzellen und der Zelldifferenzierung hin, welche durch eine Behandlung mit neuroprotektivem Erythropoietin teilweise abgeschwächt werden konnte.

Beide Modelle zeigten Ergebnisse, die auf die Beeinflussung von Stamm- und Vorläuferzell-assoziierten Zellzuständen durch Stress hinweisen und unterstützen damit die übergeordnete Annahme, dass stemness-assoziierte Veränderungen ein breiteres Antwortprinzip des ZNS auf Stress darstellen könnte. Die Stressantwort ist jedoch stark kontextabhängig und die biologische Bedeutung hängt sowohl vom Zelltyp als auch von der betrachteten Erkrankung ab.

Contents

Preface ..... **I**

Abstract ..... **II**

Zusammenfassung ..... **III**

Abbreviations ..... **IV**

1. Introduction **1**

1.1 Cellular stress in the central nervous system – Role of stemness and neural progenitor cells 1

1.2 Therapy-induced stress model - Clinical presentation of glioblastoma, heterogeneity, and therapeutic escape mechanisms 3

1.2.1 Mechanical focused ultrasound as therapeutic strategy 4

1.3 Environmentally induced stress model - Clinical presentation of myelomeningocele, pathophysiology, and damage mechanisms 7

1.3.1 Exploratory studies of the present work - Current challenges and strategies for myelomeningocele treatment 9

2. Aim of this Study **12**

3. Materials **13**

4. Methods **24**

4.1 Cell biological techniques 24

4.1.1 Cell cultivation 24

4.1.1.1 Determination of viable cell numbers 28

4.1.2 3D Hydrogel-cultures 28

4.1.3 Mechanical focused ultrasound (mFUS) – Preparation & stimulation 30

4.1.4 Myelomeningocele (MMC) patch – Preparation and cultivation 32

4.1.5 Artificial amniotic fluid preparation 34

4.1.6 Inhibition and stimulation experiments 38

4.1.7 Extreme limiting dilution assay 40

4.2 Biochemical methods 41

4.2.1 Cytotoxicity assay 41

4.2.2 Immunocytochemistry 42

4.2.3 Hematoxylin and eosin staining 43

4.2.4 Preparation of cell lysates & protein detection via Bradford assay 44

4.2.5 SDS-PAGE 45

4.2.6 Western Blot (semi-dry) 47

4.2.7 RNA isolation 48

4.2.7.1 3D hydrogel and cell culture preparation 48

4.2.7.2 Isolation with TRIzol™ 49
4.2.7.3 Isolation with ARCTURUS© PicoPure® RNA Isolation Kit 50
4.2.8 Reverse transcription 50
4.2.9 Quantitative real-time polymerase chain reaction (qPCR) 51
4.3 Statistical analysis 53
5. Results 54
5.1 mFUS-induced stress in GBOs and GBM models – Consequences for dormancy- and stemness-associated properties 54
5.1.1 mFUS setup and GBO characterisation 55
5.1.2 Assessment of dormancy- and stemness-associated properties following mFUS treatment in a region-dependent manner 62
5.1.2.1 Transcriptional changes in dormancy- and stemness-associated properties following mFUS treatment 67
5.1.2.2 Functional relevance of mFUS-induced changes: Self-renewal, therapy response, and signaling behavior 70
5.1.3 Biological consequences of mFUS-induced changes: Involved signaling 74
5.2 Effects of artificial amniotic fluid in the myelomeningocele model 76
5.2.1 Establishment of the aAF treatment framework 77
5.2.2 Stimulation of adult rat progenitor cells with artificial amniotic fluid – Comparison with neuroprotective erythropoietin treatment 79
5.2.3 Human *in vitro* model – Cytotoxic, antiproliferative and morphological effects of aAF treatment in SH-SY5Y cells 85
5.2.4 Translational Outlook – Therapeutic MMC patch development for local protection against the influence of amniotic fluid 89
6. Discussion 96
6.1 Glioblastoma model – Dormancy and stemness mechanisms after treatment with mFUS 96
6.2 Myelomeningocele model – Stemness mechanisms following stimulation with artificial amniotic fluid and potential treatment strategies 102
6.2.1 MMC Patch development 106
7. Conclusion 110
List of figures 111
List of tables 112
References .... Fehler! Textmarke nicht definiert.
A. Appendix VI
A.1 Publications and other contributions related to this thesis VI
A.3 Danksagung XXXVII

A.4 Eidesstattliche Erklärung..... XXXVIII

Abbreviations

5-ALA ..... Aminolevulinic acid
aAF ..... artificial amniotic fluid
APS ..... Ammonium peroxodisulfate
ATCC ..... American Type Culture Collection
bFGF ..... Basic fibroblast growth factor
BGN ..... Biglycan
BSA ..... Bovine Serum Albumin
cCaspase3 ..... Cleaved Caspase 3
CD11b ..... integrin alpha M (ITGAM)
CD133 ..... Cluster of differentiation 133
CD3 ..... Cluster of differentiation 3
CD31 ..... platelet endothelial cell adhesion molecule (Pecam 1)
CD68 ..... Cluster of differentiation 68
CNS ..... Central Nervous System
CT ..... Cycles of threshold
DAMP ..... Damage-associated molecular patterns
DAPI ..... 4',6-diamidino-2-phenylindole
ddH2O ..... double distilled water
DEPC ..... Diethylpyrocarbonate
DMSO ..... Dimethyl sulfoxide
DTT ..... Dithiothreitol
E22 ..... Gestational week 22
ECL ..... enhanced chemiluminescence
EDTA ..... Ethylendiaminetetraacetic acid disodium salt dihydrate
EGF ..... epidermal growth factor
ELDA ..... Extreme limiting dilution analysis
EphA5 ..... Ephrin-type-A-receptor 5
Epo ..... Erythropoietin
EpoR ..... Erythropoietin Receptor
FBS ..... Fetal bovine serum
FN1 ..... Fibronectin 1
FUS ..... Focused Ultrasound
GAPDH ..... Glyceraldehyde-3 phosphate dehydrogenase
GBM ..... Glioblastoma
GBO ..... Glioblastoma Organoids

GFAP ..... glial fibrillary acidic protein
GSC ..... Glioma stem-like cell
H&E ..... Hematoxylin and eosin
H2BK ..... histone cluster 1 H2B family member K
HRP ..... Horseraddish peroxidase
Hsp90 ..... Heat shock protein 90
Iba1 ..... calcium-binding adapter molecule 1
IF ..... Immunofluorescence
IGFBP5 ..... insulin-like growth factor-binding protein 5
JAK2 ..... Janus kinase 2
Ki67 ..... Antigen Kiel 67
Klf4 ..... Krüppel-like factor 4
MAP2 ..... Microtubule-associated protein 2
MEM ..... Minimal essential medium
mFUS ..... mechanical Focused Ultrasound
MMC ..... Myelomeningocele
MOMS ..... Management of Myelomeningocele Study
MSI1 ..... Musashi homolog 1 (Drosophila)
NEAA ..... non-essential amino acids
NF1 ..... Neurofibromin 1
NF200 ..... Neurofilament heavy polypeptide 200 kDa
NPC ..... Neural progenitor cell
OCT4 ..... octamer binding transcription factor 4
Olig2 ..... Oligodendrocyte transcription factor
pAkt ..... Protein Kinase B
PBS ..... Phosphate-buffered saline
PCNA ..... Proliferating-Cell-Nuclear-Antigen
PFA ..... Paraformaldehyde
p-GSK3β ..... Phospho-Glycogen synthase kinase 3
PI3K ..... Phosphoinositide 3-kinase
Piezo1 ..... Piezo-type mechanosensitive ion channel component 1
PIP ..... Peak incident power
PVAc ..... Polyvinyl acetate
PVDF ..... Polyvinylidene difluoride
qPCR ..... Quantitative real time polymerase chain reaction
ROS ..... Reactive oxygen species
rpm ..... rounds per minute

RT ..... Room temperature
S100b ..... S100 calcium-binding protein B
SDS ..... Sodium dodecyl sulfate
SDS-PAGE ..... sodium dodecyl sulfate polyacrylamide gel electrophoresis
SKI ..... SKI proto-oncogene
Sox2 ..... sex-determining region Y-box 2
STAT5 ..... Signal transducer and activator of transcription 5
TBS ..... Tris-buffered saline
TEMED ..... Tetramethylethylene diamine
TF ..... Transcription factor
TMZ ..... Temozolomide
Tris ..... Tris(hydroxymethyl)aminomethane
Trpc1 ..... Transient receptor potential canonical 1
Trpc6 ..... Transient receptor potential canonical 6
Trpm4 ..... Transient receptor potential cation channel subfamily M member 4
Trpp2 ..... Transient receptor potential polycystic 2
TUBB3 ..... Beta-III-Tubulin
vWF ..... Von Willebrand factor
WB ..... Western Blot
WHO ..... World Health Organization

1. Introduction

1.1 Cellular stress in the central nervous system – Role of stemness and neural progenitor cells

The central nervous system (CNS) is a highly specialized and tightly regulated system consisting of the brain and spinal cord, whose functional integrity depends on the coordinated interplay of neurons, glial cells and region-specific progenitor populations, and which integrates sensory input in order to dictate motor response [1–5]. The progenitor and stem cell compartments in particular are continuously shaped by signals that regulate quiescence, proliferation, and differentiation [6,7]. Additionally, the CNS constantly adapts to demands on energy use and information processing, regulating cell survival, metabolism, and plasticity [8–13]. Thus, the CNS is particularly sensitive to pathological disturbances such as localized injuries that can alter these regulatory mechanisms associated with stress and injury [11,13–15]. In the CNS, such stress mechanisms can arise from external triggers, including trauma and therapeutic intervention [14,16,17], as well as from internal causes such as developmental malformation and chronic exposure to a pathologic environment [18–20]. These stress mechanisms are typically characterized by combinations of oxidative stress, inflammatory signaling, metabolic imbalance, vascular dysfunction, cytotoxicity, and structural tissue disruption [19–23]. Moreover, stress is capable of triggering adaptive responses, thereby actively reshaping cellular behavior and cell-state regulation [15,24–26].

Especially, stemness-associated programs are linked to the ability of progenitor cells to enter adaptive states in response to stress conditions [27,28]. In detail and depending on the context, stress can alter progenitor cell survival, proliferation, lineage commitment, and quiescence, due to inflammatory mediators, reactive oxygen species, metabolic stress or other injury and stress-associated signaling [27,29–32]. These responses may either support repair-associated plasticity or promote maladaptive outcomes such as altered differentiation or stem cell exhaustion [27,29,31,32]. Thus, the influence of stress on neural progenitor cells (NPCs) is particularly interesting, since they retain some degree of plasticity and therefore the ability to adapt structurally and functionally in response to stress [27,33]. As stemness-associated programs are especially relevant in the CNS since they represent a biologically meaningful link between cellular stress responses and changes in cell fate, this study aimed to investigate whether stress within the CNS influences stemness-

associated cellular properties and whether this constitutes a shared response across distinct types of stress within the CNS.
To investigate whether a shared response across distinct types of stress really exist in the CNS, the present work compared the stemness-related cellular responses by addressing two fundamentally different, yet conceptually complementary forms of external-triggered stress and internal causes of stress: therapy-induced stress and stress caused by a pathological internal environment.

Since therapy-induced stress represents a defined and clinically relevant form of externally induced stress, it may offer a useful tool for studying how surviving cells respond to external stress in terms of stemness-associated programs. In line with this, the literature on cell plasticity and especially cancer stemness increasingly recognizes therapeutic stress as a driver of adaptive survival programs, including stemness-associated plasticity, dormancy, and treatment tolerance [17,34,35]. As therapeutic interventions seem to create strong selective pressure on residual (tumor) cells and thereby promote escape mechanisms associated with plasticity, stemness and dormancy [16,17,36,37], a tumor model using glioblastomas (GBMs) as highly malignant primary brain tumors was chosen to address the aforementioned aim of this study.

By contrast, internal causes of stress resulting from pathological environments can impair neurogenesis and influence NPC fate due to oxidative stress, endoplasmic reticulum stress, or inflammatory processes [38,39]. Thus, environmentally induced stress was chosen to investigate whether it impairs the regulation of progenitors and pushes NPCs toward altered stemness- or lineage-associated programs. Internal induced stress seemed particularly relevant and prominent in developmental disease settings, such as the myelomeningocele (MMC), in which vulnerable neural tissue is exposed to sustained intrauterine environmental stress [18,39]. Therefore, an MMC model was developed and established within this work.

Comparing these different models, the study aimed to investigate whether the different types of internally and externally caused stress might comprise a shared response, particularly with regard to stemness-related adaptive processes.

The following sections introduce GBM and the therapeutic intervention applied, as well as MMC and the MMC model used for this study. Furthermore, exploratory MMC treatment strategies were presented and conducted within this work.

1.2 Therapy-induced stress model - Clinical presentation of glioblastoma, heterogeneity, and therapeutic escape mechanisms

Glioblastoma (GBM) is a highly aggressive, infiltrating, and frequently recurring primary tumor in adults [40–42]. Even with the current standard of care consisting of surgical resection followed by radiation therapy and often combined with temozolomide (TMZ) chemotherapy, the prognosis remains poor [41,43], and clinical management remains difficult because of rapid adaptation and persistent therapy resistance [40,42].

A central reason for therapy resistance and rapid adaptation is the pronounced inter- and intratumoral heterogeneity of GBM [40,42,44]. Recent single-cell and spatial transcriptomic studies have also highlighted the concept of cellular plasticity in GBM. These studies indicated that malignant GBM cells are not restricted to one identity [42,45–47]. Rather, they might enter multiple transcriptional states that mirror developmental progenitor lineages of the central nervous system [44,45]. Thus, an interplay between heterogeneity and plasticity may be the driving force of cancer development, recurrence, and therapy resistance [47,48].

In this context, the terms stemness and dormancy require careful definition. In GBM, cellular stemness describes functional properties such as self-renewal, tumor propagating potential, as well as multipotency, and therefore the ability to reconstitute heterogeneity [47,49–51]. These characteristics are most prevalent in the GBM subpopulation of glioma stem-like cells (GSCs) [44,52]. However, current concepts emphasize that stemness in GBM can represent a dynamic and partially reversible cell state that is not fixed to particular subpopulations and may be acquired by GBM cells under specific conditions [42,45–47,53,54]. Furthermore, different GSC niches were identified, which support GSC maintenance, immune evasion, and recurrence [49,50,55,56].

In contrast to stemness, cellular dormancy is defined as a stage in which cells enter a reversible growth arrest (quiescence) driven by intrinsic or extrinsic factors [57–59]. This quiescence is proposed as another factor of the therapeutic escape mechanisms of tumor cells and is closely linked with the aggressiveness and recurrence of GBMs [60–63]. Furthermore, dormant GBM cells are capable of acquiring stem cell characteristics and can induce tumor recurrence [64].

Data from standard post-treatment therapy confirmed that procedures such as resection, radiation, and chemotherapy create a complex post-therapeutic environment that might promote cellular stress responses due to hypoxia or tissue disruption, and induce metabolic stress and inflammatory remodeling [34,65–67]. Such therapy-induced stress can actively drive cell state transitions, including programs associated with stemness and dormancy [46,50,60,68]. However, the extent to which therapy-induced stress applies a selection pressure and how this therapy-induced stress shapes the tumor microenvironment is not

fully understood [69]. Thus, the GBM model appeared especially suitable and informative for further evaluation.

Taken together, the underlying complexity of intratumoral heterogeneity and plasticity of GBM associated with therapy-evading mechanisms provided the foundation of the present work to explore therapy-induced stress in a GBM model. To assess whether therapy-induced stress influences stemness-associated cellular properties in the chosen GBM model and may comprise a shared response across distinct stress contexts within the CNS, the present work used mechanical focused ultrasound (mFUS) to create therapy-induced stress in patient-derived glioblastoma organoids (GBOs), more differentiated glioblastoma cells (GBMs), as well as glioma-like stem cells (GSCs). mFUS represents a relatively new potential therapeutic approach under investigation for GBM treatment, which is described in more detail in the following section.

1.2.1 Mechanical focused ultrasound as therapeutic strategy

Despite resection followed by radiotherapy and temozolomide-based chemotherapy as the current therapeutic gold standard for GBMs, long-term disease control remains rare [70,71]. Intensified search for noninvasive treatment modalities that can reach intracranial targets led to focused ultrasound (FUS) as an attractive platform technology [72,73]. FUS enables spatially and temporally precise deposition of acoustic energy deep within the brain [72–74]. In neurosurgery, current FUS applications include thermal ablation in thalamotomy, pallidotomy, and subthalamotomy for movement disorders [72,74,75]. Furthermore, clinical and preclinical trials are exploring FUS as a technology to enable transient blood-brain barrier opening for improved drug delivery or sonodynamic therapy, which involves the activation of sonosensitizing agents like aminolevulinic acid (5-ALA) to induce reactive oxygen species (ROS) leading to cell death [72,74–77]. Furthermore, neuromodulation using FUS is explored, including the modulation of the immunological microenvironment [72,74,75].

Conventional high-intensity thermal FUS uses long treatment times to raise local tissue temperature and induce coagulative necrosis [78,79]. By contrast, mechanical effects of focused ultrasound (mFUS) are primarily caused by short, high-pressure, and low-duty-cycle pulses, which simultaneously minimize heat deposition and instead exploit the mechanical effects of FUS [73,79]. This distinction is highly relevant in the brain, where thermal spread to surrounding tissue is a major concern and where a more sharply confined non-thermal lesion profile may offer biological and practical advantages [80].

The process of mechanical ablation is a direct result of the cavitation effect, which is defined as the oscillation and subsequent collapse of gas bubbles within a liquid or soft tissue environment, a consequence of the compression and refraction of ultrasonic pressure waves [80–82]. Therefore, the cavitation effect is influenced by pressure and frequency of the applied mFUS. At lower acoustic pressure and frequency, bubbles may undergo a relatively stable oscillation, generating membrane deformation, microstreaming, radiation-force effects, and shear stress. At higher pressures, inertial cavitation can occur, in which bubbles expand and collapse within a few cycles, releasing shock waves, increased deformation processes, and microjets capable of mechanically disrupting cell membranes and extracellular structures [76,82–85]. Today, stable cavitation is applied for opening the blood-brain barrier to support therapeutic drug delivery, whereas intertial cavitation produces direct mechanical damage to the surrounding tissue [80].

The physical properties of mFUS make this therapeutic approach a promising future treatment strategy for GBM, since mechanical ablation offers the possibility of sharp lesions, lower thermal burden, and potentially distinct downstream biological effects compared with heat-based ablation [86]. Murine brain tumor studies have demonstrated that mechanical ablation leads to sufficient tissue ablation, with Duclos *et al.* 2026 reporting increased survival of GBM-bearing mice due to mFUS treatment compared to untreated control [87–90]. Furthermore, magnetic resonance-guided mechanical ablation in large-animal brain tissue or skull-containing models has already been shown to generate targeted lesions [87–94]. At the same time, skull-induced attenuation, refraction, and focal distortion, as well as hemorrhagic effects, remain major translational challenges [89–92,94].
Importantly, mechanical tissue ablation creates a post-treatment stress landscape. Cavitation-based approaches have been associated with the release of tumor antigens, damage-associated molecular patterns (DAMPs), and immunostimulatory effects [95–97]. For example, mechanical ablation increased the proliferation of $CD3^+$, $CD4^+$, and $CD8^+$ T cells [75,96]. Furthermore, increased infiltration of immune cells could be observed [96,98]. This indicates that local ablation could reshape the treated microenvironment rather than merely ablating tissue. Thus, mFUS might have the potential to influence several mechanisms of therapy resistance observed in GBM. However, the biological consequences of mFUS-induced lesions are still insufficiently understood. Since cancer therapies generate a spectrum of stress responses like oxidative stress, altered inflammatory signaling, necrosis, autophagy, and altered metabolism or vascular or oxygen supply (see Figure 1) [34,65–67], a more detailed understanding of the biological effects of mFUS is likely to be important for future therapeutic applications. As described in the previous section, especially in GBM, such stress-adaptation to e.g., hypoxia, inflammation

or necrosis is tightly linked to tumor plasticity, the maintenance of GSCs, and therapy resistance (see Figure 1) [46,50]. While the immediate effect of mFUS-induced mechanical ablation might be tumor destruction, the surviving cells at the lesion site or in peri-focal areas are likely exposed to a therapy-induced stress environment. Such conditions may favor the activation of adaptive cellular programs. Since dormancy and stemness-related cellular properties are closely related to therapy resistance, those properties were of particular interest [34,50]. The present work investigated mFUS as a therapeutic approach in patient-derived GBM models, with particular emphasis on whether therapy-induced stress might be associated with the induction of dormancy- and stemness-related programs in surviving or peri-focally localized GBM cells.

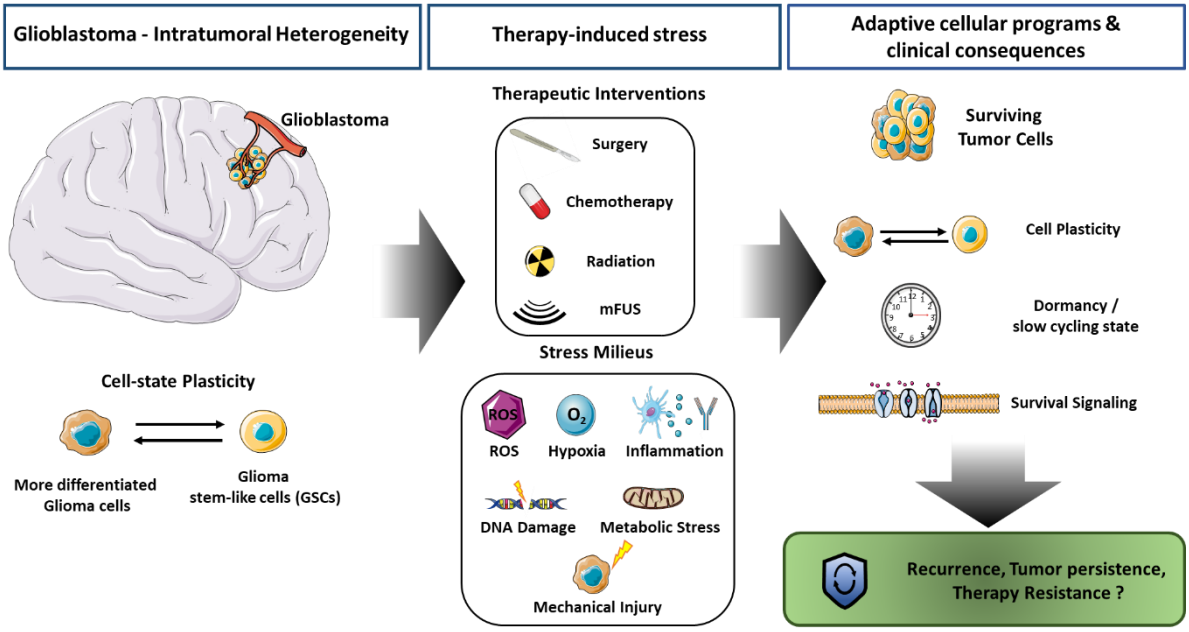


Figure 1 – Conceptual overview of glioblastoma (GBM), therapeutic interventions, and therapy-induced stress, as well as escape mechanisms. The schematic illustrates how a heterogeneous GBM cell population exposed to therapeutic interventions such as surgery, radiotherapy, chemotherapy or newer potential therapeutic approaches such as mFUS may generate a therapy-induced stress milieu characterized by e.g. hypoxia, reactive oxygen species (ROS), inflammation, DNA damage, metabolic stress or mechanical injury. In surviving tumor cells, this stress milieu might promote or select adaptive cellular programs, including stemness-associated cell plasticity, dormancy and survival signaling, and thereby might contribute to therapy resistance as well as tumor persistence and recurrence. Image(s) partially provided by Servier Medical Art (https://smart.servier.com), licensed under CC BY 4.0 (https://creativecommons.org/licenses/by/4.0/).

1.3 Environmentally induced stress model - Clinical presentation of myelomeningocele, pathophysiology, and damage mechanisms

Myelomeningocele (MMC) is considered the most severe form of open spina bifida, characterized by incomplete neural tube closure during early embryogenesis [39]. Therefore, the neural tissue is insufficiently protected by overlying mesodermal structures [39,99,100]. Infants with open spina bifida are prone to early death, depending on the severity of the lesion and the success of surgical treatment, as well as the acceptance of medical intervention. Those who survive are likely to experience severe, lifelong disabilities [101,102].

Although MMC originates developmentally rather than traumatically, the exposed neural placode is likewise subjected to persistent cellular stress and progressive degeneration [39]. In fact, experimental evidence provided by Michejda *et al.* 1984 [103] on monkeys, Meuli *et al.* 1995 [104] on sheep, Housley *et al.* 2000 [105] on rabbits, as well as Heffez *et al.* 1990 and 1993 [106,107] on rats and pigs demonstrated that prenatal trauma-induced spinal cord injuries mimic developmental malformation observed in MMC, with comparable loss of function characteristics at birth. The observed defects include progressive loss of movement in the lower extremities, tissue loss at the lesion site, and neurological consequences affecting motor and sensory functions, as well as bladder and bowel control or cognitive abilities [99,108–112]. One of the central challenges in spinal cord injury is that the primary mechanical defect is only the beginning, as the damaged tissue subsequently undergoes progressive secondary degeneration. This secondary injury cascade is characterized by ischemia, ionic imbalance, excitotoxicity, oxidative stress, inflammatory signaling, apoptosis, demyelination, and glial scar formation [20,21,113,114].

The phenomenon, in which the primary neural tube defect or malformation is followed by *in utero* neurodegeneration, is often referred to as the “two-hit” hypothesis [108,115]. The theory has its origins in the works of, among others, Hutchins *et al.* 1996, who performed significant post-mortem pathologic analyses of fetuses with MMC, which demonstrated damage and loss of neural tissue at the lesion site with normal tissue in proximity [116]. Several studies investigated the pathways and molecular changes involved in spinal cord injury, including altered homeostasis of lipids and neurofilaments, progressive inflammatory responses, oxidative damage, and apoptotic cell death [20,117]. However, the mechanisms underlying those second hit cascades are still to be fully elucidated [39].

Within this framework, amniotic fluid is likely to contribute to the second hit cascade [106,108]. The placode is exposed to a complex and dynamically changing extracellular milieu, whose composition changes throughout gestation. In fact, the presence of intestinal and digestive enzymes can be found in amniotic fluid, most likely linked to fetal defecation,

which increases in concentration during gestation [118,119]. Furthermore, Stiefel *et al.* 2007 showed that the spinal cord of mice with experimentally induced MMC developed normally in the very early stages of fetal life, followed by progressive degenerative and inflammatory changes [120]. In support, experimental exposure of fetal spinal cord tissue to amniotic fluid or meconium-containing fluid can worsen degenerative changes [121–123], and significant improvements could be observed following prenatal surgical treatment to repair the defect *in utero* [124,125].

However, even if the current literature supports the idea that amniotic fluid is a plausible contributor to MMC progression, the relative importance of its individual components remains unresolved. Thus, it is most accurate to regard amniotic fluid as part of a broader *in utero* environmental stress factor that likely also includes ongoing mechanical trauma due to ongoing vulnerability of the neural tissue [18]. This more complex view is also captured by the “third-hit” hypothesis, where the first hit remains the embryologic defect and the second hit remains the chronic exposure of the placode to the intrauterine environment. The third hit was added to describe the molecular and cellular cascades triggered by that environment, including inflammatory cytokine signaling, astroglial reactivity, and possibly traction, stretch or other mechanical damage to the exposed neural tissue [126,127].

Understanding how the cellular environment and especially NPCs are affected in MMC lesions is crucial for new therapeutic approaches. Several studies have indicated an altered development of neural cells in MMC, characterized by impaired neurogenesis and a shift in astrogenesis at the expense of normal neuronal development [108,128–130]. Motivated by this evidence, the environmental stress of MMC provided a suitable basis for evaluating whether environmental stress within the CNS influences stemness-associated cellular properties and represents a common response across distinct stress contexts within the CNS.

Taken together, MMC evolves from a primary neurulation defect into progressive cellular maldevelopment, likely shaped by ongoing exposure to amniotic fluid and secondary mechanical lesions. This environment might lead to altered developmental responses at a cellular level (see Figure 2). Since the exposed placode is not only mechanically vulnerable but may be biologically reprogrammed by its fluid environment, it is important to understand how amniotic fluid-like conditions influence proliferation, survival, and stemness-related programs. Elucidating this influence could improve our understanding of the impact of environmental stress on MMC progression. In the present work, an environment resembling amniotic fluid was created by developing artificial amniotic fluid (aAF) as a first step. Adult rat NPCs together with aAF were then used to model the environmental stress in MMC *in vitro*.

1.3.1 Exploratory studies of the present work - Current challenges and strategies for myelomeningocele treatment

Today, MMC treatment involves post- or prenatal surgery, which aims to cover the exposed spinal cord using the surrounding dura and prevent further infection [112,131,132]. The Management of Myelomeningocele Study (MOMS, 2003-2017) demonstrated that, compared to postnatal spinal cord surgery, prenatal repair of MMC can preserve neurological function and reverse hindbrain herniation, which is a common symptom of MMC resulting from a cerebrospinal fluid leak [112,133]. However, post- and prenatal surgery is associated with significant risks and fetal morbidity or maternal complications such as preterm labor or uterine dehiscence [112,131,132,134]. Because of these risks, alternative therapeutic strategies are explored (see Figure 2). This also involves the exploration of pharmacological support, including erythropoietin (Epo).

Erythropoietin (Epo) is a glycoprotein hormone with pleiotropic effects found in various tissues, comprising the CNS [135–137]. In a developmental context, Epo has been shown to promote normal brain maturation by increasing neurogenesis and angiogenesis or by stimulating growth factors required for normal brain development via Epo receptor (EpoR) signaling [138,139]. The receptor is expressed in NPCs, neurons, astrocytes, and microglia, with elevated expression levels during brain development [138–141]. Therefore, experimental studies indicated that Epo influences neurogenesis and cell fate decisions in immature neural populations [142–144].

Several clinical studies have evaluated the potential therapeutic effect of recombinant Epo in the CNS. For example, recombinant Epo has been shown to protect against neurodegenerative processes in neurological disorders [135,145]. In addition, promising results of Epo treatment used against hypoxia or ischemia have been published [146], and increased endogenous Epo in the brain has been associated with the potential prevention of ischemia damage to brain tissue [147]. From a clinical standpoint, Epo is an established drug used for hematologic indications like chronic kidney disease or chemotherapy-associated anemia, and the neuroprotective use of Epo remains translational and investigational [148,149].

For the present work, Epo provides a biologically plausible candidate for potentially modulating survival and progenitor-associated cell behavior based on the aforementioned literature. The proposed neuroprotective properties of Epo were of particular interest for the investigated environmental stress in MMC, where exposed neural tissue is subjected to the intrauterine environment, leading to cellular stress and potentially altered differentiation processes [20,115,128]. Thus, Epo was included in the performed investigations to

determine whether environmental stress-related processes could be influenced, e.g. by affecting neural progenitor cell survival or stemness-related regulation.
Another interesting and potentially combinatorial therapeutic approach is the usage of MMC patches. These patches are of particular interest since the exposed neural placode is damaged progressively throughout gestation, and current prenatal surgery is often accompanied by tethering from scar formation [150]. The patch is expected to serve as a passive barrier to protect the neural tissue from further amniotic fluid-mediated processes and mechanical forces while integrating into the repair process without adding tethering, inflammation, or additional surgical burden [134,151].

In practical terms, an MMC patch refers to a biological or synthetic material placed over the fetal lesion, which functions as a barrier between the lesion and the environment [131,134]. However, the challenge is that an MMC patch must satisfy a high number of requirements. From a surgical perspective, it must be usable and manipulable in a prenatal surgery setting, which is often performed through a fetoscopic approach, accompanied by limited working space [131,134,151]. From a biological perspective, it must provide watertight or near-watertight coverage, resist degradation in the amniotic environment, and exhibit biocompatibility features like non-inflammatory or non-tethering traits [150–152]. Furthermore, the fetal spinal cord and the fetus itself continue to evolve and move, so the material should be sufficiently deformable and ideally stretch-tolerant to accommodate fetal development [151]. Finally, if the patch itself is not biodegradable, the lesion requires postnatal neurosurgical management, and the material should not complicate later removal [134,151]. A potential benefit of MMC patches is the incorporation of bioactive agents or pharmaceuticals into the patches, thereby supporting further regeneration through a drug delivery system in addition to providing a physical barrier. Based on previous findings regarding the expression of proinflammatory cytokines of our group, patches that deliver immunomodulating or neuroprotective factors might be a promising approach [153]. In fact, first attempts to incorporate Epo into different scaffolds, such as polylactic acid with multiwalled carbon nanotubes or hyaluronan/methyl cellulose, have been tested for nervous system injuries [154].

Several MMC patch materials have been investigated, including smart polymers, layered scaffolds or hydrogel approaches that attempt to meet the various requirements of an MMC patch material for neural protection and sealing without contributing to tethering or inflammatory processes [151,155–157].
Biological patch approaches showed very promising results, with the use of human umbilical cord as the most recent advancement in this area. The human umbilical cord serves as a

skin patch, with the first animal studies in sheep showing complete regrowth of epidermal, dermal, and subdermal tissue components and no leakage of cerebrospinal fluid, as well as improved sensorimotor function [150,158].

Another promising and maybe more readily available material approach are biodegradable and water impermeable polyester-based patches, such as poly-lactic acid or poly-caprolactone. Saadai *et al.* 2011 showed promising results in MMC defect repair using poly-lactic acid scaffolds in fetal sheep, with no evidence of a surrounding inflammatory response and positive effects on neural tissue regeneration [151,159]. However, this treatment approach did not prevent cerebellar and hindbrain herniation as a possible complication of an MMC injury [159]. Nonetheless, these materials exhibit the advantage that the properties of the final material polymer can be easily tailored and that these materials can be shaped as needed or even facilitate shape memory properties, which might reduce operation times [151]. Therefore, these patches are still under investigation as a promising opportunity for MMC defect repair and form the starting point for the initial *in vitro* studies of new patch formulations conducted within this work [160].

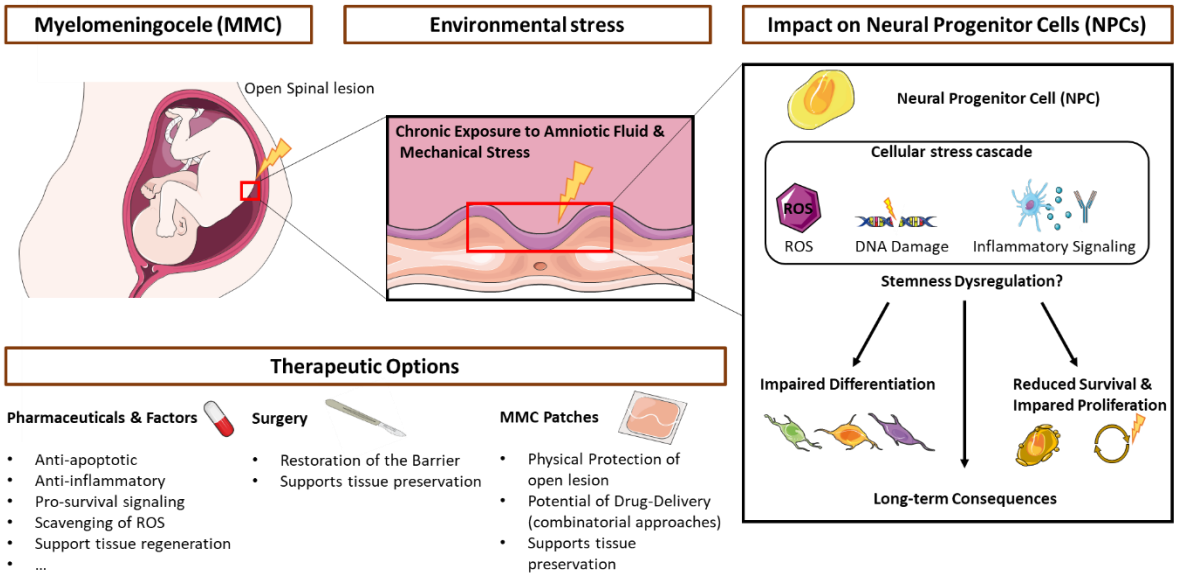


Figure 2 – Schematic overview of myelomeningocele (MMC) in which failed neural tube closure exposes neural tissue to the intrauterine environment. Chronic exposure to amniotic fluid and mechanical stress is hypothesized to contribute to secondary spinal cord injuries and to alter survival, proliferation, differentiation, as well as stemness-associated properties of neural progenitor cells (NPCs). Therapeutic concepts aim to reduce stress factors and protect the exposed spinal cord from the environment. Image(s) partially provided by Servier Medical Art (https://smart.servier.com), licensed under CC BY 4.0 (https://creativecommons.org/licenses/by/4.0/).

2. Aim of this Study

The present study aimed to investigate whether changes in stemness-related cellular properties associated with stress are stressor-specific or whether they reflect a broader principle of stress-induced regulation of cell states in the CNS. To address this question, two fundamentally different stress contexts of externally induced therapeutic stress and an internally arising environmental stress were examined, since they capture complementary modes of stress. While external therapy-induced stress reflects a controlled selective pressure on cells, environmentally induced stress reflects a persistent pathophysiological environment that progressively reshapes vulnerable cells. These different stress contexts were modeled by mechanical focused ultrasound (mFUS) as therapeutic treatment in GBM systems, including glioma stem-like cells (GSCs), as well as by artificial amniotic fluid (aAF) exposure in an MMC model using neural progenitor cells (NPCs) and cells capable of differentiation. Across both stress models, the study focused on whether stress alters survival, proliferation and stemness-associated properties.

Within this framework, further specific objectives were approached regarding other cellular plasticity alterations. The GBM model was used to assess whether mFUS-induced stress promotes adaptations associated with dormancy and stemness in surviving and peri-focal tumor cells with potential relevance for therapeutic escape and resistance. In the MMC-related model, the study aimed to evaluate whether aAF-induced environmental stress affects neural progenitor-associated properties and whether these effects can be modulated by protective strategies such as erythropoietin (Epo) treatment or by the development of MMC patch materials as a first outlook.

3. Materials

Devices

		Usage	Producer	Product – No.
Recording and measuring devices, microscopes	Neubauer Counting chamber	Cell counting	Assistent-Zählkammer, Glaswerkfabrik Karl Hecht	40441
	Tecan Microplate Reader Infinite M Plex	Measurement of fluorescence and luminescence	Tecan	INF-MPLEX
	AxioObserver.Z1	IF-Analysis, Optical microscope	Zeiss	SKU29143
	Stemi 305 KMAR	Binocular, stereomicroscope	Zeiss	305KMAR
	Axiovert 200	Zellculture, Optical microscope	Zeiss	1005-813
PCR	NanoDrop2000c	RNA/DNS Concentration measurement	Thermo Fisher Scientific Inc	ND-2000
	Thermomixer compact	Heatbloc	Eppendorf	5350 900.014-13
	Mastercycler	PCR	Eppendorf	6311000010
	QuantStudio5	qPCR - Thermocycler	Applied Biosystems	15731248
SDS-PAGE & Western Blot	Trans-Blot® Turbo	Western Blot	Bio-Rad	1704150EDU
	PowerPac Basic	SDS-PAGE	Bio-Rad	1645050
	Mini PROTEAN® Tetra Cell	SDS-PAGE	Bio-Rad	552BR
	Mini PROTEAN® Casting Stand	SDS-PAGE	Bio-Rad	1658050
Pipettes and pipetting aids	Eppendorf Research Pipette 0,5-10 uL	Pipetting	Eppendorf	Discontinued
	Eppendorf Research Pipette 10 - 100 uL	Pipetting	Eppendorf	Discontinued
	Eppendorf Research Pipette 10 - 200 uL	Pipetting	Eppendorf	Discontinued
	Eppendorf Research Pipette 100 - 1000 uL	Pipetting	Eppendorf	Discontinued
	Accu-jet® Pro	Pipetting	Brand	BN-0683
Cell culture	Herasafe KS 18 (47)	Cell culture safety workbench	Heraeus – Thermo Scientifix	10213322
	Fuego SCS Basic	Laboratory burner	WLD-TEC	8.201.000
	Hydro H20S und H22	Water Bath	Lauda	L002908 & L002903

	KM CO_2-FL	Shaker	Bühler	discontinued
	Heracell 240 & 240i	Incubator	ThermoFisher	51026331 & 61026334
Centrifuges	Eppendorf 5702	Centrifugation	Eppendorf	Z606936
	Eppendorf 5417R	Centrifugation	Eppendorf	Z366021
	Rotilab	Mini-Centrifuge	Roth	T464.1
	Biofuge Pico	Centrifugation	Heraeus	75003328
	Plate Centrifuge	Centrifugation 96WP	Starlab	N2631-0008
Other devices	Table stand for disposal bags	Waste disposal	Sarstedt AG & Co.	95.1297
	Kendro Heraeus Cytomat 6001	Drying and heating oven	Heraeus	#57670-17
	Ultra Turrax® T25 Basic	Tissue Homogenization / Tissue chopper	IKA® Werke	ULTRA-TURRAX®
	Micromot 60/E	Rotary tool	Proxxon	NO28515
	M220 Focused-ultrasonicator	Focused Ultrasound	Covaris®	500295
	Reax Top	Shaker/Vortexes	Heidolph	541-10000-00
	Flake ice machine	Ice production	Omnilab Manitowoc	MB-RF-0266AF-251
	Leica C1100 Cryostat	Microtome	Leica	N193
	Autoklav V-150	Autoclave	Systec	1150
	Miele Professional G7883CD	Dishwasher	Miele	03580711

Software

	Producer
Citavi 6	Swiss Academic Software
i-control 2.0	Tecan
Adobe Illustrator	Adobe
Word	Microsoft Office 365
Excel	Microsoft Office 365
Power Point	Microsoft Office 365
AxioVision LE	Zeiss
Zen Studio	Zeiss
QuantStudio 5	Applied Biosystems

Prism 8	GraphPad
ImageJ	Wayne Rasband (NIH)

Consumables

		Producer	Product-No.
Pipettes and pipette tips	Pipette tips 10µL, colorless	Sarstedt AG & Co.	70.1130
	Pipette tips 200µL	Sarstedt AG & Co.	70.760.002
	Pipette tips 1000µL	Sarstedt AG & Co.	70.762
	Serological pipette 5mL	Sarstedt AG & Co.	86.1253.001
	Serological pipette 10mL	Sarstedt AG & Co.	86.1254.001
	Serological pipette 25mL	Sarstedt AG & Co.	86.1685.001
	Pasteur pipettes	Labsolute	7691061
Reaction and storage vessels	Tube 50mL	Sarstedt AG & Co	62.547.255
	Tube 15 mL	Sarstedt AG & Co	62.554.502
	Tube 10 mL	Sarstedt AG & Co	62.553.020
	Tube 1.5 mL	Sarstedt AG & Co	72.690.001
	Tube 2.0 mL	Sarstedt AG & Co	72.691.002
	Tube 200 µL	Sarstedt AG & Co	72.737.002
	Petri dish 94/16mm Polystyrene	Sarstedt AG & Co	82.1472
	96-well Multiwell Plate, transparent	Sarstedt AG & Co	83.3924.300
	96-well Multiwell Plate, black – Nunclon™ Delta Surface	Thermo Fisher Scientific Inc.	137101
Cell culture	6-Well Multiwell Plate	Thermo Fisher Scientific Inc.	140675
	6-Well Multiwell Plate, Ultra-low Attachment Surface	Corning	3471
	24-Well Multiwell Plate Cell culture, transparent	Thermo Fisher Scientific Inc.	144530
	96-well Multiwell Plate Cell culture, transparent	Greiner-Cellstar® Sigma Aldrich	655180
	T25 flask	Sarstedt AG & Co.	83.3910.002
	T75 flask	Sarstedt AG & Co.	83.3911.002
	Cell Scraper	Sarstedt AG & Co.	83.1830
	Cover glass	Roth	H873.2
	BD Luer-Lok™ Syringe 50mL	BD Plastipak™	300865
	0.2 µm Filtropur S	Sarstedt AG & Co	83.1826.001
Gloves & disinfection	Hand disinfectantl Desderman®	Schülke & Mayr GmbH	16582636
	Sensiva Wash Lotion	Schülke & Mayr GmbH	SM-114006
	Terralin PAA	Schülke & Mayr GmbH	0297/13187
	Optisept	Dr. Schumacher	Sc-205-050

	Micro-Touch® Nitra-Tex™ Size M	Ansell	221285L
	Dermagrip WRP Latex Size M	Remesco	D1502-30
Immunfluorescence	ImmEdge Pen	Vector Laboratories	H-4000
	Coverslips 22x22 mm	Carl Roth®	H874.2
	Coverslips 24x40 mm	Menzel	11778691
	Coverslips 24x60mm	Carl Roth®	1870
	Coverslips 13 mm	Sarstedt AG & Co.	83.1840.002
	Microscope slides – Superfrost Plus	Menzel	J1800AMNZ
Miscellaneous	Tweezers	Carl Roth®	CH53.1
	Tapira Cosmetic wipes	GVS eG	07730012
	Precision Wipes Tissue Wipers	Kimberly-Clark Professional	05511
	Polyvinylidene difluoride Membrane	GE Healthcare	10600123
	Whatman™ filter papers	GE Healthcare	1001-932
	MilliTube 1 mL	Covaris®	520128
	Disposal bag 200x300mm	Sarstedt AG & Co.	86.1197
	Parafilm® M	NeoLab	3-1012

Enzymes, Kits, Stimulants, Inhibitors, and Standards

	Producer	**Product – No.**
AG490	Calbiochem	658411
ARCTURUS® PicoPure® RNA Isolation Kit	Applied Biosystems	KIT0204
Amphotericin B	Life Technologies	15290018
Basic fibroblast growth factor (bFGF), human	ImmunoTools	11343623
Basic fibroblast growth factor (bFGF), bovine	ImmunoTools	17343625
Bradford Reagent kit	Bio-Rad Laboratories Inc.	50000001
B27 Supplement w/o Vitamin A	Life Technologies	12587010
B27 Supplement serum free	Life Technologies	17504044
Cytotox-Fluor™ Cytotoxicity Assay	Promega	G9261
ECL Select® Western Blotting Detection Reagent	Cytivia Amersham®	RPN2235
Erythropoietin (Epo), rat	Sigma Aldrich	E8905-10UG
Halt™ Phosphatase Inhibitor Cocktail (100x)	Thermo Fisher Scientific Inc	78420
Halt™ Protease Inhibitor Cocktail (100x)	Thermo Fisher Scientific Inc.	87786

Heparin	Sigma Aldrich	3149-50KU
H&E staining ki	Abcam	ab245880
LY294004	Calbiochem®	440202
PageRuler™ Protein Ladder	ThermoFisher Scientific Inc.	#1811 (Plus) #26634 (Broad R.)
Recombinant human epidermal growth factor (EGF)	PeproTech	AF10015 1MG
Recombinant mouse epidermal growth factor (EGF)	BioTrend	C3150955
RQ1 RNase-Free DNase	Promega	M6101
RevertAid™ H-Minus Reverse Transcriptase	Thermo Fisher Scientific Inc.	EP0751
TaqMan GeneExpression PCR-Mastermix	Thermo Fisher Scientific Inc.	4370074
Temozolomide (TMZ)	Sigma Aldrich	T2577
M-MuLV Reverse Transcriptase	New England Biolabs	M0253L
N2 Supplement	Life Technologies	17502048
Insulin, human	Sigma Aldrich	I9278

Chemicals

	Producer	**Product – No.**
30% (w/v) Acrylamide / Bis Solution 29:1	Serva Electrophoresis GmbH	1610156
L-Alanine	Carl Roth®	3076.1
Ammonium peroxodisulfate (APS)	Carl Roth®	9592.2
Bromophenol blue	Fluka Chemie GmbH	18030
Bovine Serum Albumin (BSA)	Carl Roth®	11930.03
Calcium chloride (CaCl)	Carl Roth®	A119.1
Chloroform	Carl Roth®	6340.2
Casein	Carl Roth®	T145.3
4′,6-Diamidino-2-Phenylindole (DAPI)	Sigma Aldrich	D8417
Diethylpyrocarbonate (DEPC) Water	Carl Roth®	T143.5
Developer concentrate	Dürr Dental	584-08-7
Double distilled Water (ddH_2O)	Carl Roth®	3478.1
Digitonin	Merck	300410
Dipotassium hydrogenphosphate (K_2HPO_4)	Merck	1.05104.1000
Dithiothreitol (DTT)	Sigma Aldrich	43815
Ethylendiaminetetraacetic acid disodium salt dihydrate EDTA	Carl Roth®	8043

Ethanol absolute 96%	Carl Roth®	K928.4
Fixier concentrate	Dürr Dental	03398
D-(+)-Glucose	Carl Roth®	X997.2
Glycine	Carl Roth®	3908.2
Glycerol	Carl Roth®	3783.1
Hydrochloric acid (HCl)	Carl Roth®	K025.1
Isopropyl	Merck	1.09634.2500
Korsolex basic	Bode	972679
L-Glutamine	Thermo Fisher Scientific Inc.	HN08.1
Magnesium chloride ($MgCl_2$)	Carl Roth®	2189.2
Methanol	Carl Roth®	8388.2
Parafomaldehyde (PFA), 4% in PBS	Thermo Fisher Scientific Inc.	J19943.K2
Potassium chloride (KCL)	Merck	1.04936.1000
Roticlear	Carl Roth®	A538.5
Sodium bicarbonate ($NaHCO_3$)	Sigma Aldrich	55761
Sodium chloride (NaCl)	Carl Roth®	3957.1
Sodium citrate ($C_6H_5Na_3O_7 \cdot 2\ H_2O$)	Carl Roth®	3580.1
Sodium dodecyl sulfate (SDS)	Serva Electrophoresis GmbH	20765
Sodium hydroxide (NaOH)	Carl Roth®	9356.1
Sodium-Orthovanadate ($NaVO_4$)	Sigma Aldrich	56508
Sodium phosphate dihydrate ($Na_2HPO_4 \bullet 2\ H_2O$)	Merck	1.06580.1000
$pd(N)_6$ Random Hexamer 5‘-Phosphate Sodium Salt	Amersham	72166-05KU
Solvent Black 3 / Sudan Black	Carl Roth®	0292.1
Tetramethylethylene diamine (TEMED)	Carl Roth®	2367.1
Trisaminomethane (Tris) & Tris-HCl	Sigma Aldrich	T1378 & T3252
Triton-X100	Merck	1.08603
Trypan Blue [0,4 %]	Sigma Aldrich	T8154
Tween 20	Sigma Aldrich	8.22184.0500
Urea	Carl Roth®	X999.2

Ready-made buffers and media

	Producer	Product-No.
Accutase	Gibco™	11599686
DMEM (Dulbecco's Modified Eagle's medium)	Gibco™	42430082
DMEM/F12 (1:1) Nutrient Mix (Ham)	Gibco	113200033
Dimethyl sulfoxide (DMSO) - 0.01% (v/v))	Sigma Aldrich	D2650
EMEM (Eagle's Minimum Essential medium)	Sigma Aldrich	M0325
Fetal bovine serum (FBS)	Thermo Fisher Scientific Inc	A5256701
F12 Nut Mix GlutaMAX™	Gibco™	31765027
GlutaMAX (100x)	Gibco™	35050061
Hibernate®-A	Gibco™	A1247501
Immersol 518 F	Zeiss	4449620000000
Immu-Mount™	Epredia	9990402
MEM (Minimal essential medium) NEAA (Non essential amino acids) 100x	Gibco™	11140050
2-Mercaptoethanol (100x)	Life Technologies	21985023
Neurobasal® Media	Gibco™	21103049
Halt™ Phosphatase Inhibitor Cocktail (100x)	Thermo Fisher Scientific Inc	78420
Halt™ Protease Inhibitor Cocktail (100x)	Thermo Fisher Scientific Inc.	87786
Penicillin / Streptomycin [10.000 U/mL]	Thermo Fisher Scientific Inc.	15140122
RBC Lysis Buffer	Invitrogen	00433357
Reblot Plus 10x Stripping Solution	Merck	2504
RQ1 DNase 10x Reaction buffer	Promega	M198A
TRIzol® Reagent	Ambion	15596018
Trypsin- EDTA Solution	Sigma-Aldrich	T4299
Tissue-Tek O.C.T Compound	Sakura	94-4583x12
TripLE™ Express	Gibco™	12604-013
VitroGel® IKVAV High Concentration	TheWell Bioscience	TWG007
VitroGel® Cell Recovery Solution	TheWell Bioscience	MS03-100
VitroGel® Dilution Solution I	TheWell Bioscience	MS01-50

Prepared solutions, buffers and media

Solution / Buffer	Composition	Amount // Concentration
Blocking- Buffer for Immunofluorescence (IF) (Cells)	BSA (3 %) PBS	450 mg 15 mL
Blocking- Buffer for IF (Cryosections & Tissue)	BSA (0,1 %) Glycin (0,2 %) TBS buffer	50 mg 100 µL 50 mL
DMEM-Cell Media	DMEM FKS (10 %) Pen/Strep (1 %) 2 mM L-Glutamin	500 mL 56.8 mL 5.68 mL 5.68 mL
DMEM/F12-Cell Media	DMEM/F12 (1:1) Nutrient Mix BSA B27 Supplement Pen/Strep (1%) Heparin (Stock 133 mg/mL) EGF (mouse, fresh) bFGF (bovine, fresh)	500 mL 500 mg (1 mg/mL) -15 mL 10 mL 5 mL 2 µg/mL 20 ng/mL 20 ng/mL
EDTA 0.5 M	EDTA H_2O	186.1 g 1 L pH 8 (NaOH)
Electrode Buffer	Tris Glycin SDS In H_2O	7.6 g 36 g 2.5 g 2.5 L pH 8.2-8.3
EMEM/F12-Cell Media	EMEM #M0325 F12 #31765027 FKS (10%) Pen/Strep (1%) 2 mM L-Glutamin	250 mL 250 mL 56.8 mL 5.68 mL 5.68 mL
F12/B27 Cell Media	F12 Nut Mix GlutaMAX™ Pen/Strep (1%) B27 Supplement EGF (human, fresh) bFGF (human, fresh)	485 mL 5 mL 10 mL 10 ng/mL 10 ng/mL
GBO Media	DMEM/F12 (1:1) Nutrient Mix Neurobasal® Media GlutaMAX NEAAs Pen/Strep (1 %) N2 Supplement B27 Supplement Amphotericin B (fresh, stock 250 mg/mL) Mercaptoethanol (fresh) Insulin (2.5 µg/mL)	250 mL 250 mL 5 mL 5 mL 5 mL 5 mL 10 mL 1:500 1:1000 1:4000
H^+GPSA Cell Media	Hibernate A GlutaMAX (100x) Pen/Strep Amphotericin B (250 mg/mL)	500 mL 5 mL 5 mL 1 mL
Protein Lysis Buffer	Tris NaCl Trition-X-100 EDTA Orthovanadate	5 mM 10 mM 0.1% (v/v) 0.2 mM 2 mM

	Protease & Phosphatase Inhibitor 100x In H_2O	1x pH 7.2
Phosphate-buffered saline (PBS) pH 7.2	NaCl Na_2HPO_4 KCl K_2HPO_4 dH_2O	40 g [137 mM] 7.2 g [10 mM] 1 g [2 mM] 1.2 g [1.8 mM] in 5 L
Sample Buffer	Tris Glycerol SDS DTT (fresh prior use) In H_2O	62.5 mM 10% 2% 10 mM pH 6.8
Separating gel buffer	Tris SDS In H_2O	1.5 M 0.4% pH 8.8
Stacking gel buffer	Tris SDS In H_2O	0.5 M 0.4% pH 6.8
Transfer buffer	Tris Glycine Methanol In H_2O	25 mM 192 mM Glycine 10% pH 9
Tris-buffered saline (TBS)	Tris-HCl (pH 7.5) NaCl EDTA dH_2O	6.057 g [20 mM] 20.454 g [0.14 mM] 5 mL [1 mM] in 2.5 L
TBS-T buffer	TBS buffer Tween 20	2.5 L 2.5 mL [0,1%]
Hydrogel cell fixative solution (4 % PFA)	PFA PBS	40 g 800 mL

Cell lines

	Description	**Source**
SH-SY5Y	Neuroblastoma	American Type Culture Collection (ATCC)
Rat sham 39 [161]	Neural progenitor cells (NPC)	Adult male Long Evans rats, spinal cord derived cells
GBM Primary Culture	Glioblastoma	Neurosurgery UKSH – anonymized patient material
GSCs Primary Culture	Glioblastoma	Neurosurgery UKSH – anonymized patient material
Glioblastoma Organoids (GBO)	Glioblastoma	Neurosurgery UKSH – anonymized patient material

This study was conducted with patient-derived GBM cells and organoids/tumoroids (GBO). Freshly dissected tissue samples were kindly provided by the Department of Neurosurgery of the University Medical Center Schleswig-Holstein (UKSH, Kiel, Germany), with the approval of the Ethics Committee of the University of Kiel, Germany and in accordance with the Helsinki Declaration of 1975 as amended. The patients consented the use of their tumor tissue (file reference: D524/17).

According to World Health Organization criteria (WHO), the tissue samples were diagnosed and classified as IDH wild-type glioblastoma, CNS WHO grade 4 by the University Medical Center Hamburg-Eppendorf (UKE, Hamburg, Germany).

Rat sham 39 NPCs were generated as described before, and cell aliquots were used during this study [161]. Animal experiments were carried out in compliance with the European Union directive on animal protection used for scientific purposes. All protocols and procedures were approved by the Animal Care and Use Committee of the University Medical Center Schleswig-Holstein (UKSH, Kiel, Germany; 2005, 2007, 2008 [V 312–72241.121-35(34-4/05)], and 2009 [V 312–72241.121-35(77-6/09)]).

Antibodies

	Marker & Dilution	Specifity	Species	Producer	Product No.
Antibodies Western Blot (WB)	GAPDH **1:200** (WB)	*Glyceraldehyde-3 phosphate dehydrogenase, anti human*	Mouse	Santa Cruz Biotechnology Inc.	Sc-47724
	MSI1 **1:200** (WB)	*Musashi (Drosophila) homolog 1, anti human/rat*	Mouse	R&D Systems	MAB2628
	IGFBP5 **1:400** (WB)	*insulin-like growth factor-binding protein 5, anti human*	Rabbit	Santa Cruz Biotechnology Inc.	sc-13093
	EphA5 **1:150** (WB)	*Ephrin-type-A-receptor 5, anti human*	Rabbit	Santa Cruz Biotechnology Inc.	Sc-927
	pAkt (Thr308) **1:200 & 1:250** (WB)	*Protein Kinase B, anti rat*	Rabbit	Cell Signaling	9275
	p-GSK3β (Ser9) **1:250** (WB)	*Phospho-Glycogen synthase kinase-3, anti human/rat/Mouse*	Rabbit	Cell Signaling	9336
	PCNA **1:1000** (WB)	*Proliferating-Cell-Nuclear-Antigen, anti rat*	Mouse	Cell Signaling	2586
	pSTAT5 (Tyr694) **1:250** (WB)	*Signal transducer and activator of transcription 5, anti rat*	Rabbit	Cell Signaling	9351
	Hsp90 **1:1000** (WB)	*Heat shock protein 90, anti rat*	Rabbit	Santa Cruz Biotechnology Inc.	Sc-7947
	HRP-coupled secondary AB **1:10.000** (WB)	Anti-Mouse	Donkey	Thermo Fisher Scientific	A16011
	HRP-coupled secondary AB **1:12.500** (WB)	Anti-Rabbit	Donkey	Thermo Fisher Scientific	A16035

	Marker & Dilution	Specifity	Species	Producer	Product No.
Antibodies Immunofluorescence (IF)	GFAP **1:500** (IF)	*glial fibrillary acidic protein, anti human*	Mouse	Sigma Aldrich	MAB3402
	S100b **1:5000** (IF)	*S100 calcium-binding protein B, anti human*	Rabbit	Sigma Aldrich	S2644
	K**i67** **1:200** (IF)	*Antigen Kiel 67, anti human*	Rabbit	Santa Cruz Biotechnology Inc.	sc-15402
	Klf4 **1:100** (IF)	*Krüppel-like factor 4, anti human*	Rabbit	Sigma Aldrich	MAB-37846
	Sox2 **1:200** (IF)	*sex-determining region Y-box 2, anti human*	Rabbit	Santa Cruz Biotechnology Inc.	sc-20088
	MSI1 **1:200** (IF)	*Musashi (Drosophila) homolog 1, anti human/rat*	Mouse	R&D Systems	MAB2628
	CD133 **1:200** (IF)	*Cluster of differentiation 133, anti human*	Goat	Santa Cruz Biotechnology Inc.	sc-23797
	CD68 **1:200** (IF)	*cluster of differentiation 68, anti human*	Mouse	Santa Cruz Biotechnology Inc.	sc-20060
	CD3 **1:200** (IF)	*cluster of differentiation 3, anti human*	Rabbit	Thermo Fisher Scientific	PA5-29387
	CD11b **1:250** (IF)	*integrin alpha M (ITGAM), anti human/rat*	Mouse	Santa Cruz Biotechnology Inc.	sc-1186
	OCT4 **1:200** (IF)	*octamer binding transcription factor 4, anti human*	Rabbit	Cell Signaling	2750
	Iba1 **1:1000** (IF)	*calcium-binding adapter molecule 1, anti human*	Goat	Abcam	ab5076
	vWF **1:100** (IF)	*Von Willebrand factor, anti human*	Mouse	Santa Cruz Biotechnology Inc.	sc-53465
	IGFBP5 **1:400** (IF)	*insulin-like growth factor-binding protein 5, anti human*	Rabbit	Santa Cruz Biotechnology Inc.	sc-13093
	H2BK **1:400** (IF)	*histone cluster 1 H2B family member K, anti human*	Rabbit	Biorbyt	orb184226
	SKI **1:800** (IF)	*SKI proto-oncogene, anti human*	Rabbit	Thermo Fisher Scientific	PA5-66852
	cCaspase3 **1:200** (IF)	*Cleaved Caspase 3, anti human*	Rabbit	Cell Signaling	9661
	Alexa Fluor 555 **1:1000** (IF)	Anti-Rabbit	Donkey	Life Technologies	A31572
	Alexa Fluor 488 **1:1000** (IF)	Anti-Rabbit	Donkey	Life Technologies	A21206
	Alexa Fluor 555 **1:1000** (IF)	Anti-Goat	Donkey	Life Technologies	A21432
	Alexa Fluor 555 **1:1000** (IF)	Anti-Mouse	Donkey	Life Technologies	A31570
	Alexa Fluor 488 **1:1000** (IF)	Anti-Mouse	Donkey	Life Technologies	A21202

4. Methods

4.1 Cell biological techniques

4.1.1 Cell cultivation

Patient-derived glioblastoma cells

Patient-derived more differentiated GBM cells and glioma stem-like cells (GSCs) of human origin were obtained by dissociating tumor material retrieved during surgical procedures carried out at the Department of Neurosurgery, University Medical Center Schleswig-Holstein, Kiel, Germany. More differentiated GBM primary cells were cultured in DMEM with 10% FBS, 1% penicillin-streptomycin and 2 mM L-glutamine. Cell Media was changed every 2-3 days. When sufficient confluence of 80-90% was achieved, the cells were washed with PBS, detached with trypsin and passaged. Primary GSCs were cultured under stem-like conditions, using F12 medium supplemented with B27 (serum-free), 2 mM L-glutamine, 1% penicillin-streptomycin, and 10 ng/mL of freshly added human EGF and human bFGF. The cells were subcultured once every week using Accutase to separate the neurospheres. All primary cells were cultured at 5% CO_2, 95% relative humidity, and 37°C. For passaging once a week, cells were typically seeded at a density of 150,000 cells/small flask.

Patient-derived glioblastoma organoids (GBO) – Preparation and cultivation

Reliable generation of patient-derived human glioblastoma organoids/tumoroids (GBOs) required immediate processing of freshly resected tissue. Thus, the tissue was prepared on the same day of surgery according to the protocol published by Jacob *et al.* 2020 [162]. The obtained tissue sample was transported to the laboratory in Hibernate A medium and transferred under sterile conditions into a petri dish containing H+GPSA medium. Tissue processing was performed under a stereomicroscope using a fine dissection scissor. The specimen was chopped into fragments of approximately 0.5-1 mm in diameter. During this step, fragments containing substantial necrosis and any visible surrounding non-tumor tissue were removed to enrich for viable tumor material. The tissue fragments were washed in H+GPSA medium to remove debris generated during mincing. Furthermore, to reduce contamination by red blood cells, the cell fragments were incubated in RBC lysis buffer for 10 minutes at room temperature (RT) under gentle rotation at 120 rounds per minute (rpm). After incubation, the RBC lysis buffer was aspirated, and the cell fragments were washed thoroughly with H+GPSA medium to remove lysed cell material. The washed tumor fragments were transferred into ultra-low attachment 6-well plates containing 4mL/well of

GBO medium, consisting of 50% DEMEM/F12 and 50% Neurobasal medium supplemented with 1x GlutaMAX, 1x NEAAs, 1% penicillin-streptomycin, 1x N2 supplement, 1x B27 supplement without vitamin A, 1x 2-mercaptoethanol, and human insulin (2.5 µg/mL). Cultures were maintained on an orbital shaker at 120 rpm in a humidified incubator at 37°C and 5% CO_2. Medium was renewed by exchanging approximately 75% of the medium after 24 h of GBO preparation, achieved by tilting the plate to ~45° and aspirating the supernatant without disturbing the organoids. Subsequently, the GBO medium was changed every 48 h. The whole process of GBO preparation is depicted in Figure 3.

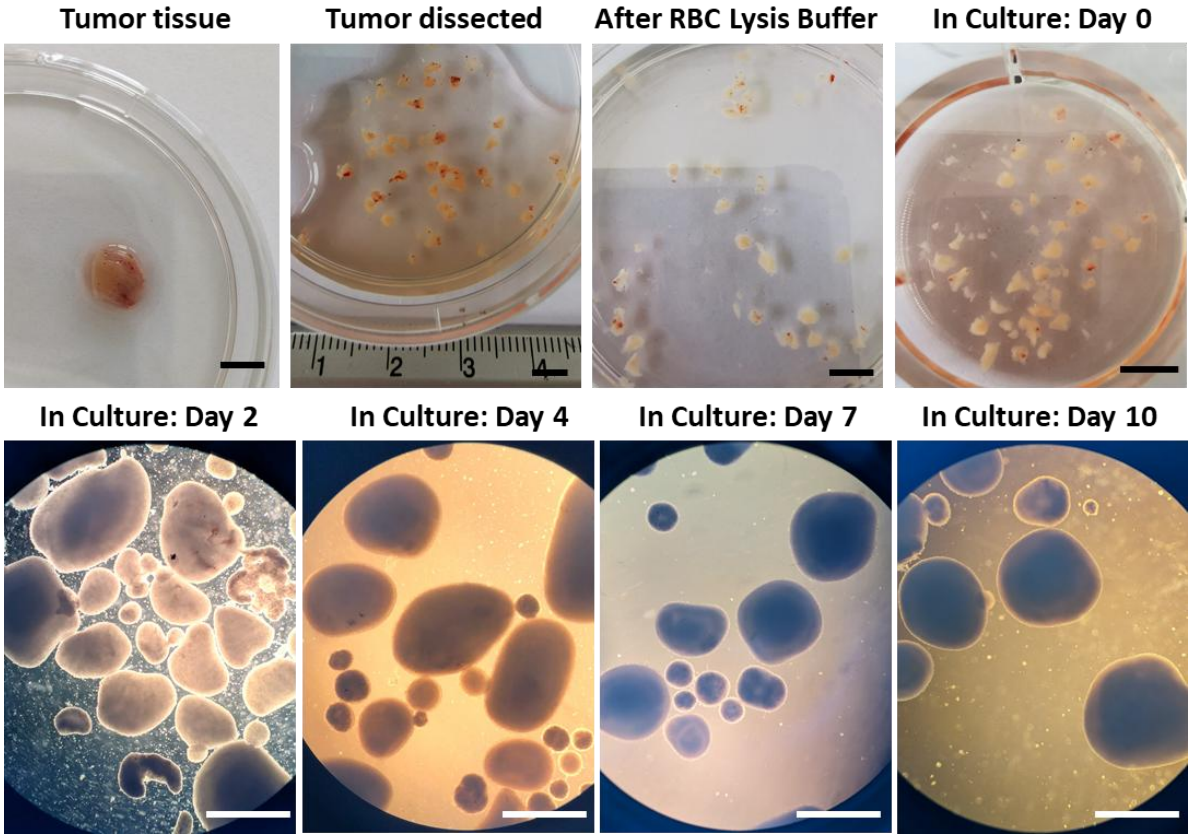


Figure 3 – GBO preparation based on Jacob *et al.* 2020 [162]. The resected tumor tissue was dissected in smaller pieces, and red blood cells were depleted using RBC lysis buffer. GBOs were cultured in ultra-low attachment 6-well plates. The scale bar of the upper row represents 0.5 cm. GBO morphology changes over time are depicted in the lower row with a scale bar representing 1 mm.

During the first week, tumor fragments frequently released cellular and blood-derived debris, visible due to transient medium turbidity. Depending on tissue quality and patient-specific tissue characteristics, fragments generally formed round, compact organoids within the first week. GBOs could be grown *in vitro* for extended periods without fetal calf serum or growth factor supplementation, replicating the intra- and intertumoral heterogeneity of GBMs in terms of cellular variety, histological characteristics and gene expression patterns of the original tumors.

SH-SY5Y

The human SH-SY5Y cell line was cultured in a 1:1 mixture of EMEM and F12, supplemented with 10% FBS, 1% penicillin-streptomycin, and 2 mM L-glutamine in a humidified incubator at 37°C and 5% CO_2. The cells were passaged at an approximate 80% confluence. Since the SH-SY5Y cells exhibit two subpopulations – an adherent cell type with rounded, nonpolar cell bodies and a few short neurite-like processes in their undifferentiated state, as well as a nonadhering cell suspension type with rounded cell bodies [163] – special care was taken during passaging to recover both subpopulations and to generate a homogeneous single-cell suspension.

Before passaging, fresh culture medium was pre-equilibrated in the incubator for approximately 15 minutes. In addition to the medium required for reseeding, an extra aliquot of medium was pre-warmed and used for washing and resuspension steps. First, the culture supernatant containing the non-adherent cells was carefully collected and transferred into a 15 mL tube. The culture flask was washed with PBS to recover remaining suspended cells. Typically, 2 mL PBS was used for small culture flasks and 5 mL PBS for larger culture flasks. The PBS was combined with the previously collected suspension cells.

The suspension fraction was centrifuged for 5 minutes at 1,100 rpm. In parallel, the processing of the adherent fraction was continued. Adherent SH-SY5Y cells were detached at RT using a dilution of 0.25% Trypsin/EDTA in PBS, with detachment monitored microscopically. The applied volume depended on the culture vessel size and was adjusted as followed: 385µL/6-well, 1mL/small flask, and 3mL for a large flask. Cells were incubated for approximately 3 minutes at RT, and detachment was supported by gently tapping the flask. Once detached, the cells were collected in 5mL pre-warmed culture medium, and the flask was rinsed with culture medium to maximize cell recovery. The rinsed flask with the detached cells in culture medium was kept upright while the suspension fraction was further processed.

After centrifugation of the suspension fraction, the supernatant was carefully aspirated. The resulting cell pellet was resuspended in 0.25% Trypsin/EDTA in PBS (1mL) and incubated for approximately 3 minutes. Afterwards, the cells were gently pipetted three times with a 5mL pipette to dissociate them into single cells. The enzymatic reaction was then stopped by adding 5mL of pre-warmed culture medium. This cell suspension was subsequently combined with the detached adherent fraction and pooled into one centrifuge tube.

The combined cell suspension was centrifuged (5 minutes, 1,100 rpm), and the supernatant was carefully removed. The cells were resuspended in 1 mL pre-equilibrated cell medium and mixed slowly to obtain a uniform cell suspension. Subsequently, up to 5 mL culture medium was added. For reseeding, cells were counted, and the corresponding volume was

taken from the middle of the freshly mixed cell stock to ensure an even distribution of both subpopulations. After seeding, flasks were moved in 10 crosswise motions with brief stops between each movement to promote homogeneous cell distribution. For passaging once a week, cells were typically seeded at a density of 300,000 cells/small flask.

Rat cells

NPCs were generated from adult male Long Evans rats, using the sham-operated control animals (details have been published previously [161]) and cultured in stem cell medium consisting of DMEM/F12 Medium, supplemented with B27 without vitamin A, 1 mg/mL BSA, 2 µg/mL heparin, and 20 ng/mL of freshly added mouse EGF and bovine bFGF in a humidified incubator at 37°C and 5% CO_2. Since the cells tend to form spheres and attach to the culture flask, the cells were dissociated once a week using Accutase.
First, the culture supernatant containing cell spheres was carefully collected, and the culture flask was washed with PBS. The PBS was combined with the previously collected supernatant and centrifuged for 5 minutes at 1,100 rpm. In parallel, adherent cells were detached at RT using Accutase (approximately 500 µL/small flask up to 1mL/large flask), incubated for approximately 3 minutes. The detachment was supported by gently tapping the flask. Once detached, the cells were collected in 5mL culture medium. After centrifugation of the previously collected supernatant, the cell medium was carefully aspirated, and the cell pellet was resuspended in 500µL Accutase and gently mixed by pipetting up and down to dissociate them into single cells. The dissociation process was monitored using the microscope. The enzymatic reaction was then stopped by adding 5mL of culture medium. The cells were pooled and centrifuged (5 minutes, 1,100 rpm), and the supernatant was carefully removed. For reseeding, cells were resuspended in cell medium, counted, and the corresponding volume was taken from the middle of the freshly mixed cell stock to ensure an even distribution of both subpopulations. After seeding, flasks were moved in 10 crosswise motions with brief stops between each movement to promote homogeneous cell distribution. For passaging once a week, cells were typically split at a ratio of 1:20/small flask.

4.1.1.1 Determination of viable cell numbers

For routine passaging as well as setting up experiments, cell density was determined using a Neubauer hemocytometer. Cells were enzymatically detached from the culture flask as described in section 4.1.1 and resuspended in fresh culture medium. The cell suspension was centrifuged at 1.100 rpm for 5 minutes. After carefully removing the supernatant, the cell pellet was resuspended in an appropriate volume of culture medium.
To assess viability and enable discrimination of dead cells, 10 µL of the resuspended cell suspension was mixed 1:1 with 10 µL of 0.4% Trypan Blue solution. The mixture was then loaded into a Neubauer counting chamber, and viable unstained cells were counted. For each sample, cell numbers were recorded across the four large corner squares and averaged. The concentration of viable cells was calculated by multiplying the mean count by the hemocytometer conversion factor 10^4 to obtain cells per milliliter and correcting for the 1:1 dilution introduced by Trypan Blue (see Equation 1).

$$\frac{Cells}{mL} = \frac{\sum(cell\ count\ 4\ quadrants) \cdot 2 \cdot 10^4}{4} \qquad \text{(Eq.1)}$$

4.1.2 3D Hydrogel-cultures

Preparation of GBM/GSC hydrogels

To prepare 3D hydrogels with GBM/GSC primary cells, cell suspensions with $24x10^6$ cells/mL were prepared in 5x respective cell media containing either 5x critical growth factors in case of GSCs or 5x FBS concentration in case of more differentiated GBM cells. For the hydrogel, VitroGel® IKVAV-Hydrogel was prepared in Eppendorf tubes using a 1:5 dilution to correspond to physiological brain stiffness (1,389 to 1,895kPa) [164], and incubated for 10 minutes at RT. Since *in vitro* mFUS treatment was applied using the Covaris M220 as described in section 4.1.3, the hydrogel cultures were prepared directly in the 1 mL Covaris tubes. In detail, Covaris tubes were pre-incubated with 1 mL PBS to increase the adhesion of the hydrogel to the glass wall of the tube. After the hydrogel incubation period, the PBS was aspirated, and the cell suspension was added to the hydrogel solution at a ratio of 4:1 (v/v). The hydrogel-cell mixture was gently stirred and slowly pipetted without introducing air bubbles to ensure uniform mixing. The mixture was transferred directly into the Covaris tubes, which were covered with Parafilm. To ensure an adequate supply of nutrients, the Covaris tubes were always filled halfway with hydrogel (400 µL), leaving space for the cell medium. The hydrogels were polymerized for 45 minutes

in a humidified incubator at 37°C with 5% CO_2, avoiding sudden movements during the incubation period. After polymerization, the hydrogel-cell mixture was carefully covered with the respective cell medium and cultured for at least 24 h before further usage.

Preparation of GBO hydrogels

For 3D hydrogel cultures with primary GBOs, approximately 30 organoids were transferred from the ultra-low attachment 6-well plate into the Covaris tube using a pipette tip with a cut tip. After preparing the VitroGel® IKVAV as described in the previous section, and incubation for 10 minutes at RT, any transferred GBO medium was aspirated from the GBOs. The hydrogel was mixed with GBO medium in a ratio of 4:1 (v/v) and transferred onto the GBOs in the Covaris tubes (filled halfway; 400 µL). After 5 to 10 minutes at RT, the hydrogel began to polymerize, allowing for adjustment of the GBO position in the hydrogel using a tweezer. After the GBOs were evenly distributed in the hydrogel, the Covaris tubes were covered with Parafilm and transferred into a humidified incubator at 37°C with 5% CO_2 for complete polymerization. After polymerization, the hydrogel was carefully covered with GBO medium and cultured for at least 24 h before further usage.

Cell recovery from a hydrogel

The enzyme-free VitroGel® Cell Recovery Solution was used to recover cells from the hydrogel. Prior use, the solution was heated to 37°C in a water bath. The hydrogel was washed twice with warm PBS and resuspended in 200 µL of recovery solution. After pipetting up and down several times, the hydrogel was transferred to a 15 mL tube containing 6 mL recovery solution to dilute 400 µL of hydrogel or 10 mL recovery solution to dilute 800 µL of hydrogel. The solution was mixed by pipetting 3 times using a 5 mL transfer pipette and incubated in a water bath for two minutes. This process was repeated twice, after which the solution was centrifuged at 1.100 rpm for 5 minutes at room temperature to retrieve the cell pellet. The cells were either seeded and further cultivated (see section 4.1.7 ELDA), used for Cytotoxicity assays (see section 4.2.1) or further processed for qPCR analysis (see section 4.2.7).
Subsequent RNA isolation involved resuspending the cells in 50 µL of extraction buffer from the ARCTURUS® PicoPure® RNA Isolation Kit. The mixture was heated at 42°C for 30 minutes, after which it was stored at -80°C until further processing.
For Cytotoxicity assays, the cell pellet was resuspended in the corresponding cell media and counted to normalize the received Cytotoxicity Data to the cells present at that time, as described in section 4.2.1.

GBO recovery from a hydrogel

To retrieve GBOs from a hydrogel culture, the GBOs were manually picked with a tweezer and cultured in GBO medium in ultra-low attachment 6-well plates until further processing. The GBOs from the peripheral area and the focal zone were picked and cultivated separately in different wells to examine regional differences using subsequent assays.

Cryofixation of a hydrogel

To prepare the whole hydrogel for cryofixation, the Covaris tubes were precooled on ice for approximately 30 minutes, after which 100 µL of the cell medium was discarded. The Covaris tube was sealed with a cotton wool and parafilm plug, and the cap was loosely screwed onto the Covaris tube to allow for pressure equalization. Using a long tweezer, the Covaris tube was slowly immersed in liquid nitrogen for approximately one minute. The Covaris tube was then cut cleanly using a rotatory tool (Proxxon Microtom 60/E) to remove the whole intact hydrogel, allowing for subsequent regional analysis. The whole intact hydrogel was stored at -80°C until further processing.

4.1.3 Mechanical focused ultrasound (mFUS) – Preparation & stimulation

During this study, the M220 ultrasound device with a 0.5 MHz solid-state transducer and geometrically focused acoustic energy made by Covaris® was used. The device applied ultrasound to the sample in a focal zone (see Fig. 4), initially developed as platform for fast and highly efficient FUS-induced mechanical preparation of biological samples. Continuous cooling of the sample prevented thermal damage to the sample and allowed the targeted use of the ultrasound-induced cavitation effect, whereby cavitation bubbles oscillated or grew to a critical size before collapsing and creating hydrodynamic shear stresses in the sample [165].

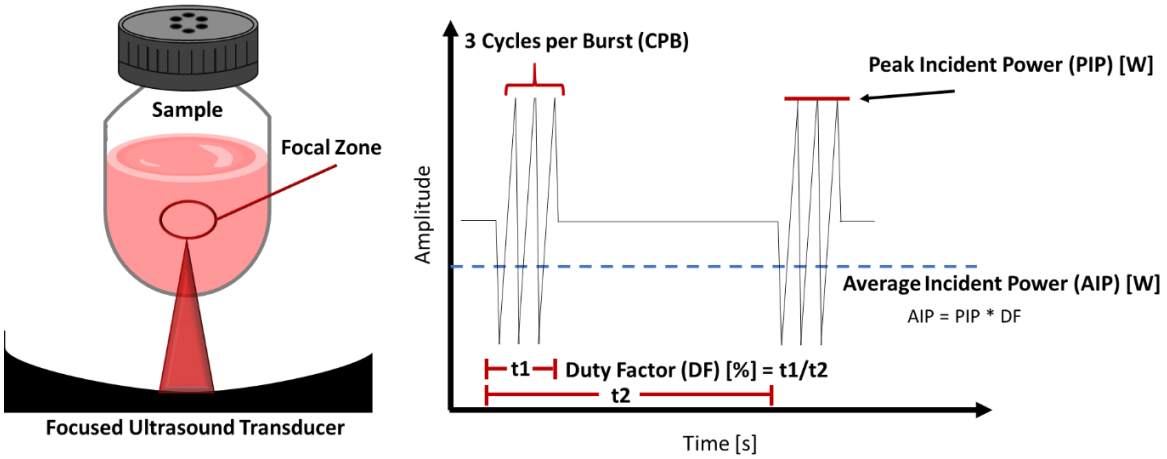


Figure 4 - Functionality and influencing factors of the mFUS transducer from Covaris®. **Left:** Focused acoustic energy is delivered in a controlled, non-contact way using a 0.5 MHz focused ultrasound transcducer. **Right:** The Average Incident Power (AIP) is the Peak Incident Power (PIP) multiplied by the Duty Factor (DF). The Transducer is driven by a train of electrical bursts. Each burst duration is defined by Cycles per Burst (CPB). The ON time is defined by the Duty Factor (DF).

The system allows the modulation of the Peak Incident Power (PIP), which describes the maximum amount of energy in a peak, the Cycles per Burst (CPB) and the Duty Factor (DF), which expresses the ratio between pulse duration and pulse repetition, and of the duration (seconds) to match the Average Incident Power (AIP) of the used mFUS settings [166]. All parameter sets used during this study are provided in Table 1.

Table 1 - mFUS Parameter sets used for this study.

Setting [AIP]	PIP [W]	CPB	DF [%]	Time [s]
5 Watts	*35*	*150*	*15*	*10*
11 Watts	*55*	*200*	*20*	*10*
15 Watts	*75*	*200*	*20*	*10*

For mFUS stimulation, we used 1 mL Covaris Tube sample vessels and prepared and operated the device according to the manufacturer's instructions. The sample was secured in the provided holder, and the depth at which the sample vessel was suspended in the water bath was tailored to our needs using a 3D-printed platform, allowing to lower the position of the focal zone.

4.1.4 Myelomeningocele (MMC) patch – Preparation and cultivation

The MMC patches were synthesized by the Department of Pharmaceutics and Biopharmaceutics, Kiel University, Germany, in collaboration with Prof. Dr. Regina Scherließ and Dr. Angelika Jüptner. The bottoms of 24-well plates were coated with a variety of MMC patch materials (see Table 2). To prepare a thin film of MMC patch, the patch material was dissolved in the solvent specified in Table 2. The solution was then stirred and poured directly into 24-well plates, or cast onto aluminium foil and cut to size manually for 24-well plates (casting method). A different way to produce MMC patches involved a process where a fine spray nozzle was used to spray the corresponding mixture of patch material and solvent (see Table 2) onto a roller. The layer was then dried, and the process could be repeated until the desired film thickness was reached (spraying method). A maximum of 0,02 g/cm^2 of Patch material was used to enable morphological assessment of the cells by light microscopy, which, depending on the coating material and the solvent used, corresponded to a coating thickness of max. 100 µm. The data were provided for consultation only and remain under the stewardship of the Department of Pharmaceutics and Biopharmaceutics, Kiel University, Germany, by Dr. Angelika Jüptner. A detailed fabrication procedure is expected to be described in a separate publication under Dr. Angelika Jüptner's supervision. In the following, the methodological description is restricted to the experimental handling and application of the supplied MMC patch materials.

Table 2 - Overview of patch materials, solvents, and manufacturing methods used for MMC patch production.

Patch Material	Solvent	Method used
5% Polyvinyl acetate	Chloroform	Casting method
10% Polyvinyl acetate	Chloroform	Casting method
10% Polyvinyl acetate	Acetone	Casting method
20% Polyvinyl acetate	Chloroform	Casting method
5% Polyvinyl acetate + 10% Polylactic acid	Chloroform	Casting method
5% Polyvinyl acetate + 10% Polycaprolactone	Chloroform	Casting method
10% Polyvinyl acetate + 10% Polycaprolactone	Chloroform	Casting method
15% Polyvinyl acetate + 10% Polycaprolactone	Chloroform	Casting method
20% Polyvinyl acetate + 10% Polycaprolactone	Chloroform	Casting method
20% Polyvinyl acetate + 20% Polycaprolactone	Chloroform	Casting method

30% Polyvinyl acetate + 10% Polycaprolactone	Chloroform	Casting method
10% Polyvinyl acetate + 10% Polylactic acid	Chloroform	Casting method
10% Polyvinyl acetate + 10% Polylactic acid	Chloroform	Spray method
10% Polyvinyl acetate + 10% Eudragit® NM	Chloroform	Casting method
5% Eudragit® NE	Water	Casting method
10% Eudragit® NM	Acetone	Casting method
10% Eudragit® NM	Chloroform	Casting method
10% Eudragit NM + 10% Polyvinyl acetate	Chloroform	Casting method
10% Vinnapas® Special	Acetone	Casting method
10% Vinnapas® Special	Chloroform	Casting method
5% Vinnapas® Special	Chloroform	Casting method
5% Vinnapas® Special + Polylactic acid	Chloroform	Casting method
5% Vinnapas® Special + Polycaprolactone	Chloroform	Casting method
10% Vinnapas® Special + 10% Polyvinyl acetate	Chloroform	Casting method
Vinnapas® Special	Ethylacetate	Spray method
Vinnapas® Special	Acetone	Spray method
5% Polyactid	Chloroform	Casting method
Gumosil AD (Silicone)	-	Casting method
Gumosil AD + Polyethylene glycol 300	-	Casting method

All solvents were evaporated under a hood prior to the plates being used for cell culture experiments. For the experiments, the 24-well plates were pre-rinsed with cell medium at least 48 h before the start of the experiment. SH-SY5Y cells were then seeded at a density of 100,000 cells/well in cell culture medium for at least 48 h. Corresponding uncoated control wells were treated in the same way. Morphological changes were assessed by brightfield microscopy after 24 h and 48 h, and representative images were acquired with the Axiovert 200 (Zeiss) to document cell morphology and overall condition. Cytotoxicity was measured after 48 h as described in section 4.2.1.

4.1.5 Artificial amniotic fluid preparation

The artificial amniotic fluid (aAF) formulation was developed based on an extensive literature review, with particular emphasis on the reported physiological ranges of salts and metabolites compiled from four key publications (Gillibrand *et al* 1969, Benzie *et al* 1974, Pettit *et al* 1979 and Oliveira *et al* 2002) [167–170], as well as the amino acid concentration compiled from three key publications (Levy *et al* 1969, Pettit *et al* 1980 and Naila *et al* 2022) [171–173]. Using literature-derived mean values (see Table 3), the aAF was designed to approximate the ionic composition (salt/electrolyte concentrations) and amino acid ratios of human amniotic fluid at gestational week 22 (E22), while also accounting for additional parameters relevant for neural tissue stability, like osmolality and avoidance of non-physiological electrolyte shifts, as described in the following.

Table 3 – Literature Review of amniotic fluid composition.

Component /Metabolite	**Gillibrand *et al.* 1969**	**Benzie *et al.* 1974**	**Pettit *et al.* 1979**	**Oliviera *et al.* 2002**	**Mean Literature [mM]**
Time	E22 [mM]	E22 [mM]	E17.4 [mM]	E13-20 [mM]	
Sodium	139.0	135.3	133.3 ± 3.2	134.08 ± 3.75	135.4 ± 2.19
Potassium	4.0	3.9	3.5 ± 0.2	3.79 ± 0.52	3.8 ± 0.18
Chloride	102.0	111.8			106.9 ± 4.90
Calcium			1.24 ± 0.35		1.24 ± 0.35
Magnesium			0.63 ± 0.1		0.63 ± 0.1
Glucose		36.4	49.01	46.88 ± 13.57	44.1 ± 5.51
Urea	24.00			23.03	23.5 ± 0.49

Amino Acid	**Levy *et al.* 1969**	**Pettit *et al.* 1980**	**Naila *et al.* 2022**		**Mean Literature [mM]**
Glycine	0.185	0.187			0.186 ± 0.001
L-Alanine		0.3241	0.295		0.309 ± 0.014
Glutamine	0.223		0.225		0.224 ± 0.001
Arginine	0.028	0.041			0.03 ± 0.007
Asparagine	-	-	-		-
Aspartic acid	-	-	-		-
Cysteine	0.071	0.041	0.066		0.06 ± 0.013

L-Glutamic Acid	0.107		0.041		0.07 ± 0.033
Glutamine	0.223		0.225		0.22 ± 0.001
Histidine	0.046		0.049		0.05 ± 0.001
Isoleucine	0.02	0.041			0.03 ± 0.011
Leucine	0.043	0.095			0.07 ± 0.027
Lysine	0.148		0.105		0.13 ± 0.021
Methionine	0.012	0.017			0.01 ± 0.003
Phenylalanine	0.038	0.059			0.04 ± 0.011
Proline	0.103	0.133	0.116		0.12 ± 0.012
Serine	0.119	0.034	0.076		0.08 ± 0.035
Threonine	0.139		0.118		0.13 ± 0.011
Trypthophan	-	-	-		0.00
Tyrosine	0.035	0.056			0.04 ± 0.011
Valine	0.067	0.187	0.129		0.09 ± 0.031
Ornithine	0.045	0.063			0.05 ± 0.009
Taurine	0.113	0.133	0.119		0.12 ± 0.009

All supplementations and their final target concentrations are summarized in Table 4 and are referred to throughout this protocol. To prepare 1 L of aAF, all mixing steps were performed under sterile conditions. Basal medium was prepared by combining 500 mL of EMEM (M3025, Sigma Aldrich) with 500 mL of F12 medium (31765027, Gibco™) (1:1). To allow for subsequent volume correction after salt and supplement addition, 200 mL of this mixture was removed and retained for later use, leaving 800 mL for supplementation. Supplements were pre-weighed in advance into separate tubes and added sequentially to promote complete dissolution. First, the sodium content was adjusted by adding sodium bicarbonate (8.286 g) and sodium citrate (1.698 g) to the medium one after another while stirring on a magnetic stirrer until the respective salts had dissolved. Afterwards, the following substances were added together: calcium chloride (0.132 g), magnesium chloride (0.07 g), potassium chloride (0.23 g), sodium chloride (2.405 g), urea (0.235 g), glucose (0.3367 g), glycine (9.5 mg), L-alanine (22.7 mg), and L-glutamine (4.11 mg).

After all supplements had dissolved, the pH of the solution was measured and, if required, adjusted cautiously using 1 N HCl. Since hyperchloremia has been associated with adverse

physiological effects on neural cells, such as acidosis and downstream cellular dysfunction, a strict upper limit was applied to prevent chloride levels from exceeding the physiological amniotic fluid range [174,175]. Therefore, chloride excess was avoided during pH adjustment, and pH correction with HCL was performed conservatively (max. 6 mL), prioritizing maintenance of the physiological chloride concentration over forcing the pH into a narrowly defined target, resulting in a slightly higher pH than stated in the literature with pH 7.1-7.3 (see Table 4) [176].

Once pH adjustment was completed or the HCl limit was reached, the retained basal medium was used to bring the solution to a final volume of 1 L. The bottle was stored at 4°C overnight to allow equilibration. On the following day, the solution was visually inspected for precipitation, and the pH was re-measured. The solution was monitored for at least 1 h to confirm relative pH stability before further processing.

Table 4 – Supplementation of salts and amino acids to create artificial amniotic fluid. mM = millimole, SD = Standard Deviation.

Component	F12/EMEM (1:1) [mM]	Literature Mean ± SD [mM]	Supplementation [mM]
Sodium	52.36	135.4 ± 2.19	44.53
Potassium	2.18	3.8 ± 0.09	1.62
Chloride	78.18	106.9 ± 4.90	27.75
Calcium	0.38	1.24 ± 0.35	0.43
Magnesium	0.16	0.63 ± 0.1	0.47
Glucose	7.78	44.1 ± 5,51	33.6
Urea		23.5 ± 0.49	23.5
Glycine	0.05	0.19 ± 0.001	0.13
L-Alanine	0.05	0.31 ± 0.014	0.25
Glutamine	0.19	0.22 ± 0.001	0.03
Arginine	0.56	0.03 ± 0.007	
Asparagine	0.51	0.00	
Aspartic acid	0.057	0.02	
Cysteine	0.066	0.06 ± 0.013	
L-Glutamic Acid	0.11	0.07 ± 0.033	
Glutamine	0.20	0.22 ± 0.001	

Histidine	0.07	0.05 ± 0.001	
Isoleucine	0.04	0.03 ± 0.011	
Leucine	0.08	0.07 ± 0.027	
Lysine	0.13	0.13 ± 0.021	
Methionine	0.02	0.01 ± 0.003	
Phenylalanine	0.03	0.04 ± 0.011	
Proline	0.15	0.12 ± 0.012	
Serine	0.05	0.08 ± 0.035	
Threonine	0.07	0.13 ± 0.011	
Trypthophan	0.01	0.00	
Tyrosine	0.04	0.04 ± 0.011	
Valine	0.07	0.09 ± 0.031	
Ornithine	0.00	0.05 ± 0.009	
Taurine	0.000	0.12 ± 0.009	
pH	7.5-7.8		
Osmolarity	300.66 mOsm/kg		

Once the preparation was considered stable and free of precipitates, the aAF was sterilized by filtration using a 0.2 µm sterile syringe filter and aliquoted into sterile 50 mL tubes (single-use aliquots). Aliquots were stored continuously at -30°C, and freeze-thaw events were minimized by thawing only one aliquot per use. Prepared aAF was used for a maximum period of one month, after which a fresh batch was prepared. As part of quality control, pH was measured during preparation and after thawing a fresh aliquot prior use.

4.1.6 Inhibition and stimulation experiments

Stimulation with temozolomide

Patient-derived more differentiated GBM cells or GSCs were embedded in a 3D hydrogel as described in section 4.1.2, exposed to mFUS (5 and 11 Watts) 24 h post-embedding as described in section 4.1.3, and recovered from the hydrogel 48 h after mFUS as described in section 4.1.2, including a medium exchange during the post-stimulation phase. Unstimulated controls underwent identical handling without ultrasound exposure. The recovered cells were seeded into 6-well plates at 25,000 cells per well in a total volume of 2 mL/well cell media. For each mFUS condition, wells were allocated to treatment groups including untreated control, vehicle control (DMSO), and TMZ (50 µM). TMZ working concentrations were prepared from a 100 mM Stock solution in DMSO, while vehicle controls received the same DMSO volume as TMZ-treated wells. Cell cultures were maintained under treatment conditions for up to 10 days. Media was refreshed every three days. Cytotoxic effects were assessed three and 10 days after mFUS treatment as described in section 4.2.1.

Stimulation with erythropoietin

Rat NPCs were expanded in standard stem cell conditions as described in section 4.1.1 and then seeded into 6-well plates at 350,000 cells per well approximately 24 h prior stimulation (see combined inhibition experiments with AG490) or with 50,000 cells per well for up to 8 days prior stimulation (combined aAF stimulation experiments), until a confluency of 80% was reached. Epo was applied from a 20 µg/mL stock prepared in sterile-filtered PBS supplemented with 0.1 % BSA to minimize protein adsorption during handling and storage at a final concentration of 20 ng/mL. The cells were stimulated experiment-specific for up to 8 days (daily media change). An unstimulated control underwent identical handling without inhibitor stimulation. To assess the influence on proliferation and cytotoxicity, cell numbers were determined after 2, 4 and 8 days of stimulation. The cell medium was changed daily. Further downstream analyses included cytotoxicity assays, Western blots and qPCR as described in the following sections.

Stimulation with artificial amniotic fluid

Stimulation experiments with aAF were performed using rat NPCs or human SH-SY5Y. Rat NPCs were seeded into 6-well plates at a density of 350,000 cells per well 24 h prior aAF stimulation (see AG490 inhibition) or of 50,000 cells per well up to 8 days prior aAF stimulation, until a confluency of 80% was reached. Once confluency was reached, aAF was applied in different ratios of 0% (control, cell media), 30%, 55%, 80% and 100%, diluted in cell culture medium. To assess the influence on proliferation, the cell numbers were determined after 4 and 7 days of stimulation. Cytotoxicity assays involved performing cell counts and taking samples of the supernatant daily for eight consecutive days, starting at day one. The cell medium was changed every two days. For qPCR analysis, daily media change was performed, and the cells were stimulated for up to 8 days.
For human SH-SY5Y, the cells were seeded into 6-well plates at a density of 400,000 cells per well three days prior stimulation. aAF was applied in different ratios of 0%, 10%, 15%, 20%, 30%, 55%, 65%, 80% and 100%, diluted in the corresponding cell culture medium (EMEM/F12 + 10% FBS) without adjusting the FBS concentration to the total volume. To assess the influence on proliferation, the cell numbers were determined after 4 days of stimulation, with media change every two days. Cytotoxicity assays were performed on days 4 and 8, with media change every two days.

Inhibition of PI3-Kinase with LY294004

Inhibition experiments with the Phosphoinositide 3-kinase (PI3K) inhibitor LY294002 (Stock 10 mM, treatment with 3-6 µM, diluted in DMSO) were conducted with 3D hydrogel GBM cell cultures 30 minutes to one-hour prior mFUS stimulation (15 Watts, media exchange with inhibitor), followed by either qPCR readout 24 h after mFUS treatment as described in sections 4.2.7 to 4.2.9 or Western blot analysis processed directly after mFUS treatment (duration approximately 20 minutes) as described in sections 4.2.4 to 4.2.6. Unstimulated controls underwent identical handling without ultrasound exposure and/or without inhibitor stimulation.

Inhibition of JAK2/STAT5/Akt with AG490

Inhibition experiments with the JAK2/STAT5/Akt signaling pathway inhibitor AG490 (Stock 100 mM, treatment with 10 µM) were performed using rat NPCs that had been expanded under routine conditions and seeded into 6-well plates at a density of 350,000 cells per well. To ensure that the targeted pathway was already pharmacologically suppressed before Epo

and/or aAF exposure, the cells were pre-treated with 10 µM AG490 in cell medium 30 minutes prior stimulation with Epo and/or aAF. Subsequently, Epo stimulation and/or aAF stimulation was carried out in the continued presence of AG490 (medium exchange with corresponding stimulants ± AG490). For Western blot analysis, short-term signaling was analyzed. Therefore, co-stimulation was performed for 15 minutes prior to preparing the cells for Western blot analysis. For assessing the cytotoxicity, the cells were stimulated with the corresponding inhibitor and stimulants (Epo/aAF ± AG490) for two days prior the supernatants being collected and viable cells were counted as described in section 4.2.1. No medium change was performed during these two days. Inhibitor conditions were prepared in three replicate wells per group to ensure sufficient material for downstream analyses.

4.1.7 Extreme limiting dilution assay

Extreme limiting dilution analysis (ELDA) was conducted to assess the self-renewal capacity of more differentiated primary GBM cells. Therefore, GBM cells were embedded in 3D hydrogels as described in section 4.1.2, treated with mFUS (5 and 11 Watts) 24 h post-embedding as described in section 4.1.3, and recovered as described in section 4.1.2 48 h after mFUS treatment. An unstimulated control underwent identical handling without ultrasound exposure. The GBM cells were seeded in a serial dilution ranging from 1 to 3,200 cells per well in F12/B27 neurosphere medium using a 24-well plate with 1 mL medium/well. Therefore, three cell suspensions containing 100,000, 10,000 and 1,000 cells/mL were prepared, from which a limiting dilution series was seeded in duplicates. Absolute cell numbers after seeding were checked and verified to ensure accuracy of the dilution series. Further cells were cultured at a density of 50,000 cells/well and processed for qPCR analysis as described in sections 4.2.7 to 4.2.9. The culture was maintained for 7 days, after which the number of spheres per well as well and the number of wells containing spheres at each plating density were recorded, or the wells were processed for qPCR analysis. The obtained data were analyzed with an ELDA online software tool (http://bioinf.wehi.edu.au/software/elda).

4.2 Biochemical methods

4.2.1 Cytotoxicity assay

Cytotoxicity was quantified using the CytoTox-Fluor™ Cytotoxicity Assay according to the manufacturer's instructions, with fluorescence derived from a dead-cell protease activity present in culture supernatants. At defined experimental time points, cell culture supernatants from treated and corresponding control conditions were collected for analysis. For each sample, 50 µL of supernatant was transferred into a black, flat-bottom 96-well plate in technical duplicates. Additionally, medium blanks were included to enable background subtraction. To convert fluorescence signals into dead cell equivalents, a standard curve was generated. Therefore, the experiment-specific cells were counted and seeded in a dilution series by mixing defined volumes of stock cell suspension and cell medium to yield a fixed total volume of 900 µL per standard (see Table 5). Importantly, the cell numbers used for the standard curve were adjusted depending on the experimental setup to ensure that sample fluorescence values fell within the range of the standard curve.

Table 5 – Example of a preparation of a standard cytotoxicity assay series.

Cell No.	Cell Media [µL]	Cell suspension 600,000 Stock in 2.7 mL [µL]
0	900	0
50.000	675	225
100.000	450	450
150.000	225	675
200.000	0	900

For full lysis, 100 µL digitonin (825 µg/mL) was added to the standard dilution series, vortexed and incubated for 1 h at 37°C. After digitonin incubation, 50 µL of each lysed standard dilution was transferred to the black 96-well assay plate in technical duplicates, matching the sample volumes. 50 µL of the CytoTox-Fluor substrate solution, consisting of substrate buffer with bis-AAF-R110 diluted 1:1000, was added to all wells (samples, standards and blanks). The plate was incubated for 1.5 h at 37°C to allow fluorophore generation. Fluorescence was then measured on a TECAN microplate reader using 485 nm excitation and ~535 nm emission. The obtained raw fluorescence values were background-corrected by subtracting the medium blank. Afterwards, a standard curve was fitted by linear regression. To express cytotoxicity as a percentage, dead cell equivalents obtained from the CytoTox-Fluor readout were related to the total number of cells present at the measured

time point. Total and viable cell numbers were determined by counting the viable cells as described in section 4.1.1.1 and calculated as seen in equation two and three.

$$Dead\ cells\ (day\ X)[\%] = \frac{\text{number of dead cells [day X]}}{\text{number of dead cells [day X]} + vital\ cells\ [day\ X]} \times 100 \quad (2)$$

$$Dead\ cells\ (day\ Y > X)[\%] = \frac{\text{number of dead cells [day Y + X]}}{\text{number of dead cells [day Y + X]} + vital\ cells\ [day\ Y]} \times 100 \quad (3)$$

Growth rates were calculated as the n-fold increase in viable cells compared to day zero of the treatment. Depending on the experimental question, cytotoxicity was additionally reported as a fold-change relative to the matched control condition at the same time point (control set to 1).

4.2.2 Immunocytochemistry

Cryostat sections of cryofixed hydrogels with GBOs and GBM cells/GSCs (section 4.1.2 – Cryofixation of a hydrogel) were prepared as 10 µm-thick cryosections using the Leica C110 cryostat. Prior staining, these sections were allowed to thaw to RT. Brightfield images of the unstained sections were taken to provide an overview of larger sections and document the exact location of the staining later on. Immunofluorescence double staining was performed using a three-day protocol. Cryosections were first outlined with a hydrophobic barrier pen (ImmEdge) to confine reagents to the sample area. The sections were fixed for 10 minutes at RT using a pre-chilled acetone/methanol 1:1 mixture (stored at -20°C). Slides were then washed in TBS-T (3x10 minutes). To reduce tissue autofluorescence, the sections were briefly dehydrated by sequential immersion in ethanol (20% for 2 minutes, 70% for 20 minutes), followed by incubation with Sudan Black (1% in 70% ethanol) for 10 minutes at RT. After the Sudan Black treatment, the sections were rehydrated by gently dipping the slides in 70% ethanol, incubation in 20% ethanol for 2 minutes, and washing 3x10 minutes in TBS-T again. Non-specific binding was reduced by blocking the slides for 60-80 minutes at room temperature in blocking-buffer consisting of TBS with 0.1% BSA and 0.2% glycine (cryosections & tissue) or 3% BSA in PBS (cells). Therefore, the slides were kept in a humidified chamber. The first primary antibody was diluted in TBS-T as listed in section 3 and incubated on the slides in a humidified chamber for 24 h at 4°C. The following day, all steps were performed under light protection. The slides were washed 3x10 minutes in TBS-T. The first secondary antibody conjugated with a fluorophore was diluted 1:1,000 in TBS-

T and incubated for 1 h at 37°C in a humidified chamber. Afterwards, the slides were washed 3x10 minutes each in TBS-T. If the two primary antibodies originated from the same host species, non-specific cross-binding was minimized by incubating sections with host-species specific F(ab) fragments (1:1,000 in TBS-T) for 1 h at RT, followed by an additional TBS-T wash series (3x10 minutes). This step was omitted when primary antibodies were derived from different species. Afterwards, the second primary antibody was diluted in TBS-T and incubated for 24 h at 4°C in a humidified chamber. At day three, sections were washed 3x10 minutes in TBS-T. The second secondary antibody was diluted 1:1,000 in TBS-T and incubated for 1 h at 37°C in the dark. Slides were washed once for 10 minutes in TBS-T, followed by 2x10 minutes in TBS. Nuclei were counterstained with DAPI diluted 1:30,000 in TBS for 30 minutes at RT. The slides were washed 3x10 minutes each in TBS, briefly rinsed in distilled water, and coverslipped using ImmuMount® mounting medium. Fluorescence images were acquired on a Zeiss AxioObserver Z1 fluorescence microscope using ZEN3 software. Negative controls were prepared by omitting the primary antibodies while keeping all subsequent steps identical, to assess non-specific secondary antibody binding and background fluorescence.

For quantification of double or single positive cells, cells positive for one or both markers were counted manually and reported as absolute counts per analyzed region/section set. For GBO preparations, quantification was performed across multiple specimens per region and across independent biological preparations, followed by calculation of mean values and standard deviations.

4.2.3 Hematoxylin and eosin staining

Hematoxylin and eosin (H&E) staining was performed using the H&E staining kit (Abcam) on cryostat sections to visualize tissue morphology, with hematoxylin staining nuclei in purple and eosin counterstaining cytoplasm and extracellular components in pink. Cyrosections mounted on microscope slides were first allowed to thaw to room temperature. Afterwards, sections were fixed in 4% PFA for 10 minutes at RT. After fixation, the slides were washed in distilled water for 5 minutes. For nuclear staining, slides were immersed in Mayers hemalum kit solution for 5 minutes. After staining, the sections were rinsed in distilled water for 2x5 minutes. The slides were incubated in Bluing Reagent for 10-15 seconds, which converted the initial hematoxylin tone into a stable dark purple stain. Afterwards, the sections were counterstained with Eosin Y kit solution for 3 minutes. After Eosin Y staining, the slides were rinsed with 96% alcohol for 2 minutes. To prepare the sections for mounting, the slides were dehydrated through an ascending ethanol series

(70% for 5 min., 96% for 5 min., 100% for 5 min.). Sections were then cleared in Roticlear for 5 minutes, performed under a fume hood. After clearing, the slides were removed from Roticlear and allowed to evaporate under the hood. Finally, sections were coverslipped using ImmuMount® medium. Stained sections were evaluated by standard brightfield microscopy to assess overall morphology and cytoarchitecture.

4.2.4 Preparation of cell lysates & protein detection via Bradford assay

Preparation of cell lysates

After treatment, the GBM or GSC cells were either recovered from the hydrogel as described in section 4.1.2 and the cell pellets were resuspended in protein lysis buffer, or GBOs were picked from the hydrogel using small forcepts and transferred into round-bottom tubes containing protein lysis buffer. The volume of protein lysis buffer was adjusted for each sample (approximately 70 to 150 µL), with only the minimum necessary protein lysis buffer volume until the suspension became noticeably viscous during pipetting. The cells were lysed by pipetting up and down several times in protein lysis buffer, while the GBO samples were lysed in 500 µL protein lysis buffer using a tissue chopper. The tissue chopper was cleaned with dH_2O and 70% ethanol before and after each use. The tissue was lysed on ice in short 5-10 second bursts until a homogeneous liquid was obtained. The protein lysates were centrifuged at 4°C and 12,000 rpm for 10 minutes, and the supernatant was frozen at -30°C for at least 24 h.

Bradford assay

Protein concentrations were determined using a Bradford assay. A standard curve was generated from a 1 mg/mL BSA stock solution by preparing a dilution series in water as described in Table 6. In parallel, protein-lysate samples were diluted by mixing 2.5 µL protein lysate with 397.5 µL dH_2O. If necessary, the sample was diluted in protein lysis buffer or the standard was adjusted to ensure that the protein concentration was within the standard range. Furthermore, the samples were standardized for protein concentration to ensure a uniform loading volume between the control and stimulated protein-lysate samples, and to minimize errors in interpreting the Western blot analysis. To obtain the necessary standardization, the protein-lysate samples were diluted in protein lysis buffer accordingly, and the following Bradford assay was performed at least twice. 100 µL of

Bradford reagent was added to each standard and diluted sample, mixed thoroughly, and incubated for 20 minutes at RT to allow color development.

Table 6 - Bradford assay standard curve.

Concentration Standard	BSA Standard [µL]	dH_2O [µL]
10 µg/µL	5	395
8 µg/µL	4	396
6 µg/µL	3	397
4 µg/µL	2	398
2 µg/µL	1	399
-	-	400

For quantification, 100 µL of each reaction mixture was transferred in triplicate into a transparent 96-well plate, and absorbance was measured at 595 nm using a Tecan plate reader. Protein concentrations were calculated from the BSA standard curve and used to prepare defined protein amounts for sodium dodecyl sulfate polyacrylamide gel electrophoresis (SDS-PAGE) and Western blot analysis.

4.2.5 SDS-PAGE

SDS-PAGE was performed using the Bio-Rad Mini-PROTEAN system. The volume of acrylamide percentage of the resolving gel was selected according to the expected molecular weight range of the proteins of interest (e.g. 12.5% for proteins in the range of 25-30kDa, 7% or less for proteins above 100 kDa), while a stacking gel was used to concentrate samples prior to entry into the resolving gel. Glass plates, spacers, and gaskets were assembled according to the manufacturer's instructions, and the inner glass surfaces were cleaned with 70% ethanol prior casting of the gel. The gel solution was prepared according to Table 7; depending on the percentage of the resolving gel, the volume of acrylamide was adjusted.

Table 7 - SDS-PAGE Gel preparation.

Ingredients	Resolving gel [10 %] – 2 Gels	Resolving gel [12.5 %] – 2 Gels	Stacking gel [4,5 %] – 4 Gels
dH_2O	4.03 mL	3.29 mL	5.79 mL
Tris-HCl (1.5 M, pH 8.8)	2.5 mL	2.5 mL	-
Tris-HCl (0.5 M, pH 6.8)	-	-	2.5 mL
Acrylamide (30%, 29:1)	3.33 mL	4.17 mL	1.67 mL
TEMED	30 µL	30 µL	30 µL
APS (10%)	60 µL	60 µL	60 µL

The resolving gel was poured to the indicated fill level and carefully overlaid with isopropyl to create a flat gel surface and exclude oxygen during polymerization. After polymerization. The isopropyl was removed, and the gel surface was dried at RT using paper towels, before pouring the stacking gel on top of the resolving gel. A comb was inserted carefully to avoid bubble formation. Polymerized gels were either used immediately or stored at 4°C, still clamped in the casting frame and wrapped in moist paper towels for up to 5 days.

Protein samples were prepared in a volume of 20 µL per lane, by mixing the protein lysates with pre-warmed sample buffer (5x stock, diluted to 1x concentration), DTT (10 mM, 1:10 dilution), and bromophenol blue (2.5% relative to sample buffer volume). The samples were denatured at 95°C for 5 minutes. For electrophoresis, gels were mounted into a tank, and the chambers were filled with electrode buffer. The comb was carefully removed and the sample bags were rinsed with running buffer before loading the samples. Depending on the abundance of the respective proteins to be detected, 6-20 µg protein lysate was loaded in each gel lane, and a suitable Protein Ladder was carried along in each gel, depending on the size of the protein of interest. Electrophoresis was performed at constant 200 V for approximately 50 minutes, with approximately 50-100 mA per gel, although current was variable and depended on the number of gels and protein size/acrylamide percentage. During the first minutes, the run was monitored to confirm the appearance of rising bubbles and proper formation of a dye front. The run was stopped when the dye front approached the bottom of the gel. After electrophoresis, the gels were removed from the tank and the gel cassette was opened by inserting the gel spatula into the gap at the top edge of the cassette. Using the spatula, the gel was loosened from the glass plates, and the stacking gel was carefully removed. The remaining resolving gel was kept in transfer buffer to prevent drying.

4.2.6 Western Blot (semi-dry)

For immunodetection of the separated proteins, the proteins were transferred to polyvinylidene difluoride (PVDF) membranes in a semi-dry technique. The SDS-PAGE gel and Whatman™ blotting papers were equilibrated in transfer buffer. In parallel, the PVDF membrane was shortly moistened in methanol (~30 seconds), and then equilibrated in transfer buffer. The transfer sandwich consisting of Whatman™ paper, PVDF membrane, SDS-PAGE gel and another Whatman™ paper was assembled in a Trans-Blot® Turbo device (Bio-Rad) and carefully rolled out from the center outward to remove air bubbles. The transfer was performed at 25 V and 1 A for 30 minutes. After blotting, membranes were blocked for 60 minutes at RT on a shaker at 120 rpm in TBS-T supplemented either with 5% BSA for phosphor-specific antibodies or with 2% casein for non-phosphorylated targets. Primary antibodies were diluted in the corresponding blocking buffer (see antibodies list in section 3) and incubated on the membranes in a sealed bag format using low volumes (approximately 1 mL) overnight at 4°C, while ensuring complete membrane coverage. After incubation, membranes were washed 3x15 minutes each in TBS-T on a shaker at 120 rpm. Horseraddish peroxidase (HRP) conjugated secondary antibodies were applied in 2% casein in TBS-T for 1 h at RT (see antibodies list in section 3) and washed 3x10 minutes again, and finally washed once for 10 minutes in TBS. For chemiluminescent detection, membranes were drained, placed on clean foil, and incubated with freshly mixed 1:1 enhanced chemiluminescence (ECL) substrate (Amersham®) for 5 minutes. Subsequently, membranes were wrapped in plastic foil to prevent drying while avoiding air bubbles and placed into a film cassette for exposure to chemiluminescence film. Exposure times were optimized empirically and antibody-specific, starting with short exposures to avoid saturation while still capturing weak bands. The chemiluminescence films were developed and fixed using developer and fixing solutions as described from the manufacturer, washed, dried and documented. Equal protein loading and protein transfer efficiency were verified by probing the membranes for housekeeping proteins such as GAPDH or HSP90, which are constitutively expressed and therefore serve as internal loading control. Comparable signal intensities of these control proteins indicated loading and transfer of similar amounts of total protein in each sample. For reblotting purposes, membranes were stripped by evenly applying 10 mL of Reblot Plus solution (1x, diluted in dH_2O) on the membrane. Stripping was performed for 15 minutes at RT on a shaker at 120 rpm, followed by flipping the membrane and incubation for additional 15 minutes to ensure uniform stripping. Membranes were re-blocked and incubated with the next primary antibody, followed by the appropriate HRP secondary antibody and ECL detection as described above.

4.2.7 RNA isolation

4.2.7.1 3D hydrogel and cell culture preparation

For cell culture sample preparation, cell culture medium was removed completely, the cells were washed once with PBS, centrifuged for 5 minutes at 1,000 rpm and the cell pellet was resuspended in 500 µL to 1 mL TRIzol™, depending on the cell pellet size. The samples were frozen at -30°C for at least 24 h until further extraction.

RNA isolation of hydrogels with GBOs or GBM cells/GSCs was performed by serial sectioning of previously snap-frozen hydrogel samples (section 4.1.2 – Cryofixation of a hydrogel), using a cryostat at -20°C. In detail, whole cryofixed GBM cells/GSCs hydrogel samples were processed by collecting 95 consecutive sections into four distinct regional pools, resulting in four primary pools (margin-margin, margin-center, center-margin, and center-center) as depicted in Figure 5 (left). The process consumed half of the sample and was repeated for the whole sample, pooling the sections in four primary pools. While margin-margin represents the outermost regions, center-center represents the focal zone of the sample. In this study, these pools were subjected to further analysis. For GBO hydrogels, another sectioning approach was used, as depicted in Figure 5 (right). After the first 20 sections were discarded, 25 sections from the margin were collected, followed by another 10 intermediate sections, which were collected on microscope slides for fluorescence staining, followed by another 25 sections from the margin. The collected sections were pooled and the cycle of discarding 10 sections for staining and 25 sections for RNA preparation was repeated twice for a total of four pooled margin samples. The same workflow was applied to the central region. The pooled sections were resuspended in 500 µL TRIzol™ frozen at -30°C for at least 24 h until further extraction.

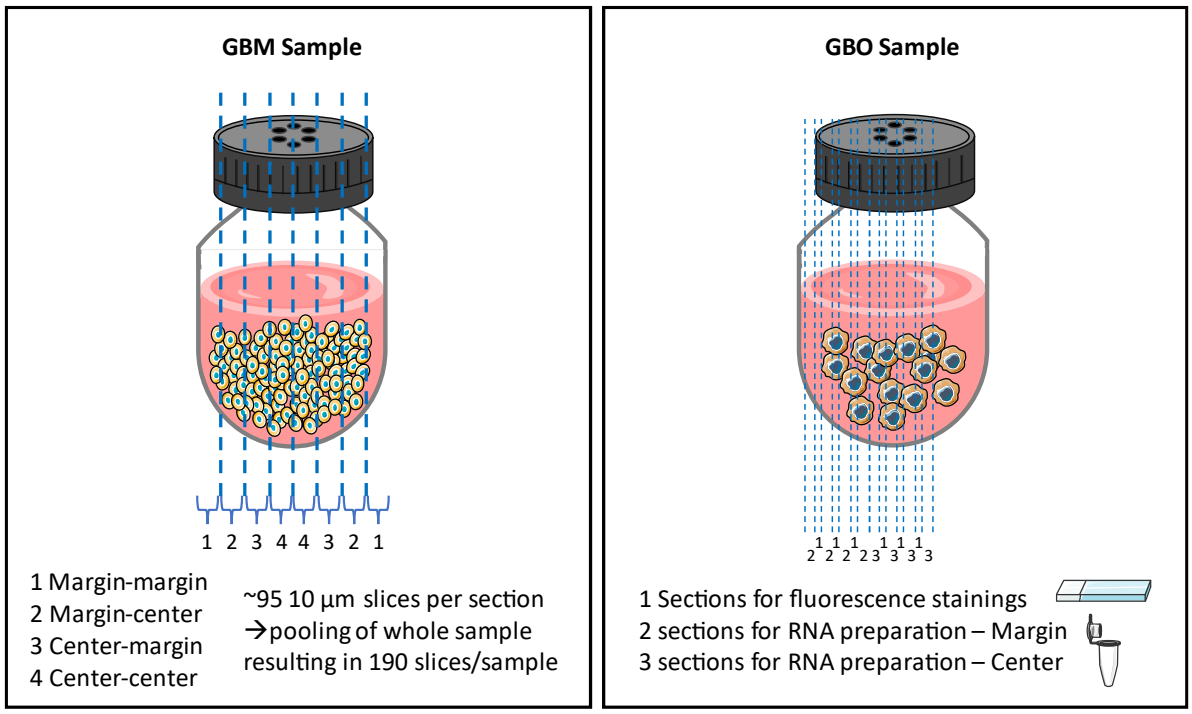


Figure 5 - Sample Preparation of Hydrogel cultures for RNA extraction. Left: GBM sample preparation. Right: GBO sample preparation. Image(s) partially provided by Servier Medical Art (https://smart.servier.com), licensed under CC BY 4.0 (https://creativecommons.org/licenses/by/4.0/).

4.2.7.2 Isolation with TRIzol™

RNA was isolated using TRIzol™ reagent, which relies on an acid-guanidinium thiocyanate-phenol-chloroform liquid extraction to separate RNA from DNA, proteins, and other cellular components. For RNA isolation, the TRIzol™ sample lysates obtained as described in section 4.2.7.1 were homogenized by gentle pipetting, and insoluble cell material was removed by centrifugation at 12,000 x g for 10 minutes at 4°C. The supernatant was transferred to a fresh 1.5 mL Tube and allowed to stand for 5 minutes at RT. Phase separation was initiated by adding 200 µL chloroform, followed by mixing by inverting the tube approximately 10 to 15 times. The mixture was incubated for 3 minutes at RT and centrifuged at 12,000 x g for 15 minutes at 4°C. After centrifugation, the upper aqueous phase containing RNA was carefully transferred to a new 1.5 mL Tube without disturbing the protein-rich interphase. RNA was precipitated by adding 500 µL ice-cold isopropyl, mixing thoroughly, and incubating the samples for at least 45 minutes on ice (~4°C). RNA was then pelleted by centrifugation at 12,000 x g for 10 minutes at 4°C. The supernatant was discarded, and the pellet was washed with 1 mL of 75% ethanol by vortexing briefly to dislodge the pellet and remove residual salts and phenol. The sample was centrifuged at 7,600 x g for 5 minutes at 4°C, after which the ethanol was removed. The pellet was air-

dried at RT until residual ethanol had evaporated. Finally, the RNA pellet was dissolved in 20-100 µL RNase-free water, adjusted to pellet size. The solution was incubated at 58°C for 10 minutes with gentle shaking. Purified RNA was either used immediately or stored at -80°C.

4.2.7.3 Isolation with ARCTURUS© PicoPure® RNA Isolation Kit

RNA from low-input samples (50,000 cells or less) was isolated using the ARCTURUS® PicoPure® RNA Isolation Kit following the manufacturer's workflow. Briefly, cells were washed once with PBS, centrifuged at 1,000 rpm for 5 minutes, and the cell pellet was lysed directly in 50 µL of the kit's extraction buffer. Lysates were incubated at 42°C for 30 minutes to promote RNA release. After incubation, lysates were stored at -80°C for at least 24 h. Column-based RNA purification was performed using PicoPure® RNA purification columns. First, the column membrane was pre-conditioned by applying 250 µL conditioning buffer, incubating for 5 minutes at RT, and centrifuging at 16,000 x g for 1 minute. RNA binding conditions were established by adding 50 µL 70% ethanol to the cell extract. The solution was transferred onto the conditioned column and centrifuged to bind the RNA by centrifugation at 100 x g for 2 minutes, immediately followed by 30s at 16,000 x g. After binding, the column was washed sequentially with 100 µL washing buffer 1, followed by centrifugation at 8,000 x g for 1 minute, and two washing steps with 100 µL washing buffer centrifuged at 8,000 x g and a high-speed spin at 16,000 x g for 2 minutes to dry the membrane. The column was transferred into a clean 0.5 mL elution tube provided with the kit. 14 µL of elution buffer was applied directly onto the membrane, incubated for 1 minute at RT, centrifuged at 1,000 x g for 1 minute, and immediately followed by 1 min at 16,000 x g to collect the RNA eluate. Purified RNA was either used immediately or stored at -80°C.

4.2.8 Reverse transcription

To generate high-quality cDNA, DNAse digestion was performed on purified RNA samples. For each sample, 2 µg RNA in a maximum volume of 7 µL (diluted with RNAse free dH_2O), was combined with 1 µL RQ1 DNase reaction buffer and 1 µL RQ1 RNAse-free DNase. The digestion was carried out at 37°C for 15 minutes using the Eppendorf Mastercycler. Afterwards, DNase activity was heat-inactivated by adding 1 µL 20mM EDTA per sample and incubating the sample at 65°C for 10 minutes. For cDNA synthesis, 2 µL random hexamer (100 ng/µL) were added to each DNase-treated RNA sample and incubated at

70°C for 5 minutes using the Eppendorf Mastercycler. Immediately after incubation, the samples were cooled on ice for 2 minutes. Reverse transcription was initiated by adding 8 µL of a freshly prepared master mix consisting of 4 µL 5xRT buffer, 2 µL 10mM dNTP mix, 1 µL RNase-free dH_2O, and 1 µL reverse transcriptase, yielding a final reaction volume of 20 µL per sample. The temperature program listed in Table 8 was carried out using the Eppendorf Mastercycler. The obtained cDNA was either used immediately or stored at -30°C.

Table 8 - Temperature program of cDNA synthesis.

Time [min.]	Temperature [°C]
10	25
60	42
10	70
∞	4

4.2.9 Quantitative real-time polymerase chain reaction (qPCR)

For quantitative real-time polymerase chain reaction (referred to as qPCR throughout this study), the obtained cDNA was diluted 1:10 with dH_2O prior plate setup. For each target gene, 2 µL of diluted cDNA (corresponding to 10 ng cDNA/reaction) were dispensed into two separate wells of a 96-well plate to obtain technical duplicates. Each well received 18 µL of a gene-specific TaqMan reaction master mix composed of 1 µL gene specific primer, 7 µL dH_2O, and 10 µL TaqMan, resulting in a final reaction volume of 20 µL per well. The primers used for qPCR are listed in Table 9. For every assay, a no-template control was included by replacing the cDNA with 2 µL dH_2O. In addition, positive control was included for assay performance control by adding 2 µL of RNA-derived GBM material for GAPDH expression assessment. After loading, the plate was sealed with film and briefly centrifuged.

Table 9 - Used qPCR Primer.

Human		
GAPDH	*glyceraldehyde-3-phosphate dehydrogenase*	Hs99999905_m1
GFAP	*glial fibrillary acidic protein*	Hs00157674_m1
S100b	*S100 calcium-binding protein B*	Hs00902901_m1
FN1	*fibronectin 1*	Hs00277509_m1
BGN	*biglycan*	Hs 00156076_m1

CD31	*IGFBP5platelet endothelial cell adhesion molecule (Pecam 1)*	Hs00169777_m1
MSI1	*Musashi (Drosophila) homolog 1*	Hs00159291_m1
KLF4	*Krüppel-like factor 4*	Hs 00358836_m1
OCT4	*octamer binding transcription factor 4*	Hs00999632-g1
SOX2	*sex-determining region Y-box 2*	Hs00602736_s1
Nestin	*neuroepithelial stem cell protein*	Hs00707120_s1
CD133	*cluster of differentiation 133*	Hs00195682_m1
CD68	*cluster of differentiation 68*	Hs00154355_m1
CD11b	*integrin alpha M (ITGAM)*	Hs00167304_m1
IBA1	*calcium-binding adapter molecule 1*	Hs00610419_g1
CD3	*cluster of differentiation 3*	Hs01062241_m1
SKI	*SKI proto-oncogene*	Hs01057032_m1
IGFBP5	*insulin-like growth factor-binding protein 5*	Hs00174435_m1
EphA5	*ephrin receptor A5*	Hs00300724_m1
H2BK	*histone cluster 1 H2B family member K*	Hs00955067_g1
MAP2	*Microtubule-associated protein 2*	Hs00258900_m1
TUBB3	*Beta-III-Tubulin*	Hs00801390_s1
NF1	*Neurofibromin 1*	Hs01035108_m1
NF200	*Neurofilament heavy polypeptide 200 kDa*	Hs00606024_m1
Piezo1	*Piezo-type mechanosensitive ion channel component 1*	Hs00207230_m1
Trpc6	*Transient receptor potential canonical 6*	Hs00988479_m1
Trpc1	*Transient receptor potential canonical 1*	Hs00608195_m1
Trpm4	*Transient receptor potential cation channel subfamily M member 4*	Hs00214167_m1
Trpp2	*Transient receptor potential polycystic 2*	Hs00960946_m1
Rat		
GAPDH	*glyceraldehyde-3-phosphate dehydrogenase*	Rn99999916_s1
SOX2	*sex-determining region Y-box 2*	Rn01286286_g1
Ki67	*Antigen Kiel 67*	Rn01451446_m1
MSI1	*Musashi (Drosophila) homolog 1*	Rn00596059_m1
GFAP	*glial fibrillary acidic protein*	Rn00566603_m1
MAP2	*Microtubule-associated protein 2*	Rn00565046_m1
TUBB3	*Beta-III-Tubulin*	Rn01431594_m1
CNPase	*CNP1*	Rn01399463_m1
Olig2	*Oligodendrocyte transcription factor*	Rn01767116_m1
Klf4	*Krüppel-like factor 4*	Rn00821506_g1
Nestin	*neuroepithelial stem cell protein*	Rn00564394_m1

qPCR was performed using the QuantStudio5, following the amplification program described in Table 10. The qPCR program was created using QuantStudio software.

Table 10 - qPCR Program

Time [min.]	Temperature [°C]	Cycles
10	95	50
0,25	95	
1	60	
∞	4	

Cycles of threshold (C_T) values were determined using the instrument's analysis software. Gene of interest C_T values were referenced to the housekeeping gene GAPDH to generate ΔC_T values ($C_{T\text{gene of interest}} - C_{T\text{GAPDH}}$). Samples with undetectable amplification values were excluded from mean expression calculations. Where treatment effects were compared to a control condition, relative expression changes were calculated for ΔC_T values using a fold-change approach ($2 - (\Delta C_{T\text{stimulated}} - \Delta C_{T\text{unstimulated}})$).

4.3 Statistical analysis

Statistical analysis was performed using GraphPad Prism software. Depending on the experimental setup, either a Student's t-test, a one-way ANOVA, or a two-way ANOVA was performed, as indicated for each experiment in the respective figure legends. Statistical significance is marked with an asterisk depending on the p-value (*p<0.05; **p<0.01; ***p<0.001). The sample size is stated in the figure legends.

5. Results

The present work addresses the question of how stressors within the central nervous system (CNS) influence stemness-associated cellular properties. To approach this question, two fundamentally different stress contexts were investigated. First, externally induced therapeutic-stress was applied by mechanical focused ultrasound (mFUS) in patient-derived GBM systems in order to analyze how therapy-associated stress affects residual tumor cells and their stemness- and dormancy-related behavior (Section 5.1). Second, the effects of environmental stress on stemness properties were studied using an *in vitro* myelomeningocele (MMC)-related model, in which exposure to artificial amniotic fluid (aAF) was used to mimic aspects of the intrauterine environment associated with maldevelopment of the spinal cord (Section 5.2). Together, this approach allowed the investigation of whether stress-associated changes in stemness-related properties represent a common response across distinct CNS models.

5.1 mFUS-induced stress in GBOs and GBM models – Consequences for dormancy- and stemness-associated properties

Focused ultrasound (FUS) is a new technology that allows ultrasound energy to be delivered precisely to different targets at specific times. Here, mechanical focused ultrasound (mFUS) exploits the mechanical effects of ultrasound for a non-thermal tumor ablation. In mFUS, cavitation-driven mechanical forces disrupt the tissue architecture, but the biological consequences of these lesions are likely to extend beyond focal cell destruction alone. This result section examines whether mFUS can be used to induce stress-related effects in peri-focal regions of GBM models, particularly with regard to altered cellular properties associated with dormancy and stemness. To address these questions, mFUS was applied to patient-derived glioblastoma organoids (GBOs), more differentiated GBMs, as well as glioma-like stem cells (GSCs).

The following results first established the experimental framework and validated the stress induction (Figures 6 to 8). In order to assess the potential mechanisms of action of the mFUS treatment, mRNA expression of mechanoreceptors following mFUS treatment was evaluated (Figure 9). Following the technical validation of mFUS, the molecular, cellular, and functional consequences of mFUS treatment were investigated. As mFUS-induced effects were expected to differ according to their spatial relationship to the focal lesion, dormancy and stemness-associated properties were examined in a region-specific manner

by immunofluorescence (IF) staining (Figures 10 to 12) and mRNA expression analysis using qPCR (Figure 13). In this context, sections designated as *center* corresponded to the focal zone of mFUS application and represented the primary lesion site, whereas sections designated as *margin* were derived from peri-focal regions surrounding the mFUS-induced lesion. Untreated sections were designated as *control* and were not exposed to mFUS. The terminology was applied consistently in the following subsections.
The biological effects of mFUS-induced alterations were classified in terms of sphere formation and chemoresistance by ELDA and temozolomide stimulation experiments (Figure 14). Furthermore, an evaluation of potential biological consequences was performed based on the analysis and inhibition of the PI3K/Akt pathway (Figure 15). This pathway serves as a critical and frequently activated survival mechanism in GBM that allows tumor cells to adapt to and overcome various forms of severe cellular stress [177,178]. The results were partially published in Hellmold *et al.* 2025, which is attached in the appendix [179]. Any data that has already been published is accompanied by a reference to the publication.

5.1.1 mFUS setup and GBO characterisation

To enable the interpretation of mFUS treatment effects on the used GBO model system, a baseline characterization of the GBO model was performed. As depicted in Figure 6, GBOs replicated the intra- and intertumoral heterogeneity of GBMs in terms of histological characteristics with vascular structures and tumor cell tissue (Figure 6 A).
Furthermore, the gene expression patterns of GBO and tumor tissue were evaluated using qPCR (Figure 6 B). The qPCR panel included markers of glial and astrocytic identity, such as GFAP and S100β, as both markers are widely used to identify the astrocytic lineage [180,181]. Additionaly, a set of genes associated with stemness and tumor-propagation, such as MSI1, CD133, KLF4, OCT4, and SOX2, was included [182–185]. Furthermore, the panel addressed the extracellular and stromal context through FN1 and BGN, which are associated with extracellular matrix organization and tumor-associated matrix remodeling [186,187]. In addition, CD31 was included to reflect endothelial and vascular components [188]. The tumor microenvironment was assessed by CD68, CD11b, and IBA1, representing the myeloid compartment [189,190]. The gene expression of GBOs resembled the original tumor and reflected its heterogeneity.

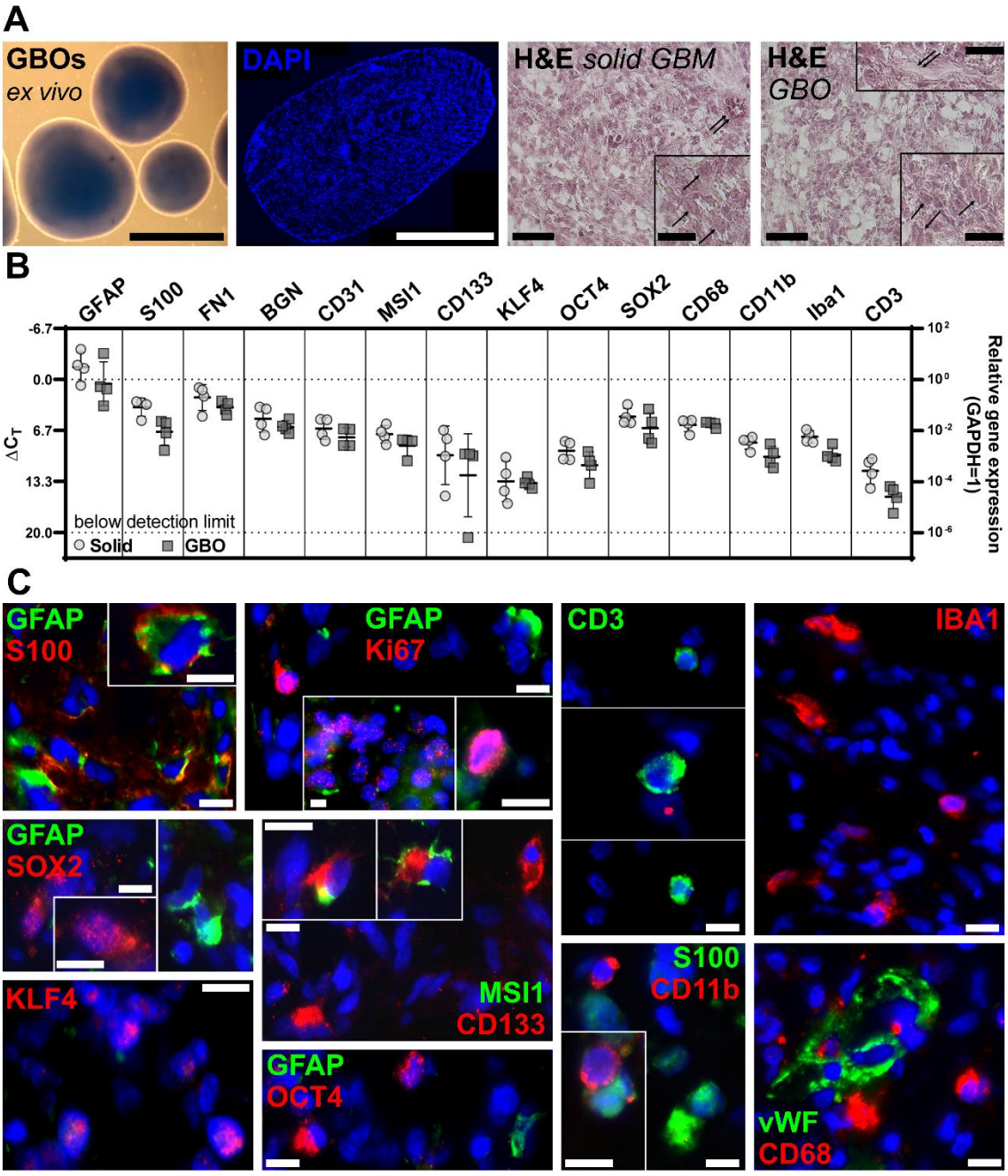


Figure 6 – Heterogeneity of GBOs. **A** Vital *in vitro* cultures of GBOs were grown for two weeks (left), and nuclear staining with DAPI revealed a homogeneous cellular structure (middle). H&E staining (right) compared to solid parental tumor revealed that GBOs replicated the intra- and intertumoral heterogeneity of freshly original tumors. The arrows point to individual tumor cells, double arrows point to vascular structures. Bar left: 1 mm, middle: 0.5 mm, right: 100 µm, inserts 20 µm. **B** mRNA expression of various cell type-specific markers (see table 9 for abbreviations) of GBO preparations and the corresponding parental tumors (n=4 biological GBO preparations). Gene expression and significances between different stimulations were determined by one-way ANOVA followed by a Tukey's multiple comparison test. No significances were detected due to the heterogeneity of the preparations. **C** Exemplary IF staining of GBOs with cell-specific markers (see table 9 and section 3 for abbreviations), nuclear staining was performed with DAPI. Bar: 20 µm.

To further characterize the cellular heterogeneity of the GBOs, a panel of IF staining was applied (Figure 6 C). GFAP/S100β staining was used to confirm the presence of a glial/astrocytic tumor cell compartment. Furthermore, immunopositivity for both markers are primarily considered as GBM tumor cells [191]. GFAP/SOX2 and GFAP/OCT4 staining were included to identify cell populations combining astrocytic features with stem cell-like transcriptional factors (TF), addressing the well-described plasticity of GBM cells between differentiated and stem cell-like states [191–193]. GFAP/Ki67 staining was used to determine the proliferative fraction within the glial tumor cell population. To assess the non-tumor microenvironmental components of the GBO, CD3 staining was performed to detect $CD3^+$ immune cells, including macrophages, microglia, NK cells, as well as T-cells [194], whereas S100β/CD11b and IBA1 staining was used to visualize myeloid compartments and to identify microglia/macrophage-like cells within the GBOs [189]. Finally, vWF/CD68 staining was applied to assess vascular structures together with associated macrophage/myeloid cells [190,195]. These results were published in Hellmold *et al.* 2025 [179], which is attached in the appendix.

As a next step, the reproducibility and technical performance of the experimental mFUS setup were established and validated. The experimental setup to study the effects of mFUS (Figure 7 A) was adapted to patient-specific *in vivo* conditions, using 3D hydrogel cultures of patient-derived GBOs or patient-derived more differentiated GBM cells, as well as patient-derived GSCs. mFUS resulted in visible agarose lesions in the sample, while temperature conditions remained constant. Furthermore, mFUS resulted in macroscopically visible defects in the focal area of the GBO and GBM cell system (Figure 7 B). These results were published in Hellmold *et al.* 2025 [179], which is attached in the appendix. The figure has been expanded to include a conceptual illustration of the experimental setup and the mechanism of action of mFUS.

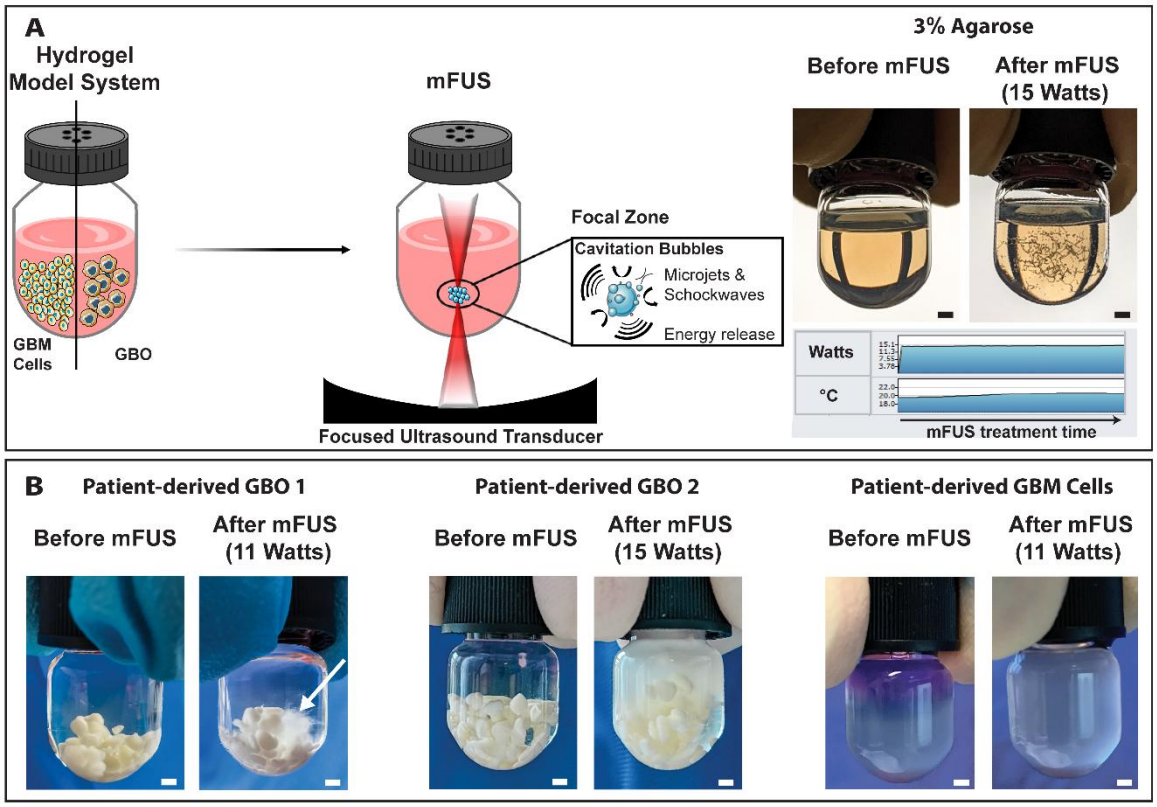


Figure 7 – mFUS system to study the effects of mFUS in an *in vivo* adapted *in vitro* system. **A** Patient-derived GBM cells, as well as GBOs, were cultured in a 3D hydrogel system, and mFUS of different intensity was applied, leading to mechanical effects within the focal zone. Lesion induction was visualized in 3% agarose treated with mFUS (15 Watts). Temperature conditions remained constant during treatment. Images were partially provided by Servier Medical Art (https://smart.servier.com), licensed under CC BY 4.0 (https://creativecommons.org/licenses/by/4.0/). **B** mFUS treatment led to macroscopically visible defects in GBOs as well as GBM cell systems. Bar: 1 mm.

DAPI staining of mFUS-treated patient-derived more differentiated GBM cells revealed a pronounced effect of mFUS treatment relative to untreated control (Figure 8 A). The mFUS-treated hydrogel displayed a reduced cell density, indicating a marked loss of cells compared with the untreated control. In addition, distinct nuclear damage in the treated samples could be observed, including nuclear deformation and the presence of nuclear fragments. These findings were supported by the results of a cytotoxicity assay performed on the same patient-derived primary GBM cells, which showed a progressive increase in cytotoxicity with increasing ultrasound intensity (Figure 8 B). The cytotoxicity assay was published in Hellmold *et al.* 2025 [179], which is attached in the appendix.

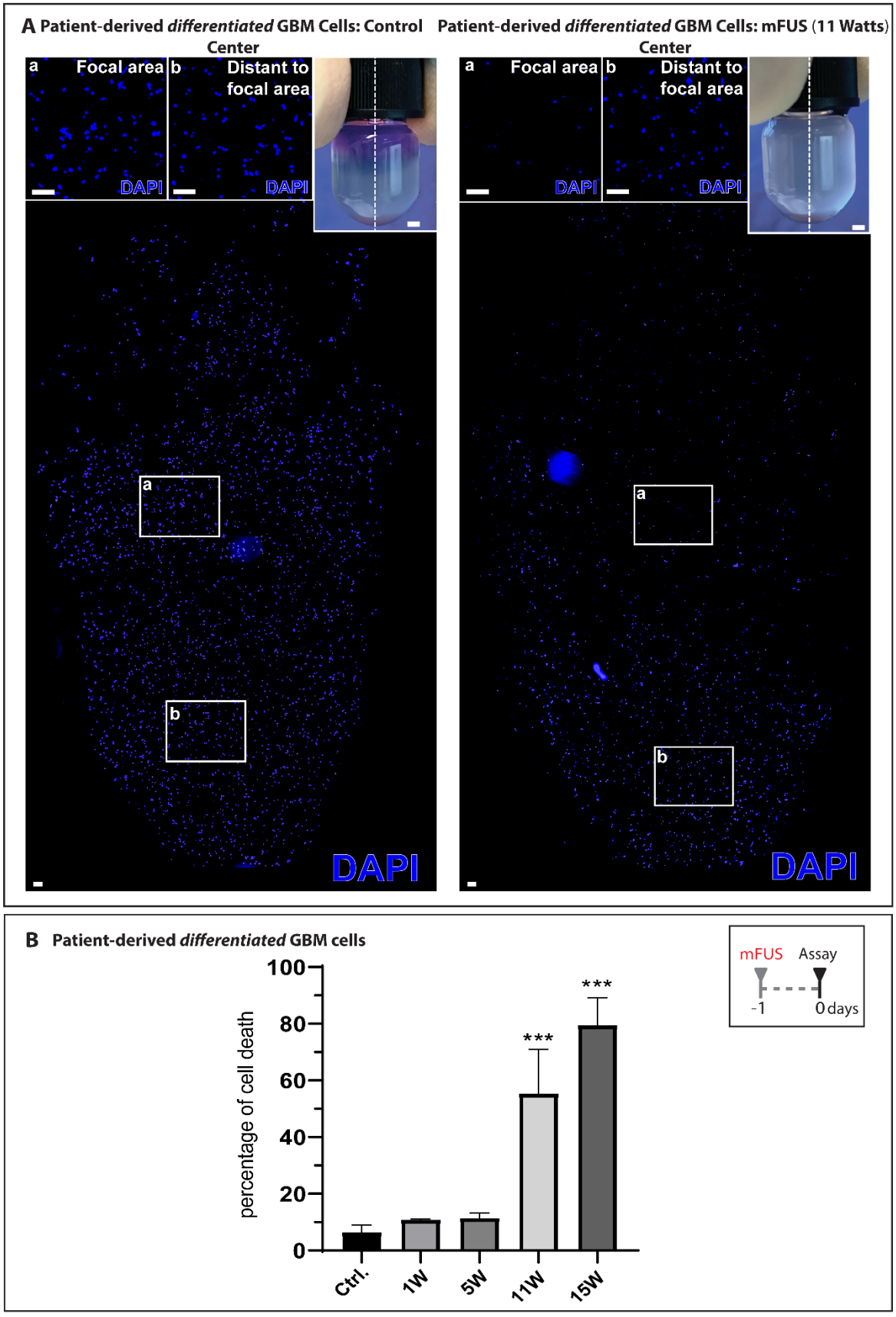


Figure 8 – mFUS application on patient-derived more differentiated GBM cells. **A** Nuclear staining with DAPI revealed a reduced cell density in mFUS treated samples, accompanied by nuclear deformation and cell debris. Bar: 100 µm. **B** mFUS treatment led to increasing numbers of dead cells with increasing average incident power (1 to 15 Watts) in patient-derived more differentiated GBM cells. N=3 biological replicates with n=1-2 technical

replicates each. Statistical analysis was performed using an ordinary one-way ANOVA followed by Tukey's multiple comparison test (*** p<0.001). Error bars correspond to the standard deviation.

mFUS represents a mechanically acting intervention, acting through microjets and shockwaves, which is proposed as a direct mechanism through which ultrasound induces changes in membrane permeability. Therefore, mFUS is likely to involve ion channels that sense and transduce mechanical stimuli (mechanoreceptors) [196]. Thus, the expression of mechanoreceptors that could be potentially influenced by mFUS was evaluated. Based on current literature regarding ultrasound-induced neuromodulation, the focus was laid on the mechanoreceptors Piezo1, Trpc1, Trpc6, Trpp2, and Trpm4 [197–199]. In particular, Piezo1 has been associated with aggressive GBM, which are characterized by mechanical tumor adaptation and poor prognosis [197,200,201]. Furthermore, TRP family channels have repeatedly been implicated in ultrasound-responsive mechanotransduction and calcium influx [197,202]. Here, TRPC1 and TRPC6 have been associated with GBM calcium signaling, migration, and hypoxia-associated tumor adaptation [203,204]. TRPP2 is recognized as a shear-stress-responsive mechanosensitive channel [205], and TRPM4 has been linked to tumor phenotypes associated with proliferation and migration [206,207]. GSCs, as well as more differentiated GBM cells, were treated with mFUS (15 Watts), and gene expression of the above-mentioned mechanoreceptors was evaluated 24 h after mFUS treatment (Figure 9). Both subpopulations demonstrated an increased expression of mechanoreceptors after mFUS treatment, with the strongest induction of Trpm4 and Trpp2 compared to untreated controls. However, Trpc6 could not be detected in more differentiated GBM cells, and no significant induction of Piezo1 and Trpc1 could be observed, while GSCs responded with an increased expression of all investigated mechanoreceptors in the focal zone (center) as well as in the peri-focal region (margin). Therefore, these data support the interpretation that mFUS acted, at least in part, by stimulating membrane-associated mechanoreceptors, which could potentially trigger intracellular signaling events. The results were published in Hellmold *et al.* 2025 [179], which is attached in the appendix.

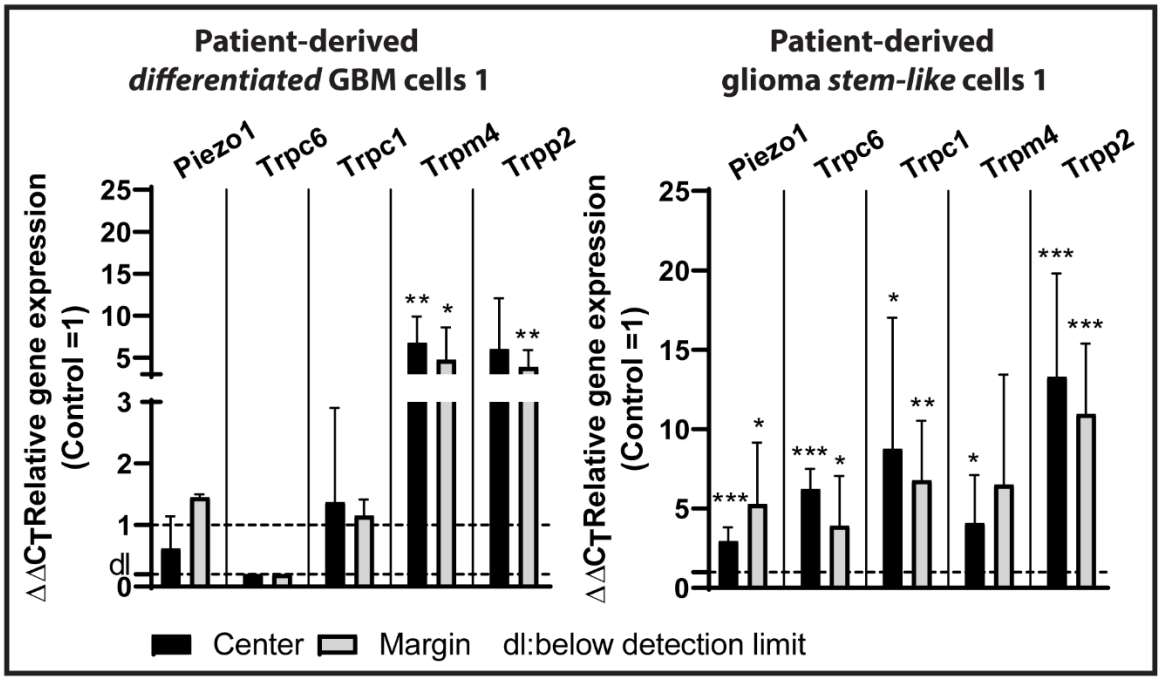


Figure 9 - mRNA expression of mechanoreceptors following mFUS (15 Watts) in patient-derived more differentiated GBM cells and GSCs 24 h after treatment showed an induction of all (GSCs) or selective (Trpm4 and Trpp2, differentiated GBM cells) mechanoreceptors compared to unstimulated control (control = 1). n=1-2 biological replicates with n=1-2 technical replicates each. Statistical analysis was performed using a nonpaired t-test. Significant differences compared to the untreated control are indicated directly above the bars (*p<0.05; **p<0.01; ***p<0.001). Error bars correspond to the standard deviation.

Taken together, these findings confirmed that the applied mFUS conditions induced a defined lesion in the investigated model systems, and triggered upregulation of mechanoreceptors most likely due to its mechanically acting intervention. Having established the technical validity of the system, the next step was to determine whether these lesions were affecting the expression of markers associated with dormancy and stemness.

5.1.2 Assessment of dormancy- and stemness-associated properties following mFUS treatment in a region-dependent manner

After technical validation of the mFUS setup and characterization, IF staining was used to evaluate the presence of an mFUS-induced lesion as well as the early effects of mFUS on dormancy- and stemness-associated marker expression in a region-dependent manner. In addition to qualitative imaging, selected markers were analyzed quantitatively.

First, staining of the cell death marker cCaspase 3 on patient-derived GBOs, embedded in hydrogel and treated with mFUS (11 Watts) was performed. After mFUS treatment, these samples were cultured for another 24 h, cryofixed, and serially sectioned to assess sections from the focal zone (center) as well as from the peri-focal mFUS zone (margin). cCaspase3 staining showed significantly increased cCaspase3 levels in the focal area (center) compared to untreated control (Figure 10, left). Furthermore, a low abundance of cCaspase3-positive cells could be detected in peri-focal regions (margin). In coherence with Figure 8, cell debris could be detected in the focal area (center) of mFUS-treated GBOs.

To assess dormancy and stemness properties, the dormancy markers IGFBP5, H2BK, and SKI, as well as the stemness markers MSI1, OCT4, and SOX2 were co-stained in GBO hydrogel samples treated with mFUS (11 Watts; Figure 10, right). In GBM, MSI1 has been linked to cancer stem cell properties, self-renewal, migration, and treatment resistance, which makes it a suitable readout for stem-like tumor cell states [208,209]. The same applies to the transcription factor OCT4, which has been shown to support glioma-initiating cell maintenance, tumorigenicity, self-renewal, and stemness-associated transcriptional programs [182,210]. Furthermore, SOX2 is one of the most established neural stem cell and glioma stem cell markers, strongly linked to tumor initiation, self-renewal, plasticity, and drug resistance [211,212]. Regarding the dormancy markers, H2BK has been a GBM-associated dormancy marker used in prior dormancy studies, primarily found in non-proliferative, Ki67-negative GBM cell populations [64,213]. IGFBP5 has repeatedly been used as a dormancy-associated marker in GBM, particularly in treatment-induced or experimentally modeled dormant GBM states [58,64]. SKI is considered as dormancy-associated marker, regulated under dormancy conditions but also linked to stemness-associated programs as shown by Kubelt *et al.* 2023 [60].

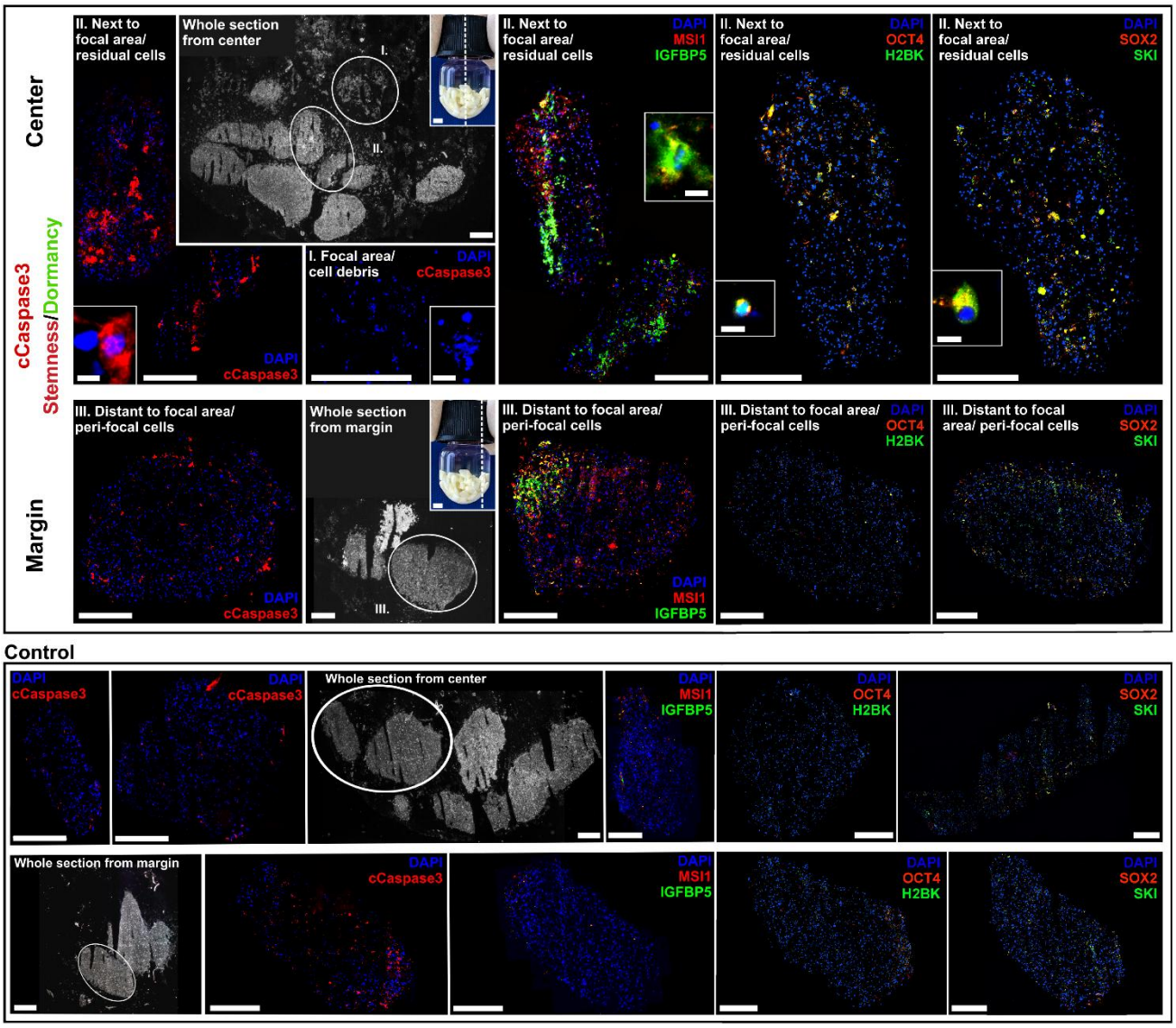


Figure 10 – IF staining of GBO sections from the focal (center) and peri-focal area (margin). Exemplary GBO hydrogel cultures were treated with mFUS (11 Watts) and cultured for another 24 h before cryofixation and serial sectioning. **Left:** Cell death staining performed with cCaspase3 revealed a predominant staining near the focal region (II) compared with more distant regions (III). Fragmented cell nuclei in the focal area (I) were observed. The untreated control sample exhibited a low level of cCaspase 3 staining. **Right:** Prominent staining of the stemness marker MSI1, OCT4 and SOX2 as well as the dormancy marker IGFBP5, H2BK and SKI could be observed in the samples center compared to untreated control. Co-staining of OCT4/H2BK and SOX2/SKI showed increased expression mainly in residual cells next to the focal area, whereas co-staining of MSI1/IGFBP5 was prominent in the center as well as margin compared to untreated control. Circled GBOs in whole sections are those stained for IF analysis. See table 9 and section 3 for marker abbreviations. Bar whole sections: 0.5 mm, inserts mFUS tubes: 1 mm, GBO samples: 400 µm, inserts: 10 µm.

The GBO preparation examined showed induced MSI1 and IGFBP5 co-staining after mFUS treatment in residual cells adjacent to the focal region and in cells located within the peri-focal region. Similarly, increased expression relative to untreated controls was observed for the OCT4/H2BK and SOX2/SKI marker combinations, although these signals were more pronounced in residual cells close to the focal area. Quantitative analysis of double-positive cell populations across two independent GBO preparations (2-7 GBOs per preparation) consistently demonstrated an overall enrichment of marker-positive cells after mFUS treatment. In particular, MSI1/IGFBP5 double-positive cells increased to 10.2 ± 4.57% in the center and 8.0 ± 2.46% in the margin, compared with 1.0 ± 0.6% and 0.5 ± 0.4% in untreated controls. Similarly, the percentage of OCT4/H2BK double-positive cells increased from 4.0 ± 2.6% to 16.6 ± 5.55% in the center and from 2.4 ± 1.0% to 22.0 ± 12.84% in the margin. SOX2/SKI double-positive cells increased to 15.5 ± 9.41% and 15.0 ± 9.39%, compared with 3.0 ± 0.5% and 9.9 ± 7.0% in untreated controls. Overall, GBOs exhibited a region-dependent increase in the expression of dormancy- and stemness-associated markers. The results were published in Hellmold *et al.* 2025 [179], which is attached in the appendix.

Since SKI is particularly interesting regarding its role in the dormancy-stemness interface [60], we separately examined SKI expression in GBO hydrogel samples treated with mFUS (11 Watts). IF staining of SKI showed increased expression of SKI within the focal area (center) as well as less pronounced in residual cells (margin), compared to untreated control (Figure 11).

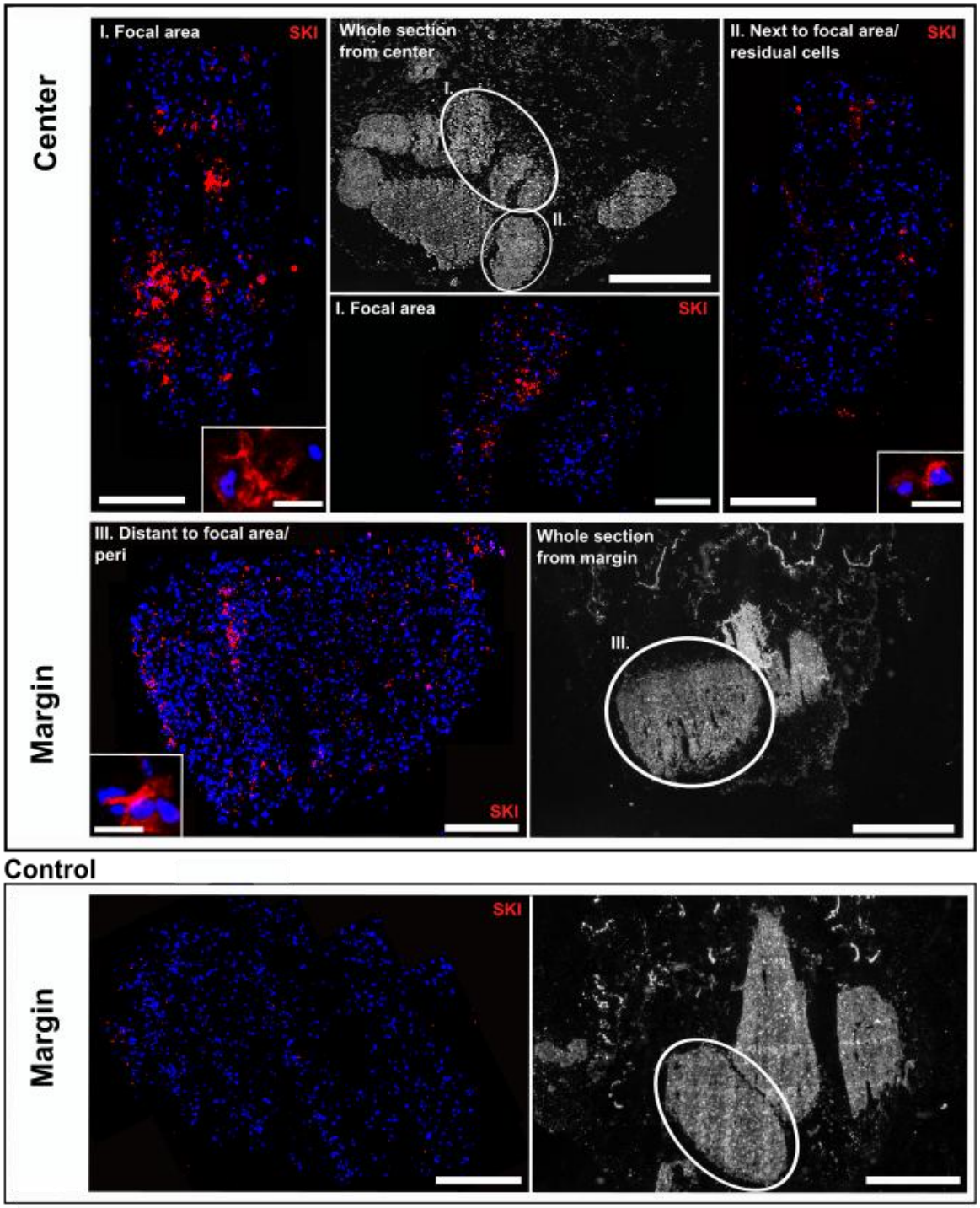


Figure 11 – IF staining of GBO samples treated with mFUS (11 Watt). Serial sections of the focal zone (center) and peri-focal zone (margin) 24 h after mFUS treatment were stained with the dormancy marker SKI. Prominent SKI staining was found in the sample's center and the margin, compared to the untreated control. Bar whole sections: 1 mm, GBO samples: 400 µm, inserts: 10 µm.

To further examine dormancy- and stemness-related properties, IF staining was performed in hydrogels with patient-derived more differentiated GBM cells, treated with mFUS (15 Watts). In alignment with GBO hydrogels, those samples were also cultured for another 24 h after mFUS treatment, cryofixed, and serially sectioned to assess center and margin of the sample. Exemplary staining of SOX2/IGFBP5 in the focal zone showed co-staining

of SOX2 and IGFBP5, with a pronounced localisation of SOX2 in the nucleus and IGFBP5 in the perinuclear region (Figure 12). Co-staining of SKI/IGFBP5 showed a prominent cytoplasmic staining of IGFBP5, whereas SKI was prominently found in the nucleus.

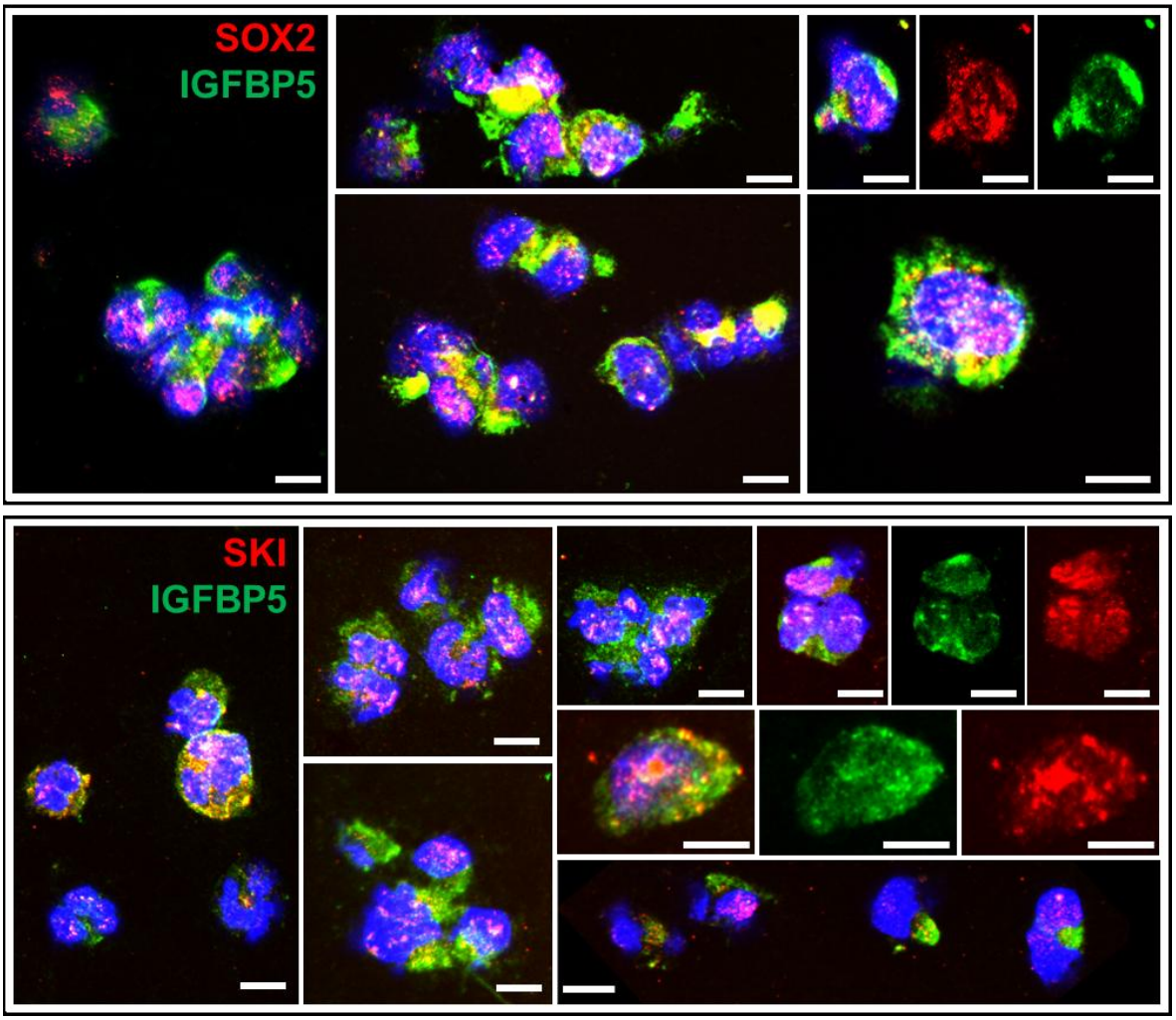


Figure 12 – IF staining of patient-derived more differentiated GBM cells 24 h after mFUS treatment (15 Watts), localized in the focal region (center). Prominent co-staining of SOX2/IGFBP5 as well as SKI/IGFBP5 was observed. See table 9 and section 3 for marker abbreviations. Scale bar = 10 µm.

Imaging-based analyses demonstrated that mFUS exposure produced measurable cellular consequences, confirming a localized lesion by cCaspase 3 staining and altered expression of dormancy- and stemness-associated markers. To determine whether these observations were accompanied by broader molecular changes, transcriptional analyses were performed in both GBOs and GBM-derived samples.

5.1.2.1 Transcriptional changes in dormancy- and stemness-associated properties following mFUS treatment

To complement the immunofluorescence-based findings, qPCR analyses were performed to assess the effect of mFUS on the expression of genes associated with dormancy and stemness. Together, these analyses allowed for a broader evaluation of the molecular response to lesion induction via mFUS treatment.

In alignment with the performed IF staining, qPCR analysis was done in a region-specific manner. Overall, the qPCR data of GBO hydrogel samples treated with mFUS (11 Watts, Figure 13 A) confirmed upregulation of dormancy- and stemness-associated markers. The stemness markers OCT4, SOX2, and MSI1 were expressed more prominently in the focal zone (center), while the dormancy markers SKI, IGFBP5, EphA5, and H2BK showed heterogeneous expression. In detail, SKI and IGFBP5 were expressed more prominently in peri-focal regions (margin), while EphA5 and H2BK were expressed more pronounced in the focal zone (center). Although the magnitude of these responses varied between individual GBO preparations, reflecting the well-known intra- and intertumoral heterogeneity of GBM [214], the overall pattern was consistent with the IF-based observations. In detail, the strongest induction of multiple markers was detected in tissue sections derived from the focal zone (center) after mFUS treatment. Nestin displayed a more uniform increase in expression in both the center and the margin. The qPCR data indicated a region-dependent transcriptional pattern of surviving cell populations expressing dormancy- and stemness-related markers. Parts of the GBO qPCR dataset have previously been published as part of a larger dataset comprising 8 biological replicates in Hellmold *et al.* 2025 [179], which is attached in the appendix. The present dissertation considers only 4 biological replicates generated within this work, each measured in two technical replicates.

To further evaluate the cellular basis of the mFUS-induced response and to determine whether the increased expression of dormancy- and stemness-associated markers after mFUS was primarily attributable to GSCs or more differentiated GBM cells, additional experiments were performed using 3D hydrogel-based patient-derived more differentiated GBM cultures as well as GSC hydrogel cultures. Both cell populations were exposed to mFUS (15 Watts), and marker expression was analyzed 24 h after treatment comparable to GBO analysis (Figure 13 B).
In alignment with the performed IF staining of IGFBP5 in the focal zone of patient-derived more differentiated GBM hydrogel samples (Figure 12), IGFBP5 was expressed more prominently in the center than in the margin after mFUS treatment, compared with untreated

control. Both patient-derived GBM subpopulations responded to mFUS with an increase in dormancy- and stemness-associated gene expression, with a prominent induction of the stemness markers OCT4 in GSCs and Nestin in more differentiated GBM cells, detectable in the focal region (center) as well as in the peri-focal region (margin). However, regional differences can be observed, with a stronger induction of SKI (~8-fold) and Nestin (~12-fold) seen in the margin of more differentiated GBM cells, whereas GSCs showed a stronger induction of SKI (~5-fold) and Nestin (~7-fold) in the center, near the focal zone. Therefore, the data extended the previous observations made in GBOs: GSCs as well as more differentiated GBM cells were capable of contributing to an increase in dormancy- and stemness-associated gene marker expression after mFUS treatment. Similar to the results made in GBOs, the response to mFUS was not restricted to a single marker or cellular compartment, but rather involved a broader induction of markers associated with stemness and dormancy. qPCR datasets have previously been published in Hellmold *et al.* 2025 as part of a larger dataset comprising two different more differentiated GBM cell primary cultures as well as two different GSC primary cultures [179]. The present dissertation considers only one primary culture of more differentiated GBM, as well as one primary culture of GSC generated within this work, each measured in three biological replicates.

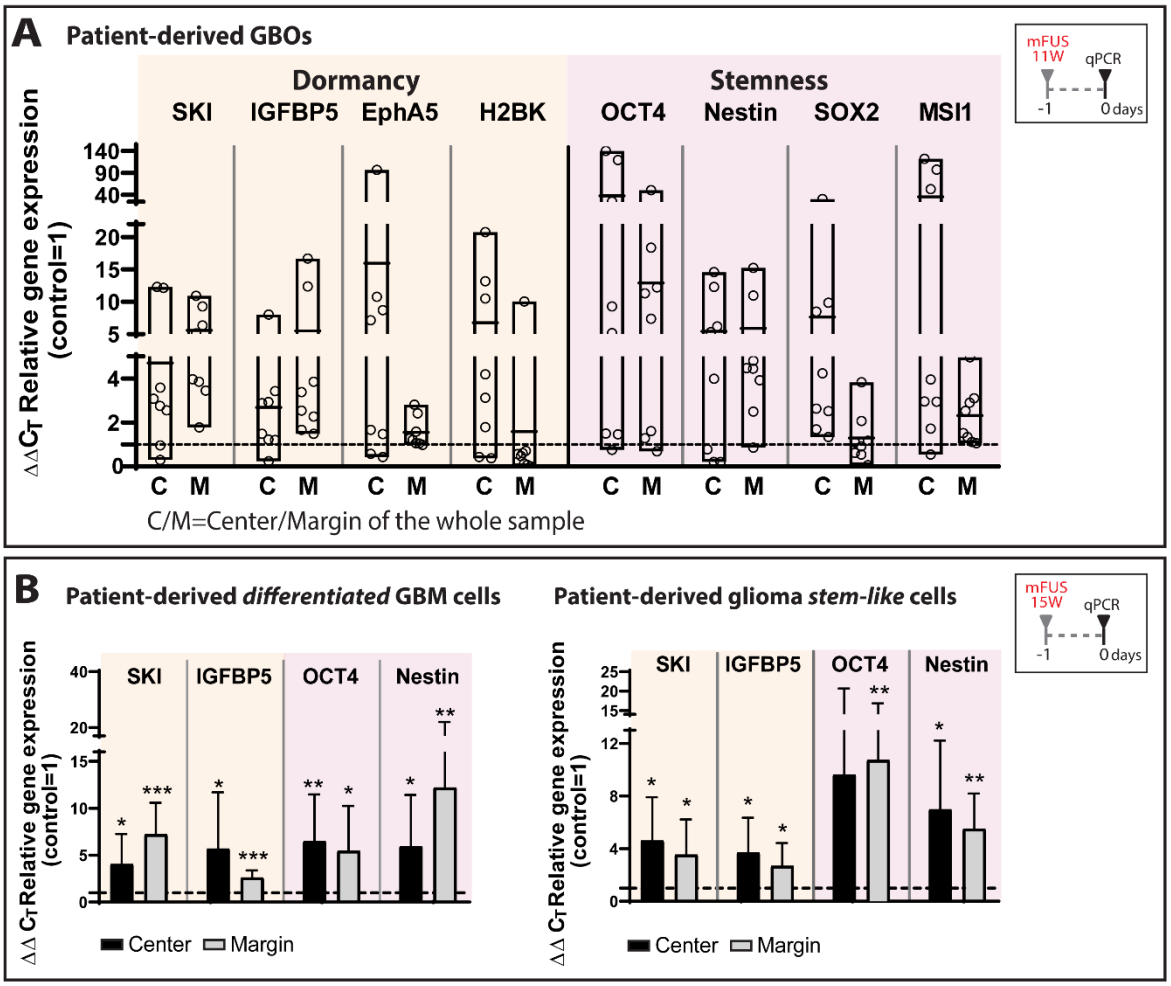


Figure 13 – mRNA expression level of mFUS-treated GBOs, as well as more differentiated GBM cells and GSCs. **A** GBOs treated with mFUS (11 and 15 Watts). **A** GBOs treated with mFUS showed a region-dependent induction of stemness- and dormancy-associated markers compared to untreated control (control = 1). n=4 biological replicates with n=2 technical replicates each. Statistical analysis was performed using a nonpaired t-test, but no significances were detected due to the heterogeneity of the preparations. The samples represent a subset of a previously published larger dataset comprising 8 biological replicates in Hellmold *et al.* 2025 [179]. **B** Patient-derived more differentiated GBM cells as well as GSCs treated with mFUS showed region-dependent induction of exemplary stemness- and dormancy markers, compared to untreated control (control = 1). n=3 biological replicates with n=1-2 technical replicates each. Significant differences compared to the untreated control were determined using a nonpaired t-test, indicated by asterisks above the bars (*p<0.05; **p<0.01; ***p<0.001). Error bars correspond to the standard deviation. See table 9 for marker abbreviations.

Collectively, these results support the conclusion that mFUS treatment induced a broad adaptive program in GBM cells. Together with the information gained regarding the cytotoxic effect of mFUS and the resulting cellular damage in the focal zone, as depicted by cCaspase3 IF staining, the observed transcriptional alterations suggest that mFUS not only induced structural damage, but also modulated molecular programs linked to tumor cell state. To evaluate the biological relevance of these changes, functional assays were subsequently used to determine whether the molecular response caused changes in self-renewal, response to therapy, or signaling behavior.

5.1.2.2 Functional relevance of mFUS-induced changes: Self-renewal, therapy response, and signaling behavior

To determine the biological relevance of the mFUS-induced increase in dormancy- and stemness-associated markers, functional assays in patient-derived more differentiated GBM cells as well as GSCs were performed. Therefore, two complementary readouts were chosen. First, the impact of mFUS treatment was further examined using extreme limiting dilution assays (ELDA), evaluating sphere-forming capacity under stem cell-promoting conditions in order to assess self-renewal and stem-like properties (Figure 14 A). Neurosphere formation under non-adherent, serum-free stem cell conditions is known to be associated with stem-like cells [215,216]. Therefore, ELDA is widely used to evaluate whether cells can actually behave more like stem-like cells, providing a quantitative framework to compare sphere-forming frequency between conditions [216,217]. For this assay, more differentiated GBM cells cultured in 3D hydrogels were treated with mFUS. After 48 h, the cells were transferred into neurosphere medium seeded at progressively lower densities (3,200 to one cell), and maintained for 7 days. Under these conditions, the capacity of more differentiated GBM cells to generate spheres increased with rising mFUS pretreatment intensity (5 vs. 11 Watts), with 24 to 28 spheres within a total number of 3,200 cells for 11 Watts compared to 13 to 15 spheres within a total number of 3,200 cells for 5 Watts mFUS treatment (untreated control ~14 spheres within a total number of 3,200 cells). Therefore, the data showed a stronger capacity to form spheres after mFUS treatment compared to unstimulated control, indicating induced stem-like behavior in more differentiated GBM cells through mFUS treatment. The results were published in Hellmold *et al.* 2025 [179], which is attached in the appendix.

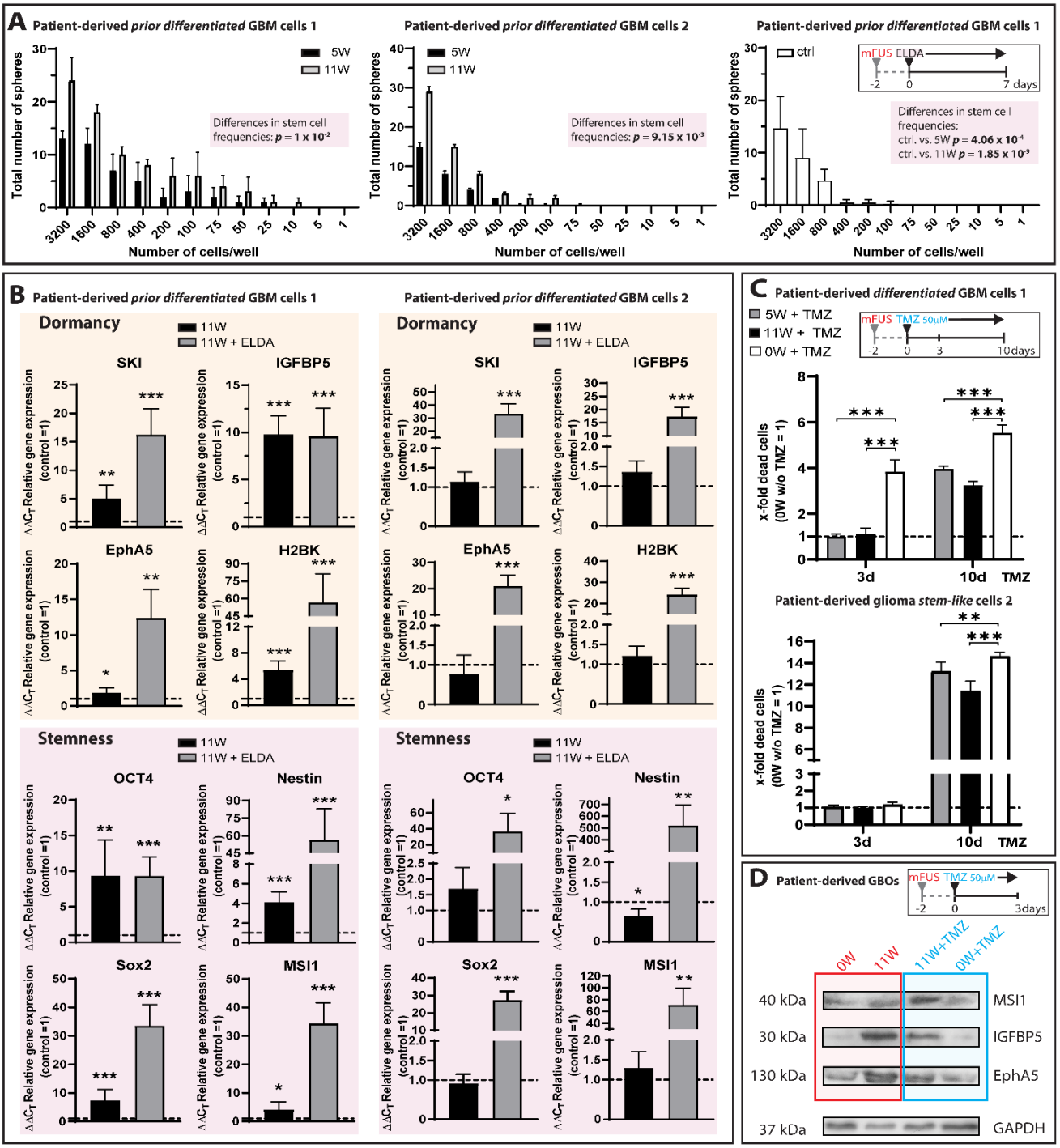


Figure 14 – **A** Effects of mFUS (5 and 11 Watts) on the ability of patient-derived more differentiated GBM cells to form stem cell-typical spheres. Performing ELDA on cells seeded at progressively lower densities, cultured for 7 days, and then counting the number of spheres per well at each seeding density, revealed an increased ability to form spheres under stem cell conditions, compared with the untreated control. n=2 different cell preparations with n=2 biological replicates each. Statistical analysis was performed using the online ELDA program 25 (https://bioinf.wehi.edu.au/software/elda/) with p = 0.01 for preparation one, p = 0.00915 for preparation two, and p = 0.000406 for ctrl. vs. 5 Watts mFUS treatment as well as p = 1.85×10^{-9} for ctrl. vs. 11 Watts mFUS treatment. **B** mRNA expression of mFUS treated more differentiated GBM cells 48 h after mFUS and continued cultivation in neurosphere medium (7 days), compared to untreated control (control = 1). Due to methodological constraints, it was not possible to make any regional distinctions. n=5 biological replicates with n=1-3 technical replicates for preparation one, and n=4 biological replicates with n=1-3 technical replicates for preparation two.

Statistical analysis was performed with a nonpaired t-test. Statisitcal significanes were indicated directly above the bars (*p<0.05; **p<0.01; ***p<0.001). Error bars correspond to the standard deviation. **C** Patient-derived more differentiated GBM cells and GSCs were treated with mFUS (5 and 11 Watts), and stimulated with 50 µM TMZ 48 h after mFUS treatment for up to 10 days. Due to lower numbers of dead cells compared to TMZ treatment alone, higher resistance to TMZ could be observed following mFUS pre-treatment, compared to untreated control (control = 1). n=2-3 biological replicates with n=1-3 technical replicates each. Significant differences were determined by a two-way ANOVA following Tukey's multiple comparison test (**p<0.01; ***p<0.001). Error bars correspond to the standard deviation. **D** GBOs treated with mFUS (11 Watts) and stimulated with 50 µM TMZ, starting 48 h after mFUS and continuing for 3 days, showed increased protein expression of the stemness marker MSI as well as the dormancy markers IGFBP5 and EphA5, compared to the untreated control. GAPDH served as loading control. See table 9 for marker abbreviations.

The increased sphere-forming ability after mFUS pretreatment was further supported by the corresponding transcriptional profile depicted in Figure 14 B. mFUS pretreatment of more differentiated GBM cellls followed by cultivation in neurosphere medium for 7 days (Figure 14 B, 11 Watts+ELDA) was associated with induction of several dormancy- and stemness-related genes compared to unstimulated control. For both primary cell cultures of more differentiated GBM cells, the induction of dormancy- and stemness-related genes was more pronounced under stem cell conditions than mFUS treatment alone (48 h after mFUS; 11 Watts). Particularly strong regulation was observed for SKI, H2BK, Nestin, MSI1, and SOX2 in preparation one, and additionally for OCT4, MSI1, and IGFBP5 in the second preparation (mFUS + stem cell conditions only). Please note that, unlike the transcriptional data presented in Figure 13 B in section 5.1.2.1, which was collected 24 h after mFUS treatment, the data presented in Figure 14 B were collected 48 h after mFUS treatment. In this setting, it was not possible to differentiate mFUS treatment in a region-specific manner. Despite the lack of regional differentiation and the observation at a later time point (48 h), in this setting, an induction of IGFBP5, OCT4, and MSI1 after mFUS treatment can be observed in both preparations. Nevertheless, the data obtained are in line with the preceding results. Together with the performed ELDA assay, an increased stem-like capacity was observed, as reflected by enhanced sphere formation under stem cell-favoring culture conditions and induced expression of stemness markers. The results were published in Hellmold *et al.* 2025 [179], which is attached in the appendix.

As a second readout, the response to temozolomide (TMZ), an alkylating cytostatic agent inhibiting DNA-replication of GBM cells [218], was investigated to assess whether mFUS pretreatment could be beneficial or is associated with a more therapy-resistant phenotype (Figure 14 C). TMZ is a foundational component of current GBM treatment, particularly in the post-surgical chemoradiotherapy setting, and its clinical benefit is closely linked to MGMT promoter methylation status, which modulates sensitivity to alkylating DNA damage

[218]. Therefore, MGMT promoter methylation is closely related to increased TMZ sensitivity [219]. In this study, both patient-derived GSCs and more differentiated GBM cells carried a methylated MGMT promoter. TMZ stimulation was performed as described in section 4.1.6. To assess the effects of mFUS treatment on the sensitivity of more differentiated GBM cells and GSCs to TMZ, mFUS pretreatment (5 and 11 Watts) was performed, followed by TMZ stimulation (50 µM) 48 h later. Cytotoxicity was analysed on days three and 10 of TMZ treatment. In both cell populations, pretreatment with mFUS significantly reduced the cytotoxic effect of TMZ compared with non-pretreated controls (0 Watts & TMZ) after 10 days of treatment (Figure 14 C). With increasing mFUS intensity, a slight increase in protection from subsequent TMZ treatment was observed in both analyzed preparations after 10 days of treatment, although this trend did not reach significance relative to the corresponding controls. Therefore, a protective effect of mFUS treatment could be observed. This protective effect was more evident in more differentiated GBM cells than in the GSCs. Taken together, these findings indicate that mFUS pretreatment promoted a more chemoresistant phenotype. As stemness and dormancy are widely considered to contribute to treatment failure, tumor persistence, and recurrence [34,220–222], an analysis of the expression of dormancy and stemness-associated proteins was performed to determine whether changes in these factors could play a role in the observed more chemoresistant phenotype.

In detail, GBOs were pretreated with mFUS (11 Watts) and stimulated with TMZ 48 h after mFUS treatment (50 µM). After three days of treatment, protein expression of MSI1, IGFBP5, and EphA5 was evaluated (Figure 14 D). An increased protein expression of MSI1, IGFBP5, and EphA5 in GBOs treated with mFUS and TMZ was detected compared with GBOs receiving TMZ without mFUS pretreatment (Figure 14 D, highlighted in blue). In line with the obtained qPCR data described in section 5.1.2.1, increased expression of MSI1, IGFBP5, and EphA5 in GBOs treated with mFUS compared with an untreated control was observed (Figure 14 D, highlighted in red). Taken together, the data suggest that mFUS pretreatment may have caused surviving GBM cells to favor a more stemness- and dormancy-associated state that is compatible with persistence under subsequent therapeutic stress. The results were published in Hellmold *et al.* 2025 [179], which is attached in the appendix.

Taken together, the ELDA sphere-formation data, cytotoxicity assays under TMZ and mFUS treatment, and Western blot analysis indicated that mFUS treatment enhanced functional properties linked to stem-like behavior and therapy resistance in different GBM subpopulations, and that mFUS-induced stress is associated with biologically relevant changes in GBM cells. As a final step, the potential mechanistic basis of the response is addressed, with a particular focus on associated signaling pathways.

5.1.3 Biological consequences of mFUS-induced changes: Involved signaling

To further explore potential downstream signaling, inhibition experiments were performed with more differentiated GBM cells using the PI3-kinase (PI3K) inhibitor LY294002. The PI3K pathway is considered a key pathway regulating GBM cells and is often hyperactivated in these cells [223]. Moreover, previous work demonstrated the involvement of the PI3K/Akt/GSK3β signaling pathway in the regulation of stemness and dormancy properties of GBM cells [224–226]. For inhibition of the PI3K pathway, the inhibitor was administered one hour before mFUS treatment (15 Watts) to evaluate changes in protein expression (Western blot analysis, Figure 15 A), and 30 minutes before mFUS (15 Watts) for qPCR readouts (Figure 15 B). Western blot analysis included the evaluation of the protein expression of p-Akt and p-GSK3β. The phosphorylation of Akt at Thr308 is an activating modification that leads to downstream signalling in the PI3K/Akt pathway [227]. This pathway is strongly involved in tumor cell survival, therapy resistance, and the maintenance of stem-like properties [228]. In contrast, the phosphorylation of GSK3β at Ser9 is an inhibitory modification [229]. Notably, both phosphorylations ultimately lead to increased expression of molecules associated with dormancy and stemness [230,231].

Western blot analysis showed that mFUS affected the phosphorylation status of both Akt and GSK3β, leading to an increased phosphorylation of both (Figure 15 A). This effect was partially reduced by LY294002 administration. The results are mechanistically consistent with the activation of the PI3K/Akt pathway and the suppression of GSK3β activity following mFUS treatment. Therefore, the results indicated that PI3K-dependent signaling contributes to the intracellular response of mFUS treatment. However, since LY294002 is not fully selective [232], the inhibition data provided should only be considered as supportive rather than definitive proof of pathway involvement. At the transcriptional level, pharmacological PI3K inhibition led to a partial reduction in the expression of dormancy- and stemness-associated genes induced by mFUS, with particularly clear effects on SKI and Nestin expression (Figure 15 B). The data further support the potential involvement of the PI3K pathway and was consistent with the obtained western blot data. At the same time, the fact

that the inhibitory effect was only partial indicated that the response to mFUS was not regulated by a single linear pathway, but rather by a more complex signaling network. The results were published in Hellmold *et al.* 2025 [179], which is attached in the appendix.

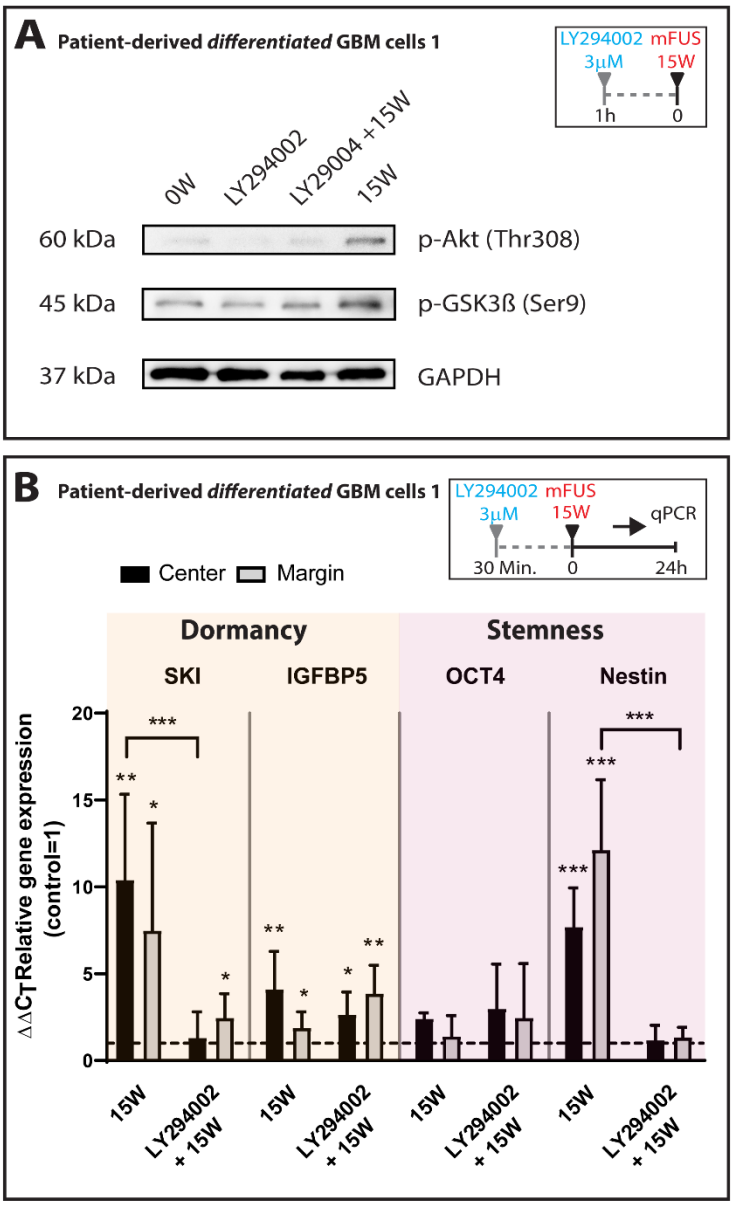


Figure 15 - **A** Protein expression in patient-derived more differentiated GBM cells treated with mFUS (15 Watts) and stimulated with the PI3-kinase inhibitor LY294002 (3 µM, 1 h prior mFUS) showed decreased phosphorylation of GSK3β (Ser9) and Akt (Thr308) compared to mFUS treatment alone. GAPDH served as loading control. **B** Patient-derived more differentiated GBM cells stimulated with mFUS (15 Watts) and the PI3-kinase inhibitor LY294002 (3 µM, 30 minutes prior mFUS) showed a partial reduction in mRNA expression of dormancy- and stemness associated markers, with statistically significant reduction of SKI and Nestin compared to mFUS treatment alone. n=2 biological replicates with n=2 technical replicates each. Statistical significance between different stimulations was determined using a one-way ANOVA followed by Tukey's multiple comparison test (***p<0.001). Statistical significance compared to the untreated control (control = 1) were determined using a nonpaired t-test (*p<0.05; **p<0.01; ***p<0.001). Error bars represent the standard deviation. See table 9 for marker abbreviations.

In summary, the data presented showed that mFUS can induce therapy-associated stress in GBM models and that this intervention is linked with measurable alterations in transcriptional programs, functional behavior, pronounced cytotoxicity, as well as altered PI3K/Akt/GSK3β signaling. The findings support the concept that mechanically induced disturbances may influence dormancy- and stemness-associated properties in a region-dependent manner.

The second part of this study addressed a conceptually related question in a developmental disease. Rather than using externally therapy-induced stress in a GBM model via mFUS treatment, the following experiments examined internal causes of stress due to potential pathologic environments in the CNS in the context of myelomeningocele (MMC). This shift enabled the investigation of whether stress-associated response in stemness-related cell properties represents a shared response across distinct CNS stress contexts, regardless of whether stress is induced externally or arises intrinsically during development. The following section therefore examined the effects of artificial amniotic fluid (aAF) on the survival, proliferation and stemness-associated regulation of spinal cord-derived adult rat neural progenitor cells (NPCs).

5.2 Effects of artificial amniotic fluid in the myelomeningocele model

In addition to the GBM model of therapy-induced stress described in the previous section, this study further examined the context of environmental stress in myelomeningocele (MMC). MMC can be understood as a progressive fetal spinal cord injury, characterized by failed neurulation [39]. As a consequence, the exposed neural placode remains in prolonged contact with amniotic fluid and is susceptible to mechanical forces [108]. This has given rise to the two-hit model, with failed neurulation and exposed placode to *in utero* environment and, more recently, to a third-hit concept that emphasizes downstream molecular injury cascades [115,126,127]. Experimental data further suggest that MMC is associated with altered progenitor cell behavior and development, including reduced neurogenesis, impaired oligodendrogenesis, and early astrogenesis [108,128–130]. In this section, the focus was placed on amniotic fluid as a potential driver of cell alterations in the context of MMC, with a particular focus on its effects on stemness-associated cellular behavior.

Furthermore, the effects of erythropoietin (Epo), which is produced during embryonic neurodevelopment and exhibits neuroprotective properties, were investigated [144,233–237]. The influence of amniotic fluid-like conditions was examined on adult NPCs from rats and on human neuron-like neuroblastoma cells SH-SY5Y, which is an established immature

neuroblastic model to study neuronal differentiation, neurotoxicity, and neurodegenerative disease mechanisms, particularly in Parkinson's disease research [238–240].

First, an *in vitro* model was developed to study the effects of amniotic fluid. Based on an extended literature review, a human-based artificial amniotic fluid (aAF) was developed (see section 4.1.5), and the effect of aAF on adult rat NPCs regarding proliferation and cell death rates was analyzed (Figure 16). Following the establishment of the model system, the molecular consequences of aAF as well as Epo treatment were examined (Figure 17 and 18), and the signaling pathways involved were investigated. Since the JAK2/STAT5 axis represents the canonical pathway for Epo-EpoR signaling, triggering further secondary pathways like the PI3K-Akt or RAS-ERK pathways [241–244], inhibition experiments with the JAK2 inhibitor AG490 were performed (Figure 19). The results were partially published in Knerlich-Lukoschus *et al.* 2025, which is attached in the appendix. Any data that has already been published is accompanied by a reference to the publication.

As an outlook, first experiments were conducted in a human *in vitro* system using SH-SY5Y cells. The influence of aAF on proliferation and cell death rates, as well as its phenotypic consequences, was analyzed (Figures 20 to 22). Furthermore, new MMC patches were evaluated, as these are intended to protect the exposed spinal cord from the amniotic fluid environment. These patches were developed in cooperation with the Department of Pharmaceutics and Biopharmaceutics, Kiel University, Germany. As biocompatibility and their influence on cell morphology, particularly cell adhesion, are essential parameters for assessing the suitability of the developed MMC patches, the following experiments examined the effects of selected patch materials on SH-SY5Y cell morphology and cytotoxicity (Figure 23) as a first screening toward their potential suitability for MMC-related applications.

5.2.1 Establishment of the aAF treatment framework

To model the effect of amniotic fluid environment on adult spinal cord-derived rat NPCs under controlled *in vitro* conditions, a human-based aAF was used. As described in section 4.1.5, the solution was based on reported mean concentrations of the metabolic composition of human amniotic fluid at approximately 22 weeks of gestation. First, the impact of different aAF concentrations on rat NPC proliferation and cell death was assessed in a concentration-response experiment (Figure 16). Exposure to different ratios of aAF with cell culture medium revealed that 30% and 55% aAF already significantly reduced NPC proliferation compared to untreated controls, demonstrating that partial replacement of the standard culture medium with aAF has a measurable antiproliferative effect. This effect was

more pronounced at 80% and 100% aAF, resulting in significantly impaired cell proliferation (Figure 16, left). Since the decrease in cell number could be associated with increased cell loss, the analysis of cytotoxicity was conducted in parallel (Figure 16, right). Based on the severity of the response regarding NPC cell number, cytotoxicity assays were performed with 30%, 55% and 80% aAF, whereas 100% aAF was excluded due to excessive cell loss, preventing meaningful downstream analysis. The shown cytotoxicity profile demonstrated a dose-dependent and progressive cytotoxicity over time. At 55% and 80% aAF, significantly increased cytotoxicity was already detectable from day one onward and continued to rise over the course of the observation period. By day 8, treatment with 80% aAF had resulted in approximately a sixfold increase in dead cells relative to untreated controls, whereas 55% aAF caused an approximately 3.5-fold increase. In contrast, the effect of 30% aAF was delayed, with cytotoxicity first becoming apparend on day three and then increasing gradually thereafter. The results were published in Knerlich-Lukoschus *et al.* 2025 [245], which is attached in the appendix.

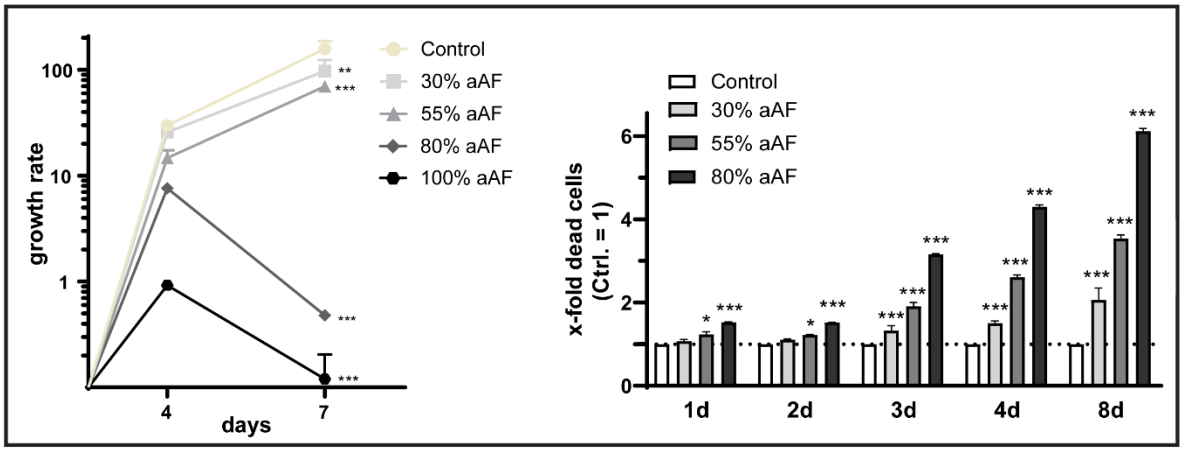


Figure 16 - Effect of artificial amniotic fluid (aAF) on spinal cord-derived rat neural progenitor cells (NPCs). **Left:** aAF stimulation resulted in an anti-proliferative effect that increased progressively with higher aAF concentrations. n = 4 biological replicates. **Right**: aAF resulted in a concentration-dependent increase in the number of dead cells. n = 2 biological replicates with n = 2 technical replicates each. Statistical significance between different stimulations was determined using an ordinary two-way ANOVA test followed by a Tukey's multiple comparison test (*p<0.05; ***p<0.001). .

Taken together, the findings showed that aAF has a pronounced antiproliferative effect on adult rat NPCs in a concentration-dependent manner, accompanied by cytotoxic effects at higher concentrations of aAF and with prolonged stimulation. The results provided the basis for the following experiments on Epo responsiveness and stemness-associated marker regulation. Furthermore, the experiments established 30-80% aAF as an informative range for subsequent analyses, with an aAF concentration of 55% showing pronounced effects on cytotoxicity and proliferation starting on day one. Thus, subsequent experiments were conducted with 55% aAF.

5.2.2 Stimulation of adult rat progenitor cells with artificial amniotic fluid – Comparison with neuroprotective erythropoietin treatment

Erythropoietin (Epo) is known to protect against neurodegenerative processes in neurological disorders and is a well-tolerated drug with clinical applicability, which makes Epo an interesting candidate for MMC treatment [135,246]. To evaluate whether Epo can mitigate the adverse effects of aAF on rat NPCs, the cells were exposed for up to 8 days to aAF in the presence or absence of 20 ng/mL Epo. For the Epo stimulation experiments, aAF was applied at 55%, as this concentration provides substantial exposure while maintaining sufficient cell yields for downstream analyses. In coherence with the results described in Figure 16, treatment with 55% aAF led to a pronounced antiproliferative effect compared with unstimulated controls (Figure 17, A left). When Epo was added together with 55% aAF, this antiproliferative effect was still present, but appeared less pronounced than under aAF treatment alone. In contrast, Epo alone did not induce a major deviation from the control proliferation pattern under standard culture conditions. As described and shown in section 5.2.1, the antiproliferative effect under aAF conditions was the dominant one that occurred. Therefore, the antiproliferative effect was further validated by analysing the proliferating cell nuclear antigen (PCNA) protein expression, as well as by Ki67 mRNA analysis. Ki67 is considered a classical proliferation marker, since it is present throughout the active phases of the cell cycle but absent in resting cells (G_0-state). Therefore, reduced Ki67 expression is generally interpreted as a decrease in the proportion of actively proliferating cells [247]. In line with the proliferation curve, 55% aAF stimulation alone led to a significant downregulation of Ki67 relative to unstimulated control. In the presence of Epo and 55% aAF, this downregulation was less pronounced. PCNA is likewise used as a proliferation-associated marker, as it functions as the DNA sliding clamp required for efficient DNA replication [248,249] and was therefore used as a complementary readout of the proliferative status. In accordance with the qPCR findings and proliferation curve, aAF treatment alone reduced PCNA expression compared to unstimulated control, supporting the conclusion that aAF suppresses proliferative activity in adult rat NPCs.

The cytotoxicity assay (Figure 17, B) provided further evidence for a protective effect of Epo. Regarding its cytotoxic effect, Epo alone remained at a level comparable to the unstimulated control throughout the examined time points. In contrast, aAF alone induced increased cytotoxicity in line with the results presented in section 5.2.1, which was already evident at the first analyzed time point and persisted at later stages. The addition of Epo to 55% aAF abolished this increase in cell death. Across the observation period, the Epo and 55% aAF condition remained below or close to the unstimulated control, with approximately 1.2-fold at day 8. Thus, while aAF alone exerted a clear cytotoxic effect, Epo significantly

attenuated this response. The results were published in Knerlich-Lukoschus *et al.* 2025 [245], which is attached in the appendix.

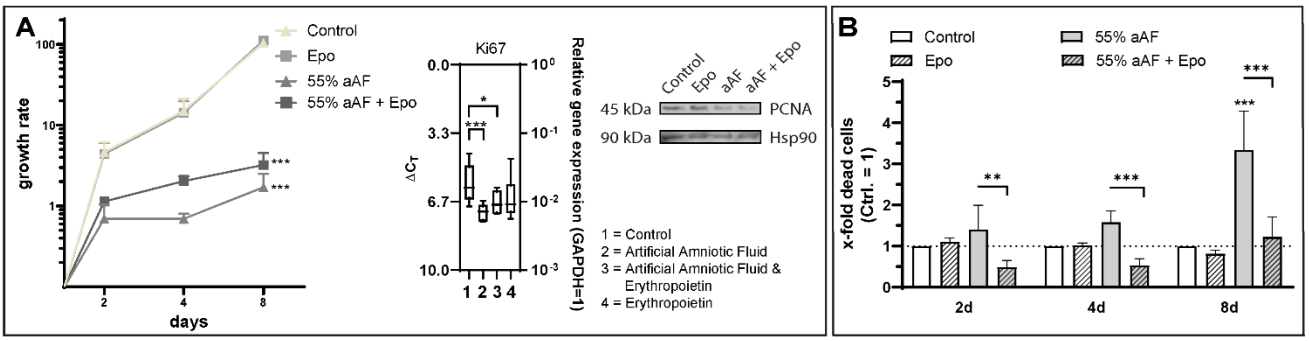


Figure 17 – Effect of erythropoietin (Epo) on spinal cord-derived rat neural progenitor cells (NPCs) treated with artificial amniotic fluid (aAF). **A** Compared to the unstimulated control (Control), stimulation with 55% aAF resulted in a pronounced antiproliferative effect. Combining stimulation of 55% aAF with Epo (20 ng/mL) resulted in a less pronounced antiproliferative effect. n=6 biological replicates. Ki67 qPCR analysis and PCNA Western blot analysis confirmed an antiproliferative effect through aAF stimulation. qPCR analysis: n=3 biological replicates, Western blot analysis: n=2 biological replicates. **B** Cytotoxicity assay revealed significant cytotoxicity of aAF, which was counteracted by Epo stimulation. n=6 biological replicates. Statistical significances were determined using an ordinary two-way ANOVA test followed by a Tukey's multiple comparison test (*p<0.05; **p<0.01; ***p<0.001).

To determine whether aAF influenced stemness-associated properties and whether the cytoprotective effect of Epo was accompanied by broader changes in cellular plasticity such as the progenitor cell state, qPCR analysis was performed as the next step. Rat NPCs were treated with Epo (20 ng/mL) in combination with 55% aAF for up to 8 days, and qPCR analysis was performed on day two and 8 of treatment (Figure 18). The qPCR panel was designed to capture several complementary aspects of the neural progenitor cell state. GFAP was included as an astroglial marker [250]. MAP2 and TUBB3 were used to monitor neuronal features, with TUBB3 reflecting relatively early neuronal commitment and MAP2 more mature neuronal differentiation [251–253]. Olig2 and CNPase were chosen to assess oligodendroglial lineage behavior, as Olig2 is a key regulator of oligodendrocyte lineage specification, whereas CNPase is commonly used as a marker of differentiating and myelin-associated oligodendroglial cells [254–257]. The panel further included markers associated with progenitor identity and stemness. MSI1 is a classical progenitor-associated RNA-binding protein [258]. SOX2 is a central regulator of neural stem cell maintenance and self-renewal, and its persistence generally indicates retention of a progenitor-like, undifferentiated state [257,259,260]. Nestin is a widely used neural progenitor marker and is typically associated with immature and proliferative precursor populations [257,261]. KLF4 is a stemness- and plasticity-associated transcription factor that has been linked to neural stem cells and is involved in the inhibition or delay of early neural differentiation in several systems [262,263]. Therefore, the panel allowed the assessment of astroglial,

neuronal, oligodendroglial, and progenitor-associated responses to prolonged aAF and/or Epo exposure.

After two days of stimulation, aAF treatment alone was associated with a broad reduction in expression across several marker classes (Figure 18, upper panel). A downregulation was observed for TUBB3, CNPase, MSI1, SOX2, Nestin, and MAP2, indicating that short-term aAF exposure initially suppressed both lineage-associated differentiation markers and genes linked to progenitor identity. Of these changes, the reduction in the core regulators of neural progenitor maintenance, MSI1 and SOX2, was particularly significant relative to the unstimulated control. A clear exception seems to be KLF4, which showed a slight, non-significant increase under aAF stimulation alone. Therefore, the early response to aAF was not a uniform collapse of all progenitor-associated programs investigated with the chosen qPCR panel but instead involved selective shifts within the regulatory network that controls the state of progenitor cells. When Epo was added together with 55% aAF, the aAF was largely counteracted. Under Epo and aAF, expression of the downregulated markers was restored to a level close to that of the unstimulated control, indicating that Epo substantially buffered the early transcriptional impact of a short aAF stimulation. Again, KLF4 behaved differently from the rest of the panel, since the combination of aAF and Epo induced a significant upregulation of KLF4 relative to the unstimulated control.

After 8 days of continuous daily stimulation, the expression pattern had shifted (Figure 19, lower panel). In contrast to the early, more suppressive response, prolonged aAF stimulation resulted in the induction of most of the genes in the panel. Except for GFAP and Nestin, all markers showed an increased expression, and this increase reached significance for TUBB3, Olig2, and KLF4. Accordingly, prolonged aAF exposure no longer appeared to be characterized primarily by transcriptional suppression, but rather by activation of a broader gene expression program involving neuronal, oligodendroglial, and stemness-associated markers. Under aAF and Epo treatment, this expression profile was comparable to or even more pronounced than that seen with aAF treatment alone. TUBB3 and Nestin were induced to a similar extent, whereas CNPase, Olig2, MSI1, SOX2, KLF4, and MAP2 showed a stronger increase and were significantly upregulated relative to the unstimulated control. Thus, while Epo largely prevented the potential early suppression of marker expression after two days of stimulation, it did not counteract the long-term transcriptional shift induced by sustained aAF exposure. Furthermore, the findings demonstrate a time-dependent response of rat NPCs to aAF, suggesting that the biological effect of aAF might depend on the duration of exposure and that a potentially protective effect of Epo might be more evident at early stages. A smaller panel consisting of MSI1, TUBB3, and MAP2, examined after two days of stimulation, was previously published in Knerlich-Lukoschus *et al.* 2025 [245], which is attached in the appendix.

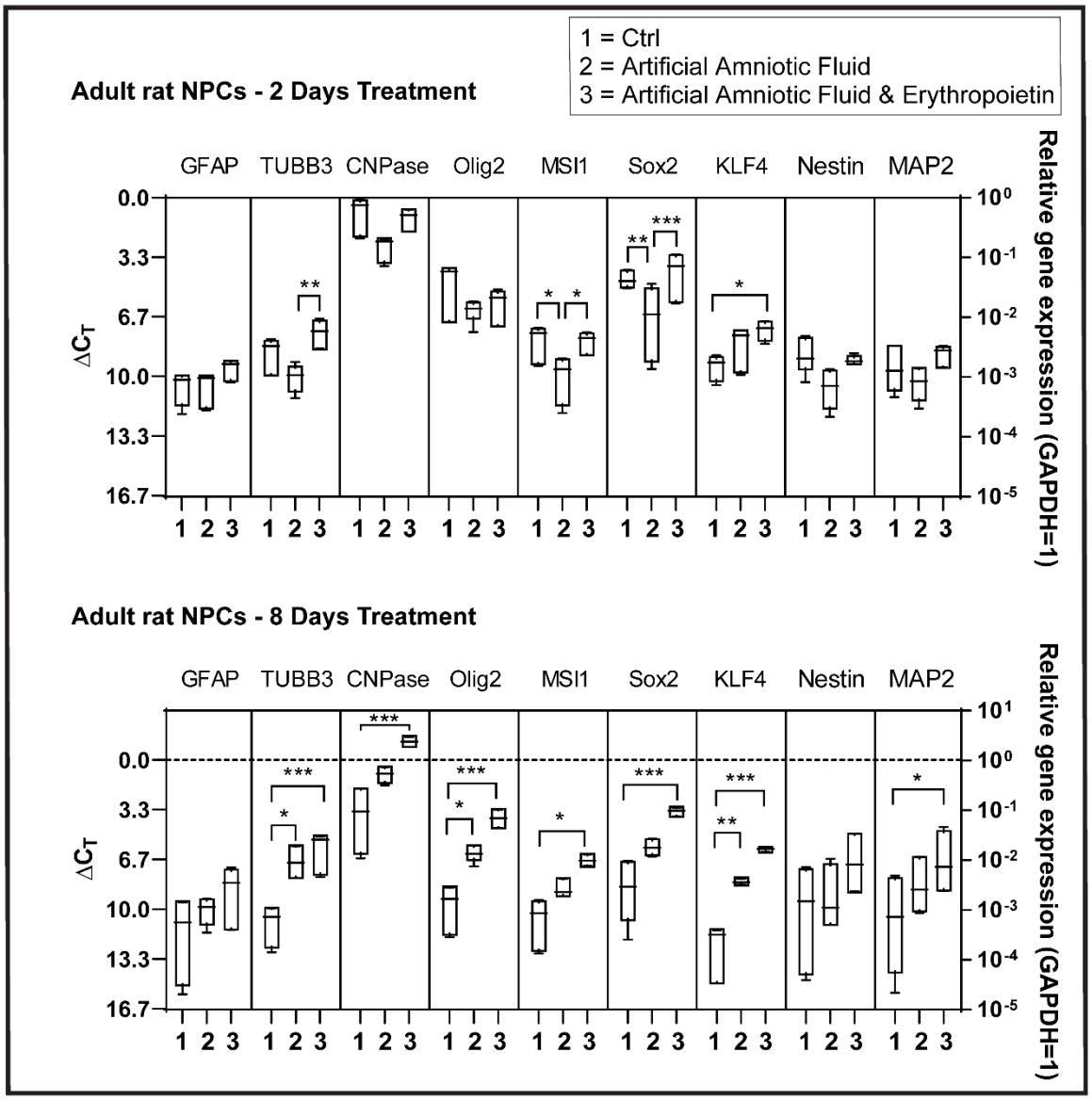


Figure 18 – Effect of erythropoietin (Epo) on spinal cord-derived adult rat neural progenitor cells (NPCs) treated with artificial amniotic fluid (aAF) at the gene expression level. The **upper panel** showed reduced expression of neuronal and stemness-associated cell markers following stimulation with aAF for two days. Stimulation with aAF and Epo tended to restore gene expression to the level of the unstimulated control. The **lower panel** showed induced expression of neuronal, oligodendroglial, and stemness-associated cell markers when cells were stimulated with aAF or aAF in combination with Epo for 8 consecutive days. n=3 biological replicates with n=2 technical replicates each. Statistical significances were determined using an ordinary two-way ANOVA test followed by a Tukey's multiple comparison test (*p<0.05; **p<0.01; ***p<0.001).

To further evaluate the signaling pathways involved in Epo-mediated effects under aAF-induced stress, the canonical EpoR-associated JAK2/STAT5/Akt signaling pathway-axis was examined. In neural systems, these pathway-axis have been linked to cytoprotective effects of Epo under stress conditions such as hypoxia or ischemia, contributing to cell survival and anti-apoptotic signaling [244,246,264–266]. After binding of Epo to its receptor, receptor-associated JAK2 is activated, which in turn triggers phosphorylation of

downstream effectors, including STAT5 and Akt [135]. Therefore, pharmacological inhibition experiments with the JAK2 inhibitor AG490 (10 µM, 30 minutes pre-incubation before Epo treatment) were performed, and the phosphorylation of STAT5 and Akt was examined. Western blot analysis of stimulated cells with aAF and/or Epo in presence or absence of the JAK2 inhibitor AG490 revealed altered phosphorylation of STAT5 and Akt (Figure 19). In detail, aAF and Epo stimulation led to an increase in phosphorylation of both STAT5 and Akt, supporting the concept of a stress-responsive Epo signaling mechanism in the nervous system. In contrast, this phosphorylation response was markedly attenuated when AG490 was applied, demonstrating that the observed pathway activation depended largely on upstream JAK2 activity. By comparison, Epo alone did not induce a comparably clear induction of phosphorylation under basal conditions (Figure 19). In accordance with the literature mentioned above, this pattern is consistent with the concept that Epo signaling may become particularly prominent or functionally relevant under cellular stress, whereas under basal conditions, the pathway response can remain weak or less detectable [246,264–267].

Since the antiproliferative effect under aAF conditions was the dominant one that occurred, further analysis of the effect of inhibiting the JAK2/STAT5/Akt signaling pathway-axis was performed. In line with the previous results, aAF treatment alone resulted in the lowest cell numbers (Figure 19). The supplementation of Epo partially counteracted this reduction in cell number. Together with the inhibitor AG490, this Epo-associated rescue was counteracted. Therefore, the partial recovery of cell growth observed with aAF and Epo treatment was no longer maintained once EpoR-JAK2-mediated pathways were blocked pharmacologically. This indicates that the beneficial effect of Epo in aAF-induced cellular stress requires, at least in part, the intracellular EpoR-JAK2-associated pathway and its downstream effectors. Taken together, these experiments demonstrated the loss of Epo rescue under JAK2/STAT5/Akt signaling pathway inhibition and strengthened a mechanistic link between Epo-mediated intracellular signaling and the observed biological consequences in the chosen experimental design. The results were published in Knerlich-Lukoschus *et al.* 2025 [245], which is attached in the appendix.

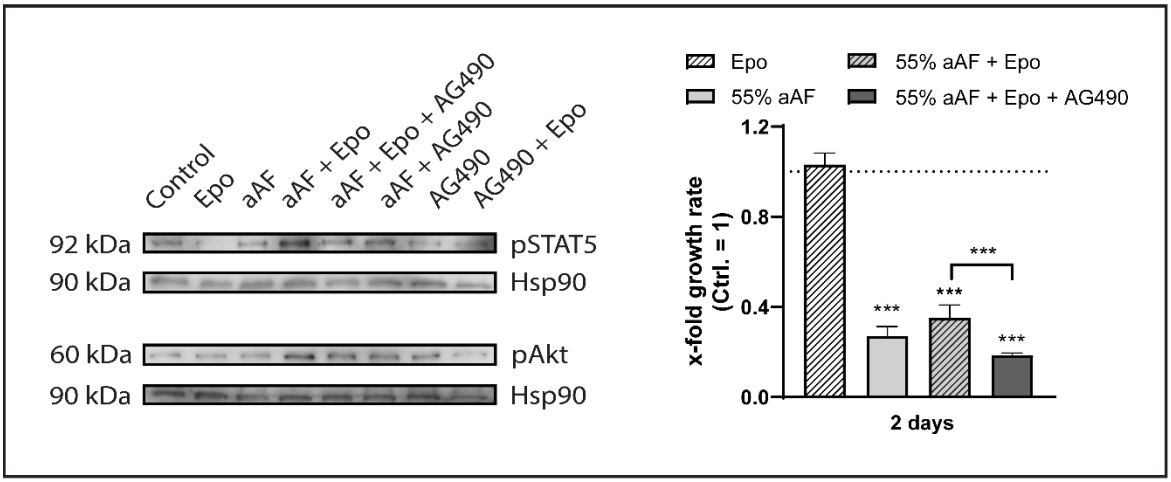


Figure 19 – Western blot analysis of the JAK2-mediated STAT5 and Akt phosphorylation confirmed robust phosphorylation of both markers in response to Epo treatment under aAF conditions, which was markedly attenuated with application of the JAK2 inhibitor AG490 (10 µM). n=2 biological replicates. Further proliferation analysis revealed the lowest cell numbers under aAF treatment, which was counteracted to a certain extent by Epo stimulation. However, this Epo-mediated effect was inhibited by the JAK2 inhibitor AG490 (10 µM). n=6 biological replicates. Statistical significance was determined using an ordinary two-way ANOVA test followed by a Tukey's multiple comparison test (***p<0.001).

Overall, the combined results obtained under aAF and Epo stimulation support a model in which aAF leads to a strong antiproliferative as well as cytotoxic response on spinal cord-derived progenitor cells, with Epo partially counteracting this stress response, mainly by preserving cell survival mechanisms as indicated by cytotoxicity and proliferation assessment. The pathway inhibition experiments further indicated that this rescue depends, at least in part, on EpoR-mediated JAK2/STAT5/Akt signaling.

As an initial translational outlook, the findings obtained in the rat system were examined in a human cellular context. To this end, first exploratory experiments were performed in human SH-SY5Y cells to determine whether exposure to aAF would likewise affect cell survival and proliferation. Furthermore, the effect of aAF treatment on cell morphology was explored. At the same time, the human SH-SY5Y cells also served as the basis for the investigation of a second therapeutically relevant approach, namely MMC patch treatment strategies.

5.2.3 Human *in vitro* model – Cytotoxic, antiproliferative and morphological effects of aAF treatment in SH-SY5Y cells

As an initial step in transferring the experimental approach from the spinal cord-derived rat NPCs to a human cellular system, SH-SY5Y neuroblastoma cells were exposed to aAF for up to 8 days using a broad concentration range of 10%, 15%, 20%, 30%, 55%, 65%, 80% and 100%. Cytotoxicity was assessed on day 4 and day 8. As seen in Figure 20, the strongest cytotoxic effects were observed at the highest concentrations, with 65%, 80%, and 100% aAF resulting in complete cell death by day 8. At lower concentrations, the effect was markedly less pronounced. A statistically significant increase in cytotoxicity became apparent from 30% aAF onwards, with moderate effects, where 55% aAF corresponded to an approximate 1.5-fold increase relative to unstimulated control (Figure 20, upper panel). Since the lower concentrations showed none or only moderate cell death, 30% and 55% aAF were selected for a more detailed analysis of cytotoxicity and proliferation after a shorter stimulation period of 4 days (Figure 20, lower panel). At this earlier point, 55% aAF had already reached a cytotoxicity level of approximately 1.5-fold relative to the unstimulated control, indicating that the modest cytotoxic effect observed after 8 days of treatment was already established by day 4 and did not further increase over time. In contrast, 30% aAF did not induce measurable cytotoxicity on day 4 and remained close to the unstimulated control. Thus, the direct cytotoxic effect of aAF in SH-SY5Y cells remained relatively limited at the concentrations investigated. In contrast to this moderate cytotoxic response, the effect of aAF on cell proliferation was more pronounced. Treatment with 30% aAF resulted in a proliferation rate that remained close to the unstimulated control, while stimulation with 55% aAF caused a significant loss of proliferation, with cell growth reduced to less than half of that seen in the unstimulated control (Figure 20, lower panel). Accordingly, in line with the rat NPC system, the dominant biological effect of aAF treatment on human SH-SY5Y cells appeared to be a pronounced antiproliferative effect.

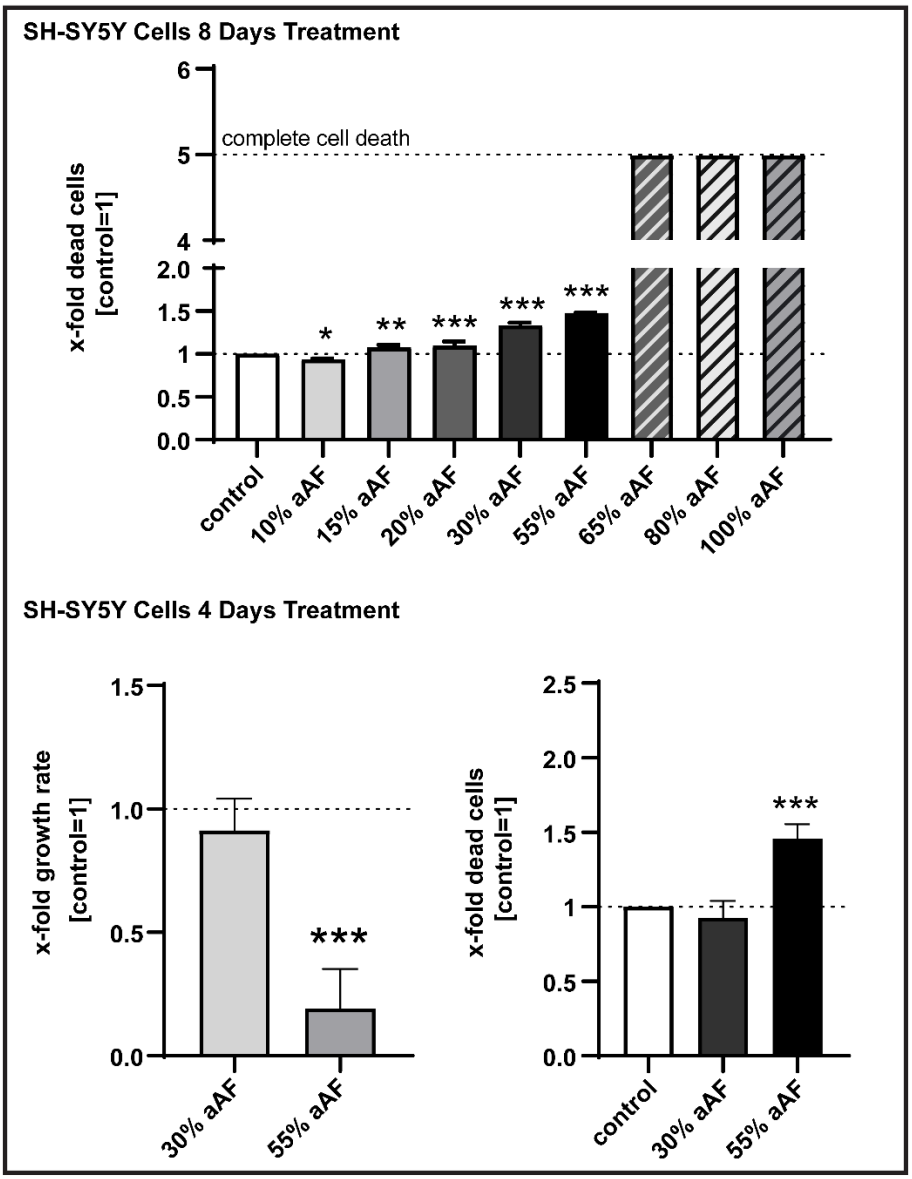


Figure 20 – Effect of aAF treatment on human SH-SY5Y cells. The results were expressed as the x-fold increase in dead cells relative to unstimulated control. The **upper panel** showed that aAF treatment for 8 days resulted in higher numbers of dead cells in a concentration-dependent manner. Complete cell death occurred at concentrations of 65% aAF and above, while moderate effects were observed at 30% and 55% aAF. n=2 biological replicates, with n=3 technical replicates each. Statistical significance was determined using an ordinary two-way ANOVA test followed by a Tukey's multiple comparison test (*p<0.05; **p<0.01; ***p<0.001). The **lower panel** confirmed moderate cytotoxicity for 55% aAF after 4 days of treatment, whereas no cytotoxicity could be detected for 30% aAF. Furthermore, a pronounced antiproliferative effect could be observed for 55% aAF treatment, compared to untreated control. n=4 biological replicates. Statistical significance was determined using an ordinary two-way ANOVA test followed by a Tukey's multiple comparison test (***p<0.001).

To further characterize this aAF response, brightfield microscopy was used to assess treatment-associated morphological changes over time. Under unstimulated conditions, SH-SY5Y cells displayed their expected mixed growth pattern, consisting of both floating and adherent cells organized in smaller cell islands. With increasing cell density obtained

through further cultivation, these cultures progressively formed more compact and partially vertical spherical aggregates, as seen in the control cultures as dense cell clusters (Figure 21).

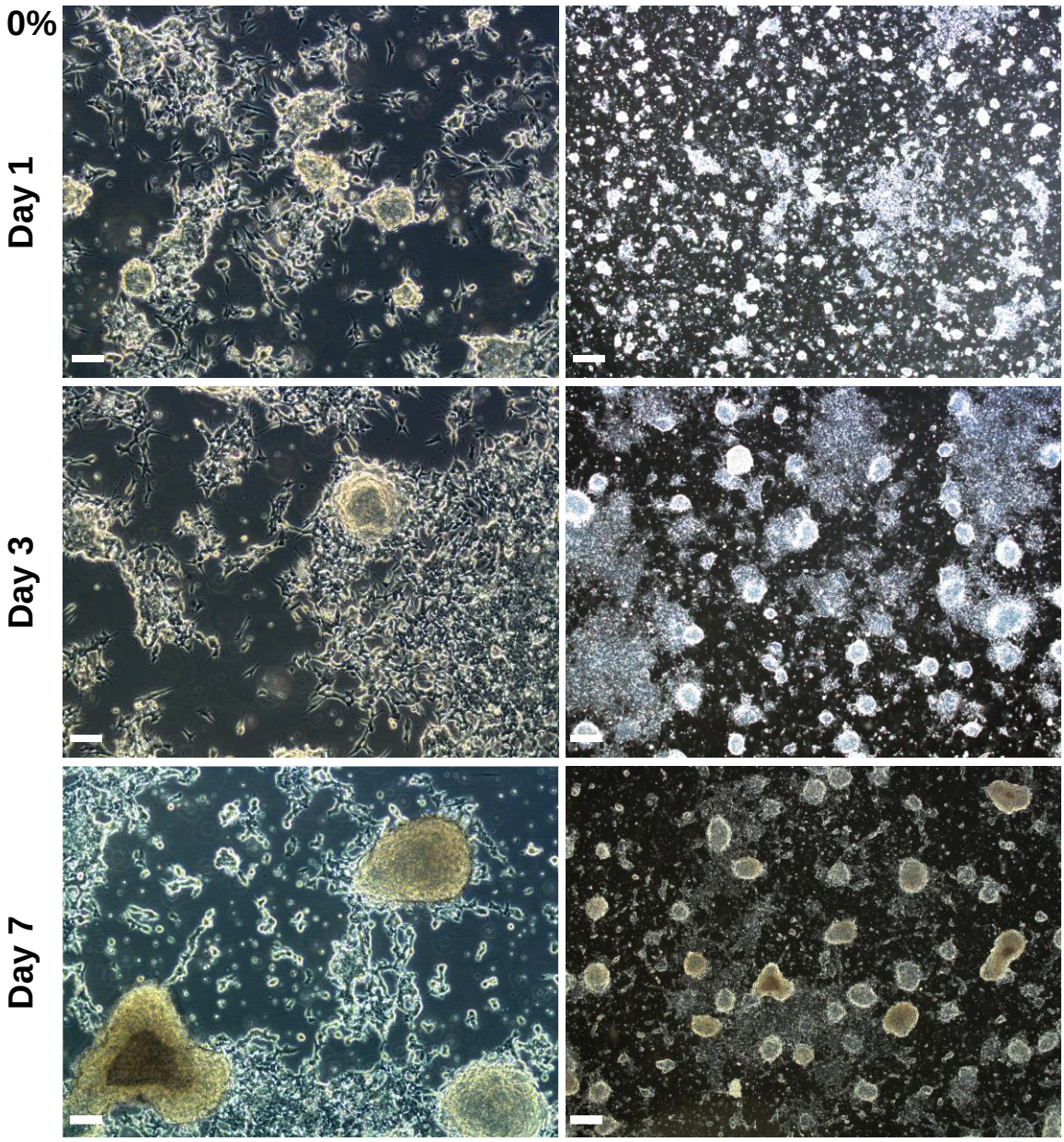


Figure 21 – Morphology of unstimulated SH-SY5Y cells during 7 consecutive days of cultivation. Under control conditions, SH-SY5Y cells exhibited a typical mixed growth pattern of floating cells and adherent cell islands, which formed more compact and partially vertical spherical aggregates with prolonged cultivation, visible as light absorbing darker structures. The brightfield images were captured using a Zeiss Axiovert 200. Scale bar = 20 µm.

In contrast, cells exposed to 55% aAF already showed altered morphology after one day of treatment (Figure 22). The cultures appeared less dense with elongated spindle-shaped cells extending long neurite-like processes, thereby forming a loose and more widely

distributed cellular network. Over time, the number of floating cells and floating cell clusters increased, indicating a progressive alteration of growth behavior and cell-cell organization under aAF exposure. Therefore, in addition to the observed pronounced antiproliferative effect under 55% aAF treatment, a morphological remodeling of SH-SY5Y cultures could be observed.

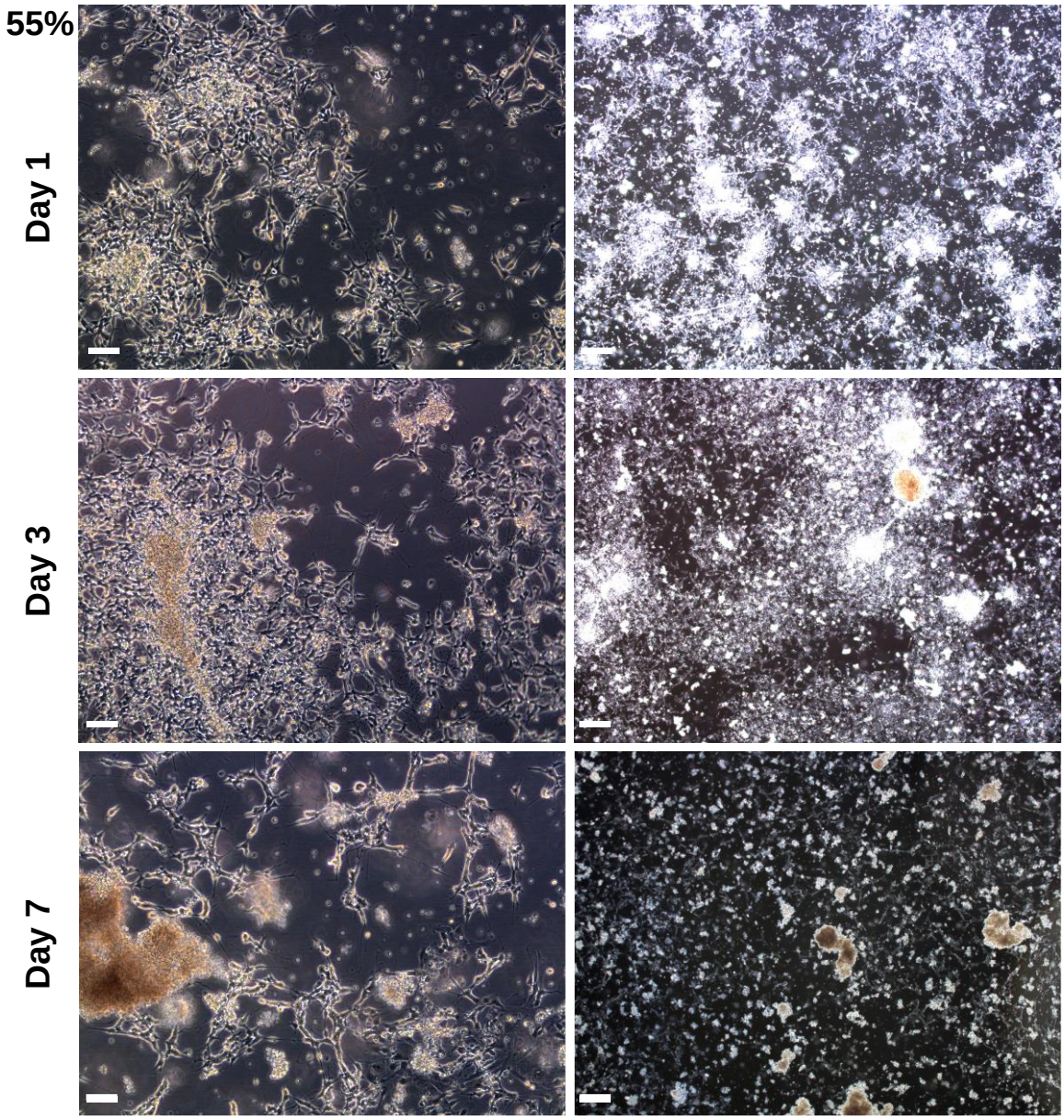


Figure 22 – Morphology of SH-SY5Y cells after stimulation with 55% aAF over 7 consecutive days. aAF-treated cells displayed reduced culture density and elongated spindle-shaped morphology with long neurite-like processes, forming a loose cellular network. Over time, the number of floating cells and floating cell aggregates increased. The brightfield images were captured using a Zeiss Axiovert 200. Scale bar = 20 µm.

Taken together, these findings confirmed that aAF treatment also affects human SH-SY5Y cells, albeit with a slightly different response pattern to that observed in the rat NPC system. While rat NPCs displayed a stronger cytotoxic response even at intermediate

concentrations, SH-SY5Y cells were characterized more prominently by an antiproliferative effect and marked morphological changes. Nevertheless, both systems confirmed a pronounced antiproliferative effect of aAF treatment. In the next step, another therapy strategy using MMC patches was explored with SH-SY5Y cells. These patch-based approaches are highly relevant for prenatal MMC repair to provide a protective barrier for the exposed spinal cord and to prevent secondary damage cascades that may result from contact with the amniotic fluid environment of the open neural tube [115,268].

5.2.4 Translational Outlook – Therapeutic MMC patch development for local protection against the influence of amniotic fluid

MMC Patches may offer a protective barrier over the exposed spinal cord to protect the lesion from the amniotic fluid environment [131,134]. However, an MMC patch must satisfy demanding and requirements, since they should be watertight or near-watertight, remain manageable in surgery processes, avoid direct adhesion to the neural tissue, and ideally support healing without increasing thethering or later surgical difficulty [131,134,150].
Given these demanding characteristics of an MMC patch, there are still many synthetic and bioactive patch concepts under active development [134,151,155,156], and further material screening remains necessary. The following experiments, thus, evaluated several synthetic polymers, focusing on biocompatibility aspects. In detail, initial tests were conducted to assess the suitability of the polymers for MMC patch development, focusing on cell adhesion, morphology, and cytotoxicity.
A total of 30 different materials or combinations of materials were analyzed (see Table 11). For this purpose, SH-SY5Y cells were seeded onto the patches, and their morphology and adhesion properties were observed and evaluated over a period of 48 h. Next, a cytotoxicity assay was performed to evaluate cell viability. The results for each material or material combination are recorded in Table 11. Regarding morphological aspects, adhesion, and low cytotoxicity, the combination of 5% polyvinyl acetate (PVAc) with 10% polylactic acid, as well as 5% Vinnapas® Special proved particularly promising (see Table 11, marked in red), as these materials exhibited low cytotoxicity and cell adhesion on the patch material, as well as viable cell morphologies. Please note that not every patch was evaluated regarding morphology and adhesion due to its density and composition.

Table 11 – Material screening for potential MMC patches, synthesized by the Department of Pharmaceutics and Biopharmaceutics, Kiel University, Germany, in collaboration with Prof. Dr. Regina Scherließ and Dr. Angelika Jüptner. If not stated otherwise, the MMC Patch was generated using the casting method described in section 4.1.4.

No.	MMC Patch [Solvent]	Observations
1	5% Polyvinyl acetate (PVAc) [Chloroform]	**Morphology:** Cells floating or semi-adherent, grown spherical in small to larger spheroids, a few adherent spindle-shaped cells with extensions grown in smaller to larger groups/islands - partly enlarged and potential apoptotic cells after 48 h. **Cytotox-Assay Result:** 25.37% cell death (n=1)
2	10% Polyvinyl acetate (PVAc) [Chloroform]	**Morphology:** Cells slightly adherent, floating in cell spheroids on patch material which appeared vital. After 48 h predominantly adherent growth with isolated spindle-shaped cells. **Cytotox-Assay Result:** 13.53% cell death (n=1)
3	10% Polyvinyl acetate (PVAc) [Acetone]	**Morphology:** Cell morphology and adherence analogous to untreated control, dense & vital, neurite formation. After 48 h deformed, dislocated cells of various sizes, appear damaged. **Cytotox-Assay Result:** 5.93% cell death (n=1)
4	20% Polyvinyl acetate (PVAc) [Chloroform]	**Morphology:** Scattered, low-density, spindle-shaped with elongated neurites. Unchanged throughout the cultivation period. **Cytotox-Assay Result**: 58.26% cell death (n=1)
5	5% PVAc + 10% Polylactic acid [Chloroform]	**Morphology:** Semi-adherent spheroids, appeared vital. After 48 h, large adherent spheroids with single spindle-shaped cells. **Cytotox-Assay Result:** 5.57±3.2% cell death (n=3)
6	5% PVAc + 10% Polycaprolactone [Chloroform]	**Morphology:** Semi-adherent spheroids, appeared vital. After 48 h, enlarged adherent spheroids with single spindle-shaped cells. **Cytotox-Assay Result:** 12.25% cell death (n=1)
7	10% PVAc + 10% Polylactic acid [Chloroform]	**Morphology:** Cells grew predominantly adherent, spindle-shaped morphology with neurite formation analogous to untreated control. Unchanged throughout the cultivation period. **Cytotox-Assay Result:** 5.46 % cell death (n=1)
8	10% PVAc + 10% Polylactic acid [Chloroform] *Spray method*	**Morphology:** Poorly microscopable, occasional vital cells are recognisable on patch material. Unchanged throughout the cultivation period. **Cytotox-Assay Result:** 5.88% cell death (n=1)
9	10% PVAc + 10% Polycaprolactone [Chloroform]	**Morphology:** Adherent, strongly singularized, low density, spindle-shaped with short neurites. Unchanged throughout the cultivation period. **Cytotox-Assay Result:** 51.44% cell death (n=1)

No.	MMC Patch [Solvent]	Observations
10	15% PVAc + 10% Polycaprolactone [Chloroform]	**Morphology:** Predominantly adherent growth, short spindle-shaped cells without observable neurites, few cell groups, number of single cells increased during the cultivation period. **Cytotox-Assay Result:** 65.61% cell death (n=1)
11	20% PVAc + 20% Polycaprolactone [Chloroform]	**Morphology:** Poorly microscopable - unclear whether cells are on patch material. Next to patch long spindle-shaped and increasingly spherical cells, partly blebbing, few cell debris. **Cytotox-Assay Result:** 69,19% cell death (n=1)
12	30% PVAc + 10% Polycaprolactone [Chloroform]	**Morphology:** Unclear whether cells are on patch, blebbing and cell debris observed next to patch. Unchanged throughout the cultivation period. **Cytotox-Assay Result:** 85.93% cell death (n=1)
13	20% PVAc + 10% Polycaprolactone [Chloroform]	**Morphology:** Unclear whether cells are on patch, blebbing and cell debris observed next to patch. Unchanged throughout the cultivation period. **Cytotox-Assay Result:** 70.22% cell death (n=1)
14	10% PVAc + 10% Eudragit® NM [Chloroform]	**Morphology:** Unclear whether cells are on patch, emerging cell death observed adjacent to patch, cells spherical and adherent with few spindle-shaped cells. Unchanged throughout the cultivation period. **Cytotox-Assay Result:** 62.79% cell death (n=1)
15	5% Eudragit® NE [Water]	**Morphology:** Patch not microscopically analysable (thickness, cloudy). **Cytotox-Assay Result:** 11.09% cell death (n=1)
16	10% Eudragit® NM [Acetone]	**Morphology:** Unclear whether cells are on patch, spherical adherent growing next to patch, over time increased blebbing and cell debris next to patch. **Cytotox-Assay Result:** 90.58% cell death (n=1)
17	10% Eudragit® NM [Chloroform]	**Morphology:** Unclear whether cells are on patch, blebbing and cell debris observed next to patch. Unchanged throughout the cultivation period. **Cytotox-Assay Result:** 85.65% cell death (n=1)
18	10% Eudragit® NM + 10% PVAc [Chloroform]	**Morphology:** Unclear whether cells are on patch, blebbing and cell debris observed next to patch. Unchanged throughout the cultivation period. **Cytotox-Assay Result:** 86.75% cell death (n=1)
19	10% Vinnapas® Special [Acetone]	**Morphology:** Semi-adherent spheroids, mostly spherical and spindle-shaped adherent cells, neurite formation. Unchanged throughout the cultivation period. **Cytotox-Assay Result:** 22.19±1.54% cell death (n=3)

No.	MMC Patch [Solvent]	Observations
20	5% Vinnapas® Special [Chloroform]	**Morphology:** After 24 h, floating and adherent cells comparable to untreated control, with preliminarily spherical cells. After 48 h predominantly floating cells with isolated semi-adherent. Cells/spheroids that reacted to movement of the well plate. **Cytotox-Assay Result:** 4.61±2.1 % cell death (n=3)
21	10% Vinnapas® Special [Chloroform]	**Morphology:** Sporadic adherent after 24 h, predominantly floating or semi-adherent cells with little reaction to movement. Adherent cells with spindle-shaped morphology. After 48 h, the majority of cells grew adherent to semi-adherent with little reaction to movement. **Cytotox-Assay Result:** 19.50±5.1% cell death (n=2)
22	5% Vinnapas® Special + Polycaprolactone [Chloroform]	**Morphology:** Semi-adherent spheroids and isolated spindle-shaped cells, mostly adherent after 48 h. **Cytotox-Assay Result:** 26.07% cell death (n=1)
23	5% Vinnapas® Special + Polylactic acid [Chloroform]	**Morphology:** Cell blebbing recognisable, partly adherent spindle-shaped cells, unchanged throughout the cultivation period **Cytotox-Assay Result:** 17.22% cell death (n=1)
24	10% Vinnapas® Special + 10% PVAc [Chloroform]	**Morphology:** Grown predominantly adherent to slightly loose, strongly scattered. Low cell density, decoupling observable over 48 h, few cell groups/isles detectable. **Cytotox-Assay Result:** 20.42% cell death (n=1)
25	Vinnapas® Special [Ethyl acetate] *Spray method*	**Morphology:** Cells grew adherent, strongly singularized. After 48 h, cell debris in the medium as well as vital adherent cells and neurite formation observed. **Cytotox-Assay Result:** 9.66% cell death (n=1)
26	Vinnapas® Special [Chloroform] *Spray method*	**Morphology:** Cells mostly adherent, occasionally blebbing, predominantly spherical morphology. Unchanged throughout the cultivation period. **Cytotox-Assay Result:** 23.31% cell death (n=1)
27	Vinnapas® Special [Acetone] *Spray method*	**Morphology:** Cells mostly adherent, occasionally blebbing, predominantly spherical. Unchanged throughout the cultivation period. **Cytotox-Assay Result:** 9.65% cell death (n=1)
28	5% Polyactid [Chloroform]	**Morphology:** Cell blebbing recognizable, predominantly in spheroids semi-adherent, occasional spindle-shaped cells. Unchanged throughout the cultivation period. **Cytotox-Assay Result:** 12.78% cell death (n=1)
29	Gumosil AD (Silicone)	**Morphology:** Completely floating cell clusters. Unchanged throughout the cultivation period.

No.	MMC Patch [Solvent]	Observations
		Cytotox-Assay Result: 4.07% cell death (n=1)
30	Gumosil AD + Polyethylene glycol 300	**Morphology:** Patch not microscopically analysable (thickness, cloudy), cells next to the patch material showed blebbing after 48 h. **Cytotox-Assay Result:** 8.82% cell death (n=1)

To provide a clearer context for the obtained results, various observed morphologies and adhesion properties, as well as the cytotoxicity of the most promising patch materials, are illustrated in Figure 23. All patch materials were compared to the untreated control (Figure 23, E), which was seeded into the same well plates without any patch material. The control exhibited the typical morphology of SH-SY5Y cells, characterized by floating and partially adherent cells with a spindle-shaped morphology that grew in small clusters, distributed homogeneously throughout the wells. Figure 23 A and B show SH-SY5Y cells on wells which contained 5% and 10% PVAc, with enlarged cells indicating apoptotic processes (Figure 23, A – indicated by an arrow), as well as adherent cells and cell clusters (Figure 23, B – indicated by an arrow). In contrast, the polyester polylactic acid (Figure 23, C) showed large, floating cell clusters with partial cell blebbing and debris. Vinnapas® Special exhibited completely floating cell clusters with rounded morphology (Figure 23, D – indicated by an arrow) and individual viable floating cells. The cytotoxicity of the most promising material combinations was comparable to that of the unstimulated control (Figure 23).

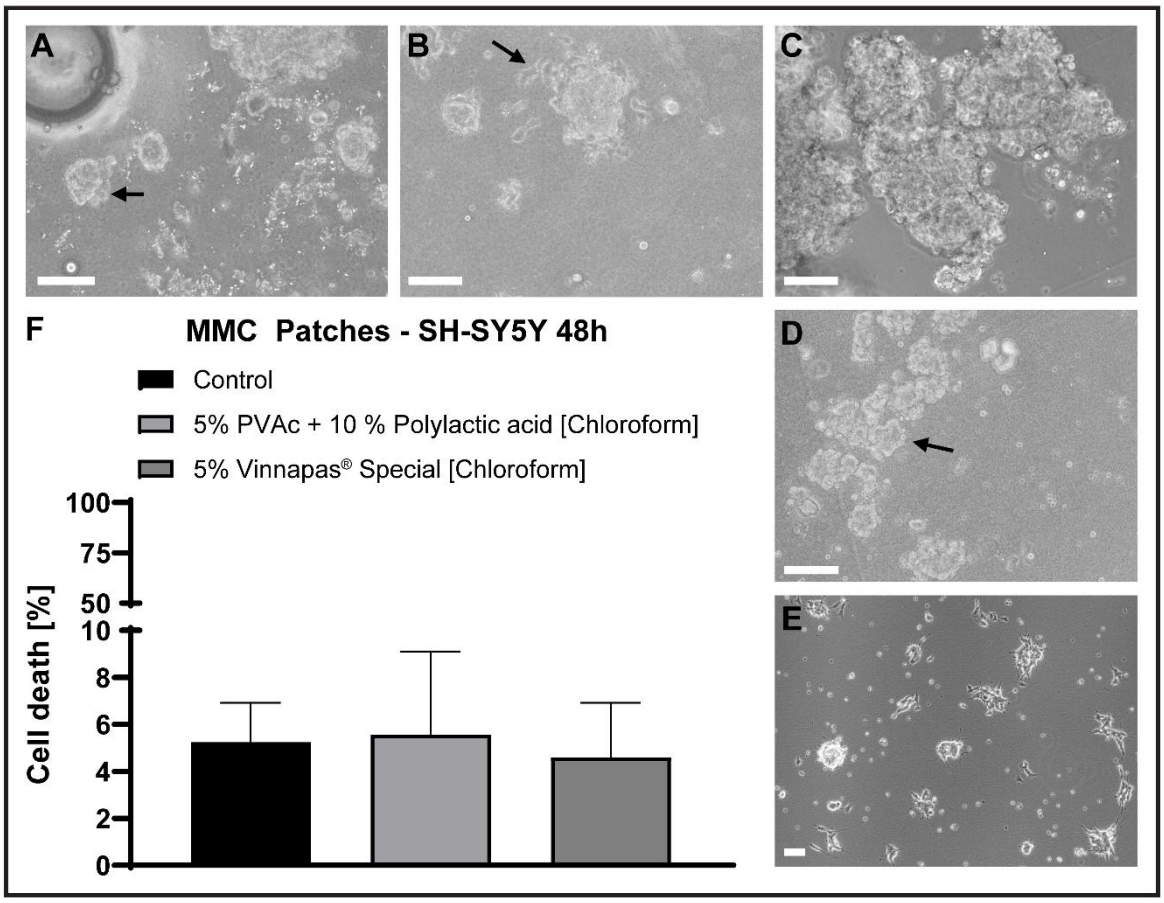


Figure 23 – Representative morphologies of SH-SY5Y cells observed on different MMC patch materials after 48 h of culture and cytotoxicity of the most promising patch materials. Scale bar 100 µm. **A** 5% Polyvinal acetate (PVAc). The arrow points to enlarged cells. **B** 10% PVAc. The arrow indicates adherent cells and small cell clusters that are attached to the patch material. **C** 5% Polylactic acid showed large and loose cell aggregates; some of them exhibited partial blebbing and extracellular debris. **D** 10% Vinnapas® Special. The arrow highlights completely detached, rounded cell clusters, indicative of a non-adhesive surface. **E** Control well of SH-SY5Y cells. **F** The cytotoxicity of the most promising material combinations 5% PVAc together with 10% polylactic acid, as well as 5% Vinnapas® Special did not differ significantly from the unstimulated control. n=3 biological replicates.

Taken together, the results obtained in the MMC-related lesion framework demonstrated that amniotic fluid-like conditions created by the usage of aAF induced strong antiproliferative and cytotoxic effects in rat spinal cord-derived NPCs, accompanied by time-dependent alterations in lineage- and stemness-associated gene expression. Epo partially counteracted the early effects of aAF treatment, particularly at the level of cell survival, and this rescue could be partially linked to activation of the canonical JAK2/STAT5/Akt signaling pathway. In the human SH-SY5Y system, aAF likewise altered cellular behavior, although the response was characterized more prominently by reduced proliferation and marked morphological changes. Therefore, these findings could indicate that a developmental disease such as MMC, which is characterized by an amniotic fluid environment, might induce substantial cellular stress and modulate stemness-associated programs. In addition,

the initial screening of MMC patch candidate materials with SH-SY5Y cells provided a first outlook on the biocompatibility of new material approaches.

Overall, the findings of this work showed that stress in the CNS can influence stemness-related properties across two fundamentally different models. In the GBM model, externally induced, therapy-associated stress generated by mFUS was associated with region-specific enrichment of dormancy- and stemness-related markers in surviving and peri-focal tumor cells, together with functional changes linked to sphere formation, chemoresistance, and adaptive signaling. In the MMC-related model, internally arising environmental stress, mimicked by aAF exposure, induced pronounced alterations in survival, proliferation, morphology, and progenitor-associated gene regulation in neural cell systems. The following discussion section will place these findings in the context of current literature, critically evaluate their translational significance, and address how externally induced therapeutic stress and internally arising environmentally induced stress may each reshape stemness-related programs in the CNS.

6. Discussion

The study of both therapy-induced external stress leading to selective pressure for the tumor cells and environmentally induced internal stress reflecting a persistent pathological environment for NPCs seemed especially suitable for addressing the broader question of how stress within the CNS influences stemness-associated cellular properties. Furthermore, the study addresses whether stemness-associated changes are limited to specific stress settings or might represent a more general cellular response of the CNS. While the GBM model allowed the study of therapy-induced stress in a tumor setting characterized by adaptive plasticity and clinically relevant escape mechanisms, the MMC model enabled the study of environmental stress marked by vulnerable progenitor populations and altered neural differentiation.
It has to be noted that therapy-induced stress could be defined as acute stress impact according to the duration of the applied stress, whereas environmentally induced stress could be considered as chronic stress due to the duration of the applied stressor in an *in vivo* context [15]. In the experimental setups used, we attempted to address this issue by administering the therapy-induced stress using mFUS as a single treatment and examining the effects of the stressor. In the MMC model, we administered prolonged stimulation with amniotic fluid over a period of up to 8 days.

In the following sections, the obtained results are placed into the context of current literature and are critically evaluated. Particular emphasis will be placed on the question of how the observed changes should be interpreted and how a better understanding of the observed processes may influence future therapeutic approaches.

6.1 Glioblastoma model – Dormancy and stemness mechanisms after treatment with mFUS

This section focuses on whether therapy-induced stress in the CNS can alter stemness-associated properties, and if the observed alterations can be interpreted as an adaptive protective response, an escape mechanism, or as a general stress response. This question is particularly relevant in GBM since heterogeneity, cellular plasticity and residual cell niches are closely linked to recurrence and therapy resistance [40,45,47,48].

In the present work, mFUS was used to trigger therapy-induced stress on either GBOs, more differentiated GBM cells or GSCs. The selected patient-derived GBO model system preserved important features of the parental tumor, including its histological organization, genetic alterations, and inter- and intratumoral heterogeneity [162,269]. However, this strength can also be viewed as a limitation regarding the readout, since the organoids retain mixed cell populations, and molecular readouts from GBOs cannot be assigned with certainty to a specific subpopulation. To overcome this limitation, differentiated GBM and GSCs were analysed to complement the results obtained with GBOs.

Adaptive cell-state transitions in GBM, including stemness-associated plasticity and slow-cycling therapy-tolerant states, are increasingly recognized as major drivers of resistance and recurrence [34,50,270]. The key question is, therefore, whether mFUS might actively promote a stress-induced shift towards these stemness or dormancy-associated phenotypes. Importantly, mFUS acted as a damaging intervention in the GBM models, as validated by cCaspase3 staining, reduced cell density and nuclear damage, as well as increased cytotoxicity. However, the regional assessment made clear that these effects were not uniformly distributed across the treated tissue. Instead, the data indicated a region-specific response, with prominent cell death near the induced focal lesion.

The conducted IF staining of dormancy- and stemness-associated markers suggests that mFUS treatment induced a spatially heterogeneous response in GBOs, characterized by surviving cell populations with dormancy- and stemness-associated features in both residual and peri-focal areas. The qPCR data extended the IF observations by showing that mFUS was associated with a region-dependent transcriptional change of surviving cell populations expressing dormancy- and stemness-related markers, indicating that residual cells close to the lesion site exhibited a pronounced enrichment of transcriptional programs associated with dormancy, stemness, and cellular plasticity. In fact, it has already been reported that surgery-induced lesions and chemotherapy can trigger surviving GBM cells to acquire stemness properties [16,271]. These stemness-associated properties seem to be associated with elevated resistance to therapy-related stress [272,273]. Furthermore, stress can impose a strong selective pressure on residual cells and, at the same time, promote phenotypic plasticity [27,33,274]. Against this background, the presented IF and qPCR findings of an elevated expression of stemness markers such as MSI1, OCT4, and SOX2 in human patient-derived GBO tissue are consistent with previous reports, indicating the generation of a spatially heterogeneous stress milieu in which surviving and peri-focal cells display increased stemness-associated features.

By contrast, the dormancy markers IGFBP5 and SKI exhibited their most prominent induction in the peri-focal regions (margin) of the GBO model. Thus, the peri-focal induction

of IGFBP5 and SKI might suggest that cells surrounding the primary lesion reflect a regional stress-response program that preferentially might adopt a more dormancy-associated molecular profile. In line with this, quiescent or slow-cycling GBM cells have repeatedly been localized to hypoxic and peri-necrotic niches, where they are thought to survive adverse conditions and contribute to later tumor recurrence [50,275,276].
Interestingly, the upregulation of dormancy and stemness markers was not restricted to the GSC cultures, but was also evident in the more differentiated GBM cell fraction. Therefore, it could be hypothesized that mFUS not only enriches pre-existing stem-like cells, but may also promote phenotypic reprogramming or adaptive state changes in more differentiated tumor cells. The finding of gene expression upregulation of dormancy and stemness markers in GSCs, as well as more differentiated GBM cells is particularly relevant in the context of treatment resistance and tumor recurrence, as it might indicate that mFUS-induced stress responses are not confined to an intrinsically stem-like tumor cell compartment. Instead, the data suggest that more differentiated GBM cells retain phenotypic plasticity and can adopt molecular features associated with dormancy and stemness following mechanical stress induced by mFUS. Furthermore, they support the concept of cellular plasticity in GBM [46,47] and emphasize that stemness in GBM can represent a dynamic cell state that may be acquired by adult GBM cells [42,53,54].

Further evaluation by sphere formation assay (ELDA) and TMZ response was conducted to determine whether the obtained data suggest that therapy-induced stress in GBM triggered functionally relevant changes in dormancy- and stemness-associated cellular behavior, and whether TMZ treatment might have altered the mFUS-induced stress response.
ELDA confirmed an increased stem-like behavior of mFUS-treated, more differentiated GBM cells, correlating with increasing mFUS intensity. Treatment with TMZ of more differentiated GBM cells, as well as GSCs, led to cytotoxicity at later time points for GSCs compared to more differentiated GBM cells, which aligns with the known relative treatment resilience of GSCs [277,278]. Interestingly, stimulation with TMZ after mFUS pretreatment reduced the cytotoxic effect of subsequent TMZ exposure compared to non-pretreated controls (TMZ only). Importantly, this effect was observed in both, more differentiated GBM cells and GSCs, although the protective effect appeared more pronounced in the more differentiated population. This finding suggests that mFUS pretreatment did not sensitize residual GBM cells to chemotherapy under the tested conditions. Furthermore, the stress-related response due to mFUS could not be attenuated via a sequential mFUS and TMZ treatment. Instead, mFUS pretreatment seems to be associated with reduced TMZ susceptibility. This interpretation would be consistent with the broader concept that therapy

resistance could be induced by stress-related cellular plasticity and heterogeneity in tumor cells [34,46,50,60,64,68,279–281], including the acquisition of stemness and dormancy-like features by GBM cells due to therapeutic measures [63,64,224,282]. Wang *et al.* 2025 demonstrated that while TMZ treatment eliminated many GBM cells, the corresponding therapy-induced stress milieu predominantly led to dormancy of the surviving subpopulations, and later tumor recurrence was associated with increased stemness and resistance to therapy [16]. Our data identified increased expression of the proteins MSI1 (stemness-associated marker), IGFBP5 and EphA5 (dormancy-associated markers in GBM), in GBOs pretreated with mFUS and stimulated with TMZ for three days, compared to TMZ treatment without mFUS stimulation. This further supports a phenotypic shift towards a more treatment-tolerant phenotype associated with dormancy and stemness-associated properties due to mFUS pretreatment. Furthermore, the elevated protein expression fits well with the earlier findings obtained in the absence of chemotherapy, where mFUS alone had already elevated the expression of dormancy- and stemness-associated markers.

Considering the results obtained and the current literature discussed so far, the mFUS-induced stress milieu, in which surviving residual and peri-focal GBM cells acquired stem- and dormancy-associated phenotypes that seem to correspond to reduced TMZ susceptibility, may indicate an escape mechanism towards a more therapy-resistant cell state. Notably, ELDA and the subsequent TMZ treatment results do not demonstrate sustained tumor-initiating capacity, recurrence potential, or invasive behavior following mFUS-induced stress. Nevertheless, the combined ELDA and TMZ studies demonstrated an association between mFUS pretreatment and reduced TMZ cytotoxicity, increased sphere-forming capacity, and enhanced expression of dormancy- and stemness-associated markers and proteins, which seems to be of particular interest for the therapeutic interpretation of an mFUS treatment.

While mFUS effectively eliminated parts of the tumor mass, residual surviving GBM cells at or near the focal zone responded by entering an adaptive cell state associated with stemness, dormancy, and reduced susceptibility to subsequent TMZ treatment. Current literature on TMZ resistance supports the concept that overcoming GBM therapy resistance will likely require multifactorial strategies [224,283,284]. Future mFUS experiments could therefore investigate whether the observed phenotypic changes can be prevented or reversed by altering treatment sequences with further combinatorial therapeutic approaches. The tested experimental schedule with mFUS pretreatment might have allowed residual/peri-focal GBM cells to establish a stress-adapted, therapy-tolerant state due to dormancy- and stemness-associated cell state adaptations before chemotherapy exposure. Therefore, future studies could systematically test whether the biological

outcome depends on treatment sequence and timing, including simultaneous mFUS and TMZ treatment, TMZ pretreatment before mFUS, shorter or longer intervals between mFUS and TMZ, as well as repeated or fractionated exposure schemes. Furthermore, these approaches could include pathway-directed interventions targeting stress-response, survival, dormancy, or stemness-associated signaling, which would help to clarify whether the mFUS-induced phenotypic changes in residual and surviving cells can be therapeutically exploited, prevented, or reversed.

To further elucidate which intracellular stress-response pathways might be involved in the mFUS-induced cellular adaptations, and might therefore be a suitable target for further combinatorial therapeutic approaches, the PI3K/Akt/GSK3β pathway was investigated. This pathway has been linked to survival signaling, stress adaptation, and stemness properties of GBM cells, and is strongly activated in these cells [224,225,285]. In particular, the PI3K/Akt signaling axis has been associated with GSC self-renewal and survival under stress-associated microenvironmental conditions, suggesting that this pathway might contribute to the adaptive phenotype after mFUS treatment [178,286,287].
mFUS induced the phosphorylation of Akt and GSK3β. However, pharmacological inhibition of PI3K using LY29402 partially reduced these phosphorylation events, which were associated with increased expression of molecules linked to dormancy and stemness [230,231]. Accordingly, partial reduction of mFUS-induced SKI and Nestin expression after LY294002 treatment could be observed. The inhibitor experiments provide the first evidence for the involvement of PI3K/Akt/GSK3β signaling in mFUS-treated GBM cells, but they do not fully resolve the upstream triggers or downstream effectors of the mFUS-induced stress response neither do they prove, that this pathway is the sole mediator of the observed mFUS effects. In particular, the influence of ROS or mechanosensitive signaling remain other plausible mechanisms that could be further investigated, as partially indicated by the investigation of ROS formation and regulation of mechanoreceptor expression provided in our study [179]. Furthermore, other pathways might play a role in mFUS-associated signaling. Since we observed increased inhibitory phosphorylation of GSK3β [228,229], which is positioned at the interface of the Wnt/β-catenin pathway and regulates β-catenin phosphorylation and therefore the off-state of this pathway [288], the Wnt/β-catenin pathway might be another signaling pathway worth investigating. This pathway is known to drive maintenance, proliferation, and therapeutic resistance, especially in GSCs [289–291]. To validate whether the conducted PI3K pathway inhibition would attenuate the functional consequences of mFUS treatment, such as sphere formation or reduced TMZ cytotoxicity, it would be necessary to perform further experiments combining mFUS with specific PI3K/Akt inhibitors.

In summary, the present findings indicate that mFUS induced a stress response in residual and peri-focal areas beyond an immediate focal cytotoxic effect under the tested conditions. Surviving residual and peri-focal GBM cells displayed a complex induction of dormancy- and stemness-associated properties that varied by region- and marker. These changes were reflected by increased sphere-forming capacity and reduced cytotoxicity to subsequent TMZ treatment. Notably, these changes were not restricted to GSCs but were also observed in more differentiated GBM cells. Thus, an adaptive GBM cell state associated with persistence, plasticity, and treatment escape due to mFUS-induced stress could be described. Therefore, the obtained results support the broader concept that therapy-induced stress within the CNS could reshape the biological state of surviving cells [17,35,69] and is consistent with current models of cellular plasticity in the CNS and GBM [26,46]. In the GBM model of this study, this response may represent a tumor-protective escape mechanism associated with cellular stemness and dormancy properties, enabling residual and peri-focal cells to persist after focal injury and to withstand subsequent treatments.

However, it remains unclear whether the induced dormancy- and stemness-associated changes are transient stress responses or stable cell-state transitions with long-term relevance for recurrence, invasion, or tumor regrowth. Furthermore, the provided data does not unambiguously distinguish whether the observed phenotype is the result of the selective survival of pre-existing resistant cells, an active phenotypic conversion of GBM cells, or a combination of both. Although the findings in more differentiated GBM cells support the possibility of mFUS-induced phenotypic plasticity, longitudinal analyses, single-cell profiling, lineage tracing and *in vivo* validation could provide definitive evidence. Paired with extended follow-ups after mFUS treatment, these methods might help determine whether the observed residual cell-state is reversible or targetable, or whether it might be involved in tumor recurrence.

Despite these limitations, the findings also identified important therapeutic opportunities. mFUS represents a promising spatially precise therapeutic approach for mechanical tumor ablation, which should not only aim to optimize focal ablation efficiency, but also needs to prevent or counteract stress-induced adaptive plasticity of the surviving GBM cells. Since the molecular mechanisms that regulate GBM adaptation to therapy-induced stress remain unclear [274], further exploration of these mechanisms could reveal new targets for novel therapeutic strategies that might overcome these adaptations and mechanisms of therapy resistance. Thus, combining mFUS with interventions that suppress stress-induced alterations of dormancy and stemness-associated cellular properties may help to prevent the emergence of therapy-tolerant residual and peri-focal GBM cells.

6.2 Myelomeningocele model – Stemness mechanisms following stimulation with artificial amniotic fluid and potential treatment strategies

To evaluate whether environmental stress might be associated with shifts in stemness-associated cell properties, an MMC *in vitro* model was developed. In MMC, the primary neurulation defect is followed by progressive secondary injury to the exposed spinal cord during gestation, due to chronic exposure of the unprotected neural placode to the intrauterine environment [108,115]. Accordingly, the *in vitro* model included the development of artificial amniotic fluid (aAF) to mimic environmental stress.

The aAF was based on human amniotic fluid, which is comprehensively documented across gestation and allows reproducible formulation [168–170,173]. Since amniotic fluid represents a biologically active and dynamic fetal environment that changes across different gestational time points [292], we anchored our aAF composition to a clear gestational stage of week 22 of gestation, representing an early gestational time point not altered by increasing fetal contributions such as urea [293]. Notably, data for rat AF remain limited and do not provide comprehensive reference values across gestation. At the same time, available rodent data indicate that key electrolytes are broadly within a comparable physiological range, supporting the use of a controlled human-based formulation [294,295]. This approach is consistent with recent rodent fetal-therapy studies that used synthetic amniotic fluid matched to normal human midtrimester amniotic fluid [296]. However, the pH of the aAF was slightly higher than the reported physiological values, as maintaining the physiological chloride value was prioritized over adjusting the pH due to the adverse physiological side effects of hyperchloremia [174,175].

Since the aim was to assess general, conserved cellular responses in a standardized, reproducible model, adult rat spinal cord-derived NPCs were exposed to human-based aAF. These cells are a useful experimental model since they can be maintained as relatively stable neurosphere-like cultures, retain self-renewal properties, and display multipotency [297–299], whereas embryonic cultures differ substantially depending on the gestational stage, as demonstrated by transcriptomic analysis and several transplantation studies involving different developmental stages of embryonic spinal cord NPCs [300–302]. Furthermore, core principles and molecular regulators of neurogenesis are shared between the embryonic and adult central nervous systems [303].

The model was first evaluated by cytotoxicity and proliferation assays to determine whether aAF exposure induces a measurable cellular stress response. Exposure to aAF caused a concentration-dependent impairment of NPC viability and growth.

Animal studies described progressive damage to the exposed spinal cord during gestation, including structural degeneration and loss of function [100,109,304]. In retinoic acid-induced rat MMC models, progressive astrogliosis and neuronal cell loss were documented, and cCaspase3 staining revealed elevated apoptosis in the exposed areas of the spinal cord [108,128]. Furthermore, lowered cell proliferation has been reported [305].
Thus, the results obtained support the assumption that aAF stimulation can induce at least components of the MMC-associated intrauterine stress environment, and contribute to the known secondary MMC damage cascade. Furthermore, the results are consistent with the concept that exposed MMC tissue is subjected to a potentially harmful intrauterine environment during gestation [18,39,304,306]. Importantly for our setting, the use of 55% aAF diluted in cell culture medium represented a suitable compromise that supported biologically relevant stress responses while preserving sufficient cell numbers for longitudinal and molecular analyses.

As the next step, stimulation with the neuroprotective cytokine Epo was used to test whether aAF-induced impairments might reflect a modifiable or even reversible, regulated cellular stress response.
Regarding the potential administration of Epo, *in vivo* studies revealed a dose-dependent effect of Epo [307]. Even single-dose treatments led to persistent neuroregenerative processes two to 6 weeks after administration, as demonstrated by Gonzalez *et al.* 2007 in rats with induced brain injuries [142]. However, studies investigating long-term outcomes in rat brains that administered multiple doses over a long period revealed better performance than with a single-dose treatment [307,308]. For this study, Epo was administered daily for up to 8 consecutive days.
Protective effects of Epo could be evaluated, with reduced cytotoxicity under aAF treatment and partial counteraction of the antiproliferative effect. These findings are consistent with the current literature, indicating that Epo can regulate survival and differentiation in fetal NPCs [309–311]. In the context of spinal cord injury, Epo has also been associated with increased neurogenesis and oligodendrogenesis of neural stem cells [310,312]. Notably, since embryonic NPCs may show stronger mitogenic responses to Epo due to higher EpoR expression [236,237], the effect of Epo in embryonic NPCs might differ from the observed results obtained in this study. Confirmatory experiments using fetal rat NPCs would be required to determine whether Epo exerts stronger or different effects.

To evaluate whether stemness-associated changes are limited to specific stress settings like therapeutic interventions as described above or might represent a broader cellular response to stress in the CNS, gene expression analysis was conducted.

In MMC, altered developmental cell-fate regulation is described. During normal spinal cord development, NPCs generate neurons during neurogenesis, followed by the generation of oligodendrocytes and astrocytes [313,314]. Current literature indicates that this temporal sequence is disturbed, with reduced neurogenesis and decreasing neuronal numbers during gestation, impaired oligodendrogenesis, as well as premature astrocytic differentiation [128–130]. Recent experimental work by Oria *et al.* 2022 further supports the idea of altered astrocytic fate at the expense of normal neuronal and oligodendroglial development [108]. Reis *et al.* 2008 found increased $GFAP^+$ astrocytosis at and above the lesion site compared to the normal spinal cord using a mouse model of MMC [315]. This premature astrogliosis in MMC implies that even *in utero*, the exposed spinal cord triggers an injury-like response. However, we were unable to detect increased GFAP gene expression in the short timeframe of 8 consecutive days of stimulation with aAF. This could be related to the fact that adult rat NPCs were chosen as the test system instead of developing embryonic spinal cord-derived cells or the chosen experimental setup, which does not fully reproduce the intrauterine environment. A full setup may potentially include factors such as mechanical trauma, altered tissue architecture, and inflammatory signaling, in addition to exposure to amniotic fluid [18,39,111,316]. Furthermore, the timeframe may have been too short, since elevated GFAP expression is primarily triggered by long-lasting or more severe injuries [317].

Regarding other effects of aAF and Epo treatment on the gene expression profile, the findings demonstrated a strong time-dependent response. At the early time point of two days of stimulation, aAF induced a broad reduction in several neuronal, oligodendroglial, and stemness-associated markers, which was largely counteracted by Epo treatment. At the later time point of 8 days of stimulation, aAF exposure was associated with an induction of most of these genes, and this shift was not prevented by additional Epo treatment. One plausible interpretation of the observed early two-day downregulation is that it may reflect a transient acute stress response. In many cell systems, acute stress triggers temporary repression of large parts of the transcriptional and translational programs, which might allow the cells to reduce energetically costly processes such as proliferation and differentiation, while reallocating resources toward survival and adaptation [318–321]. This pattern of an early, broad repression phase followed by recovery or selective reactivation of specific gene programs during adaptation is often described as stress-induced transcriptional attenuation (SITA), which is not yet fully understood [322].

Furthermore, progenitor cells such as the NPC model used are highly adaptable to stress signaling or stimuli, and NPCs might be able to enter a reversible state of reduced proliferative activity, known as quiescence, as a protection and repair mechanism in response to stress [323–327].

The later induction observed for many markers after 8 days of consecutive treatment may then represent a secondary adaptive or reprogramming phase. In neural injury settings, progenitor and glial cells can reacquire or elevate immature features, shift lineage-related transcriptional programs, and exhibit reactive phenotypes [328–333]. This is especially relevant for the investigated stemness markers such as Nestin, SOX2, and KLF4, whose expression can be seen not only in progenitor cells, but also in injury-responsive cell states [108,261,330,334–336]. Accordingly, the induction of neuronal, oligodendroglial, and stemness-associated genes after prolonged aAF exposure may reflect a maladaptive or compensatory reorganisation of cell state.

The obtained results suggest that aAF-induced stress interferes with the maintenance of stemness- and differentiation-associated cellular programs, in line with the reported impairment of altered NPC fate decision in animal MMC model systems [108,128–130].

Based on the results, Epo might appear most effective during the early (acute) stress response phase, when transcriptional suppression is still reversible. Once prolonged aAF exposure has driven broader transcriptional reprogramming, Epo no longer seems to be able to return the cellular system to an unstimulated cell state, supporting the idea that timing of intervention may be critical. Future experiments could systematically vary the timing of Epo administration relative to aAF exposure to test the hypothesis that Epo might be most effective during an early and possibly reversible stress phase. Validation in fetal spinal cord-derived progenitor cells (and possibly *in vivo*) would further clarify the extent to which the observed timing dependency is influenced by the maturational state of the model system.

To evaluate whether the potential protective effect of Epo on aAF-induced stress in adult NPCs might be linked to canonical Epo-responsive signaling pathways [241–244], we investigated the JAK2/STAT5/Akt pathway-axis by conducting inhibition experiments using the JAK2 inhibitor AG490. Particularly in neural cells, this pathway-axis can be associated with reduced apoptosis, improved mitochondrial integrity, attenuation of oxidative stress, and modulation of inflammatory responses, as shown by several experimental studies [135,244,337–340]. Since EpoR signaling classically proceeds via JAK2 and its downstream effectors, including STAT5 and Akt, AG490 has been widely used as a JAK2-directed inhibitor and has been shown to reduce downstream phosphorylation of STAT5 and Akt in several Epo-responsive models [246,264–267]. In line with these previous studies, STAT5 and Akt phosphorylation predominantly occurred under stress conditions with aAF and Epo treatment compared to basal conditions in our system. The fact that AG490 strongly reduced this phosphorylation pattern further supports the interpretation that the protective Epo effect was mediated through the canonical EpoR/JAK2-dependent

signaling pathway. In line with current literature [135,244,337–340], the observed pSTAT/pAkt activation provides a plausible mechanism for the protective effects of Epo regarding the aAF-induced environmental stress.
In the broader context of this study, the Akt finding is particularly interesting, since it provides a bridge to the GBM model results obtained. In the GBM experiments, mFUS-induced stress was linked to PI3K/Akt/GSK3β-associated signaling in surviving tumor cells, indicating that Akt-associated signaling may have contributed to maladaptive survival, stemness, and potential therapy tolerance mechanisms. In the MMC model, Epo activated Akt together with STAT5 under aAF-associated stress conditions, which appears to support the preservation of NPC viability under environmental stress. Thus, both disease models seem to converge on Akt-associated stress-response signaling, which supports the idea that CNS stress responses may share signaling pathways or effectors across disease contexts. However, the functional consequences may depend on the cell type, developmental state, and disease biology.

Taken together, environmental stress induced by aAF stimulation prominently reduced cellular growth and impaired stemness and progenitor marker expression at early time points, which may reflect loss or destabilization of developmental cellular programs in NPCs under stress conditions. Epo partially counteracted this response by reducing aAF-associated cytotoxicity and growth inhibition. Furthermore, it tends to restore altered progenitor and stemness marker expression in early transient acute stress responses toward the unstimulated control state. Therefore, the Epo stimulation experiments suggest that stress-induced changes in cellular properties might be modifiable.
Thus, the chosen MMC model supports the broader concept that CNS stress can indeed modulate stemness-associated cellular properties across different disease settings. However, the biological consequence of this modulation appears to be context-dependent.

6.2.1 MMC Patch development

Since environmental stress seems to alter progenitor-associated cellular properties, a patch-based approach could provide protection from the potential toxic environment. There are several compelling reasons to continue developing suitable MMC patches, despite the lack of defect coverage in severe cases of larger lesions, where the dura is not sufficient to cover the whole defect [134]. One of the main advantages is that they can function not only as a cover for the open neural tube, but also as a localized therapeutic delivery system, which might be especially attractive in fetal surgery, where systemic drug exposure to the

fetus without causing maternal side effects might be difficult to achieve. Ideally, an MMC patch could combine mechanical coverage and local modulation of the stress environment, while avoiding additional cellular stress and ideally contributing to a permissive microenvironment for neural tissue preservation.
Early tissue-engineering studies already used gelatin-based scaffolds incorporating bFGF to support regenerative responses in fetal MMC models [341,342]. Newer studies have incorporated signaling modulators such as noggin into polylactic acid and polycaprolactone patches to locally influence neural differentiation pathways [343]. Cell-based therapeutic concepts are also advancing [306]. For instance, fibrin-based or biologic patches loaded with placental or umbilical cord-derived mesenchymal stromal cells have shown promising preclinical effects, including improved locomotor outcomes, reduced fibrosis, and better preservation of the neural and neuronal tissue [306,344]. These findings have shifted the role of the patch a passive barrier to an active regenerative microenvironment. First explorations of including stem cells as a therapeutic option were conducted in the last years [345,346], and promising results were achieved in a first-in-human phase 1 trial, which was published in 2026 [347].

The present work explored the highly interesting field of suitable MMC patches that could provide environmental protection with the necessary material characteristics in a first approach. The focus was on synthetic materials, which might be more cost-effective and easier to handle and store than biological approaches [348,349].
Biocompatibility was assessed using the human cell line SH-SY5Y, which is widely used as a model for human neuronal-like cells in studies of neurotoxicity and neurodegenerative diseases [238–240]. If the tested patch material neither induced relevant cytotoxicity nor altered cellular morphology, and if the cells did not preferentially grow onto the patch material, the material was considered especially compatible for an MMC patch approach. However, the results should be considered as an early compatibility assessment, since SH-SY5Y cells do not fully recapitulate fetal spinal cord neuroplacode tissue.

Among the synthetic MMC patches, polylactic acid as well as polycaprolactone are especially notable since both showed favorable characteristics, such as biocompatibility, biodegradability, stretchability, hydrophobicity, as well as drug loading capabilities [151,343,350]. Furthermore, Benabdderrahmane *et al.* 2025 explored the *in vitro* degradation of polycaprolactone in FBS medium over 24 weeks. They confirmed that polycaprolactone has an anti-adhesive surface accompanied by ongoing hydrolysis, which further confirmed the biodegradation of the patch material [351]. A first *in vivo* study in rats proved to be safe, showing no adverse or inflammatory responses, and demonstrated the

inhibition of astrogliosis and other functional alterations [160]. Going beyond current literature testing polycaprolactone or polylactic acid as potential MMC patch materials, this study tested formulations containing polycaprolactone or polylactic acid together with other unexplored polymers.

One of these materials was polyvinyl acetate (PVAc), which is a stretchable and flexible thermoplast primarily used for coating applications [352]. Furthermore, PVAc has shape memory characteristics, although these are limited due to its weak mechanical properties [353,354], and it has been reported as a suitable material for drug release approaches [355]. In the present study, PVAc alone exhibited concentration-dependent cytotoxicity levels. The combination with 10% polycaprolactone further resulted in an increase in cell death in a PVAc concentration-dependent manner. Together with the observation that the SH-SY5Y cells tend to adhere to the material, PVAc alone as well as in combination with polycaprolactone does not seem to be a suitable material for MMC patch design. However, when combined with polylactic acid, the cytotoxicity decreased, with semi-adherent effects with regard to the attachment of SH-SY5Y cells. Thus, combination of PVAc with polylactic acid seems promising for further investigations.

Another material tested was Vinnapas® Special, a thermoplastic polymer based on vinyl acetate, characterized by hydrophobic effects and stretchable design not yet tested in biological or medical applications to our knowledge [356]. However, their characteristics and FDA-approved usage in food as an additive for gum-based products make them an interesting material. Vinnapas® Special demonstrated a concentration-dependent increase in cytotoxicity. Together with polycaprolactone or polylactic acid, visible cell blebbing and semi-adherent spheroids with elevated cytotoxicity were observed. Although these combination experiments remain preliminary, the data suggest that Vinnapas® Special at a concentration of 5% may be the most promising candidate for further evaluation, where cytotoxicity remained low. In addition, SH-SY5Y cells remained predominantly non-adherent and floating, which may be advantageous for MMC patch development.

Further tested materials included Eudragit® NM and NE, which are used in pharmaceuticals as film coating polymers for sustained drug release and are highly flexible [357]. However, since these polymers are not accessible via light microscopy and showed high cytotoxicity, those materials were not tested in further combinations with the known polycaprolactone or polylactic acid.

Silicones were also briefly included in the tests as an additional material class, although, unlike the other materials tested, they are not biodegradable and require subsequent prenatal surgery [157,358]. Silicones such as Silastic have already been successfully tested in *in vitro* animal models using sheep [157,358]. However, due to their lack of biodegradability, the material needs to be removed at later stages, and exploration of this

material has become unpopular [358]. The Gumosil AD tested in this study exhibited low cytotoxicity and showed free-floating, non-adherent SH-SY5Y, confirming the suitability of these materials in line with the literature [134].

The experiments conducted within this work represent only the initial testing of the biocompatibility of potential MMC patches. Further testing of the material properties of the most promising combinations, such as PVAc with polylactic acid and Vinnapas® Special, is necessary to determine whether other useful properties of an MMC patch, such as water-repellency, shape-memory, or biodegradability, also apply to the investigated materials. Furthermore, different bioactive protein coatings or pharmaceutical approaches could be explored with first *in vitro* studies.

7. Conclusion

Both stress models converged on the central observation that cells exposed to stress are subject to damage-associated processes, but can also adopt altered cell states linked to progenitor behavior or stemness-associated regulation. At the same time, it needs to be noted that these responses seem to be context-dependent. The GBM model indicated that therapy-induced stress caused by mFUS treatment can spatially and functionally alter cellular properties in a CNS disease context. In this stress milieu, surviving residual and peri-focal GBM cells acquired dormancy and stemness-associated properties, which might represent a potential therapy escape mechanism indicated by decreased TMZ cytotoxicity following mFUS pretreatment. At the same time, it provides a clinically relevant opportunity. By understanding and targeting the residual cell-response of mFUS-induced stress, future combinatorial therapeutic strategies may convert local mechanical ablation into a potent anti-tumor approach.

In the developmental spinal cord context, aAF exposure led to altered NPC growth and revealed an early-phase stress-associated impairment of progenitor and stemness-associated properties of NPCs, which could at least partially be counteracted by Epo through JAK/STAT5/Akt-associated signaling. Thus, the observed impairment of progenitor-associated cellular properties in NPCs seemed to be part of a regulated, modifiable acute stress-response program, possibly affecting NPC maintenance. Furthermore, first patch-screening experiments pointed towards potential protective intervention strategies.

Therefore, the obtained findings support a more general cellular stress response in the CNS. This response appears to reshape stemness and progenitor-associated properties, whose biological consequences depend on the affected cell population and the time duration.

.

List of figures

Figure 1 – Conceptual overview of glioblastoma & therapy-induced stress. 6
Figure 2 – Schematic overview of MMC and environmental stress.....11
Figure 3 – GBO preparation based on Jacob *et a*l. 2020.....25
Figure 4 - Functionality and influencing factors of the mFUS transducer 31
Figure 5 – Sample Preparation of Hydrogel cultures for RNA extraction. 49
Figure 6 – Heterogeneity of GBOs 56
Figure 7 – Sample Preparation of Hydrogel cultures for RNA extraction. 58
Figure 8 – mFUS application on patient-derived more differentiated GBM cells. 60
Figure 9 – mRNA expression of mechanoreceptors following mFUS. 61
Figure 10 – IF staining of GBO sections from the focal and peri-focal area. 62
Figure 11 – GBO samples treated with mFUS and IF stained with SKI. 65
Figure 12 – IF staining of patient-derived more differentiated GBM cells.....66
Figure 13 – mRNA expression level of mFUS-treated GBOs, more differentiated GBM cells, and GSCs. 69
Figure 14 – Impact of mFUS treatment – ELDA analysis and TMZ stimulation.....72
Figure 15 – PI3K pathway analysis. 75
Figure 16 – Effect of aAF on rat NPCs. 78
Figure 17 – Effect of Epo on rat NPCs treated with aAF on proliferation and cell death. .80
Figure 18 – Effect of Epo on rat NPCs treated with aAF at the gene expression level.....82
Figure 19 – Western blot and proliferation analysis of JAK2-mediated pathways. 84
Figure 20 – Effect of aAF treatment on human SH-SY5Y cells.....86
Figure 21 – Morphology of unstimulated SH-SY5Y cells. 87
Figure 22 – Morphology of SH-SY5Y cells treated with 55% aAF.....88
Figure 23 – Representative morphologies of SH-SY5Y cells on different MMC patch materials. 94

List of tables

Table 1 - mFUS Parameter sets used for this study.....31
Table 2 - Overview of patch materials, solvents, and manufacturing methods used for MMC patch production. 32
Table 3 – Literature Review of amniotic fluid composition.....34
Table 4 – Supplementation of salts and amino acids to create artificial amniotic fluid. mM = millimole, SD = Standard Deviation.....36
Table 5 – Example of a preparation of a standard cytotoxicity assay series. 41
Table 6 - Bradford assay standard curve. 45
Table 7 - SDS-PAGE Gel preparation. 46
Table 8 - Temperature program of cDNA synthesis. 51
Table 9 - Used qPCR Primer. 51
Table 10 - qPCR Program 53
Table 11 – Material screening for potential MMC patches. 90

References

[1] Margetis K., Reddy V., and Singh P., 2026. *StatPearls: Anatomy, Central Nervous System*, Treasure Island (FL).

[2] Asan A. S., McIntosh J. R., and Carmel J. B., 2021*,"Targeting Sensory and Motor Integration for Recovery of Movement After CNS Injury,"* Frontiers in neuroscience, **15**, p. 791824. doi:10.3389/fnins.2021.791824.

[3] Bigbee J. W., 2023*,"Cells of the Central Nervous System: An Overview of Their Structure and Function,"* Advances in neurobiology, **29**, pp. 41–64. doi:10.1007/978-3-031-12390-0_2.

[4] Martínez-Cerdeño V., and Noctor S. C., 2018*,"Neural Progenitor Cell Terminology,"* Frontiers in neuroanatomy, **12**, p. 104. doi:10.3389/fnana.2018.00104.

[5] Chaker Z., Makarouni E., and Doetsch F., 2024*,"The Organism as the Niche: Physiological States Crack the Code of Adult Neural Stem Cell Heterogeneity,"* Annual review of cell and developmental biology, **40**(1), pp. 381–406. doi:10.1146/annurev-cellbio-120320-040213.

[6] Urbán N., Blomfield I. M., and Guillemot F., 2019*,"Quiescence of Adult Mammalian Neural Stem Cells: A Highly Regulated Rest,"* Neuron, **104**(5), pp. 834–848. doi:10.1016/j.neuron.2019.09.026.

[7] Mannino G., Russo C., Maugeri G., Musumeci G., Vicario N., Tibullo D., Giuffrida R., Parenti R., and Lo Furno D., 2022*,"Adult stem cell niches for tissue homeostasis,"* Journal of cellular physiology, **237**(1), pp. 239–257. doi:10.1002/jcp.30562.

[8] Gazerani P., 2025*,"The neuroplastic brain: current breakthroughs and emerging frontiers,"* Brain research, **1858**, p. 149643. doi:10.1016/j.brainres.2025.149643.

[9] McEwen B. S., 2017*,"Neurobiological and Systemic Effects of Chronic Stress,"* Chronic stress (Thousand Oaks, Calif.), **1**. doi:10.1177/2470547017692328.

[10] Kugler E. C., Greenwood J., and MacDonald R. B., 2021*,"The "Neuro-Glial-Vascular" Unit: The Role of Glia in Neurovascular Unit Formation and Dysfunction,"* Frontiers in cell and developmental biology, **9**, p. 732820. doi:10.3389/fcell.2021.732820.

[11] Rothman S. M., and Mattson M. P., 2013*,"Activity-dependent, stress-responsive BDNF signaling and the quest for optimal brain health and resilience throughout the lifespan,"* Neuroscience, **239**, pp. 228–240. doi:10.1016/j.neuroscience.2012.10.014.

[12] Porcari C., Cattaneo S., Crippa L., Simonato M., and Bettegazzi B., 2025*,"Exploring the diversity of biological processes regulated by glial cell line-derived neurotrophic factor, a pleiotropic molecule with therapeutic potential,"* Frontiers in physiology, **16**, p. 1618330. doi:10.3389/fphys.2025.1618330.

[13] Sun J., and Nan G., 2017*,"The extracellular signal-regulated kinase 1/2 pathway in neurological diseases: A potential therapeutic target (Review),"* International journal of molecular medicine, **39**(6), pp. 1338–1346. doi:10.3892/ijmm.2017.2962.

[14] Kaniuk J. K., Kumar D., Mazurek C., Khavari S., Sollenberger C., Ahuja A., Mossner J. M., and Ahuja C. S., 2025*,"From Acute Injury to Chronic Neurodegeneration: Molecular Mechanisms Linking Secondary Brain Injury to Long-Term Pathology,"* International journal of molecular sciences, **26**(15). doi:10.3390/ijms26157191.

[15] Guo H., Zheng L., Xu H., Pang Q., Ren Z., Gao Y., and Wang T., 2022*,"Neurobiological Links between Stress, Brain Injury, and Disease,"* Oxidative medicine and cellular longevity, **2022**, p. 8111022. doi:10.1155/2022/8111022.

[16] Wang P., Liao B., Gong S., Guo H., Zhao L., Liu J., and Wu N., 2025*,"Temozolomide promotes glioblastoma stemness expression through senescence-associated reprogramming via HIF1α/HIF2α regulation,"* Cell death & disease, **16**(1), p. 317. doi:10.1038/s41419-025-07617-w.

[17] Ghorbian S., 2025*,"Cancer cell plasticity and therapeutic resistance: mechanisms, crosstalk, and translational perspectives,"* Hereditas, **162**(1), p. 188. doi:10.1186/s41065-025-00564-8.

[18] Athiel Y., Jouannic J.-M., Lépine M., Maillet C., Saint Denis T. de, Larghero J., and Guilbaud L., 2024*,"Role of Amniotic Fluid Toxicity in the Pathophysiology of Myelomeningocele: A Narrative Literature Review,"* Prenatal diagnosis, **44**(12), pp. 1530–1535. doi:10.1002/pd.6681.

[19] Boccardi V., Mancinetti F., and Mecocci P., 2025*,"Oxidative Stress, Advanced Glycation End Products (AGEs), and Neurodegeneration in Alzheimer's Disease: A Metabolic Perspective,"* Antioxidants (Basel, Switzerland), **14**(9). doi:10.3390/antiox14091044.

[20] Hu X., Xu W., Ren Y., Wang Z., He X., Huang R., Ma B., Zhao J., Zhu R., and Cheng L., 2023*,"Spinal cord injury: molecular mechanisms and therapeutic interventions,"* Signal transduction and targeted therapy, **8**(1), p. 245. doi:10.1038/s41392-023-01477-6.

[21] Anjum A., Yazid M. D., Fauzi Daud M., Idris J., Ng A. M. H., Selvi Naicker A., Ismail O. H. R., Athi Kumar R. K., and Lokanathan Y., 2020*,"Spinal Cord Injury: Pathophysiology, Multimolecular Interactions, and Underlying Recovery Mechanisms,"* International journal of molecular sciences, **21**(20). doi:10.3390/ijms21207533.

[22] Dash U. C., Bhol N. K., Swain S. K., Samal R. R., Nayak P. K., Raina V., Panda S. K., Kerry R. G., Duttaroy A. K., and Jena A. B., 2025*,"Oxidative stress and inflammation in the pathogenesis of neurological disorders: Mechanisms and implications,"* Acta pharmaceutica Sinica. B, **15**(1), pp. 15–34. doi:10.1016/j.apsb.2024.10.004.

[23] Guo X., and Zhao Z., 2022*,"Vascular inflammation in the central nervous system,"* Neural regeneration research, **17**(8), pp. 1728–1730. doi:10.4103/1673-5374.332140.

[24] Ginsberg S. D., Joshi S., Sharma S., Guzman G., Wang T., Arancio O., and Chiosis G., 2021*,"The penalty of stress - Epichaperomes negatively reshaping the brain in neurodegenerative disorders,"* Journal of neurochemistry, **159**(6), pp. 958–979. doi:10.1111/jnc.15525.

[25] Bravo-Jimenez M. A., Sharma S., and Karimi-Abdolrezaee S., 2025*,"The integrated stress response in neurodegenerative diseases,"* Molecular neurodegeneration, **20**(1), p. 20. doi:10.1186/s13024-025-00811-6.

[26] Shoshani O., and Zipori D., 2015*,"Stress as a fundamental theme in cell plasticity,"* Biochimica et biophysica acta, **1849**(4), pp. 371–377. doi:10.1016/j.bbagrm.2014.07.006.

[27] Torrisi F., Denaro S., Ragonese J., D'Aprile S., Zappalà A., and Parenti R., 2025*,"Neural stem cells fate under neuroinflammatory conditions and oxidative stress response,"* Frontiers in cellular neuroscience, **19**, p. 1736865. doi:10.3389/fncel.2025.1736865.

[28] Bacigaluppi M., Sferruzza G., Butti E., Ottoboni L., and Martino G., 2020*,"Endogenous neural precursor cells in health and disease,"* Brain research, **1730**, p. 146619. doi:10.1016/j.brainres.2019.146619#.

[29] Martino G., Pluchino S., Bonfanti L., and Schwartz M., 2011*,"Brain regeneration in physiology and pathology: the immune signature driving therapeutic plasticity of neural stem cells,"* Physiological reviews, **91**(4), pp. 1281–1304. doi:10.1152/physrev.00032.2010.

[30] Piltti K. M., Lakatos A., Benavente-Perez F., Elrachid Z. H., Nava A. A., Addonizio N. T., Nguyen V., Zahedi A., Song W. A., Chen X., David J., Portillo A., Manughian-Peter A. O., Rodriguez A. N., Anzalone A., Cahill C. M., and Anderson A. J., 2025*,"C1q drives neural stem cell quiescence by regulating cell cycle and metabolism through BAI1,"* Nature communications, **16**(1), p. 11386. doi:10.1038/s41467-025-66185-x.

[31] Semkova V., Haupt S., Segschneider M., Bell C., Ingelman-Sundberg M., Hajo M., Weykopf B., Muthukottiappan P., Till A., and Brüstle O., 2022*,"Dynamics of Metabolic Pathways and Stress Response Patterns during Human Neural Stem Cell Proliferation and Differentiation,"* Cells, **11**(9). doi:10.3390/cells11091388.

[32] Karam M., Ortega-Gascó A., and Tornero D., 2025*,"Emerging Insights into Brain Inflammation: Stem-Cell-Based Approaches for Regenerative Medicine,"* International journal of molecular sciences, **26**(7). doi:10.3390/ijms26073275.

[33] Tataranu L. G., and Rizea R. E., 2025*,"Neuroplasticity and Nervous System Recovery: Cellular Mechanisms, Therapeutic Advances, and Future Prospects,"* Brain sciences, **15**(4). doi:10.3390/brainsci15040400.

[34] Francescangeli F., Angelis M. L. de, Rossi R., Cuccu A., Giuliani A., Maria R. de, and Zeuner A., 2023*,"Dormancy, stemness, and therapy resistance: interconnected players in cancer evolution,"* Cancer metastasis reviews, **42**(1), pp. 197–215. doi:10.1007/s10555-023-10092-4.

[35] Pan Y., Yuan C., Zeng C., Sun C., Xia L., Wang G., Chen X., Zhang B., Liu J., and Ding Z.-Y., 2025*,"Cancer stem cells and niches: challenges in immunotherapy resistance,"* Molecular cancer, **24**(1), p. 52. doi:10.1186/s12943-025-02265-2.

[36] Shi Z.-D., Pang K., Wu Z.-X., Dong Y., Hao L., Qin J.-X., Wang W., Chen Z.-S., and Han C.-H., 2023*,"Tumor cell plasticity in targeted therapy-induced resistance: mechanisms and new strategies,"* Signal transduction and targeted therapy, **8**(1), p. 113. doi:10.1038/s41392-023-01383-x.

[37] Amirmahani F., Kumar S., and Muthukrishnan S. D., 2025*,"Epigenetic mechanisms of plasticity and resistance in glioblastoma: therapeutic targets and implications,"* Front. Epigenet. Epigenom., **3**. doi:10.3389/freae.2025.1519449.

[38] Zhang Z., Wen W., Di Hu, Li H., Lin H., and Luo J., 2025*,"Environmental adversity, endoplasmic reticulum stress, and neurogenesis,"* Neurotoxicology, **109**, pp. 32–45. doi:10.1016/j.neuro.2025.05.010.

[39] Janik K., Manire M. A., Smith G. M., and Krynska B., 2020*,"Spinal Cord Injury in Myelomeningocele: Prospects for Therapy,"* Frontiers in cellular neuroscience, **14**, p. 201. doi:10.3389/fncel.2020.00201.

[40] Singh S., Dey D., Barik D., Mohapatra I., Kim S., Sharma M., Prasad S., Wang P., Singh A., and Singh G., 2025*,"Glioblastoma at the crossroads: current understanding and future therapeutic horizons,"* Signal transduction and targeted therapy, **10**(1), p. 213. doi:10.1038/s41392-025-02299-4.

[41] Vaz-Salgado M. A., Villamayor M., Albarrán V., Alía V., Sotoca P., Chamorro J., Rosero D., Barrill A. M., Martín M., Fernandez E., Gutierrez J. A., Rojas-Medina L. M., and Ley L., 2023*,"Recurrent Glioblastoma: A Review of the Treatment Options,"* Cancers, **15**(17). doi:10.3390/cancers15174279.

[42] Yabo Y. A., and Heiland D. H., 2024*,"Understanding glioblastoma at the single-cell level: Recent advances and future challenges,"* PLoS biology, **22**(5), e3002640. doi:10.1371/journal.pbio.3002640.

[43] Rodgers L. T., Villano J. L., Hartz A. M. S., and Bauer B., 2024*,"Glioblastoma Standard of Care: Effects on Tumor Evolution and Reverse Translation in Preclinical Models,"* Cancers, **16**(15). doi:10.3390/cancers16152638.

[44] Couturier C. P., Ayyadhury S., Le P. U., Nadaf J., Monlong J., Riva G., Allache R., Baig S., Yan X., Bourgey M., Lee C., Wang Y. C. D., Wee Yong V., Guiot M.-C., Najafabadi H., Misic B., Antel J., Bourque G., Ragoussis J., and Petrecca K., 2020*,"Single-cell RNA-seq reveals that glioblastoma recapitulates a normal neurodevelopmental hierarchy,"* Nature communications, **11**(1), p. 3406. doi:10.1038/s41467-020-17186-5.

[45] Neftel C., Laffy J., Filbin M. G., Hara T., Shore M. E., Rahme G. J., Richman A. R., Silverbush D., Shaw M. L., Hebert C. M., Dewitt J., Gritsch S., Perez E. M., Gonzalez Castro L. N., Lan X., Druck N., Rodman C., Dionne D., Kaplan A., Bertalan M. S., Small J., Pelton K., Becker S., Bonal D., Nguyen Q.-D., Servis R. L., Fung J. M., Mylvaganam R., Mayr L., Gojo J., Haberler C., Geyeregger R., Czech T., Slavc I., Nahed B. V., Curry W. T., Carter B. S., Wakimoto H., Brastianos P. K., Batchelor T. T., Stemmer-Rachamimov A., Martinez-Lage M., Frosch M. P., Stamenkovic I., Riggi N., Rheinbay E., Monje M., Rozenblatt-Rosen O., Cahill D. P., Patel A. P., Hunter T., Verma I. M., Ligon K. L., Louis D. N., Regev A., Bernstein B. E., Tirosh I., and Suvà M. L., 2019*,"An Integrative Model of Cellular States, Plasticity, and Genetics for Glioblastoma,"* Cell, **178**(4), 835-849.e21. doi:10.1016/j.cell.2019.06.024.

[46] Yabo Y. A., Niclou S. P., and Golebiewska A., 2022*,"Cancer cell heterogeneity and plasticity: A paradigm shift in glioblastoma,"* Neuro-oncology, **24**(5), pp. 669–682. doi:10.1093/neuonc/noab269.

[47] Sloan A. R., Silver D. J., Kint S., Gallo M., and Lathia J. D., 2024*,"Cancer stem cell hypothesis 2.0 in glioblastoma: Where are we now and where are we going?,"* Neuro-oncology, **26**(5), pp. 785–795. doi:10.1093/neuonc/noae011.

[48] Mitchell K., Troike K., Silver D. J., and Lathia J. D., 2021*,"The evolution of the cancer stem cell state in glioblastoma: emerging insights into the next generation of functional interactions,"* Neuro-oncology, **23**(2), pp. 199–213. doi:10.1093/neuonc/noaa259.

[49] Tang J., Amin M. A., and Campian J. L., 2025*,"Glioblastoma Stem Cells at the Nexus of Tumor Heterogeneity, Immune Evasion, and Therapeutic Resistance,"* Cells, **14**(8). doi:10.3390/ cells14080562.

[50] Wang Z., Zhang H., Xu S., Liu Z., and Cheng Q., 2021*,"The adaptive transition of glioblastoma stem cells and its implications on treatments,"* Signal transduction and targeted therapy, **6**(1), p. 124. doi:10.1038/s41392-021-00491-w.

[51] Lathia J. D., Mack S. C., Mulkearns-Hubert E. E., Valentim C. L. L., and Rich J. N., 2015*,"Cancer stem cells in glioblastoma,"* Genes & development, **29**(12), pp. 1203–1217. doi:10.1101/gad.261982.115.

[52] Visioli A., Trivieri N., Mencarelli G., Giani F., Copetti M., Palumbo O., Pracella R., Cariglia M. G., Barile C., Mischitelli L., Soriano A. A., Palumbo P., Legnani F., DiMeco

F., Gorgoglione L., Pesole G., Vescovi A. L., and Binda E., 2023*,"Different states of stemness of glioblastoma stem cells sustain glioblastoma subtypes indicating novel clinical biomarkers and high-efficacy customized therapies,"* Journal of experimental & clinical cancer research CR, **42**(1), p. 244. doi:10.1186/s13046-023-02811-0.

[53] Dirkse A., Golebiewska A., Buder T., Nazarov P. V., Muller A., Poovathingal S., Brons N. H. C., Leite S., Sauvageot N., Sarkisjan D., Seyfrid M., Fritah S., Stieber D., Michelucci A., Hertel F., Herold-Mende C., Azuaje F., Skupin A., Bjerkvig R., Deutsch A., Voss-Böhme A., and Niclou S. P., 2019*,"Stem cell-associated heterogeneity in Glioblastoma results from intrinsic tumor plasticity shaped by the microenvironment,"* Nature communications, **10**(1), p. 1787. doi:10.1038/s41467-019-09853-z.

[54] Hattermann K., Flüh C., Engel D., Mehdorn H. M., Synowitz M., Mentlein R., and Held-Feindt J., 2016*,"Stem cell markers in glioma progression and recurrence,"* International journal of oncology, **49**(5), pp. 1899–1910. doi:10.3892/ijo.2016.3682.

[55] He J., Yan X., and Hu S., 2025*,"Glioma stem cells: drivers of tumor progression and recurrence,"* Stem cell research & therapy, **16**(1), p. 293. doi:10.1186/s13287-025-04352-z.

[56] Filatova A., Acker T., and Garvalov B. K., 2013*,"The cancer stem cell niche(s): the crosstalk between glioma stem cells and their microenvironment,"* Biochimica et biophysica acta, **1830**(2), pp. 2496–2508. doi:10.1016/j.bbagen.2012.10.008.

[57] Adamski V., Hattermann K., Kubelt C., Cohrs G., Lucius R., Synowitz M., Sebens S., and Held-Feindt J., 2020*,"Entry and exit of chemotherapeutically-promoted cellular dormancy in glioblastoma cells is differentially affected by the chemokines CXCL12, CXCL16, and CX3CL1,"* Oncogene, **39**(22), pp. 4421–4435. doi:10.1038/s41388-020-1302-8.

[58] Satchi-Fainaro R., Ferber S., Segal E., Ma L., Dixit N., Ijaz A., Hlatky L., Abdollahi A., and Almog N., 2012*,"Prospective identification of glioblastoma cells generating dormant tumors,"* PloS one, **7**(9), e44395. doi:10.1371/journal.pone.0044395.

[59] Kangwan N., Park J.-M., Kim E.-H., and Hahm K. B., 2014*,"Chemoquiescence for ideal cancer treatment and prevention: where are we now?,"* Journal of cancer prevention, **19**(2), 89-6. doi:10.15430/JCP.2014.19.2.89.

[60] Kubelt C., Hellmold D., Esser D., Ahmeti H., Synowitz M., and Held-Feindt J., 2023*,"Insights into Gene Regulation under Temozolomide-Promoted Cellular Dormancy and Its Connection to Stemness in Human Glioblastoma,"* Cells, **12**(11). doi:10.3390/cells12111491.

[61] Antonica F., Santomaso L., Pernici D., Petrucci L., Aiello G., Cutarelli A., Conti L., Romanel A., Miele E., Tebaldi T., and Tiberi L., 2022*,"A slow-cycling/quiescent cells*

subpopulation is involved in glioma invasiveness," Nature communications, **13**(1), p. 4767. doi:10.1038/s41467-022-32448-0.

[62] Almog N., 2010*,"Molecular mechanisms underlying tumor dormancy,"* Cancer letters, **294**(2), pp. 139–146. doi:10.1016/j.canlet.2010.03.004.

[63] Tong L., Yi L., Liu P., Abeysekera I. R., Hai L., Li T., Tao Z., Ma H., Xie Y., Huang Y., Yu S., Li J., Yuan F., and Yang X., 2018*,"Tumour cell dormancy as a contributor to the reduced survival of GBM patients who received standard therapy,"* Oncology reports, **40**(1), pp. 463–471. doi:10.3892/or.2018.6425.

[64] Adamski V., Hempelmann A., Flüh C., Lucius R., Synowitz M., Hattermann K., and Held-Feindt J., 2017*,"Dormant glioblastoma cells acquire stem cell characteristics and are differentially affected by Temozolomide and AT101 treatment,"* Oncotarget, **8**(64), pp. 108064–108078. doi:10.18632/oncotarget.22514.

[65] Reveilles J., Ballestin A., Pichol-Thievend C., Thomas A., Ribecco V., Anezo O., Bourmeau G., Blanchard B., Cavalli F. M., Borst G. R., Alanio C., Heiland D., Golebiewska A., Binder Z. A., van Rheenen J., Roncaroli F., Joseph K., Ravi V. M., and Seano G., 2025*,"P02.09.B SURGICAL RESECTION OF GLIOBLASTOMA INDUCES IMMUNOSUPPRESSION,"* Neuro-oncology, **27**(Supplement_3), iii43-iii43. doi:10.1093/neuonc/noaf193.136.

[66] Gupta K., and Burns T. C., 2018*,"Radiation-Induced Alterations in the Recurrent Glioblastoma Microenvironment: Therapeutic Implications,"* Frontiers in oncology, **8**, p. 503. doi:10.3389/fonc.2018.00503.

[67] Yao R., Rivera I., Maldonado J., Best-Popescu C. A., Xu H., Sarkaria J. N., Wang J., Lu Y., Selting K. A., Harley B. A. C., and Pedrón-Haba S., 2026*,"Biomimetic model for the identification of distinctive microenvironmental factors in glioblastoma radiosensitivity,"* bioRxiv the preprint server for biology. doi:10.64898/2026.01.14.699525.

[68] Pichol-Thievend C., Anezo O., Pettiwala A. M., Bourmeau G., Montagne R., Lyne A.-M., Guichet P.-O., Deshors P., Ballestín A., Blanchard B., Reveilles J., Ravi V. M., Joseph K., Heiland D. H., Julien B., Leboucher S., Besse L., Legoix P., Dingli F., Liva S., Loew D., Giani E., Ribecco V., Furumaya C., Marcos-Kovandzic L., Masliantsev K., Daubon T., Wang L., Diaz A. A., Schnell O., Beck J., Servant N., Karayan-Tapon L., Cavalli F. M. G., and Seano G., 2024*,"VC-resist glioblastoma cell state: vessel co-option as a key driver of chemoradiation resistance,"* Nature communications, **15**(1), p. 3602. doi:10.1038/s41467-024-47985-z.

[69] Wang L., Jung J., Babikir H., Shamardani K., Jain S., Feng X., Gupta N., Rosi S., Chang S., Raleigh D., Solomon D., Phillips J. J., and Diaz A. A., 2022*,"A single-cell atlas of glioblastoma evolution under therapy reveals cell-intrinsic and cell-extrinsic*

therapeutic targets," Nature cancer, **3**(12), pp. 1534–1552. doi:10.1038/s43018-022-00475-x.

[70] Delgado-López P. D., and Corrales-García E. M., 2016*,"Survival in glioblastoma: a review on the impact of treatment modalities,"* Clinical & translational oncology official publication of the Federation of Spanish Oncology Societies and of the National Cancer Institute of Mexico, **18**(11), pp. 1062–1071. doi:10.1007/s12094-016-1497-x.

[71] Cruz J. V. R., Batista C., Afonso B. d. H., Alexandre-Moreira M. S., Dubois L. G., Pontes B., Moura Neto V., and Mendes F. d. A., 2022*,"Obstacles to Glioblastoma Treatment Two Decades after Temozolomide,"* Cancers, **14**(13). doi:10.3390/cancers14133203.

[72] Giammalva G. R., Gagliardo C., Marrone S., Paolini F., Gerardi R. M., Umana G. E., Yağmurlu K., Chaurasia B., Scalia G., Midiri F., La Grutta L., Basile L., Gulì C., Messina D., Pino M. A., Graziano F., Tumbiolo S., Iacopino D. G., and Maugeri R., 2021*,"Focused Ultrasound in Neuroscience. State of the Art and Future Perspectives,"* Brain sciences, **11**(1). doi:10.3390/brainsci11010084.

[73] Bell M. S., Walton C. M., Williams M. J., Eckert T., Brown J. C., Rowland N. C., Sahin O., and Strickland B. A., 2026*,"Engineering focused ultrasound for glioblastoma,"* Brain stimulation, **19**(1), p. 102986. doi:10.1016/j.brs.2025.102986.

[74] Alrashidi M., Ferro F., Almohammadi A., Alyoubi N. H., Alsarheed G. S., Joseph J., and Banerjee S., 2026*,"Efficacy and safety of low- and high-intensity focused ultrasound in glioblastoma: a systematic review of preclinical and clinical studies,"* British journal of cancer, **134**(7), pp. 977–995. doi:10.1038/s41416-025-03325-6.

[75] Roberts J. W., Powlovich L., Sheybani N., and LeBlang S., 2022*,"Focused ultrasound for the treatment of glioblastoma,"* Journal of neuro-oncology, **157**(2), pp. 237–247. doi:10.1007/s11060-022-03974-0.

[76] Noel R. L., Kugelman T., Karakatsani M. E., Shahriar S., Willner M. J., Jimenez D. A., Choi C. S., Nimi Y., Ji R., Agalliu D., and Konofagou E. E., 2026*,"Safe focused ultrasound-mediated blood-brain barrier opening is driven primarily by transient reorganization of tight junctions,"* Communications engineering, **5**(1). doi:10.1038/s44172-026-00597-5.

[77] Woodworth G. F., Anastasiadis P., Ozair A., Chabros J., Bettegowda C., Chen C., Gerstl J. V. E., Douville C., Mekary R. A., Smith T. R., Meng Y., Hawkins C., Pople C. B., Abrahao A., Llinas M., Heyn C., Bunevicius A., Rezai A. R., Ball A. J. S., Henry K., Sahgal A., Torio E., Ren H., Ahmad H., Arora H., Eisenberg H., Perry J., Carpenter J. S., Hynynen K., Pham L. C., Anketell M. B., Lim-Fat M. J., Xu Z., Cifarelli C. P., Sheehan J. P., McDannold N. J., Gandhi D., Golby A. J., and Lipsman N., 2025*,"Microbubble-enhanced transcranial focused ultrasound with temozolomide for patients with high-*

grade glioma (BT008NA): a multicentre, open-label, phase 1/2 trial," The Lancet. Oncology, **26**(12), pp. 1651–1664. doi:10.1016/S1470-2045(25)00492-9.

[78] Maio A. de, Alfieri G., Mattone M., Ghanouni P., and Napoli A., 2024*,"High-Intensity Focused Ultrasound Surgery for Tumor Ablation: A Review of Current Applications,"* Radiology. Imaging cancer, **6**(1), e230074. doi:10.1148/rycan.230074.

[79] Xu Z., Hall T. L., Vlaisavljevich E., and Lee F. T., 2021*,"Histotripsy: the first noninvasive, non-ionizing, non-thermal ablation technique based on ultrasound,"* International journal of hyperthermia the official journal of European Society for Hyperthermic Oncology, North American Hyperthermia Group, **38**(1), pp. 561–575. doi:10.1080/02656736.2021.1905189.

[80] Hersh A. M., Bhimreddy M., Weber-Levine C., Jiang K., Alomari S., Theodore N., Manbachi A., and Tyler B. M., 2022*,"Applications of Focused Ultrasound for the Treatment of Glioblastoma: A New Frontier,"* Cancers, **14**(19). doi:10.3390/cancers14194920.

[81] Kodama T., and Tomita Y., 2000*,"Cavitation bubble behavior and bubble-shock wave interaction near a gelatin surface as a study of in vivo bubble dynamics,"* Applied Physics B: Lasers and Optics, **70**(1), pp. 139–149. doi:10.1007/s003400050022.

[82] Supponen O., Obreschkow D., Kobel P., Tinguely M., Dorsaz N., and Farhat M., 2017*,"Shock waves from nonspherical cavitation bubbles,"* Phys. Rev. Fluids, **2**(9). doi:10.1103/PhysRevFluids.2.093601.

[83] Laborde J.-L., Bouyer C., Caltagirone J.-P., and Gérard A., 1998*,"Acoustic bubble cavitation at low frequencies,"* Ultrasonics, **36**(1-5), pp. 589–594. doi:10.1016/S0041-624X(97)00105-4.

[84] Yang Y., Zhang X., Ye D., Laforest R., Williamson J., Liu Y., and Chen H., 2019*,"Cavitation dose painting for focused ultrasound-induced blood-brain barrier disruption,"* Scientific reports, **9**(1), p. 2840. doi:10.1038/s41598-019-39090-9.

[85] Kerboua K., Hamdaoui O., and Alghyamah A., 2021*,"Numerical Characterization of Acoustic Cavitation Bubbles with Respect to the Bubble Size Distribution at Equilibrium,"* Processes, **9**(9), p. 1546. doi:10.3390/pr9091546.

[86] Pallumeera M., Hong M., Giang J. C., and Makary M. S., 2025*,"Histotripsy: Recent Advances, Clinical Applications, and Future Prospects,"* Cancers, **17**(18). doi:10.3390/cancers17183072.

[87] Choi S. W., Duclos S., Camelo-Piragua S., Chaudhary N., Sukovich J., Hall T., Pandey A., and Xu Z., 2023*,"Histotripsy Treatment of Murine Brain and Glioma: Temporal Profile of Magnetic Resonance Imaging and Histological Characteristics Post-treatment,"* Ultrasound in medicine & biology, **49**(8), pp. 1882–1891. doi:10.1016/j.ultrasmedbio.2023.05.002.

[88] Duclos S., Kaovasia T. P., Fox A., Cornett A., Pandey A. S., and Xu Z., 2026*,"First Report of Histotripsy-Induced Survival Benefit in Murine Glioblastomas,"* Cancers, **18**(4). doi:10.3390/cancers18040622.

[89] Duclos S., Golin A., Fox A., Chaudhary N., Camelo-Piragua S., Pandey A., and Xu Z., 2023*,"Transcranial histotripsy parameter study in primary and metastatic murine brain tumor models,"* International journal of hyperthermia the official journal of European Society for Hyperthermic Oncology, North American Hyperthermia Group, **40**(1), p. 2237218. doi:10.1080/02656736.2023.2237218.

[90] Kaovasia T. P., Duclos S., Gupta D., Kalayeh K., Fabiilli M., Noll D. C., Sukovich J., Pandey A., Xu Z., and Hall T. L., 2025*,"A pre-clinical MRI-guided all-in-one focused ultrasound system for murine brain studies,"* Scientific reports, **15**(1), p. 144. doi:10.1038/s41598-024-84078-9.

[91] Lu N., Hall T. L., Choi D., Gupta D., Daou B. J., Sukovich J. R., Fox A., Gerhardson T. I., Pandey A. S., Noll D. C., and Xu Z., 2021*,"Transcranial MR-Guided Histotripsy System,"* IEEE transactions on ultrasonics, ferroelectrics, and frequency control, **68**(9), pp. 2917–2929. doi:10.1109/TUFFC.2021.3068113.

[92] Gupta D., Kaovasia T. P., Komaiha M., Nielsen J.-F., Allen S. P., Hall T. L., Noll D. C., and Xu Z., 2025*,"Transcranial MRI-guided Histotripsy Targeting Using MR-thermometry and MR-ARFI,"* Ultrasound in medicine & biology, **51**(2), pp. 330–335. doi:10.1016/j.ultrasmedbio.2024.10.010.

[93] Lu N., Gupta D., Daou B. J., Fox A., Choi D., Sukovich J. R., Hall T. L., Camelo-Piragua S., Chaudhary N., Snell J., Pandey A. S., Noll D. C., and Xu Z., 2022*,"Transcranial Magnetic Resonance-Guided Histotripsy for Brain Surgery: Pre-clinical Investigation,"* Ultrasound in medicine & biology, **48**(1), pp. 98–110. doi:10.1016/j.ultrasmedbio.2021.09.008.

[94] Lu N., Yeats E. M., Sukovich J. R., Hall T. L., Pandey A. S., and Xu Z., 2024*,"Treatment envelope of transcranial histotripsy: challenges and strategies to maximize the treatment location profile,"* Physics in medicine and biology, **69**(22). doi:10.1088/1361-6560/ad8d9f.

[95] Li S., Wei Y., Zhang B., and Li X., 2023*,"Research progress and clinical evaluation of histotripsy: a narrative review,"* Annals of translational medicine, **11**(6), p. 263. doi:10.21037/atm-22-2578.

[96] Qu S., Worlikar T., Felsted A. E., Ganguly A., Beems M. V., Hubbard R., Pepple A. L., Kevelin A. A., Garavaglia H., Dib J., Toma M., Huang H., Tsung A., Xu Z., and Cho C. S., 2020*,"Non-thermal histotripsy tumor ablation promotes abscopal immune responses that enhance cancer immunotherapy,"* Journal for immunotherapy of cancer, **8**(1). doi:10.1136/jitc-2019-000200.

[97] Sandilos G., Butchy M. V., Koneru M., Gongalla S., Sensenig R., and Hong Y. K., 2024*,"Histotripsy - hype or hope? Review of innovation and future implications,"* Journal of gastrointestinal surgery official journal of the Society for Surgery of the Alimentary Tract, **28**(8), pp. 1370–1375. doi:10.1016/j.gassur.2024.05.038.

[98] Pepple A. L., Guy J. L., McGinnis R., Felsted A. E., Song B., Hubbard R., Worlikar T., Garavaglia H., Dib J., Chao H., Boyle N., Olszewski M., Xu Z., Ganguly A., and Cho C. S., 2023*,"Spatiotemporal local and abscopal cell death and immune responses to histotripsy focused ultrasound tumor ablation,"* Frontiers in immunology, **14**, p. 1012799. doi:10.3389/fimmu.2023.1012799.

[99] Copp A. J., and Greene N. D. E., 2013*,"Neural tube defects--disorders of neurulation and related embryonic processes,"* Wiley interdisciplinary reviews. Developmental biology, **2**(2), pp. 213–227. doi:10.1002/wdev.71.

[100] Copp A. J., Stanier P., and Greene N. D. E., 2013*,"Neural tube defects: recent advances, unsolved questions, and controversies,"* The Lancet. Neurology, **12**(8), pp. 799–810. doi:10.1016/S1474-4422(13)70110-8.

[101] Botto L. D., Moore C. A., Khoury M. J., and Erickson J. D., 1999*,"Neural-tube defects,"* The New England journal of medicine, **341**(20), pp. 1509–1519. doi:10.1056/NEJM199911113412006.

[102] Kancherla V., Ma C., Grant G., Lee H. C., Hintz S. R., and Carmichael S. L., 2021*,"Factors Associated with Early Neonatal and First-Year Mortality in Infants with Myelomeningocele in California from 2006 to 2011,"* American journal of perinatology, **38**(12), pp. 1263–1270. doi:10.1055/s-0040-1712165.

[103] Michejda M., 1984*,"Intrauterine treatment of spina bifida: primate model,"* Zeitschrift fur Kinderchirurgie organ der Deutschen, der Schweizerischen und der Osterreichischen Gesellschaft fur Kinderchirurgie = Surgery in infancy and childhood, **39**(4), pp. 259–261. doi:10.1055/s-2008-1044221.

[104] Meuli M., Meuli-Simmen C., Yingling C. D., Hutchins G. M., Hoffman K. M., Harrison M. R., and Adzick N. S., 1995*,"Creation of myelomeningocele in utero: a model of functional damage from spinal cord exposure in fetal sheep,"* Journal of pediatric surgery, **30**(7), 1028-32; discussion 1032-3. doi:10.1016/0022-3468(95)90335-6.

[105] Housley H. T., Graf J. L., Lipshultz G. S., Calvano C. J., Harrison M. R., Farmer D. L., and Jennings R. W., 2000*,"Creation of myelomeningocele in the fetal rabbit,"* Fetal diagnosis and therapy, **15**(5), pp. 275–279. doi:10.1159/000021021.

[106] Heffez D. S., Aryanpur J., Hutchins G. M., and Freeman J. M., 1990*,"The paralysis associated with myelomeningocele: clinical and experimental data implicating a preventable spinal cord injury,"* Neurosurgery, **26**(6), pp. 987–992.

[107] Heffez D. S., Aryanpur J., Rotellini N. A., Hutchins G. M., and Freeman J. M., 1993*,"Intrauterine repair of experimental surgically created dysraphism,"* Neurosurgery, **32**(6), pp. 1005–1010. doi:10.1227/00006123-199306000-00021.

[108] Oria M., Pathak B., Li Z., Bakri K., Gouwens K., Varela M. F., Lampe K., Murphy K. P., Lin C.-Y., and Peiro J. L., 2022*,"Premature Neural Progenitor Cell Differentiation Into Astrocytes in Retinoic Acid-Induced Spina Bifida Rat Model,"* Frontiers in molecular neuroscience, **15**, p. 888351. doi:10.3389/fnmol.2022.888351.

[109] Meuli M., Meuli-Simmen C., Hutchins G. M., Seller M. J., Harrison M. R., and Adzick N. S., 1997*,"The spinal cord lesion in human fetuses with myelomeningocele: implications for fetal surgery,"* Journal of pediatric surgery, **32**(3), pp. 448–452. doi:10.1016/S0022-3468(97)90603-5.

[110] Lindquist B., Jacobsson H., Strinnholm M., and Peny-Dahlstrand M., 2022*,"A scoping review of cognition in spina bifida and its consequences for activity and participation throughout life,"* Acta paediatrica (Oslo, Norway 1992), **111**(9), pp. 1682–1694. doi:10.1111/apa.16420.

[111] Pastuszka A., Bohosiewicz J., Olejek A., Zamłyński J., Horzelska E., and Koszutski T., 2022*,"In utero myelomeningocele repair reduces intensification of inflammatory changes in the dura mater and the skin,"* The journal of spinal cord medicine, **45**(2), pp. 180–185. doi:10.1080/10790268.2020.1736434.

[112] Adzick N. S., 2013*,"Fetal surgery for spina bifida: past, present, future,"* Seminars in pediatric surgery, **22**(1), pp. 10–17. doi:10.1053/j.sempedsurg.2012.10.003.

[113] Bhatt M., Sharma M., and Das B., 2024*,"The Role of Inflammatory Cascade and Reactive Astrogliosis in Glial Scar Formation Post-spinal Cord Injury,"* Cellular and molecular neurobiology, **44**(1), p. 78. doi:10.1007/s10571-024-01519-9.

[114] Nivrenjeet S., Mohd-Zin S. W., Nisheljeet S., Azizi A. B., Palaniandy K., Firdaus-Raih M., Muhamad Ariffin M. H., Greene N. D. E., and Abdul-Aziz N. M., 2022*,"Inflammation in embryology: A review of neuroinflammation in spina bifida,"* Neurosci Res Notes, **5**(1), p. 132. doi:10.31117/neuroscirn.v5i1.132.

[115] Meuli M., and Moehrlen U., 2014*,"Fetal surgery for myelomeningocele is effective: a critical look at the whys,"* Pediatric surgery international, **30**(7), pp. 689–697. doi:10.1007/s00383-014-3524-8.

[116] Hutchins G. M., Meuli M., Meuli-Simmen C., Jordan M. A., Heffez D. S., and Blakemore K. J., 1996*,"Acquired spinal cord injury in human fetuses with myelomeningocele,"* Pediatric pathology & laboratory medicine journal of the Society for Pediatric Pathology, affiliated with the International Paediatric Pathology Association, **16**(5), pp. 701–712.

[117] Yip P. K., and Malaspina A., 2012*,"Spinal cord trauma and the molecular point of no return,"* Molecular neurodegeneration, **7**, p. 6. doi:10.1186/1750-1326-7-6.

[118] Gulbis B., Gervy C., and Jauniaux E., 1998*,"Amniotic fluid biochemistry in second-trimester trisomic pregnancies: relationships to fetal organ maturation and dysfunction,"* Early human development, **52**(3), pp. 211–219. doi:10.1016/S0378-3782(98)00023-1.

[119] Fernandez de Castro A., Usategui-Gomez M., and Spellacy W. N., 1973*,"Amniotic fluid amylase,"* American journal of obstetrics and gynecology, **116**(7), pp. 931–936. doi:10.1016/S0002-9378(16)33839-X.

[120] Stiefel D., and Meuli M., 2007*,"Scanning electron microscopy of fetal murine myelomeningocele reveals growth and development of the spinal cord in early gestation and neural tissue destruction around birth,"* Journal of pediatric surgery, **42**(9), pp. 1561–1565. doi:10.1016/j.jpedsurg.2007.04.019.

[121] Drewek M. J., Bruner J. P., Whetsell W. O., and Tulipan N., 1997*,"Quantitative analysis of the toxicity of human amniotic fluid to cultured rat spinal cord,"* Pediatric neurosurgery, **27**(4), pp. 190–193. doi:10.1159/000121250.

[122] Olguner M., Akgür F. M., Ozdemir T., Aktuğ T., and Ozer E., 2000*,"Amniotic fluid exchange for the prevention of neural tissue damage in myelomeningocele: an alternative minimally invasive method to open in utero surgery,"* Pediatric neurosurgery, **33**(5), pp. 252–256. doi:10.1159/000055964.

[123] Correia-Pinto J., Reis J. L., Hutchins G. M., Baptista M. J., Estevão-Costa J., Flake A. W., and Leite-Moreira A. F., 2002*,"In utero meconium exposure increases spinal cord necrosis in a rat model of myelomeningocele,"* Journal of pediatric surgery, **37**(3), pp. 488–492. doi:10.1053/jpsu.2002.30872.

[124] Adzick N. S., Thom E. A., Spong C. Y., Brock J. W., Burrows P. K., Johnson M. P., Howell L. J., Farrell J. A., Dabrowiak M. E., Sutton L. N., Gupta N., Tulipan N. B., D'Alton M. E., and Farmer D. L., 2011*,"A randomized trial of prenatal versus postnatal repair of myelomeningocele,"* The New England journal of medicine, **364**(11), pp. 993–1004. doi:10.1056/NEJMoa1014379.

[125] Moldenhauer J. S., and Adzick N. S., 2017*,"Fetal surgery for myelomeningocele: After the Management of Myelomeningocele Study (MOMS),"* Seminars in fetal & neonatal medicine, **22**(6), pp. 360–366. doi:10.1016/j.siny.2017.08.004.

[126] Knerlich-Lukoschus F., 2023*,"Perspective on inflammatory cytokines in open spinal dysraphism,"* Neural regeneration research, **18**(2), pp. 329–330. doi:10.4103/1673-5374.343901.

[127] Corroenne R., Mehollin-Ray A. R., Johnson R. M., Whitehead W. E., Espinoza J., Castillo J., Castillo H., Orman G., Donepudi R., Huisman T. A. G. M., Nassr A. A., Belfort M. A., Sanz Cortes M., and Shamshirsaz A. A., 2021*,"Impact of the volume of the*

myelomeningocele sac on imaging, prenatal neurosurgery and motor outcomes: a retrospective cohort study," Scientific reports, **11**(1), p. 13189. doi:10.1038/s41598-021-92739-2.

[128] Oria M., Figueira R. L., Scorletti F., Sbragia L., Owens K., Li Z., Pathak B., Corona M. U., Marotta M., Encinas J. L., and Peiro J. L., 2018*,"CD200-CD200R imbalance correlates with microglia and pro-inflammatory activation in rat spinal cords exposed to amniotic fluid in retinoic acid-induced spina bifida,"* Scientific reports, **8**(1), p. 10638. doi:10.1038/s41598-018-28829-5.

[129] Reis J. L., Correia-Pinto J., Monteiro M. P., and Hutchins G. M., 2007*,"In utero topographic analysis of astrocytes and neuronal cells in the spinal cord of mutant mice with myelomeningocele,"* Journal of neurosurgery, **106**(6 Suppl), pp. 472–479. doi:10.3171/ped.2007.106.6.472.

[130] Murphy K. P., Pathak B., Peiro J. L., and Oria M., 2021*,"Time Course Transcriptome Analysis of Spina Bifida Progression in Fetal Rats,"* Brain sciences, **11**(12). doi:10.3390/brainsci11121593.

[131] Cruz S. M., Hameedi S., Sbragia L., Ogunleye O., Diefenbach K., Isaacs A. M., Etchegaray A., and Olutoye O. O., 2025*,"Fetoscopic Myelomeningocele (MMC) Repair: Evolution of the Technique and a Call for Standardization,"* Journal of clinical medicine, **14**(5). doi:10.3390/jcm14051402.

[132] Castillo J., Locastro M. M., Corroenne R., Malhotra A., van Speybroeck A., Lai G., Belfort M. A., Sanz Cortes M., and Castillo H., 2025*,"Maternal-fetal surgery for myelomeningocele longitudinal follow-up model: Mitigation of care fragmentation through care coordination and outcomes reporting,"* Journal of pediatric rehabilitation medicine, **18**(2), pp. 146–154. doi:10.1177/18758894251331335.

[133] Farmer D. L., Thom E. A., Brock J. W., Burrows P. K., Johnson M. P., Howell L. J., Farrell J. A., Gupta N., and Adzick N. S., 2018*,"The Management of Myelomeningocele Study: full cohort 30-month pediatric outcomes,"* American journal of obstetrics and gynecology, **218**(2), 256.e1-256.e13. doi:10.1016/j.ajog.2017.12.001.

[134] Miyabe M. M., Murphy K. P., Oria M., Duru S., Lin C.-Y., and Peiro J. L., 2022*,"Dural substitutes for spina bifida repair: past, present, and future,"* Child's nervous system ChNS official journal of the International Society for Pediatric Neurosurgery, **38**(5), pp. 873–891. doi:10.1007/s00381-022-05486-8.

[135] Hemani S., Lane O., Agarwal S., Yu S. P., and Woodbury A., 2021*,"Systematic Review of Erythropoietin (EPO) for Neuroprotection in Human Studies,"* Neurochemical research, **46**(4), pp. 732–739. doi:10.1007/s11064-021-03242-z.

[136] Tóthová Z., Šemeláková M., Solárová Z., Tomc J., Debeljak N., and Solár P., 2021*,"The Role of PI3K/AKT and MAPK Signaling Pathways in Erythropoietin*

Signalization," International journal of molecular sciences, **22**(14). doi:10.3390/ijms22147682.

[137] Marti H. H., Wenger R. H., Rivas L. A., Straumann U., Digicaylioglu M., Henn V., Yonekawa Y., Bauer C., and Gassmann M., 1996*,"Erythropoietin gene expression in human, monkey and murine brain,"* The European journal of neuroscience, **8**(4), pp. 666–676. doi:10.1111/j.1460-9568.1996.tb01252.x.

[138] Chen Z.-Y., Warin R., and Noguchi C. T., 2006*,"Erythropoietin and normal brain development: receptor expression determines multi-tissue response,"* Neuro-degenerative diseases, **3**(1-2), pp. 68–75. doi:10.1159/000092096.

[139] Alnaeeli M., Wang L., Piknova B., Rogers H., Li X., and Noguchi C. T., 2012*,"Erythropoietin in brain development and beyond,"* Anatomy research international, **2012**, p. 953264. doi:10.1155/2012/953264.

[140] Liu C., Shen K., Liu Z., and Noguchi C. T., 1997*,"Regulated human erythropoietin receptor expression in mouse brain,"* The Journal of biological chemistry, **272**(51), pp. 32395–32400. doi:10.1074/jbc.272.51.32395.

[141] Noguchi C. T., Asavaritikrai P., Teng R., and Jia Y., 2007*,"Role of erythropoietin in the brain,"* Critical reviews in oncology/hematology, **64**(2), pp. 159–171. doi:10.1016/j.critrevonc.2007.03.001.

[142] Gonzalez F. F., McQuillen P., Mu D., Chang Y., Wendland M., Vexler Z., and Ferriero D. M., 2007*,"Erythropoietin enhances long-term neuroprotection and neurogenesis in neonatal stroke,"* Developmental neuroscience, **29**(4-5), pp. 321–330. doi:10.1159/000105473.

[143] Niemann T., Greiner J. F. W., Kaltschmidt C., and Kaltschmidt B., 2023*,"EPO regulates neuronal differentiation of adult human neural-crest derived stem cells in a sex-specific manner,"* BMC neuroscience, **24**(1), p. 19. doi:10.1186/s12868-023-00789-1.

[144] Tsai P. T., Ohab J. J., Kertesz N., Groszer M., Matter C., Gao J., Liu X., Wu H., and Carmichael S. T., 2006*,"A critical role of erythropoietin receptor in neurogenesis and post-stroke recovery,"* The Journal of neuroscience the official journal of the Society for Neuroscience, **26**(4), pp. 1269–1274. doi:10.1523/JNEUROSCI.4480-05.2006.

[145] Ehrenreich H., Garcia-Agudo L. F., Steixner-Kumar A. A., Wilke J. B. H., and Butt U. J., 2022*,"Introducing the brain erythropoietin circle to explain adaptive brain hardware upgrade and improved performance,"* Molecular psychiatry, **27**(5), pp. 2372–2379. doi:10.1038/s41380-022-01551-5.

[146] Juul S. E., Mayock D. E., Comstock B. A., and Heagerty P. J., 2015*,"Neuroprotective potential of erythropoietin in neonates; design of a randomized trial,"* Maternal health, neonatology and perinatology, **1**, p. 27. doi:10.1186/s40748-015-0028-z.

[147] Carelli S., Ghilardi G., Bianciardi P., Latorre E., Rubino F., Bissi M., Di Giulio A. M., Samaja M., and Gorio A., 2016*,"Enhanced brain release of erythropoietin, cytokines and NO during carotid clamping,"* Neurological sciences official journal of the Italian Neurological Society and of the Italian Society of Clinical Neurophysiology, **37**(2), pp. 243–252. doi:10.1007/s10072-015-2398-4.

[148] Galli L., Ricci C., and Egan C. G., 2015*,"Epoetin beta for the treatment of chemotherapy-induced anemia: an update,"* OncoTargets and therapy, **8**, pp. 583–591. doi:10.2147/OTT.S77497.

[149] Provatopoulou S. T., and Ziroyiannis P. N., 2011*,"Clinical use of erythropoietin in chronic kidney disease: outcomes and future prospects,"* Hippokratia, **15**(2), pp. 109–115.

[150] Papanna R., Moise K. J., Mann L. K., Fletcher S., Schniederjan R., Bhattacharjee M. B., Stewart R. J., Kaur S., Prabhu S. P., and Tseng S. C. G., 2016*,"Cryopreserved human umbilical cord patch for in-utero spina bifida repair,"* Ultrasound in obstetrics & gynecology the official journal of the International Society of Ultrasound in Obstetrics and Gynecology, **47**(2), pp. 168–176. doi:10.1002/uog.15790.

[151] Tatu R., Oria M., Pulliam S., Signey L., Rao M. B., Peiro J. L., and Lin C.-Y., 2019*,"Using poly(l-lactic acid) and poly(ε-caprolactone) blends to fabricate self-expanding, watertight and biodegradable surgical patches for potential fetoscopic myelomeningocele repair,"* Journal of biomedical materials research. Part B, Applied biomaterials, **107**(2), pp. 295–305. doi:10.1002/jbm.b.34121.

[152] Mann L. K., Won J. H., Trenton N. J., Garnett J., Snowise S., Fletcher S. A., Tseng S. C. G., Diehl M. R., and Papanna R., 2020*,"Cryopreserved human umbilical cord versus acellular dermal matrix patches for in utero fetal spina bifida repair in a pregnant rat model,"* Journal of neurosurgery. Spine, **32**(2), pp. 321–331. doi:10.3171/2019.7.SPINE19468.

[153] Cohrs G., Blumenröther A.-K., Sürie J.-P., Synowitz M., Held-Feindt J., and Knerlich-Lukoschus F., 2021*,"Fetal and Perinatal Expression Profiles of Proinflammatory Cytokines in the Neuroplacodes of Rats with Myelomeningoceles: A Contribution to the Understanding of Secondary Spinal Cord Injury in Open Spinal Dysraphism,"* Journal of neurotrauma, **38**(24), pp. 3376–3392. doi:10.1089/neu.2021.0091.

[154] Wu X.-Y., Zhu Y.-M., Qi Y., Xu W.-W., and Jing-Zhai, 2021*,"Erythropoietin, as a biological macromolecule in modification of tissue engineered constructs: A review,"* International journal of biological macromolecules, **193**(Pt B), pp. 2332–2342. doi:10.1016/j.ijbiomac.2021.11.065.

[155] Lazow S. P., Labuz D. F., Freedman B. R., Rock A., Zurakowski D., Mooney D. J., and Fauza D. O., 2021*,"A novel two-component, expandable bioadhesive for exposed*

defect coverage: Applicability to prenatal procedures," Journal of pediatric surgery, **56**(1), pp. 165–169. doi:10.1016/j.jpedsurg.2020.09.030.

[156] Benabdderrahmane K., Stirnemann J., Ramtani S., and Falentin-Daudré C., 2024*,"Development of a double-layer electrospun patch as a potential prenatal treatment for myelomeningocele,"* Wound repair and regeneration official publication of the Wound Healing Society [and] the European Tissue Repair Society, **32**(3), pp. 246–256. doi:10.1111/wrr.13123.

[157] Fontecha C. G., Peiro J. L., Aguirre M., Soldado F., Añor S., Fresno L., and Martinez-Ibañez V., 2009*,"Inert patch with bioadhesive for gentle fetal surgery of myelomeningocele in a sheep model,"* European journal of obstetrics, gynecology, and reproductive biology, **146**(2), pp. 174–179. doi:10.1016/j.ejogrb.2009.06.022.

[158] Mann L. K., Won J. H., Patel R., Bergh E. P., Garnett J., Bhattacharjee M. B., Narayana P. A., Jain R., Fletcher S. A., Lai D., and Papanna R., 2021*,"Allografts for Skin Closure during In Utero Spina Bifida Repair in a Sheep Model,"* Journal of clinical medicine, **10**(21). doi:10.3390/jcm10214928.

[159] Saadai P., Nout Y. S., Encinas J., Wang A., Downing T. L., Beattie M. S., Bresnahan J. C., Li S., and Farmer D. L., 2011*,"Prenatal repair of myelomeningocele with aligned nanofibrous scaffolds-a pilot study in sheep,"* Journal of pediatric surgery, **46**(12), pp. 2279–2283. doi:10.1016/j.jpedsurg.2011.09.014.

[160] Oria M., Tatu R. R., Lin C.-Y., and Peiro J. L., 2019*,"In Vivo Evaluation of Novel PLA/PCL Polymeric Patch in Rats for Potential Spina Bifida Coverage,"* The Journal of surgical research, **242**, pp. 62–69. doi:10.1016/j.jss.2019.04.035.

[161] Knerlich-Lukoschus F., Krossa S., Krause J., Mehdorn H. M., Scheidig A., and Held-Feindt J., 2015*,"Impact of chemokines on the properties of spinal cord-derived neural progenitor cells in a rat spinal cord lesion model,"* Journal of neuroscience research, **93**(4), pp. 562–571. doi:10.1002/jnr.23527.

[162] Jacob F., Salinas R. D., Zhang D. Y., Nguyen P. T. T., Schnoll J. G., Wong S. Z. H., Thokala R., Sheikh S., Saxena D., Prokop S., Liu D.-A., Qian X., Petrov D., Lucas T., Chen H. I., Dorsey J. F., Christian K. M., Binder Z. A., Nasrallah M., Brem S., O'Rourke D. M., Ming G.-L., and Song H., 2020*,"A Patient-Derived Glioblastoma Organoid Model and Biobank Recapitulates Inter- and Intra-tumoral Heterogeneity,"* Cell, **180**(1), 188-204.e22. doi:10.1016/j.cell.2019.11.036.

[163] Kovalevich J., and Langford D., 2013*,"Considerations for the use of SH-SY5Y neuroblastoma cells in neurobiology,"* Methods in molecular biology (Clifton, N.J.), **1078**, pp. 9–21. doi:10.1007/978-1-62703-640-5_2.

[164] Budday S., Nay R., Rooij R. de, Steinmann P., Wyrobek T., Ovaert T. C., and Kuhl E., 2015*,"Mechanical properties of gray and white matter brain tissue by indentation,"*

Journal of the mechanical behavior of biomedical materials, **46**, pp. 318–330. doi:10.1016/j.jmbbm.2015.02.024.

[165] Ashokkumar M., 2011*,"The characterization of acoustic cavitation bubbles - an overview,"* Ultrasonics sonochemistry, **18**(4), pp. 864–872. doi:10.1016/j.ultsonch.2010.11.016.

[166] Covaris (R), 010157 Rev-L*,"M220 Focused-ultrasonicator Setup & Instruction Manual:* M220 Focused-ultrasonicator for Sample Processing using Adaptive Focused Acoustic," https://www.covaris.com/wp/wp-content/uploads/resources_pdf/pn_010157.pdf.

[167] Gillibrand P. N., 1969*,"Changes in the electrolytes, urea and osmolality of the amniotic fluid with advancing pregnancy,"* The Journal of obstetrics and gynaecology of the British Commonwealth, **76**(10), pp. 898–905. doi:10.1111/j.1471-0528.1969.tb15727.x.

[168] Benzie R. J., Doran T. A., Harkins J. L., Owen V. M., and Porter C. J., 1974*,"Composition of the amniotic fluid and maternal serum in pregnancy,"* American journal of obstetrics and gynecology, **119**(6), pp. 798–810. doi:10.1016/0002-9378(74)90093-3.

[169] Pettit B. R., Baker S. P., and King G. S., 1979*,"The composition of amniotic fluid in pregnancies complicated by fetal anencephaly or spina bifida,"* British journal of obstetrics and gynaecology, **86**(8), pp. 637–641. doi:10.1111/j.1471-0528.1979.tb10826.x.

[170] Oliveira F. R., Barros E. G., and Magalhães J. A., 2002*,"Biochemical profile of amniotic fluid for the assessment of fetal and renal development,"* Brazilian journal of medical and biological research = Revista brasileira de pesquisas medicas e biologicas, **35**(2), pp. 215–222. doi:10.1590/s0100-879x2002000200010.

[171] Levy H. L., and Montag P. P., 1969*,"Free amino acids in human amniotic fluid. A quantitative study by ion-exchange chromatography,"* Pediatric research, **3**(2), pp. 113–120. doi:10.1203/00006450-196903000-00002.

[172] Pettit B. R., and Allen J. T., 1980*,"Comparison of amino acid concentrations in amniotic fluid from fetal neural tube defective and normal pregnancies,"* Clinica chimica acta; international journal of clinical chemistry, **104**(1), pp. 43–46. doi:10.1016/0009-8981(80)90132-1.

[173] Naila D., Sadanand S., and Sussman D., 2022*,"Artificial amniotic fluid for nuclear magnetic resonance spectroscopy studies,"* Analytical science advances, **3**(5-6), pp. 174–187. doi:10.1002/ansa.202100055.

[174] Handy J. M., and Soni N., 2008*,"Physiological effects of hyperchloraemia and acidosis,"* British journal of anaesthesia, **101**(2), pp. 141–150. doi:10.1093/bja/aen148.

[175] Raut S. K., Singh K., Sanghvi S., Loyo-Celis V., Varghese L., Singh E. R., Gururaja Rao S., and Singh H., 2024*,"Chloride ions in health and disease,"* Bioscience reports, **44**(5). doi:10.1042/BSR20240029.

[176] Olarinoye A. O., Olaomo N. O., Adesina K. T., Ezeoke G. G., and Aboyeji A. P., 2021*,"Comparative diagnosis of premature rupture of membrane by nitrazine test, urea, and creatinine estimation,"* International journal of health sciences, **15**(6), pp. 16–22.

[177] Westhoff M.-A., Karpel-Massler G., Brühl O., Enzenmüller S., La Ferla-Brühl K., Siegelin M. D., Nonnenmacher L., and Debatin K.-M., 2014*,"A critical evaluation of PI3K inhibition in Glioblastoma and Neuroblastoma therapy,"* Molecular and cellular therapies, **2**, p. 32. doi:10.1186/2052-8426-2-32.

[178] Zhang Z.-Q., Wang X., Xue B.-H., Zhao Y., Xie F., Wang S.-D., Xue C., Wang Y., Zhang Y.-S., and Qian L.-J., 2021*,"Chronic stress promotes glioma cell proliferation via the PI3K/Akt signaling pathway,"* Oncology reports, **46**(3). doi:10.3892/or.2021.8153.

[179] Hellmold D., Johanning L., Clüver J., Holler J., Schröder N. O., Bayler F., Ahmeti H., Kubelt-Kwamin C., Wieker S., Helmers A.-K., Synowitz M., and Held-Feindt J., 2025*,"Effect of focused ultrasound-induced mechanical ablation on stemness and dormancy properties of residual/peri-focally localized glioblastoma cells,"* Neuro-oncology advances, **7**(1), vdaf184. doi:10.1093/noajnl/vdaf184.

[180] Hol E. M., and Pekny M., 2015*,"Glial fibrillary acidic protein (GFAP) and the astrocyte intermediate filament system in diseases of the central nervous system,"* Current opinion in cell biology, **32**, pp. 121–130. doi:10.1016/j.ceb.2015.02.004.

[181] Preston A. N., Cervasio D. A., and Laughlin S. T., 2019*,"Visualizing the brain's astrocytes,"* Methods in enzymology, **622**, pp. 129–151. doi:10.1016/bs.mie.2019.02.006.

[182] Ikushima H., Todo T., Ino Y., Takahashi M., Saito N., Miyazawa K., and Miyazono K., 2011*,"Glioma-initiating cells retain their tumorigenicity through integration of the Sox axis and Oct4 protein,"* The Journal of biological chemistry, **286**(48), pp. 41434–41441. doi:10.1074/jbc.M111.300863.

[183] Ray S. K., 2016*,"The Transcription Regulator Krüppel-Like Factor 4 and Its Dual Roles of Oncogene in Glioblastoma and Tumor Suppressor in Neuroblastoma,"* Forum on immunopathological diseases and therapeutics, **7**(1-2), pp. 127–139. doi:10.1615/ForumImmunDisTher.2016017227.

[184] Novak K., 2005*,"First and foremost,"* Nat Rev Cancer, **5**(1), p. 8. doi:10.1038/nrc1532.

[185] Yarmishyn A. A., Yang Y.-P., Lu K.-H., Chen Y.-C., Chien Y., Chou S.-J., Tsai P.-H., Ma H.-I., Chien C.-S., Chen M.-T., and Wang M.-L., 2020*,"Musashi-1 promotes*

cancer stem cell properties of glioblastoma cells via upregulation of YTHDF1," Cancer cell international, **20**(1), p. 597. doi:10.1186/s12935-020-01696-9.

[186] Spada S., Tocci A., Di Modugno F., and Nisticò P., 2021*,"Fibronectin as a multiregulatory molecule crucial in tumor matrisome: from structural and functional features to clinical practice in oncology,"* Journal of experimental & clinical cancer research CR, **40**(1), p. 102. doi:10.1186/s13046-021-01908-8.

[187] Karsdal M. A., Nielsen M. J., Sand J. M., Henriksen K., Genovese F., Bay-Jensen A.-C., Smith V., Adamkewicz J. I., Christiansen C., and Leeming D. J., 2013*,"Extracellular matrix remodeling: the common denominator in connective tissue diseases. Possibilities for evaluation and current understanding of the matrix as more than a passive architecture, but a key player in tissue failure,"* Assay and drug development technologies, **11**(2), pp. 70–92. doi:10.1089/adt.2012.474.

[188] Skill N. J., Avanzino K., Bren-Mattison Y., Boudreaux J. P., Thiagarajan R., and Maluccio M., 2026*,"The Vascular Density/Angiogenesis Marker CD31/PECAM1 does not Correlate with Overall Survival in Neuroendocrine Tumors,"* Journal of gastrointestinal cancer, **57**(1), p. 4. doi:10.1007/s12029-025-01381-y.

[189] Zheng Y., Fuse H., Alzoubi I., and Graeber M. B., 2025*,"Microglia-Derived Brain Macrophages Associate with Glioblastoma Stem Cells: A Potential Mechanism for Tumor Progression Revealed by AI-Assisted Analysis,"* Cells, **14**(6). doi:10.3390/cells14060413.

[190] Le Wang, Zhang C., Zhang Z., Han B., Shen Z., Li L., Liu S., Zhao X., Ye F., and Zhang Y., 2018*,"Specific clinical and immune features of CD68 in glioma via 1,024 samples,"* Cancer management and research, **10**, pp. 6409–6419. doi:10.2147/CMAR.S183293.

[191] Grube S., Freitag D., Kalff R., Ewald C., and Walter J., 2021*,"Characterization of adherent primary cell lines from fresh human glioblastoma tissue, defining glial fibrillary acidic protein as a reliable marker in establishment of glioblastoma cell culture,"* Cancer reports (Hoboken, N.J.), **4**(2), e1324. doi:10.1002/cnr2.1324.

[192] Bulstrode H., Johnstone E., Marques-Torrejon M. A., Ferguson K. M., Bressan R. B., Blin C., Grant V., Gogolok S., Gangoso E., Gagrica S., Ender C., Fotaki V., Sproul D., Bertone P., and Pollard S. M., 2017*,"Elevated FOXG1 and SOX2 in glioblastoma enforces neural stem cell identity through transcriptional control of cell cycle and epigenetic regulators,"* Genes & development, **31**(8), pp. 757–773. doi:10.1101/gad.293027.116.

[193] Berezovsky A. D., Poisson L. M., Cherba D., Webb C. P., Transou A. D., Lemke N. W., Hong X., Hasselbach L. A., Irtenkauf S. M., Mikkelsen T., and deCarvalho A. C., 2014*,"Sox2 promotes malignancy in glioblastoma by regulating plasticity and astrocytic*

differentiation," Neoplasia (New York, N.Y.), **16**(3), 193-206, 206.e19-25. doi:10.1016/j.neo.2014.03.006.

[194] Janardhan K. S., Jensen H., Clayton N. P., and Herbert R. A., 2018*,"Immunohistochemistry in Investigative and Toxicologic Pathology,"* Toxicologic pathology, **46**(5), pp. 488–510. doi:10.1177/0192623318776907.

[195] McComb R. D., Jones T. R., Pizzo S. V., and Bigner D. D., 1982*,"Immunohistochemical detection of factor VIII/von Willebrand factor in hyperplastic endothelial cells in glioblastoma multiforme and mixed glioma-sarcoma,"* Journal of neuropathology and experimental neurology, **41**(5), pp. 479–489.

[196] Quarato C. M. I., Lacedonia D., Salvemini M., Tuccari G., Mastrodonato G., Villani R., Fiore L. A., Scioscia G., Mirijello A., Saponara A., and Sperandeo M., 2023*,"A Review on Biological Effects of Ultrasounds: Key Messages for Clinicians,"* Diagnostics (Basel, Switzerland), **13**(5). doi:10.3390/diagnostics13050855.

[197] Yoo S., Mittelstein D. R., Hurt R. C., Lacroix J., and Shapiro M. G., 2022*,"Focused ultrasound excites cortical neurons via mechanosensitive calcium accumulation and ion channel amplification,"* Nature communications, **13**(1), p. 493. doi:10.1038/s41467-022-28040-1.

[198] Pathak M. M., Nourse J. L., Tran T., Hwe J., Arulmoli J., Le D. T. T., Bernardis E., Flanagan L. A., and Tombola F., 2014*,"Stretch-activated ion channel Piezo1 directs lineage choice in human neural stem cells,"* Proceedings of the National Academy of Sciences of the United States of America, **111**(45), pp. 16148–16153. doi:10.1073/pnas.1409802111.

[199] Matsushita Y., Yoshida K., Yoshiya M., Shimizu T., Tsukamoto S., Kudo N., Takeuchi Y., Higuchi M., and Shimojo M., 2024*,"TRPC6 is a mechanosensitive channel essential for ultrasound neuromodulation in the mammalian brain,"* Proceedings of the National Academy of Sciences of the United States of America, **121**(50), e2404877121. doi:10.1073/pnas.2404877121.

[200] Chen X., Wanggou S., Bodalia A., Zhu M., Dong W., Fan J. J., Yin W. C., Min H.-K., Hu M., Draghici D., Dou W., Li F., Coutinho F. J., Whetstone H., Kushida M. M., Dirks P. B., Song Y., Hui C.-C., Sun Y., Wang L.-Y., Li X., and Huang X., 2018*,"A Feedforward Mechanism Mediated by Mechanosensitive Ion Channel PIEZO1 and Tissue Mechanics Promotes Glioma Aggression,"* Neuron, **100**(4), 799-815.e7. doi:10.1016/j.neuron.2018.09.046.

[201] Zhou W., Liu X., van Wijnbergen J. W. M., Yuan L., Liu Y., Zhang C., and Jia W., 2020*,"Identification of PIEZO1 as a potential prognostic marker in gliomas,"* Scientific reports, **10**(1), p. 16121. doi:10.1038/s41598-020-72886-8.

[202] Prieto M. L., and Maduke M., 2024,*"Towards an ion-channel-centric approach to ultrasound neuromodulation,"* Current opinion in behavioral sciences, **56**. doi:10.1016/j.cobeha.2024.101355.

[203] Chigurupati S., Venkataraman R., Barrera D., Naganathan A., Madan M., Paul L., Pattisapu J. V., Kyriazis G. A., Sugaya K., Bushnev S., Lathia J. D., Rich J. N., and Chan S. L., 2010,*"Receptor channel TRPC6 is a key mediator of Notch-driven glioblastoma growth and invasiveness,"* Cancer research, **70**(1), pp. 418–427. doi:10.1158/0008-5472.CAN-09-2654.

[204] Elzamzamy O. M., Penner R., and Hazlehurst L. A., 2020,*"The Role of TRPC1 in Modulating Cancer Progression,"* Cells, **9**(2). doi:10.3390/cells9020388.

[205] Tsiokas L., 2009,*"Function and regulation of TRPP2 at the plasma membrane,"* American journal of physiology. Renal physiology, **297**(1), F1-9. doi:10.1152/ajprenal.90277.2008.

[206] Borgström A., Peinelt C., and Stokłosa P., 2021,*"TRPM4 in Cancer-A New Potential Drug Target,"* Biomolecules, **11**(2). doi:10.3390/biom11020229.

[207] Armisén R., Marcelain K., Simon F., Tapia J. C., Toro J., Quest A. F. G., and Stutzin A., 2011,*"TRPM4 enhances cell proliferation through up-regulation of the β-catenin signaling pathway,"* Journal of cellular physiology, **226**(1), pp. 103–109. doi:10.1002/jcp.22310.

[208] Pötschke R., Haase J., Glaß M., Simmermacher S., Misiak C., Penalva L. O. F., Kühnöl C. D., and Hüttelmaier S., 2020,*"MSI1 Promotes the Expression of the GBM Stem Cell Marker CD44 by Impairing miRNA-Dependent Degradation,"* Cancers, **12**(12). doi:10.3390/cancers12123654.

[209] Lin J.-C., Tsai J.-T., Chao T.-Y., Ma H.-I., and Liu W.-H., 2019,*"Musashi-1 Enhances Glioblastoma Migration by Promoting ICAM1 Translation,"* Neoplasia (New York, N.Y.), **21**(5), pp. 459–468. doi:10.1016/j.neo.2019.02.006.

[210] Chen X., Niu W., Fan X., Yang H., Zhao C., Fan J., Yao X., and Fang Z., 2023,*"Oct4A palmitoylation modulates tumorigenicity and stemness in human glioblastoma cells,"* Neuro-oncology, **25**(1), pp. 82–96. doi:10.1093/neuonc/noac157.

[211] Lopez-Bertoni H., Lal B., Li A., Caplan M., Guerrero-Cázares H., Eberhart C. G., Quiñones-Hinojosa A., Glas M., Scheffler B., Laterra J., and Li Y., 2015,*"DNMT-dependent suppression of microRNA regulates the induction of GBM tumor-propagating phenotype by Oct4 and Sox2,"* Oncogene, **34**(30), pp. 3994–4004. doi:10.1038/onc.2014.334.

[212] Song W.-S., Yang Y.-P., Huang C.-S., Lu K.-H., Liu W.-H., Wu W.-W., Lee Y.-Y., Lo W.-L., Lee S.-D., Chen Y.-W., Huang P.-I., and Chen M.-T., 2016,*"Sox2, a stemness gene, regulates tumor-initiating and drug-resistant properties in CD133-positive*

glioblastoma stem cells," Journal of the Chinese Medical Association JCMA, **79**(10), pp. 538–545. doi:10.1016/j.jcma.2016.03.010.

[213] Almog N., Ma L., Raychowdhury R., Schwager C., Erber R., Short S., Hlatky L., Vajkoczy P., Huber P. E., Folkman J., and Abdollahi A., 2009*,"Transcriptional switch of dormant tumors to fast-growing angiogenic phenotype,"* Cancer research, **69**(3), pp. 836–844. doi:10.1158/0008-5472.CAN-08-2590.

[214] Eisenbarth D., and Wang Y. A., 2023*,"Glioblastoma heterogeneity at single cell resolution,"* Oncogene, **42**(27), pp. 2155–2165. doi:10.1038/s41388-023-02738-y.

[215] Laks D. R., Masterman-Smith M., Visnyei K., Angenieux B., Orozco N. M., Foran I., Yong W. H., Vinters H. V., Liau L. M., Lazareff J. A., Mischel P. S., Cloughesy T. F., Horvath S., and Kornblum H. I., 2009*,"Neurosphere formation is an independent predictor of clinical outcome in malignant glioma,"* Stem cells (Dayton, Ohio), **27**(4), pp. 980–987. doi:10.1002/stem.15.

[216] Nguyen H. P., Daniel P. M., Filiz G., and Mantamadiotis T., 2018*,"Investigating Neural Stem Cell and Glioma Stem Cell Self-renewal Potential Using Extreme Limiting Dilution Analysis (ELDA),"* Bio-protocol, **8**(17), e2991. doi:10.21769/BioProtoc.2991.

[217] Hu Y., and Smyth G. K., 2009*,"ELDA: extreme limiting dilution analysis for comparing depleted and enriched populations in stem cell and other assays,"* Journal of immunological methods, **347**(1-2), pp. 70–78. doi:10.1016/j.jim.2009.06.008.

[218] Jezierzański M., Nafalska N., Stopyra M., Furgoł T., Miciak M., Kabut J., and Gisterek-Grocholska I., 2024*,"Temozolomide (TMZ) in the Treatment of Glioblastoma Multiforme-A Literature Review and Clinical Outcomes,"* Current oncology (Toronto, Ont.), **31**(7), pp. 3994–4002. doi:10.3390/curroncol31070296.

[219] Ashkan K., Baig Mirza A., Soumpasis C., Syrris C., Kalaitzoglou D., Sharma C., James Z. J., Khoja A. K., Ahmed R., Vastani A., Bartram J., Chia K., Al-Salihi O., Swampilai A., Brazil L., Laxton R., Reisz Z., Bodi I., King A., Gullan R., Vergani F., Bhangoo R., Al-Sarraj S., and Lavrador J. P., 2023*,"MGMT Promoter Methylation: Prognostication beyond Treatment Response,"* Journal of personalized medicine, **13**(6). doi:10.3390/jpm13060999.

[220] Liang Y., Chen W.-M., Zhang Y., and Li L., 2026*,"Remodeling the tumor dormancy ecosystem to prevent recurrence and metastasis,"* Signal transduction and targeted therapy, **11**(1), p. 1. doi:10.1038/s41392-025-02328-2.

[221] Mengistu B. A., Demessie Y., Kinde M. Z., Getnet K., Bitew A. B., Berrie K., Sendeku W., Berihun A. M., Abat A. S., Mebratu A. S., Feleke M. G., Yesist N. T., Ferede M. M., and Fenta M. D., 2025*,"Biology of stem cell paradox: a double-edged sword-implications for cancer therapy,"* Cancer cell international, **25**(1), p. 380. doi:10.1186/s12935-025-03981-x.

[222] Lee H., Kim B., Park J., Park S., Yoo G., Yum S., Kang W., Lee J.-M., Youn H., and Youn B., 2025*,"Cancer stem cells: landscape, challenges and emerging therapeutic innovations,"* Signal transduction and targeted therapy, **10**(1), p. 248. doi:10.1038/s41392-025-02360-2.

[223] Li X., Wu C., Chen N., Gu H., Yen A., Cao L., Wang E., and Wang L., 2016*,"PI3K/Akt/mTOR signaling pathway and targeted therapy for glioblastoma,"* Oncotarget, **7**(22), pp. 33440–33450. doi:10.18632/oncotarget.7961.

[224] Hellmold D., Kubelt C., Daunke T., Beckinger S., Janssen O., Hauck M., Schütt F., Adelung R., Lucius R., Haag J., Sebens S., Synowitz M., and Held-Feindt J., 2023*,"Sequential Treatment with Temozolomide Plus Naturally Derived AT101 as an Alternative Therapeutic Strategy: Insights into Chemoresistance Mechanisms of Surviving Glioblastoma Cells,"* International journal of molecular sciences, **24**(10). doi:10.3390/ijms24109075.

[225] Gulaia V., Kumeiko V., Shved N., Cicinskas E., Rybtsov S., Ruzov A., and Kagansky A., 2018*,"Molecular Mechanisms Governing the Stem Cell's Fate in Brain Cancer: Factors of Stemness and Quiescence,"* Frontiers in cellular neuroscience, **12**, p. 388. doi:10.3389/fncel.2018.00388.

[226] Majewska E., and Szeliga M., 2017*,"AKT/GSK3β Signaling in Glioblastoma,"* Neurochemical research, **42**(3), pp. 918–924. doi:10.1007/s11064-016-2044-4.

[227] Vincent E. E., Elder D. J. E., Thomas E. C., Phillips L., Morgan C., Pawade J., Sohail M., May M. T., Hetzel M. R., and Tavaré J. M., 2011*,"Akt phosphorylation on Thr308 but not on Ser473 correlates with Akt protein kinase activity in human non-small cell lung cancer,"* British journal of cancer, **104**(11), pp. 1755–1761. doi:10.1038/bjc.2011.132.

[228] He Y., Sun M. M., Zhang G. G., Yang J., Chen K. S., Xu W. W., and Li B., 2021*,"Targeting PI3K/Akt signal transduction for cancer therapy,"* Signal transduction and targeted therapy, **6**(1), p. 425. doi:10.1038/s41392-021-00828-5.

[229] Beurel E., Grieco S. F., and Jope R. S., 2015*,"Glycogen synthase kinase-3 (GSK3): regulation, actions, and diseases,"* Pharmacology & therapeutics, **148**, pp. 114–131. doi:10.1016/j.pharmthera.2014.11.016.

[230] Domoto T., Uehara M., Bolidong D., and Minamoto T., 2020*,"Glycogen Synthase Kinase 3β in Cancer Biology and Treatment,"* Cells, **9**(6). doi:10.3390/cells9061388.

[231] Molina J. R., Hayashi Y., Stephens C., and Georgescu M.-M., 2010*,"Invasive glioblastoma cells acquire stemness and increased Akt activation,"* Neoplasia (New York, N.Y.), **12**(6), pp. 453–463. doi:10.1593/neo.10126.

[232] Gharbi S. I., Zvelebil M. J., Shuttleworth S. J., Hancox T., Saghir N., Timms J. F., and Waterfield M. D., 2007*,"Exploring the specificity of the PI3K family inhibitor LY294002,"* The Biochemical journal, **404**(1), pp. 15–21. doi:10.1042/BJ20061489.

[233] Fernandez Garcia-Agudo L., Steixner-Kumar A. A., Curto Y., Barnkothe N., Hassouna I., Jähne S., Butt U. J., Grewe K., Weber M. S., Green K., Rizzoli S., Nacher J., Nave K.-A., and Ehrenreich H., 2021*,"Brain erythropoietin fine-tunes a counterbalance between neurodifferentiation and microglia in the adult hippocampus,"* Cell reports, **36**(8), p. 109548. doi:10.1016/j.celrep.2021.109548.

[234] Hassouna I., Ott C., Wüstefeld L., Offen N., Neher R. A., Mitkovski M., Winkler D., Sperling S., Fries L., Goebbels S., Vreja I. C., Hagemeyer N., Dittrich M., Rossetti M. F., Kröhnert K., Hannke K., Boretius S., Zeug A., Höschen C., Dandekar T., Dere E., Neher E., Rizzoli S. O., Nave K.-A., Sirén A.-L., and Ehrenreich H., 2016*,"Revisiting adult neurogenesis and the role of erythropoietin for neuronal and oligodendroglial differentiation in the hippocampus,"* Molecular psychiatry, **21**(12), pp. 1752–1767. doi:10.1038/mp.2015.212.

[235] Sirén A.-L., Fasshauer T., Bartels C., and Ehrenreich H., 2009*,"Therapeutic potential of erythropoietin and its structural or functional variants in the nervous system,"* Neurotherapeutics the journal of the American Society for Experimental NeuroTherapeutics, **6**(1), pp. 108–127. doi:10.1016/j.nurt.2008.10.041.

[236] Wallach I., Zhang J., Hartmann A., van Landeghem F. K. H., Ivanova A., Klar M., and Dame C., 2009*,"Erythropoietin-receptor gene regulation in neuronal cells,"* Pediatric research, **65**(6), pp. 619–624. doi:10.1203/PDR.0b013e31819ea3b8.

[237] Knabe W., Knerlich F., Washausen S., Kietzmann T., Sirén A. L., Brunnett G., Kuhn H. J., and Ehrenreich H., 2004*,"Expression patterns of erythropoietin and its receptor in the developing midbrain,"* Anatomy and embryology, **207**(6), pp. 503–512. doi:10.1007/s00429-003-0365-y.

[238] Xicoy H., Wieringa B., and Martens G. J. M., 2017*,"The SH-SY5Y cell line in Parkinson's disease research: a systematic review,"* Molecular neurodegeneration, **12**(1), p. 10. doi:10.1186/s13024-017-0149-0.

[239] Lopez-Suarez L., Awabdh S. A., Coumoul X., and Chauvet C., 2022*,"The SH-SY5Y human neuroblastoma cell line, a relevant in vitro cell model for investigating neurotoxicology in human: Focus on organic pollutants,"* Neurotoxicology, **92**, pp. 131–155. doi:10.1016/j.neuro.2022.07.008.

[240] D'Aloia A., Pastori V., Blasa S., Campioni G., Peri F., Sacco E., Ceriani M., Lecchi M., and Costa B., 2024*,"A new advanced cellular model of functional cholinergic-like neurons developed by reprogramming the human SH-SY5Y neuroblastoma cell line,"* Cell death discovery, **10**(1), p. 24. doi:10.1038/s41420-023-01790-7.

[241] Peng B., Kong G., Yang C., and Ming Y., 2020*,"Erythropoietin and its derivatives: from tissue protection to immune regulation,"* Cell death & disease, **11**(2), p. 79. doi:10.1038/s41419-020-2276-8.

[242] Leroy E., Dusa A., Colau D., Motamedi A., Cahu X., Mouton C., Huang L. J., Shiau A. K., and Constantinescu S. N., 2016*,"Uncoupling JAK2 V617F activation from cytokine-induced signalling by modulation of JH2 αC helix,"* The Biochemical journal, **473**(11), pp. 1579–1591. doi:10.1042/BCJ20160085.

[243] Adlung L., Kar S., Wagner M.-C., She B., Chakraborty S., Bao J., Lattermann S., Boerries M., Busch H., Wuchter P., Ho A. D., Timmer J., Schilling M., Höfer T., and Klingmüller U., 2017*,"Protein abundance of AKT and ERK pathway components governs cell type-specific regulation of proliferation,"* Molecular systems biology, **13**(1), p. 904. doi:10.15252/msb.20167258.

[244] Ma R., Hu J., Huang C., Wang M., Xiang J., and Li G., 2014*,"JAK2/STAT5/Bcl-xL signalling is essential for erythropoietin-mediated protection against apoptosis induced in PC12 cells by the amyloid β-peptide Aβ25-35,"* British journal of pharmacology, **171**(13), pp. 3234–3245. doi:10.1111/bph.12672.

[245] Knerlich-Lukoschus F., Clüver J., Manczuk I., Bayler F., Hellmold D., Synowitz M., and Held-Feindt J., 2025*,"Neuroprotective properties of erythropoietin (Epo) and its receptor (EpoR) in open spinal dysraphism (OSD): an investigation of EpoR expression in a rat OSD model, along with in vitro studies on the neuroprotective effects of Epo on rat spinal cord-derived neural progenitor cells,"* Child's nervous system ChNS official journal of the International Society for Pediatric Neurosurgery, **41**(1), p. 358. doi:10.1007/s00381-025-07032-8.

[246] Nguyen A. Q., Cherry B. H., Scott G. F., Ryou M.-G., and Mallet R. T., 2014*,"Erythropoietin: powerful protection of ischemic and post-ischemic brain,"* Experimental biology and medicine (Maywood, N.J.), **239**(11), pp. 1461–1475. doi:10.1177/1535370214523703.

[247] Scholzen T., and Gerdes J., 2000*,"The Ki-67 protein: from the known and the unknown,"* Journal of cellular physiology, **182**(3), pp. 311–322. doi:10.1002/(SICI)1097-4652(200003)182:3<311:AID-JCP1>3.0.CO;2-9.

[248] Wang S.-C., 2014*,"PCNA: a silent housekeeper or a potential therapeutic target?,"* Trends in pharmacological sciences, **35**(4), pp. 178–186. doi:10.1016/j.tips.2014.02.004.

[249] Cardano M., Tribioli C., and Prosperi E., 2020*,"Targeting Proliferating Cell Nuclear Antigen (PCNA) as an Effective Strategy to Inhibit Tumor Cell Proliferation,"* Current cancer drug targets, **20**(4), pp. 240–252. doi:10.2174/1568009620666200115162814.

[250] Bramanti V., Tomassoni D., Avitabile M., Amenta F., and Avola R., 2010*,"Biomarkers of glial cell proliferation and differentiation in culture,"* Frontiers in bioscience (Scholar edition), **2**(2), pp. 558–570. doi:10.2741/s85.

[251] Cáceres A., Banker G. A., and Binder L., 1986*,"Immunocytochemical localization of tubulin and microtubule-associated protein 2 during the development of hippocampal neurons in culture,"* The Journal of neuroscience the official journal of the Society for Neuroscience, **6**(3), pp. 714–722. doi:10.1523/JNEUROSCI.06-03-00714.1986.

[252] Duly A. M. P., Kao F. C. L., Teo W. S., and Kavallaris M., 2022*,"βIII-Tubulin Gene Regulation in Health and Disease,"* Frontiers in cell and developmental biology, **10**, p. 851542. doi:10.3389/fcell.2022.851542.

[253] Hisaoka M., Okamoto S., Koyama S., Ishida T., Imamura T., Kanda H., Kameya T., Meis-Kindblom J. M., Kindblom L.-G., and Hashimoto H., 2003*,"Microtubule-associated protein-2 and class III beta-tubulin are expressed in extraskeletal myxoid chondrosarcoma,"* Modern pathology an official journal of the United States and Canadian Academy of Pathology, Inc, **16**(5), pp. 453–459. doi:10.1097/01.MP.0000067422.61241.64.

[254] Zhang K., Chen S., Yang Q., Guo S., Chen Q., Liu Z., Li L., Jiang M., Li H., Hu J., Pan X., Deng W., Xiao N., Wang B., Wang Z.-X., Zhang L., and Mo W., 2022*,"The Oligodendrocyte Transcription Factor 2 OLIG2 regulates transcriptional repression during myelinogenesis in rodents,"* Nature communications, **13**(1), p. 1423. doi:10.1038/s41467-022-29068-z.

[255] Mauney S. A., Pietersen C. Y., Sonntag K.-C., and Woo T.-U. W., 2015*,"Differentiation of oligodendrocyte precursors is impaired in the prefrontal cortex in schizophrenia,"* Schizophrenia research, **169**(1-3), pp. 374–380. doi:10.1016/j.schres.2015.10.042.

[256] Markusson S., Raasakka A., Schröder M., Sograte-Idrissi S., Rahimi A. M., Asadpour O., Körner H., Lodygin D., Eichel-Vogel M. A., Chowdhury R., Sutinen A., Muruganandam G., Iyer M., Cooper M. H., Weigel M. K., Ambiel N., Werner H. B., Zuchero J. B., Opazo F., and Kursula P., 2025*,"Nanobodies against the myelin enzyme CNPase as tools for structural and functional studies,"* Journal of neurochemistry, **169**(1), e16274. doi:10.1111/jnc.16274.

[257] Zhang J., and Jiao J., 2015*,"Molecular Biomarkers for Embryonic and Adult Neural Stem Cell and Neurogenesis,"* BioMed research international, **2015**, p. 727542. doi:10.1155/2015/727542.

[258] Kaneko Y., Sakakibara S., Imai T., Suzuki A., Nakamura Y., Sawamoto K., Ogawa Y., Toyama Y., Miyata T., and Okano H., 2000*,"Musashi1: an evolutionally conserved marker for CNS progenitor cells including neural stem cells,"* Developmental neuroscience, **22**(1-2), pp. 139–153. doi:10.1159/000017435.

[259] Mercurio S., Serra L., and Nicolis S. K., 2019*,"More than just Stem Cells: Functional Roles of the Transcription Factor Sox2 in Differentiated Glia and Neurons,"* International journal of molecular sciences, **20**(18). doi:10.3390/ijms20184540.

[260] Graham V., Khudyakov J., Ellis P., and Pevny L., 2003*,"SOX2 functions to maintain neural progenitor identity,"* Neuron, **39**(5), pp. 749–765. doi:10.1016/S0896-6273(03)00497-5.

[261] Bernal A., and Arranz L., 2018*,"Nestin-expressing progenitor cells: function, identity and therapeutic implications,"* Cellular and molecular life sciences CMLS, **75**(12), pp. 2177–2195. doi:10.1007/s00018-018-2794-z.

[262] Qin S., and Zhang C.-L., 2012*,"Role of Kruppel-like factor 4 in neurogenesis and radial neuronal migration in the developing cerebral cortex,"* Molecular and cellular biology, **32**(21), pp. 4297–4305. doi:10.1128/MCB.00838-12.

[263] Qin S., Liu M., Niu W., and Zhang C.-L., 2011*,"Dysregulation of Kruppel-like factor 4 during brain development leads to hydrocephalus in mice,"* Proceedings of the National Academy of Sciences of the United States of America, **108**(52), pp. 21117–21121. doi:10.1073/pnas.1112351109.

[264] Zhang F., Wang S., Cao G., Gao Y., and Chen J., 2007*,"Signal transducers and activators of transcription 5 contributes to erythropoietin-mediated neuroprotection against hippocampal neuronal death after transient global cerebral ischemia,"* Neurobiology of disease, **25**(1), pp. 45–53. doi:10.1016/j.nbd.2006.08.007.

[265] Um M., and Lodish H. F., 2006*,"Antiapoptotic effects of erythropoietin in differentiated neuroblastoma SH-SY5Y cells require activation of both the STAT5 and AKT signaling pathways,"* The Journal of biological chemistry, **281**(9), pp. 5648–5656. doi:10.1074/jbc.M510943200.

[266] Sola A., Rogido M., Lee B. H., Genetta T., and Wen T.-C., 2005*,"Erythropoietin after focal cerebral ischemia activates the Janus kinase-signal transducer and activator of transcription signaling pathway and improves brain injury in postnatal day 7 rats,"* Pediatric research, **57**(4), pp. 481–487. doi:10.1203/01.PDR.0000155760.88664.06.

[267] Porpiglia E., Hidalgo D., Koulnis M., Tzafriri A. R., and Socolovsky M., 2012*,"Stat5 signaling specifies basal versus stress erythropoietic responses through distinct binary and graded dynamic modalities,"* PLoS biology, **10**(8), e1001383. doi:10.1371/journal.pbio.1001383.

[268] Adzick N. S., 2010*,"Fetal myelomeningocele: natural history, pathophysiology, and in-utero intervention,"* Seminars in fetal & neonatal medicine, **15**(1), pp. 9–14. doi:10.1016/j.siny.2009.05.002.

[269] Nojszewski J., Schröder N. O., Clüver J., Holler J., Ahmeti H., Synowitz M., and Held-Feindt J., 2026*,"Cellular and inflammatory characteristics of patient-derived*

glioblastoma organoids during in vitro cultivation," Oncology reports, **55**(5). doi:10.3892/or.2026.9090.

[270] Estabillo L. L., Skaga E., Halldorsson S., Vik-Mo E. O., and Sandberg C. J., 2025*,"Drug resistant glioblastoma stem cells exhibit enriched stemness signatures and share extracellular matrix overexpression,"* BMC cancer, **25**(1), p. 1655. doi:10.1186/s12885-025-15163-z.

[271] Knudsen A. M., Halle B., Cédile O., Burton M., Baun C., Thisgaard H., Anand A., Hubert C., Thomassen M., Michaelsen S. R., Olsen B. B., Dahlrot R. H., Bjerkvig R., Lathia J. D., and Kristensen B. W., 2022*,"Surgical resection of glioblastomas induces pleiotrophin-mediated self-renewal of glioblastoma stem cells in recurrent tumors,"* Neuro-oncology, **24**(7), pp. 1074–1087. doi:10.1093/neuonc/noab302.

[272] Garnier D., Renoult O., Alves-Guerra M.-C., Paris F., and Pecqueur C., 2019*,"Glioblastoma Stem-Like Cells, Metabolic Strategy to Kill a Challenging Target,"* Frontiers in oncology, **9**, p. 118. doi:10.3389/fonc.2019.00118.

[273] Mattei V., Santilli F., Martellucci S., Delle Monache S., Fabrizi J., Colapietro A., Angelucci A., and Festuccia C., 2021*,"The Importance of Tumor Stem Cells in Glioblastoma Resistance to Therapy,"* International journal of molecular sciences, **22**(8). doi:10.3390/ijms22083863.

[274] Xiao T., Wei Z., and Wu M., 2026*,"Glioblastoma cell plasticity: A new paradigm in glioblastoma therapeutic resistance,"* Biochimica et biophysica acta. Reviews on cancer, **1881**(2), p. 189557. doi:10.1016/j.bbcan.2026.189557.

[275] Chédeville A. L., and Madureira P. A., 2021*,"The Role of Hypoxia in Glioblastoma Radiotherapy Resistance,"* Cancers, **13**(3). doi:10.3390/cancers13030542.

[276] Ishii A., Kimura T., Sadahiro H., Kawano H., Takubo K., Suzuki M., and Ikeda E., 2016*,"Histological Characterization of the Tumorigenic "Peri-Necrotic Niche" Harboring Quiescent Stem-Like Tumor Cells in Glioblastoma,"* PloS one, **11**(1), e0147366. doi:10.1371/journal.pone.0147366.

[277] Eckerdt F., and Platanias L. C., 2023*,"Emerging Role of Glioma Stem Cells in Mechanisms of Therapy Resistance,"* Cancers, **15**(13). doi:10.3390/cancers15133458.

[278] Auffinger B., Tobias A. L., Han Y., Lee G., Guo D., Dey M., Lesniak M. S., and Ahmed A. U., 2014*,"Conversion of differentiated cancer cells into cancer stem-like cells in a glioblastoma model after primary chemotherapy,"* Cell death and differentiation, **21**(7), pp. 1119–1131. doi:10.1038/cdd.2014.31.

[279] Angelis M. L. de, Francescangeli F., La Torre F., and Zeuner A., 2019*,"Stem Cell Plasticity and Dormancy in the Development of Cancer Therapy Resistance,"* Frontiers in oncology, **9**, p. 626. doi:10.3389/fonc.2019.00626.

[280] Johnson K. C., Anderson K. J., Courtois E. T., Gujar A. D., Barthel F. P., Varn F. S., Luo D., Seignon M., Yi E., Kim H., Estecio M. R. H., Zhao D., Tang M., Navin N. E., Maurya R., Ngan C. Y., Verburg N., Witt Hamer P. C. de, Bulsara K., Samuels M. L., Das S., Robson P., and Verhaak R. G. W., 2021*,"Single-cell multimodal glioma analyses identify epigenetic regulators of cellular plasticity and environmental stress response,"* Nature genetics, **53**(10), pp. 1456–1468. doi:10.1038/s41588-021-00926-8.

[281] Hjelmeland A. B., Wu Q., Heddleston J. M., Choudhary G. S., MacSwords J., Lathia J. D., McLendon R., Lindner D., Sloan A., and Rich J. N., 2011*,"Acidic stress promotes a glioma stem cell phenotype,"* Cell death and differentiation, **18**(5), pp. 829–840. doi:10.1038/cdd.2010.150.

[282] Gao X.-Y., Zang J., Zheng M.-H., Zhang Y.-F., Yue K.-Y., Cao X.-L., Cao Y., Li X.-X., Han H., Jiang X.-F., and Liang L., 2021*,"Temozolomide Treatment Induces HMGB1 to Promote the Formation of Glioma Stem Cells via the TLR2/NEAT1/Wnt Pathway in Glioblastoma,"* Frontiers in cell and developmental biology, **9**, p. 620883. doi:10.3389/fcell.2021.620883.

[283] Singh N., Miner A., Hennis L., and Mittal S., 2021*,"Mechanisms of temozolomide resistance in glioblastoma - a comprehensive review,"* Cancer drug resistance (Alhambra, Calif.), **4**, pp. 17–43. doi:10.20517/cdr.2020.79.

[284] Smerdi D., Moutafi M., Kotsantis I., Stavrinou L. C., and Psyrri A., 2024*,"Overcoming Resistance to Temozolomide in Glioblastoma: A Scoping Review of Preclinical and Clinical Data,"* Life (Basel, Switzerland), **14**(6). doi:10.3390/life14060673.

[285] Shen J., Zhou L., Ye K., Gong J., Wu F., Mo K., Zhu Y., Chen C., and Zhan R., 2025*,"The role of SPI1/VSIG4/THBS1 on glioblastoma progression through modulation of the PI3K/AKT pathway,"* Journal of advanced research, **71**, pp. 487–500. doi:10.1016/j.jare.2024.06.023.

[286] Gu D., Hu L., Yang K., Yuan W., Shan D., Gao J., Li J., Gimple R. C., Dixit D., Zhu Z., Li D., Wu Q., Shi Z., Wang Y., Zhao N., Yang K., Shao J., Lin F., Wang Q., Jin G., Chen Y., Qian X., Hu Z., Li C., Zhang N., You Y., Liu J., Zhang Q., Zhang J., Rich J. N., and Wang X., 2025*,"Stress-induced pro-inflammatory glioblastoma stem cells secrete TNFAIP6 to enhance tumor growth and induce suppressive macrophages,"* Developmental cell, **60**(19), 2558-2575.e6. doi:10.1016/j.devcel.2025.04.027.

[287] Esteban-Román N. F., Taddei E., Castro-Velázquez E., Villafuentes-Vidal L., Velez-Herrera A., Rubio-Osornio M., and Rubio C., 2025*,"Redox-Regulated Pathways in Glioblastoma Stem-like Cells: Mechanistic Insights and Therapeutic Implications,"* Brain sciences, **15**(8). doi:10.3390/brainsci15080884.

[288] Liu J., Xiao Q., Xiao J., Niu C., Li Y., Zhang X., Zhou Z., Shu G., and Yin G., 2022*,"Wnt/β-catenin signalling: function, biological mechanisms, and therapeutic*

opportunities," Signal transduction and targeted therapy, **7**(1), p. 3. doi:10.1038/s41392-021-00762-6.

[289] Guan R., Zhang X., and Guo M., 2020*,"Glioblastoma stem cells and Wnt signaling pathway: molecular mechanisms and therapeutic targets,"* Chinese neurosurgical journal, **6**, p. 25. doi:10.1186/s41016-020-00207-z.

[290] Latour M., Her N.-G., Kesari S., and Nurmemmedov E., 2021*,"WNT Signaling as a Therapeutic Target for Glioblastoma,"* International journal of molecular sciences, **22**(16). doi:10.3390/ijms22168428.

[291] Adamo A., Fiore D., Martino F. de, Roscigno G., Affinito A., Donnarumma E., Puoti I., Ricci Vitiani L., Pallini R., Quintavalle C., and Condorelli G., 2017*,"RYK promotes the stemness of glioblastoma cells via the WNT/ β-catenin pathway,"* Oncotarget, **8**(8), pp. 13476–13487. doi:10.18632/oncotarget.14564.

[292] Underwood M. A., Gilbert W. M., and Sherman M. P., 2005*,"Amniotic fluid: not just fetal urine anymore,"* Journal of perinatology official journal of the California Perinatal Association, **25**(5), pp. 341–348. doi:10.1038/sj.jp.7211290.

[293] Dasgupta S., Arya S., Choudhary S., and Jain S. K., 2016*,"Amniotic fluid: Source of trophic factors for the developing intestine,"* World journal of gastrointestinal pathophysiology, **7**(1), pp. 38–47. doi:10.4291/wjgp.v7.i1.38.

[294] Kirksey A., Pike R. L., and Callahan J. A., 1962*,"Some effects of high and low sodium intakes during pregnancy in the rat. II. Electrolyte concentrations of maternal plasma, muscle, bone and brain and of placenta, amniotic fluid, fetal plasma and total fetus in normal pregnancy,"* The Journal of nutrition, **77**(1), pp. 43–51. doi:10.1093/jn/77.1.43.

[295] Koski K. G., and Fergusson M. A., 1992*,"Amniotic fluid composition responds to changes in maternal dietary carbohydrate and is related to metabolic status in term fetal rats,"* The Journal of nutrition, **122**(2), pp. 385–392. doi:10.1093/jn/122.2.385.

[296] Forde B., Martin S., and Peiro J. L., 2024*,"Development and Validation of a Rodent Model of Amniotic Fluid Exchange: A Prospective Laboratory-Based Study,"* Clin. Exp. Obstet. Gynecol., **51**(8). doi:10.31083/j.ceog5108185.

[297] Mothe A. J., Zahir T., Santaguida C., Cook D., and Tator C. H., 2011*,"Neural stem/progenitor cells from the adult human spinal cord are multipotent and self-renewing and differentiate after transplantation,"* PloS one, **6**(11), e27079. doi:10.1371/journal.pone.0027079.

[298] Shihabuddin L. S., Horner P. J., Ray J., and Gage F. H., 2000*,"Adult spinal cord stem cells generate neurons after transplantation in the adult dentate gyrus,"* The Journal of neuroscience the official journal of the Society for Neuroscience, **20**(23), pp. 8727–8735. doi:10.1523/JNEUROSCI.20-23-08727.2000.

[299] Chan W. S., Sideris A., Sutachan J. J., Montoya G J. V., Blanck T. J. J., and Recio-Pinto E., 2013*,"Differential regulation of proliferation and neuronal differentiation in adult rat spinal cord neural stem/progenitors by ERK1/2, Akt, and PLCγ,"* Frontiers in molecular neuroscience, **6**, p. 23. doi:10.3389/fnmol.2013.00023.

[300] Aceves M., Tucker A., Chen J., Vo K., Moses J., Amar Kumar P., Thomas H., Miranda D., Dampf G., Dietz V., Chang M., Lukose A., Jang J., Nadella S., Gillespie T., Trevino C., Buxton A., Pritchard A. L., Green P., McCreedy D. A., and Dulin J. N., 2023*,"Developmental stage of transplanted neural progenitor cells influences anatomical and functional outcomes after spinal cord injury in mice,"* Communications biology, **6**(1), p. 544. doi:10.1038/s42003-023-04893-0.

[301] Delile J., Rayon T., Melchionda M., Edwards A., Briscoe J., and Sagner A., 2019*,"Single cell transcriptomics reveals spatial and temporal dynamics of gene expression in the developing mouse spinal cord,"* Development (Cambridge, England), **146**(12). doi:10.1242/dev.173807.

[302] Reier P. J., Perlow M. J., and Guth L., 1983*,"Development of embryonic spinal cord transplants in the rat,"* Brain research, **312**(2), pp. 201–219. doi:10.1016/0165-3806(83)90137-2.

[303] Chouly M., and Bally-Cuif L., 2024*,"Generating neurons in the embryonic and adult brain: compared principles and mechanisms,"* Comptes rendus biologies, **347**, pp. 199–221. doi:10.5802/crbiol.167.

[304] Stiefel D., Copp A. J., and Meuli M., 2007*,"Fetal spina bifida in a mouse model: loss of neural function in utero,"* Journal of neurosurgery, **106**(3 Suppl), pp. 213–221. doi:10.3171/ped.2007.106.3.213.

[305] Wei X., Li H., Miao J., Zhou F., Liu B., Di Wu, Li S., Wang L., Fan Y., Wang W., and Yuan Z., 2012*,"Disturbed apoptosis and cell proliferation in developing neuroepithelium of lumbo-sacral neural tubes in retinoic acid-induced spina bifida aperta in rat,"* International journal of developmental neuroscience the official journal of the International Society for Developmental Neuroscience, **30**(5), pp. 375–381. doi:10.1016/j.ijdevneu.2012.03.340.

[306] Evangelista A., Ruccolo L., Friuli V., Benazzo M., Conti B., and Pisani S., 2026*,"Advances in Fetal Repair of Spina Bifida Integrating Prenatal Surgery, Stem Cells, and Biomaterials,"* Biomedicines, **14**(1). doi:10.3390/biomedicines14010136.

[307] Kellert B. A., McPherson R. J., and Juul S. E., 2007*,"A comparison of high-dose recombinant erythropoietin treatment regimens in brain-injured neonatal rats,"* Pediatric research, **61**(4), pp. 451–455. doi:10.1203/pdr.0b013e3180332cec.

[308] Gonzalez F. F., Abel R., Almli C. R., Mu D., Wendland M., and Ferriero D. M., 2009*,"Erythropoietin sustains cognitive function and brain volume after neonatal stroke,"* Developmental neuroscience, **31**(5), pp. 403–411. doi:10.1159/000232558.

[309] Sollinger C., Lillis J., Malik J., Getman M., Proschel C., and Steiner L., 2017*,"Erythropoietin Signaling Regulates Key Epigenetic and Transcription Networks in Fetal Neural Progenitor Cells,"* Scientific reports, **7**(1), p. 14381. doi:10.1038/s41598-017-14366-0.

[310] Zhang H., Fang X., Huang D., Luo Q., Zheng M., Wang K., Le Cao, and Yin Z., 2018*,"Erythropoietin signaling increases neurogenesis and oligodendrogenesis of endogenous neural stem cells following spinal cord injury both in vivo and in vitro,"* Molecular medicine reports, **17**(1), pp. 264–272. doi:10.3892/mmr.2017.7873.

[311] Yu X., Shacka J. J., Eells J. B., Suarez-Quian C., Przygodzki R. M., Beleslin-Cokic B., Lin C.-S., Nikodem V. M., Hempstead B., Flanders K. C., Costantini F., and Noguchi C. T., 2002*,"Erythropoietin receptor signalling is required for normal brain development,"* Development (Cambridge, England), **129**(2), pp. 505–516. doi:10.1242/dev.129.2.505.

[312] Nekoui A., Del Carmen Escalante Tresierra V., Abdolmohammadi S., Shedid D., and Blaise G., 2015*,"Neuroprotective Effect of Erythropoietin in Postoperation Cervical Spinal Cord Injury: Case Report and Review,"* Anesthesiology and pain medicine, **5**(6), e28849. doi:10.5812/aapm.28849.

[313] Reemst K., Noctor S. C., Lucassen P. J., and Hol E. M., 2016*,"The Indispensable Roles of Microglia and Astrocytes during Brain Development,"* Frontiers in human neuroscience, **10**, p. 566. doi:10.3389/fnhum.2016.00566.

[314] Kriegstein A., and Alvarez-Buylla A., 2009*,"The glial nature of embryonic and adult neural stem cells,"* Annual review of neuroscience, **32**, pp. 149–184. doi:10.1146/annurev.neuro.051508.135600.

[315] Reis J. L., Correia-Pinto J., Monteiro M. P., Costa M., Ribeiro A., and Hutchins G. M., 2008*,"Immunocytochemical characterization of astrocytosis along the spinal cord of loop-tail/curly-tail mice with myelomeningocele,"* Pediatric neurosurgery, **44**(4), pp. 288–295. doi:10.1159/000131677.

[316] Kowitzke B., Cohrs G., Leuschner I., Koch A., Synowitz M., Mehdorn H. M., Held-Feindt J., and Knerlich-Lukoschus F., 2016*,"Cellular Profiles and Molecular Mediators of Lesion Cascades in the Placode in Human Open Spinal Neural Tube Defects,"* Journal of neuropathology and experimental neurology, **75**(9), pp. 827–842. doi:10.1093/jnen/nlw057.

[317] Schiweck J., Eickholt B. J., and Murk K., 2018*,"Important Shapeshifter: Mechanisms Allowing Astrocytes to Respond to the Changing Nervous System During Development,*

Injury and Disease," Frontiers in cellular neuroscience, **12**, p. 261. doi:10.3389/fncel.2018.00261.

[318] Badjatia N., Rossi M. J., Bataille A. R., Mittal C., Lai W. K. M., and Pugh B. F., 2021*,"Acute stress drives global repression through two independent RNA polymerase II stalling events in Saccharomyces,"* Cell reports, **34**(3), p. 108640. doi:10.1016/j.celrep.2020.108640.

[319] Himanen S. V., and Sistonen L., 2019*,"New insights into transcriptional reprogramming during cellular stress,"* Journal of cell science, **132**(21). doi:10.1242/jcs.238402.

[320] Pessa J. C., Joutsen J., and Sistonen L., 2024*,"Transcriptional reprogramming at the intersection of the heat shock response and proteostasis,"* Molecular cell, **84**(1), pp. 80–93. doi:10.1016/j.molcel.2023.11.024.

[321] Aprile-Garcia F., Tomar P., Hummel B., Khavaran A., and Sawarkar R., 2019*,"Nascent-protein ubiquitination is required for heat shock-induced gene downregulation in human cells,"* Nature structural & molecular biology, **26**(2), pp. 137–146. doi:10.1038/s41594-018-0182-x.

[322] Sawarkar R., 2022*,"Transcriptional lockdown during acute proteotoxic stress,"* Trends in biochemical sciences, **47**(8), pp. 660–672. doi:10.1016/j.tibs.2022.03.020.

[323] Hwang I., Tang D., and Paik J., 2021*,"Oxidative stress sensing and response in neural stem cell fate,"* Free radical biology & medicine, **169**, pp. 74–83. doi:10.1016/j.freeradbiomed.2021.03.043.

[324] Urbán N., 2022*,"Could a Different View of Quiescence Help Us Understand How Neurogenesis Is Regulated?,"* Frontiers in neuroscience, **16**, p. 878875. doi:10.3389/fnins.2022.878875.

[325] Elkin A. M., Robbins S., Barros C. S., and Bossing T., 2025*,"The Critical Balance Between Quiescence and Reactivation of Neural Stem Cells,"* Biomolecules, **15**(5). doi:10.3390/biom15050672.

[326] Daviaud N., Chevalier C., Friedel R. H., and Zou H., 2019*,"Distinct Vulnerability and Resilience of Human Neuroprogenitor Subtypes in Cerebral Organoid Model of Prenatal Hypoxic Injury,"* Frontiers in cellular neuroscience, **13**, p. 336. doi:10.3389/fncel.2019.00336.

[327] Urbán N., and Cheung T. H., 2021*,"Stem cell quiescence: the challenging path to activation,"* Development (Cambridge, England), **148**(3). doi:10.1242/dev.165084.

[328] Robel S., Berninger B., and Götz M., 2011*,"The stem cell potential of glia: lessons from reactive gliosis,"* Nature reviews. Neuroscience, **12**(2), pp. 88–104. doi:10.1038/nrn2978.

[329] Lattke M., and Guillemot F., 2022*,"Understanding astrocyte differentiation: Clinical relevance, technical challenges, and new opportunities in the omics era,"* WIREs mechanisms of disease, **14**(5), e1557. doi:10.1002/wsbm.1557.

[330] Balint V., Peric M., Dacic S., Stanisavljevic Ninkovic D., Marjanovic J., Popovic J., Stevanovic M., and Lazic A., 2024*,"The Role of SOX2 and SOX9 Transcription Factors in the Reactivation-Related Functional Properties of NT2/D1-Derived Astrocytes,"* Biomedicines, **12**(4). doi:10.3390/biomedicines12040796.

[331] Cao L., Wang Y., and Huang Z., 2021*,"Reversion of Injured Adult Neurons to an Embryonic State by Grafts of Neural Progenitor Cells After Spinal Cord Injury,"* Neuroscience bulletin, **37**(2), pp. 271–274. doi:10.1007/s12264-020-00584-6.

[332] Zhang Q., Wu X., Fan Y., Zhang H., Yin M., Xue X., Yin Y., Jin C., Quan R., Jiang P., Liu Y., Yu C., Kuang W., Chen B., Li J., Chen Z., Hu Y., Xiao Z., Zhao Y., and Dai J., 2025*,"Characterizing progenitor cells in developing and injured spinal cord: Insights from single-nucleus transcriptomics and lineage tracing,"* Proceedings of the National Academy of Sciences of the United States of America, **122**(2), e2413140122. doi:10.1073/pnas.2413140122.

[333] Bayin N. S., Mizrak D., Stephen D. N., Lao Z., Sims P. A., and Joyner A. L., 2021*,"Injury-induced ASCL1 expression orchestrates a transitory cell state required for repair of the neonatal cerebellum,"* Science advances, **7**(50), eabj1598. doi:10.1126/sciadv.abj1598.

[334] Zhang S., and Cui W., 2014*,"Sox2, a key factor in the regulation of pluripotency and neural differentiation,"* World journal of stem cells, **6**(3), pp. 305–311. doi:10.4252/wjsc.v6.i3.305.

[335] Gu J., Bao Y., Chen J., Huang C., Zhang X., Jiang R., Liu Q., Liu Y., Xu X., and Shi W., 2016*,"The Expression of NP847 and Sox2 after TBI and Its Influence on NSCs,"* Frontiers in cellular neuroscience, **10**, p. 282. doi:10.3389/fncel.2016.00282.

[336] Cui D.-M., Zeng T., Ren J., Wang K., Jin Y., Zhou L., and Gao L., 2017*,"KLF4 Knockdown Attenuates TBI-Induced Neuronal Damage through p53 and JAK-STAT3 Signaling,"* CNS neuroscience & therapeutics, **23**(2), pp. 106–118. doi:10.1111/cns.12633.

[337] Tóthová Z., Tomc J., Debeljak N., and Solár P., 2021*,"STAT5 as a Key Protein of Erythropoietin Signalization,"* International journal of molecular sciences, **22**(13). doi:10.3390/ijms22137109.

[338] Wu H., Chen M., Yan P., Yao Q., Fan J., Gao Z., and Wang H., 2018*,"Erythropoietin suppresses D-galactose-induced aging of rats via the PI3K/Akt/Nrf2-ARE pathway,"* International journal of clinical and experimental pathology, **11**(4), pp. 2227–2240.

[339] Kilic E., Kilic U., Soliz J., Bassetti C. L., Gassmann M., and Hermann D. M., 2005*,"Brain-derived erythropoietin protects from focal cerebral ischemia by dual activation of ERK-1/-2 and Akt pathways,"* FASEB journal official publication of the Federation of American Societies for Experimental Biology, **19**(14), pp. 2026–2028. doi:10.1096/fj.05-3941fje.

[340] Sun Y., Song B., Zhang Y., Zhang Y., and Zhou L., 2025*,"Phase-targeted erythropoietin derivatives for traumatic brain injury: bridging mechanisms to precision therapy,"* Frontiers in neurology, **16**, p. 1665405. doi:10.3389/fneur.2025.1665405.

[341] Watanabe M., Li H., Roybal J., Santore M., Radu A., Jo J.-I., Kaneko M., Tabata Y., and Flake A., 2011*,"A tissue engineering approach for prenatal closure of myelomeningocele: comparison of gelatin sponge and microsphere scaffolds and bioactive protein coatings,"* Tissue engineering. Part A, **17**(7-8), pp. 1099–1110. doi:10.1089/ten.tea.2010.0390.

[342] Watanabe M., Li H., Kim A. G., Weilerstein A., Radu A., Davey M., Loukogeorgakis S., Sánchez M. D., Sumita K., Morimoto N., Yamamoto M., Tabata Y., and Flake A. W., 2016*,"Complete tissue coverage achieved by scaffold-based tissue engineering in the fetal sheep model of Myelomeningocele,"* Biomaterials, **76**, pp. 133–143. doi:10.1016/j.biomaterials.2015.10.051.

[343] Hawes J., Gonzalez-Manteiga A., Murphy K. P., Sanchez-Petidier M., Moreno-Manzano V., Pathak B., Lampe K., Lin C.-Y., Peiro J. L., and Oria M., 2024*,"Noggin-Loaded PLA/PCL Patch Inhibits BMP-Initiated Reactive Astrogliosis,"* International journal of molecular sciences, **25**(21). doi:10.3390/ijms252111626.

[344] Athiel Y., Cariot L., Jouannic J.-M., Maillet C., Mauffré V., Adam C., Huet H., Larghero J., Nasone J., and Guilbaud L., 2024*,"Safety and efficacy of human umbilical cord-derived mesenchymal stromal cells in fetal ovine myelomeningocele repair,"* Stem cell research & therapy, **15**(1), p. 444. doi:10.1186/s13287-024-03991-y.

[345] Assunção Silva R. C., Pinto L., and Salgado A. J., 2022*,"Cell transplantation and secretome based approaches in spinal cord injury regenerative medicine,"* Medicinal research reviews, **42**(2), pp. 850–896. doi:10.1002/med.21865.

[346] Blando S., Anchesi I., Mazzon E., and Gugliandolo A., 2022*,"Can a Scaffold Enriched with Mesenchymal Stem Cells Be a Good Treatment for Spinal Cord Injury?,"* International journal of molecular sciences, **23**(14). doi:10.3390/ijms23147545.

[347] Farmer D. L., Kumar P., Reynolds E., Lee S. Y., Powne A. B., Pivetti C. D., Zwienenberg M., McLennan A. S., Nolta J. A., Brown E. G., Saadai P., Hirose S., and Wang A., 2026*,"Feasibility and safety of cellular therapy for in-utero repair of myelomeningocele (CuRe Trial): a first-in-human, phase 1, single-arm study,"* Lancet (London, England), **407**(10531), pp. 867–875. doi:10.1016/S0140-6736(25)02466-3.

[348] Hakimi O., Mouthuy P.-A., and Carr A., 2013*,"Synthetic and degradable patches: an emerging solution for rotator cuff repair,"* International journal of experimental pathology, **94**(4), pp. 287–292. doi:10.1111/iep.12030.

[349] FitzGerald J. F., and Kumar A. S., 2014*,"Biologic versus Synthetic Mesh Reinforcement: What are the Pros and Cons?,"* Clinics in colon and rectal surgery, **27**(4), pp. 140–148. doi:10.1055/s-0034-1394155.

[350] Tatu R. R., Oria M., Rao M. B., Peiro J. L., and Lin C.-Y., 2022*,"Biodegradation of poly(L-lactic acid) and poly(ε-caprolactone) patches by human amniotic fluid in an in-vitro simulated fetal environment,"* Scientific reports, **12**(1), p. 3950. doi:10.1038/s41598-022-07681-8.

[351] Benabdderrahmane K., Stirnemann J., Ramtani S., and Falentin-Daudré C., 2025*,"Biodegradation study in FBS media of polycaprolactone patch as a potential prenatal treatment for myelomeningocele,"* Journal of biomaterials applications, **39**(9), pp. 1097–1114. doi:10.1177/08853282251316894.

[352] Hourston D. J., 2016, Degradation of Plastics and Polymers, *Reference Module in Materials Science and Materials Engineering*, Elsevier. doi:10.1016/B978-0-12-803581-8.01658-1.

[353] Srinivasan A., Murugesan S., and Mahendran A. R., 2022. *Progress in Polymer Research for Biomedical, Energy and Specialty Applications*, CRC Press, Boca Raton.

[354] Alassaf M., Alqahtani S. M., Al Khulaifi R. S., Saeed W. S., Alsubaie F. S., Semlali A., and Aouak T., 2023*,"Mevacor/Poly(vinyl acetate/2-hydroxyethyl methacrylate) as Solid Solution: Preparation, Solubility Enhancement and Drug Delivery,"* Polymers, **15**(19). doi:10.3390/polym15193927.

[355] Gonzalez Novoa G. A., Heinämäki J., Mirza S., Antikainen O., Colarte A. I., Paz A. S., and Yliruusi J., 2005*,"Physical solid-state properties and dissolution of sustained-release matrices of polyvinylacetate,"* European journal of pharmaceutics and biopharmaceutics official journal of Arbeitsgemeinschaft fur Pharmazeutische Verfahrenstechnik e.V, **59**(2), pp. 343–350. doi:10.1016/j.ejpb.2004.07.012.

[356] Wacker Chemie AG*,"Vinnapas:* Brochures," https://www.wacker.com/cms/de-de/products/brands/vinnapas/vinnapas.html.

[357] Patra C. N., Priya R., Swain S., Kumar Jena G., Panigrahi K. C., and Ghose D., 2017*,"Pharmaceutical significance of Eudragit: A review,"* Future Journal of Pharmaceutical Sciences, **3**(1), pp. 33–45. doi:10.1016/j.fjps.2017.02.001.

[358] Boop F. A., and Chadduck W. M., 1991*,"Silastic duraplasty in pediatric patients,"* Neurosurgery, **29**(5), 785-7; discussion 788. doi:10.1097/00006123-199111000-00026.

A. Appendix

A.1 Publications and other contributions related to this thesis

This dissertation consists partly of previously published work of the following two publications:

Hellmold, D.*, Johanning, L.*, **Clüver, J.***, Holler, J., Schröder, N.O., Bayler, F., Ahmeti, H., Kubelt-Kwamin, C., Wieker, S., Helmers, A., Synowitz, M., Held-Feindt, J., Effect of focused ultrasound-induced mechanical ablation on stemness and dormancy properties of residual/peri-focally localized glioblastoma cells, *Neuro-Oncology Advances*, Vol. 7,1 (2025), doi:10.1093/noajnl/vdaf184

* these authors contributed in equal measure

Own contribution presented in this article:
I was closely involved in planning the publication in consultation with Prof. Dr. Dr. Janka Held-Feindt and Dr. Dana Hellmold. I collected and analyzed the data described in this dissertation, which includes cell and GBO culture, as well as the conduction and analysis of the aforementioned assays. Together with Dr. Dana Hellmold the visuals and figures were prepared, respectively, in equal measure, partially supported by Levi Johanning and in consultation with Prof. Dr. Dr. Janka Held-Feindt. The draft was written by Prof. Dr. Dr. Janka Held-Feindt in coordination with all first authors, and reviewed as well as edited by all corresponding authors in equal measure.

Knerlich-Lukoschus, F.*, **Clüver, J.*,** Manczuk, I., Bayler, F., Hellmold, D., Synowitz, M., Held-Feindt, J., Neuroprotective properties of erythropoietin (Epo) and its receptor (EpoR) in open spinal dysraphism (OSD): an investigation of EpoR expression in a rat OSD model, along with *in vitro* studies on the neuroprotective effects of Epo on rat spinal cord-derived neural progenitor cells. *Childs Nerv Syst,* Vol. 41,1 358 (2025), doi: 10.1007/s00381-025-07032-8

* these authors contributed in equal measure

Own contribution presented in this article:

The conceptualization and planning of this article was conducted by me together with Prof. Dr. Friederike Knerlich-Lukoschus and Prof. Dr. Dr. Janka Held-Feindt. I collected and analyzed the data described in this dissertation, which includes all *in vitro* cell experiments, as well as the analysis of the aforementioned experiments, in close consultation with Prof. Dr. Dr. Janka Held-Feindt. The corresponding sections of the article were written by me in close consultation with Prof. Dr. Dr. Janka Held-Feindt. The visualizations were prepared by me, Prof. Dr. Friederike Knerlich-Lukoschus and Dr. Dana Hellmold. The collection of additional data gathered and presented in the publication was supervised in part by me in collaboration with Prof. Dr. Dr. Janka Held-Feindt and was carried out in close consultation with Prof. Dr. Friederike Knerlich-Lukoschus. The manuscript was written by Prof. Dr. Friederike Knerlich-Lukoschus in collaboration with me and Prof. Dr. Dr. Janka Held-Feindt, as well as reviewed by all corresponding authors.

Additional publications partially related to this thesis:

Nojszewski, J. Schröder, N.O., **Clüver, J**., Holler, J., Ahmeti, H., Synowitz, M., Held-Feindt, J., Cellular and inflammatory characteristics of patient-derived glioblastoma organoids during *in vitro* cultivation. *Oncology reports,* Vol. 55,5 85 (2026), doi:10.3892/or.2026.9090

Own contribution: assistance in preparation of experiments and data analysis

Bayler, F., Holler, J., **Clüver, J.**, Johanning, L., Hellmold, H., Schröder, N.O., Nojszewski, J., Ahmeti, H., Kubelt-Kwamin, C., Synowitz, M., Held-Feindt, J., Focused Ultrasound-Induced Mechanical Ablation Affects the Carbohydrate Metabolism of Residual/Peri-Focally Localized Glioblastoma Cells. *International journal of cancer*, (2026), doi:10.1002/ijc.70483

Own contribution: Assistance in preparation of experiments, data analysis and the revision process. Preparation of the Graphical Abstract.

Additional conference contributions related to this thesis (Poster presentations)

- Holler J, Hellmold D, **Clüver J**, Ahmeti H, Kubelt C, Wieker S, Helmers A-K, Synowitz M, Held-Feindt J (2024) Region-dependent expression of key molecules of tumor metabolism after focused ultrasound-induced mechanical ablation - an investigation in glioblastoma organoids and primary cell. Brain Tumor Meeting 2024, 23.-24. Mai 2024, Berlin, Abstract Book p. 27, poster 10.

- **Clüver J**, Hellmold D, Ahmeti H, Kubelt C, Wieker S, Helmers A-K, Synowitz M, Held-Feindt J (2024) Impact of focused Ultrasound-induced mechanical ablation on the Stemness and Dormancy Characteristics of residual/peri-focally located Glioblastoma Cells. Brain Tumor Meeting 2024, 23.-24. Mai 2024, Berlin, Abstract Book p. 28, poster 11.
- Knerlich-Lukoschus F*, Manczuk I*, Hellmold D, **Clüver J**, Synowitz M, Held-Feindt J (2024) Investigation of Erythropoietin (EPO) and its receptor (EPOR) in relation to hypoxia inducible factors, cellular and neural progenitor markers in neuroplacodes obtained from fetal time points in a retinoic acid-induced myelomeningocele (mmc) rat model. 50th Annual Meeting of the International Society for Pediatric Neurosurgery, ISPN 2024, Toronto. Childs Nerv Syst (2024), pp 283 (Poster). doi: 10.1007/s00381-024-06562-x.
  **shared first authorship*
- Manczuk I*, Knerlich-Lukoschus F*, Hellmold D, **Clüver J**, Synowitz M, Held-Feindt J (2024) Fetal expression profiles of Erythropoietin (EPO) and its receptor (EPOR) in the neuroplacodes in a retinoic acid-induced myelomeningocele rat model. 75. Jahrestagung der Deutschen Gesellschaft für Neurochirurgie. Conventus Congressmanagement & Marketing GmbH, Jena. ISBN: 978-3-948023-38-6. URN: urn:nbn:de:101:1-2406050947223.933641293237. p208 (Vortrag)
  **shared first authorship*

Neuro-Oncology Advances

1

7(1), vdaf184, 2025 | https://doi.org/10.1093/noajnl/vdaf184 | Advance Access date 30 August 2025

Effect of focused ultrasound-induced mechanical ablation on stemness and dormancy properties of residual/peri-focally localized glioblastoma cells

Dana Hellmold[†], Levi Johanning[†], Jacqueline Clüver[†], Jonna Holler, Nils Oliver Schröder, Frieda Bayler, Hajrullah Ahmeti, Carolin Kubelt-KwaminSina Wieker, Ann-Kristin Helmers, Michael Synowitz, and Janka Held-Feindt[*]

All author affiliations are listed at the end of the article
[†]These authors contributed equally to this work.

[*]**Corresponding Author.** Janka Held-Feindt, PhD, MD, Department of Neurosurgery, University Medical Schleswig-Holstein (UKSH), Campus Kiel, Arnold-Heller-Str. 3, House D, 24105 Kiel, Germany (Janka.Held-Feindt@uksh.de).

Abstract

Background. Focused ultrasound (FUS) is a new technology that enables the spatially and temporally precise delivery of ultrasound energy to various targets. In addition to its known applications in treating tumors, cavitation-based mechanical focused ultrasound (mFUS) is gaining importance. Due to the novelty of this technique, little is known about the effects of mFUS on peri-focally localized or surviving tumor cells. Glioblastomas (GBMs) are highly malignant intracranial tumors with a pronounced intra- and intertumoral heterogeneity, which, eg leads to their evasion of appropriate treatment regimens.

Methods. The impact of mFUS was investigated in patient-derived GBM organoids (GBOs), glioma stem-like cells (GSCs), and differentiated GBM cells in an in vitro 3D hydrogel culture model. Particular attention was paid to investigating the stemness and dormancy properties of residual/peri-focally localized GBM cells, as these may be important for tumor progression.

Results. In GBOs and different primary cells, increased expression of dormancy- and stemness-associated markers was found in a complex region- and marker-dependent manner mediated via PI3-kinase/Akt/GSK3β signaling, suggesting an effect of mFUS beyond the focal area. mFUS resulted in an increased ability of residual/peri-focal, formerly differentiated patient-derived GBM cells to form stem cell-typical spheres associated with increased expression of various dormancy and stemness markers. Residual/peri-focal patient-derived cells were characterized by a higher resistance to temozolomide, resulting in fewer dead cells compared to temozolomide treatment alone.

Conclusion. The ablation of defined regions by mFUS appears to regulate the stemness and dormancy properties of the residual/peri-focally localized GBM cells in a region-specific manner.

Key Points

- Mechanical FUS is a relevant future therapy for treating brain tumors.
- Presentation of an in vitro mechanical FUS organoid/3D cell model.
- Mechanical FUS regulates dormancy/stemness properties of residual GBM cells.

Focused ultrasound (FUS) is a new technology that enables spatially and temporally precise delivery of ultrasound energy. Various FUS effects using continuous (cFUS) or pulsed ultrasound (pFUS) are used for therapeutic purposes. Here, cFUS provides a localized increase in temperature above 43 °C to induce permanent tissue necrosis or thermal lesions in the focal area of the transducers.[1,2] In comparison, pFUS mediates a nonthermal mechanism, the so-called cavitation effect.[3]

© The Author(s) 2025. Published by Oxford University Press, the Society for Neuro-Oncology and the European Association of Neuro-Oncology.
This is an Open Access article distributed under the terms of the Creative Commons Attribution License (https://creativecommons.org/licenses/by/4.0/), which permits unrestricted reuse, distribution, and reproduction in any medium, provided the original work is properly cited.

Importance of the Study

Ablation with mechanically focused ultrasound (mFUS) is considered an important future therapy for the treatment of malignant brain tumors. This study is the first to demonstrate the effects of mFUS on the dormancy and stemness properties of surviving or peri-focally localized glioblastoma (GBM) cells. Since commercially available in vivo mFUS systems for mechanical ablation of brain tumors in rodents are limited, the studies were performed in an in vitro mFUS setup using patient-derived GBM organoids, glioma stem-like cells (GSCs), and differentiated GBM cells. Dormancy- and stemness-associated molecules were regulated by mFUS in a complex region- and marker-dependent manner, and the residual/peri-focal GBM cells exhibited enhanced characteristics of GSCs. As mFUS represents an important future therapeutic option and dormancy and stemness properties may play a central role in tumor progression, the results may provide a basis for a better understanding of the clinically relevant effects of mFUS in GBMs.

The cavitation effect describes the formation, growth, and collapse of gas-filled bubbles in liquids under the influence of an ultrasonic field.[3] In the so-called stable cavitation at low sound intensity, the bubbles exist over several cycles, oscillate, and maintain a stable resonance size. In contrast, inertial cavitation at high sound pressure describes bubbles that exist for only a few cycles, as they regularly collapse.[3] The oscillation and collapse of bubbles under the influence of pFUS lead to an abrupt release of energy and generation of oxygen species, shock waves, and microjets, disrupting the cell membrane and ablating the surrounding tissue structure.[3–6] Therefore, this FUS mechanism is also called high-intensity mechanical FUS (mFUS). Since mFUS is characterized by less thermal energy deposition, which protects the surrounding healthy tissue,[7,8] it is also becoming increasingly important in medical therapy. Recent research has shown that mFUS is a promising mechanism for treating malignant brain tumors and is a relevant future therapy.[4,5,7]

Glioblastomas (GBM) are highly malignant primary intracranial tumors characterized by rapid progression and poor patients' prognosis due to frequent relapses and resistance to chemo- and radiotherapy.[9,10] Indeed, subpopulations with stem cell characteristics, so-called glioma stem-like cells (GSCs), which are slowly cycling, have tumorigenic potential, are pluripotent and show high resistance to chemotherapy, as well as dormant tumor (single) cells, which reversible enter a resting state (cellular dormancy) to escape from (chemo)therapeutic treatment, are closely associated with the aggressiveness of GBMs.[11–15] Dormant and tumor stem-like cells share some similarities,[16,17] can wax and wane depending on environmental conditions, may increase the aggressive potential of GBMs, and may trigger GBM recurrence.[11–13,18]

Despite these challenges, recent studies have demonstrated successful transmission of ultrasound waves for thermoablation of GBMs.[19,20] In addition, the opening of the blood–brain barrier by low-intensity FUS or the activation of chemical compounds known as sonosensitizers, which lead to cell death (sonodynamic therapy), has been extensively studied.[7,19,21] Regarding the potential use of mFUS in GBM, Sukovich et al. have shown in a first in vivo study that a homemade mechanical ablation device can produce well-defined lesions in the porcine cerebral cortex after partial craniectomy.[22] Furthermore, a team of researchers at the University of Michigan recently developed a transcranial MR-guided mFUS system. It successfully created target lesions in 2 ex vivo porcine brains encased in a human skull without causing major hemorrhage or edema. Moreover, they started to evaluate the transcranial mFUS parameters required to study mouse brain tumor models.[23–25] However, due to significant attenuation and deviations in the passage of ultrasound through the skull,[5] current commercially available in vivo mFUS systems can only be used for mechanical ablation of brain tumors with reservations and require further development.

Accordingly, given the pronounced cell heterogeneity and high cellular adaptability of GBMs, it is clear that further studies are urgently needed to better understand this technique's biological impact. Thus, this study investigates the effects of mFUS on patient-derived glioblastoma organoids (GBOs) and primary GBM cells as a novel therapeutic approach in an in vitro 3D hydrogel culture model. Since the stemness and dormancy properties of GBM cells may play a central role in tumor progression,[11–15] a particular focus was placed on investigating the effect of mFUS on these properties in peri-focally localized or surviving tumor cells.

Materials and Methods

Preparation of Patient-derived Glioblastoma Organoids/Tumoroids

Patient-derived glioblastoma organoids/tumoroids (GBOs) were prepared according to the protocol published by Jacob et al.[26] Human GBM tissue samples were obtained directly from surgical resections performed by the Department of Neurosurgery (University Medical Center Schleswig-Holstein, Kiel, Germany), with the approval of the Ethics Committee of the University of Kiel, Germany, after the written informed consent of donors (file reference: D524/17) and following the Helsinki Declaration of 1975. According to World Health Organization (WHO) criteria, the tissue samples were diagnosed and classified by a neuropathologist as IDH wild-type GBMs, CNS WHO grade 4 (University Medical Center Hamburg-Eppendorf, UKE, Hamburg, Germany).

The GBOs were cultured in ultra-low attachment 6-well plates (Corning, NY, USA) with GBO medium (consisting of 50% DMEM/F12 (Thermo Fisher Scientific, Waltham, MA, USA), 50% Neurobasal medium (Thermo Fisher Scientific), GlutaMAX™, nonessential amino acids (NEAAs; Thermo Fisher Scientific), penicillin–streptomycin, N2 and B27 supplements without vitamin A (Thermo Fisher Scientific), 2-mercaptoethanol (Thermo Fisher Scientific), and human insulin (Sigma–Aldrich, St. Louis, MO, USA; Merck Millipore)) without growth factors or fetal calf/horse serum as described.[26] The plates were incubated on an orbital shaker (#8012-1771, Binder GmbH, Tuttlingen, Germany) at 120 rpm in a humidified incubator at 37 °C and 5% CO_2. The GBOs replicated the intra- and intertumoral heterogeneity of GBMs in terms of histological characteristics, cellular variety, and gene expression patterns of the original tumors (Figure 1A-C).

Cultivation of Patient-derived Primary Glioblastoma Cells

Patient-derived primary GBM cells and GSCs were obtained by dissociating tumor material collected during surgical procedures performed at the Department of Neurosurgery, University Medical Center Schleswig-Holstein, Kiel, Germany. The process was approved by the University of Kiel's ethics committee (file reference: D524/17), with written informed consent from donors, and adhered to the 1975 Declaration of Helsinki principles. The isolated GBM cells were cultured in DMEM (Thermo Fisher Scientific) supplemented with 10% (v/v) fetal bovine serum (FBS, Thermo Fisher Scientific) following previously established protocols.[27] GSCs were maintained under stem-like conditions in F12 media supplemented with B27 supplement (Thermo Fisher Scientific), 2 mM L-glutamine, and 1% penicillin–streptomycin (10,000 U/mL). Epidermal growth factor (Peprotech, Cranbury, NJ, USA) and basic fibroblast growth factor (Immunotools, Friesoythe, Germany) were added at a concentration of 10 ng/mL as described before.[27] GSCs were identified by their ability to form neurospheres, survive and proliferate under stem cell conditions, and differentiate into more mature cell types, as previously validated.[13,28,29] The purity of different primary cells was confirmed through immunostaining with cell type-specific markers and by ensuring the absence of mycoplasma contamination.

3D Hydrogel GBO/Cell Cultures for In Vitro mFUS Application

For the 3D hydrogel cultures, VitroGel IKVAV-Hydrogel (The Well Bioscience, Monmouth Junction, NJ, USA) was used at a 1:5 dilution (stiffness corresponds to brain stiffness[30]) and was prepared according to the manufacturer's protocol. To apply an in vitro mFUS treatment, the 3D hydrogel GBO/cell cultures were prepared directly in Covaris tubes (1 mL; Covaris LLC., Woburn, MA, USA) suitable for the in vitro mFUS setup. The hydrogel was prepared in Eppendorf tubes (Sarstedt; 1.5 mL; PP 72.690.300, Nürnbrecht, Germany) by mixing the dilution solution type I (The Well Bioscience) with IKVAV-hydrogel in a 1:5 dilution, which was then incubated for 10 min at room temperature (RT).

In the case of GBO 3D hydrogel cultures, approximately 30 GBOs were transferred into the Covaris tube, and any transferred medium was aspirated from the GBOs. The GBO medium was mixed in a ratio of 4:1 v/v with the hydrogel and then transferred onto the GBOs in the Covaris tubes. After 5 min at RT, the hydrogel began to polymerize, allowing the GBOs to be adjusted and positioned within the gel. The tubes were covered with Parafilm (Amcor, Zürich, Switzerland) and incubated at 37 °C with 5% CO_2 for 45 min. After polymerization, the hydrogel was carefully covered with GBO medium and cultured for another 24 h before mFUS application. The GBO medium was renewed directly before mFUS treatment.

In the case of 3D hydrogel cell cultures, the Covaris tubes and the IKVAV-hydrogel solution were prepared as described above. Depending on the cell type used, a cell suspension containing 24×10^6 cells/ml in the respective growth media containing 5× critical growth factors was prepared. The cell suspension was added to the hydrogel solution in a 4:1 (v/v) ratio. The hydrogel–cell mixture was then transferred into the Covaris tubes. The tubes were covered with Parafilm (Amcor) and incubated at 37 °C with 5% CO_2 for 45 min. After polymerization, the hydrogel was carefully covered with the respective growth medium containing 1× of the critical growth factors and cultured for another 24 h before mFUS application. The medium was renewed directly before mFUS treatment.

In Vitro Mechanical Focused Ultrasound Setup

The M220 ultrasound generator with a 0.5-MHz solid-state ultrasound transducer and geometrically focused acoustic energy was used (Covaris LLC.; https://www.covaris.com/technology/afa-technology). The instrument was initially developed as a platform for fast and highly efficient FUS-induced mechanical preanalytical preparation of diverse biological samples. As defined by Covaris, the system generates a wavelength of only a few millimeters, which allows ultrasound energy to be focused in a focal zone within a sample vessel immersed in a water bath. Through local pressure fluctuations, focused ultrasonic energy bursts control the generation and collapse of millions of cavitation bubbles within the sealed sample vessel in an isothermal, noncontact environment that avoids thermal molecular damage. As defined by Covaris, in this process, the cavitation bubbles oscillate or grow to a critical size and then collapse, creating hydrodynamic shear stresses in the sample. The system allows (i) customization of the peak incident power (PIP, W), duty cycle (DF, %), cycles per burst (CPB, number), and duration (s) to match the AIP (W) of required mFUS settings while maintaining constant temperature conditions; and (ii) insertion of spherical reaction vessels of appropriate size (up to 1 ml).

The validation of the in vitro mFUS setup was performed by addressing several points: First, we showed that mFUS with high acoustic pressure under constant temperature conditions (average incident power [AIP] 1 W: PIP 10 W, DF 10%, CPB 100, 10 s; AIP 5 W: PIP 35 W, DF 15%, CPB 150, 10 s; AIP 11 W: PIP 55 W, DF 20%, CPB 200, 10 s; AIP

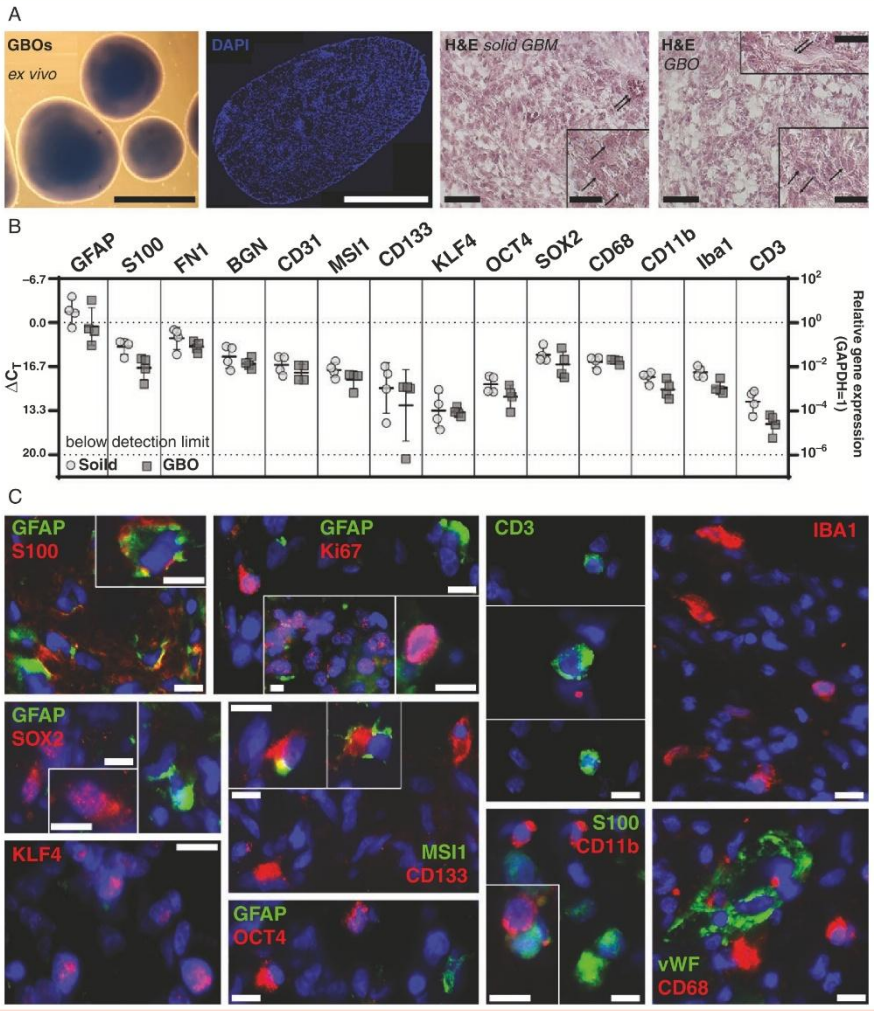


Figure 1. GBOs replicate the intra- and intertumoral heterogeneity in histological characteristics, cellular variety, and gene expression patterns of the freshly original tumors. (A) GBOs grown as vital cultures in vitro for 2 weeks (left), and after preparation of histological sections, followed by nuclear staining with DAPI (middle) or H&E staining compared to the corresponding solid parental tumor (right; single arrows point to individual tumor cells, double arrows point to vascular structures). (B) Comparison of the mRNA expression of various cell type-specific markers between *n*=4 independent GBO preparations and the corresponding parental tumors. BGN, biglycan; CD, cluster of differentiation. Significances between different stimulations were determined using an ordinary one-way ANOVA test followed by a Tukey's multiple comparison test; no significances were detected due to the heterogeneity of the GBO preparations. (C) Immunofluorescence staining of GBOs with cell type-specific markers. DAPI, 4',6-diamidino-2-phenylindole; FN1, fibronectin 1; GAPDH, glyceraldehyde-3-phosphate dehydrogenase; GFAP, glial fibrillary acidic protein; IBA1, calcium-binding adapter molecule 1; Ki67, Kiel67 (proliferation); KLF4, Krüppel-like factor 4; MSI1, Musashi (Drosophila) homolog 1; OCT4, octamer binding transcription factor 4; SOX2, sex-determining region Y-box 2; vWF, von-Willebrand-factor. Bar: 1 mm (A, left), 0.5 mm (A, middle); 100 µm (A right; inserts 20 µm); others (C) 20 µm.

15 W: PIP 75 W, DF 20%, CPB 200, 10 s; pulse repetition frequency (PRF) of 300-350 Hz corresponded to preclinical studies using mechanical ablation for, eg liver tumors[4–6]) led to (macroscopically visible) defects in the focal area of exemplary agarose samples, as well as in GBM cells grown as a cellular network and GBOs, both embedded in hydrogels (Figure 2A). Next, when mFUS settings with increasing AIP were used, increasing numbers of dying GBM cells were detectable 24 h after mFUS (Figure 2B), regardless of whether pure cultures of patient-derived GSCs or more differentiated primary GBM cells were used. Here, the individual cultures reacted to varying degrees, so no consistently increased sensitivity of a specific cell population could be observed. In addition, pronounced expression of activated/cleaved (c)Caspase 3 as a cell death marker was observed in the residual cells, as illustrated for GBOs, predominantly near the focal region compared to more distant regions (AIP 11 W, 24 h after mFUS) (Figure 2C). Furthermore, since mFUS facilitates an abrupt release of energy, generating shear stress and reactive oxygen species (ROS),[3–6] we examined whether we could detect ROS formation in our in vitro mFUS setup. Due to ROS's short-lived nature, we indirectly examined ROS formation by detecting lipid oxidation resulting from the cells' contact with ROS molecules through immunofluorescence staining of malondialdehyde (MDA; methodical details see below). MDA forms a degradation product of lipid hydroperoxides generated by the reaction of polyunsaturated fatty acids with ROS or free radicals.[31] After validating the specificity of MDA staining (induction of ROS without mFUS by applying Menadione for 1 h in more differentiated GBM cells [1 M, dissolved in ethanol, #M57405, Sigma–Aldrich]), we demonstrated that ROS was generated in GBOs in our mFUS setup (AIP 11 W, 24 h after mFUS) (Figure 2D). Finally, we analyzed the regulation of ion channels (mechanoreceptors) following mFUS (AIP 15 W, 24 h after mFUS), focusing on piezo-type mechanosensitive ion channel component 1 (Piezo1), transient receptor potential canonical (Trpc) 1 and 6, transient receptor potential polycystic 2 (Trpp2), and transient receptor potential cation channel subfamily M member 4 (Trpm4), which are known to be affected by FUS-mediated shear stress, ultimately leading to changes in membrane permeability.[32] Indeed, increased expression of mechanoreceptors was detected after mFUS, as demonstrated in both patient-derived, pure GSCs and more differentiated GBM cell cultures. Whereas GSCs responded to mFUS treatment with an increased expression of all investigated mechanoreceptors (focal area and peri-focally), more differentiated GBM cells were mainly characterized by an upregulation of Trpp2 and Trpm4 (focal area and peri-focally) (Figure 2E).

Quantitative Polymerase Chain Reaction

To assess regional differences in gene expression profiles of GBOs or GBM cell cultures after mFUS treatment (AIP 11 or 15 W), the respective 3D hydrogel GBO/cell cultures were snap-frozen in liquid nitrogen and carefully removed from the Covaris tubes for sectioning. This procedure ensured that the orientation of the sample remained intact, allowing regional analysis of the mFUS-treated samples. Serial sections of the whole sample were prepared using a cryostat (#CM 1100, Leica Biosystems, Nussloch, Germany) at a consistent temperature of –20 °C to enable RNA isolation and immunofluorescence (see below) of sections from focal and peri-focal regions (center and margin). In the case of the GBOs, 100 sections each were pooled for the margin and the center, and in the case of the primary cells, 190 sections each were pooled for the margin and center and used for RNA processing, respectively.

RNA from the different samples was extracted using TRIzol® reagent (Invitrogen, Carlsbad, CA, USA) or the ARCTURUS® PicoPure® RNA isolation kit (Applied Biosystems, Foster City, CA, USA) according to the manufacturer's instructions. DNase digestion, cDNA synthesis, reverse transcription, and qPCR were performed as described before[13,27–29] using TaqMan primer probes (Applied Biosystems). Gene-specific primers and probes are listed in Supplementary Table 1. Cycles of threshold (C_T) were determined, and the ΔC_T values of each sample were calculated as $C_{T\text{gene of interest}} - C_{T\text{ glyceraldehyde-3-phosphate dehydrogenase (GAPDH)}}$. Samples with undetectable expression were excluded from mean expression calculations. The figures display either ΔC_T or linearized ΔC_T values ($2 - \Delta C_T$). The regulation of gene expression upon stimulation/treatment is shown as relative gene expression, calculated as n-fold expression changes = $2\Delta C_T$ control – ΔC_T stimulus.

Immunofluorescence

For staining, cryostat sections were incubated with primary antibodies overnight at 4 °C, followed by incubation with secondary antibodies for 1 h at 37 °C and nuclei staining as described before.[13,28] The embedded slides were analyzed by fluorescence microscopy (AxioObserver.Z1; Carl Zeiss AG, Oberkochen, Germany) using the ZEN 3.5 (blue edition) software (Carl Zeiss AG). The primary antibodies used are listed in Supplementary Table 2. If primary antibodies were derived from the same species, nonspecific binding was blocked with species-specific $F_{(ab)}$ fragments (1:1000, from Jackson ImmunoResearch, West Grove, PA, USA). For negative controls, primary antibodies were omitted. Secondary antibodies were donkey anti-mouse or anti-rabbit IgG labeled with Alexa Fluor 488 or Alexa Fluor 555 (1:1000; Thermo Fisher Scientific). Double-positive cells were quantified manually by counting the number of cells positive for both markers, and assessing the absolute cell count in 2 to 7 GBOs for 2 independent GBO preparations for each region examined. Afterward, the mean values and standard deviations were calculated.

Cytotoxicity Assay

After mFUS treatment, the cells were recovered from the 3D hydrogels using the Cell Recovery Solution (The Well Bioscience) according to the manufacturer's protocol and subjected to further analysis. The cytotoxic effects were assessed using the CytoTox-Fluor™ Cytotoxicity Assay (Promega, Madison, WI, USA) according to the manufacturer's instructions and as described.[11,13] Supernatants from treated and control cells were collected

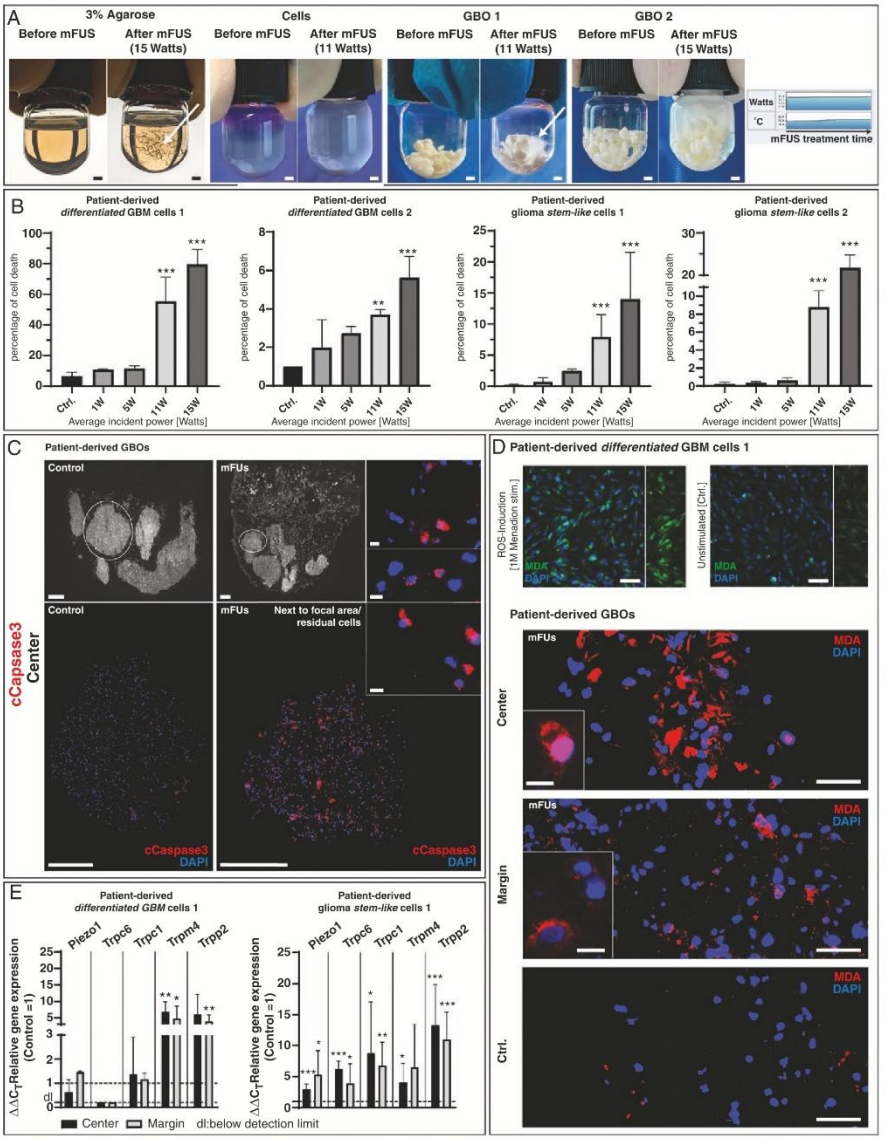


Figure 2. (A) Mechanical focused ultrasound (mFUS) resulted in visible agarose lesions and increased destruction in GBOs- or GBM cells-containing samples while temperature and wattage remained constant (white arrows point to destroyed agarose/GBOs in the focal area after mFUS). Bar: 1 mm. (B) mFUS settings with increasing average incident power resulted in increasing numbers of dead cells in pure cultures of patient-derived, more differentiated GBM cells and GSCs. The individual cultures reacted to varying degrees, so no consistently increased sensitivity of a specific cell population could be observed. $n = 3$ biological replicates of individual cell preparations with $n = 1$-2 technical replicates each; the significances between different stimulations were determined using an ordinary one-way ANOVA test followed by a Tukey's multiple comparison test (** $P < 0.01$; *** $P < 0.001$). Error bars correspond to the standard deviation. (C) mFUS-treated (average incident power 11 W) GBO-containing samples cultured for 24 h after mFUS and cryofixed were serially sectioned. Immunofluorescence staining was performed with cCapase3 (cell death marker). cCaspase3 appeared predominantly in mFUS-treated samples compared to the untreated control. Bar: 0.4 mm

(whole sections), 400 µm (GBO samples), 10 µm (inserts). Circled GBOs in whole sections show those GBOs that were visualized in detail in the immunofluorescence. (D) Determination of ROS after mFUS (average incident power 11 W) by MDA immunofluorescence staining. After validation of the specificity of MDA staining (induction of ROS without mFUS by 1-hour administration of Menadione (1 M) in pure cultures of more differentiated GBM cells), ROS generation after mFUS could be detected in GBO-containing samples to a significantly higher extent than in untreated control samples. Bar: 50 µM (overviews), 10 µm (inserts). (E) mRNA expression of ion channels (mechanoreceptors) following mFUS (average incident power 15 W) in pure cultures of patient-derived, more differentiated GBM cells and GSCs, focusing on piezo-type mechanosensitive ion channel component 1 (Piezo1), transient receptor potential canonical (Trpc) 1 and 6, transient receptor potential polycystic 2 (Trpp2), and transient receptor potential cation channel subfamily M member 4 (Trpm4). Increased expression of mechanoreceptors of all (GSCs) or Trpm4 and Trpp2 (more differentiated GBM cells) was detected after mFUS compared to individual, average unstimulated controls (control = 1); $n = 1$-2 biological replicates with $n = 1$-2 technical replicates each. Significant differences compared to the untreated control were determined by a nonpaired *t*-test and are indicated directly above the bars (* $P < 0.05$; ** $P < 0.01$; *** $P < 0.001$). Error bars correspond to the standard deviation.

at defined time points, and fluorescence was measured using a microplate reader (Infinite M200Pro, TECAN, Zürich, Switzerland) at 485/535 nm. Dead cell numbers were determined using a standard curve from digitonin-lysed cell dilutions (82.5 µg/ml; Merck Millipore, Darmstadt, Germany). The percentage of dead cells was calculated as the ratio of dead to total cells, as described before.[11,13] Cell viability and proliferation were determined by counting viable cells using a hemocytometer at defined time points.

Extreme Limiting Dilution Assay

The self-renewal capacity of primary cells pretreated with different conditions (control without mFUS, AIP 5 or 11 W, 48 h after mFUS) was assessed using an extreme limiting dilution analysis (ELDA), as described.[11,13] The cell count was determined after mFUS and isolation of the cells from 3D hydrogels as described above, and serial dilutions (ranging from 1 to 3,200 cells per well) were plated in neurosphere medium. Cultures were maintained for 7 days, after which the number of spheres per well and the number of wells containing spheres (positive cultures) at each plating density were recorded. Data were analyzed using the ELDA online software tool (http://bioinf.wehi.edu.au/software/elda), and the results were plotted to estimate the self-renewal capacity. In addition, 5×10^4 remaining cells/well were cultured in neurosphere medium for 7 days and processed for qPCR analysis.

CD11b and CD3 Cell Depletion Using Magnetically Activated Cell Sorting

GBOs located more focally or peri-focally of the whole GBO-containing sample were picked from the 3D hydrogels immediately after mFUS treatment (AIP 11 W) and cultured separately for 24 h in GBO medium under gentle rotation. Subsequently, the regionally distinct GBOs were processed using MACS® technology to deplete CD11b- and CD3-expressing cells, including macrophages, microglia, T lymphocytes, and NK cells, as previously described.[27,33] Specifically, single-cell suspensions were prepared from 400 mg of GBOs using the Neural Dissociation Kit (T) (Miltenyi Biotech GmbH, Gladbach, Germany), labeled with CD11b and CD3 MicroBeads (Miltenyi Biotech GmbH), and separated using MACS LS columns following the manufacturer's protocol. Further analyses were performed by qPCR.

Inhibition Experiments

Patient-derived more differentiated GBM cells were stimulated with the broad PI3-kinase inhibitor LY294002 (3 µM, #440204; Sigma–Aldrich; stock dissolved at 10 mM in DMSO). The inhibitor was administered 30 min (read out qPCR) to 1 h (read out Western blot) before mFUS (AIP 15 W) and during mFUS treatment using 3D hydrogel cell cultures, as described above. If a qPCR was subsequently performed, the samples were cultivated for a further 24 h without inhibitor stimulation; in the case of a Western blot, the samples were processed directly after mFUS.

Western Blot

3D hydrogel GBO cultures or primary cell cultures from inhibiting experiments were prepared as described above. Twenty-four hours after the preparation of the 3D hydrogels, the samples were treated with mFUS (AIP 11 for GBOs, 15 W for LY294002-treated primary cells). Cells were recovered from hydrogels using the Cell Recovery Solution (The Well Bioscience) directly after mFUS in the case of LY294002-treated samples. In the case of GBOs, samples were cultured for an additional 48 h, followed by treatment with 50 µM Temozolomide (TMZ, stock dissolved at 100 mM DMSO; Sigma–Aldrich) for another 3 d. Afterwards, GBOs were picked from the 3D hydrogel. All samples were transferred into tubes containing lysis buffer (5 mM Tris–HCl (pH 7.8) supplemented with 10 mM NaCl, 0.1% (v/v) Triton X-100, 0.2 mM EDTA, 2 mM orthovanadate, and 1% (v/v) phosphatase inhibitor cocktail (100X, Thermo Fisher Scientific)) and homogenized using a tissue chopper (IKA-Ultra-Turrax®T 25 basic; IKA-Factory GmbH & Co. KG, Staufen, Germany). As described, 6-10 µg protein per sample was used for Western blotting experiments.[27] Primary antibodies used were anti-MSI1 (1:500, mouse; MAB2628, R&D Systems, Minneapolis, MN, USA), anti-IGFBP5 (1:150, rabbit; sc-13093, Santa Cruz Biotechnology, Dallas, TX, USA), and anti-EphA5 (1:150, rabbit; sc-927, Santa Cruz Biotechnology), anti-phospho-GSK3β (Ser9) (1:250, rabbit; #9336, Cell Signaling, Danvers, MA, USA), and anti-phospho-Akt (Thr308) (1:200, rabbit; #9275, Cell Signaling) in 2% (w/v) casein/Tris-buffered saline with 0.1% tween (TBS-T) or 5% (w/v) bovine serum albumin/TBS-T for phosphorylated antibodies. The secondary antibody was donkey anti-rabbit IgG-HRP (1:12,500; A16035, Thermo Fisher Scientific) and donkey-anti-mouse IgG-HRP (1:10,000; A16011, Thermo Fisher Scientific) in 2% (w/v)

casein/TBS-T. Equal protein loading was confirmed by stripping and incubating the membranes with anti-GAPDH (1:200; sc-47724; mouse, Santa Cruz) in 2% (w/v) casein/TBS-T with the secondary antibody donkey anti-mouse IgG-HRP (1:10000, A16011; Thermo Fisher Scientific) in 2% (w/v) casein/TBS-T as described.[27]

Temozolomide Stimulation

3D hydrogel cultures of patient-derived differentiated GBM cells and GSCs were prepared as described above. Twenty-four hour after preparation, the 3D hydrogel cultures were treated with mFUS (AIP 5 and 11 W) and cultivated for 48 h. The cells were recovered from the 3D hydrogels using the Cell Recovery Solution (The Well Bioscience), seeded into 6-well plates at a density of 25,000 cells/well, and cultivated in the respective growth media supplemented with 50 µM TMZ (stock dissolved at 100 mM in DMSO; Merck Millipore) for up to 10 days. Controls were stimulated with an equal volume of DMSO (0.01% (v/v)) or cultivated in growth medium without any supplements (untreated control). Cytotoxic effects of TMZ and DMSO treatment following mFUS were investigated with the CytoTox-Fluor™ Cytotoxicity Assay (Promega) according to the manufacturer's instructions and as described above.

Statistical Analysis

The data were statistically analyzed using the GraphPad Prism 8.4® software (GraphPad Software, San Diego, CA, USA). Depending on the experimental setup, a Student's *t*-test or a one-way or two-way ANOVA was performed, as indicated for each experiment in the figure captions. The sample size is stated in the figure captions. Statistical significance is marked with asterisks depending on the *P*-value: * $P < 0.05$, ** $P < 0.01$, and *** $P < 0.001$.

Results

mFUS Promotes Increased Expression of Dormancy- and Stemness-Associated Markers in GBOs in a Complex, Region- and Marker-Dependent Way

First, we analyzed the impact of mFUS (AIP 11 W, 24 h after mFUS) on patient-derived GBOs as complex, in vivo-adapted cellular systems cultured in 3D hydrogels. The characterization and quality control of the used GBOs are illustrated in the Materials and Methods section and shown in Figure 1A-C. The mFUS setup was validated as described in the Materials and Methods section and shown in Figure 2A-E. Markers studied in the following section were Sloan–Kettering Institute (SKI), insulin-like growth factor-binding protein 5 (IGFPB5), ephrin receptor A5 (EphA5), and histone cluster 1 H2B family member K (H2BK) as known dormancy-associated markers, and octamer binding transcription factor 4 (OCT4), Nestin, sex-determining region Y-box 2 (SOX2), and Musashi (Drosophila) homolog 1 (MSI1) as known stemness-associated markers.[11–15,28,29] Notably, mFUS-treated sections referred to as margins were GBOs from peri-focal regions, whereas sections referred to as the center were in the focal region of mFUS. Sections referred to as controls obtained no mFUS-treatment.

Using immunofluorescence multi-staining, a region- and marker-dependent induction of dormancy- and stemness-associated molecules was measured depending on the GBO preparation examined, eg for the combinations MSI/IGFBP5, OCT4/H2BK, and SOX2/SKI (Figure 3). In the GBO specimen illustrated, the combination MSI/IGFPB5, in particular, was induced after mFUS, both in the residual cells next to the focal area and peri-focally. However, OCT4/H2BK and SOX2/SKI also showed increased protein expression compared to the controls without mFUS. Although these results differed between individual GBO preparations, quantification of double-positive cell populations after mFUS (2-7 GBOs of 2 independent GBO preparations) revealed an overall increase in the double-positive cells of the mFUS-treated samples ($10.2 \pm 4.57\%$ and $8.0 \pm 2.46\%$ double-positive cells from the center/margin of mFUS-treated samples in case MSI/IGFPB5 [untreated controls with $1.0 \pm 0.6\%$ and $0.5 \pm 0.4\%$ double-positive cells], $16.6 \pm 5.55\%$ and 22.0 ± 12.84 % in case of OCT4/H2BK [controls $4.0 \pm 2.6\%$ and $2.4 \pm 1.0\%$], and $15.5 \pm 9.41\%$ and $15.0 \pm 9.39\%$ in case SOX2/SKI [controls 3.0 ± 0.5 % and 9.9. ± 7.0%]). Analysis of cell death induced by mFUS revealed a significantly increased occurrence of cCaspase3-positive cells next to the focal area (particularly in areas that did not show clear expression of dormancy- and stemness-related molecules). In contrast, only a low abundance of cCaspase3-positive cells was observed in the peri-focal regions, comparable to the controls (Figure 3).

Accordingly, various GBOs showed an increased mRNA expression of dormancy- and stemness-associated molecules depending on the region studied and the markers analyzed (Figure 4A). A clear induction of EphA5, H2BK, OCT4, SOX2, and MSI1 was measured in most cases, especially near the focal region (center). In contrast, the mRNA expression of IGFBP5 and SKI was especially induced in peri-focal regions (margin) after mFUS treatment. Nestin showed a uniform induction both near the focal region and peri-focally (Figure 4A). However, due to the pronounced intra- and intercellular heterogeneity of GBOs, the various effects differed between the individual GBO preparations (no statistical significance could be obtained overall from preparations), but were clearly detectable on average (Figure 4A).

To obtain an initial indication of the cellular source of the increased expression of dormancy- and stemness-associated markers after mFUS, exemplary GBO preparations with/without mFUS treatment were subjected to tissue processing with subsequent depletion of CD11b- and CD3-positive immune cells using MACS. After validation of the successful depletion of the immune cells (Figure 4B, left), a determination of the mRNA expression of dormancy- and stemness-associated markers showed an increased expression of almost all markers to varying degrees (~2-fold and above on average) in the GBM cell-enriched fraction after mFUS (Figure 4B, middle), while only a slight increase of H2BK, Nestin, and SOX2 or no expression (EphA5) was observed in the immune

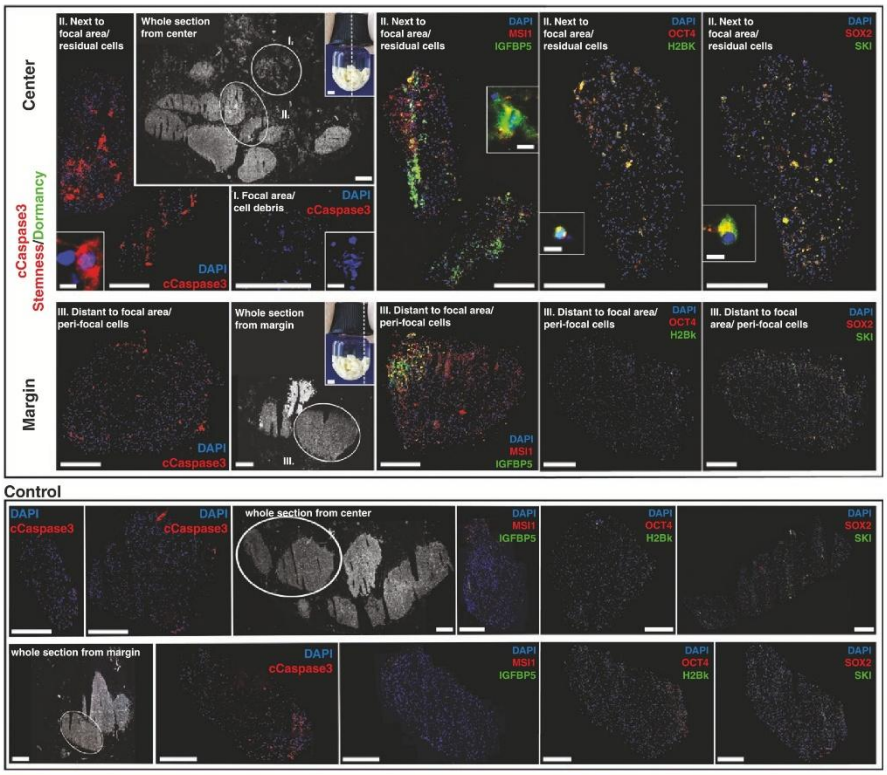


Figure 3. mFUS-treated (average incidence power 11 W) exemplary GBO-containing sample was cultured for another 24 h, cryofixed, and serially sectioned. Multi-immunofluorescence staining of sections from the sample's focal (center) and peri-focal (margin) mFUS regions were performed with cCaspase3 (cell death marker), MSI1 (stemness marker), IGFBP5 (dormancy marker), OCT4 (stemness marker), H2BK (dormancy marker), SOX2 (stemness marker), and SKI (dormancy marker). Fragmented cell nuclei were observed in the focal region (I) after mFUS treatment, and cCaspase3 appeared predominantly near the focal region (II) compared with more distant regions (III). The untreated control showed a low incidence of cCaspase3. Prominent co-staining of MSI1 and IGFBP5 was found in both the sample´s center (residual cells) and the margin (peri-focal cells), while co-staining of OCT4 with H2BK and SOX2 with SKI showed increased expression compared to the untreated control, mainly in residual cells next to the focal area. Bar: 0.5 mm (whole sections), 1 mm (inserts with mFUS-tubes), 400 µm (GBO samples), 10 µm (inserts). Circled GBOs in whole sections show those GBOs that were visualized in detail in the immunofluorescence. H2BK, histone cluster 1 H2B family member K; IGFPB5, insulin-like growth factor-binding protein 5; SKI, SKI proto-oncogene. For further abbreviations, please refer to the previous figures.

cell-enriched fraction (Figure 4B, right). This finding indicated that the tumor cells themselves responded to mFUS treatment.

mFUS-induced Expression of Dormancy- and Stemness-associated Markers Can be Attributed to Specific GBM Cell Subpopulations

To substantiate the findings of the GBOs and to clarify whether mFUS further promoted the stemness and dormancy properties of patient-derived GSCs or whether more differentiated patient-derived GBM cells developed an enhanced dormancy- and stemness-associated potential by mFUS treatment, 3D hydrogel-based, pure cultures of GSCs and more differentiated GBM cells were subjected to mFUS (AIP 15 W, 24 h after mFUS treatment) (Figure 4C).

Both pure cultures of GBM subpopulations (2 independent preparations of GSCs and more differentiated GBM cells each) responded to mFUS treatment with increased mRNA expression of dormancy- and stemness-associated markers, with the most consistent findings for SKI, IGFBP5, OCT4, and Nestin. The induction of expression was detectable both next to the focal region (center) and peri-focally (margin), ranging from ~2.5- to 16-fold induction compared to controls without mFUS, depending on

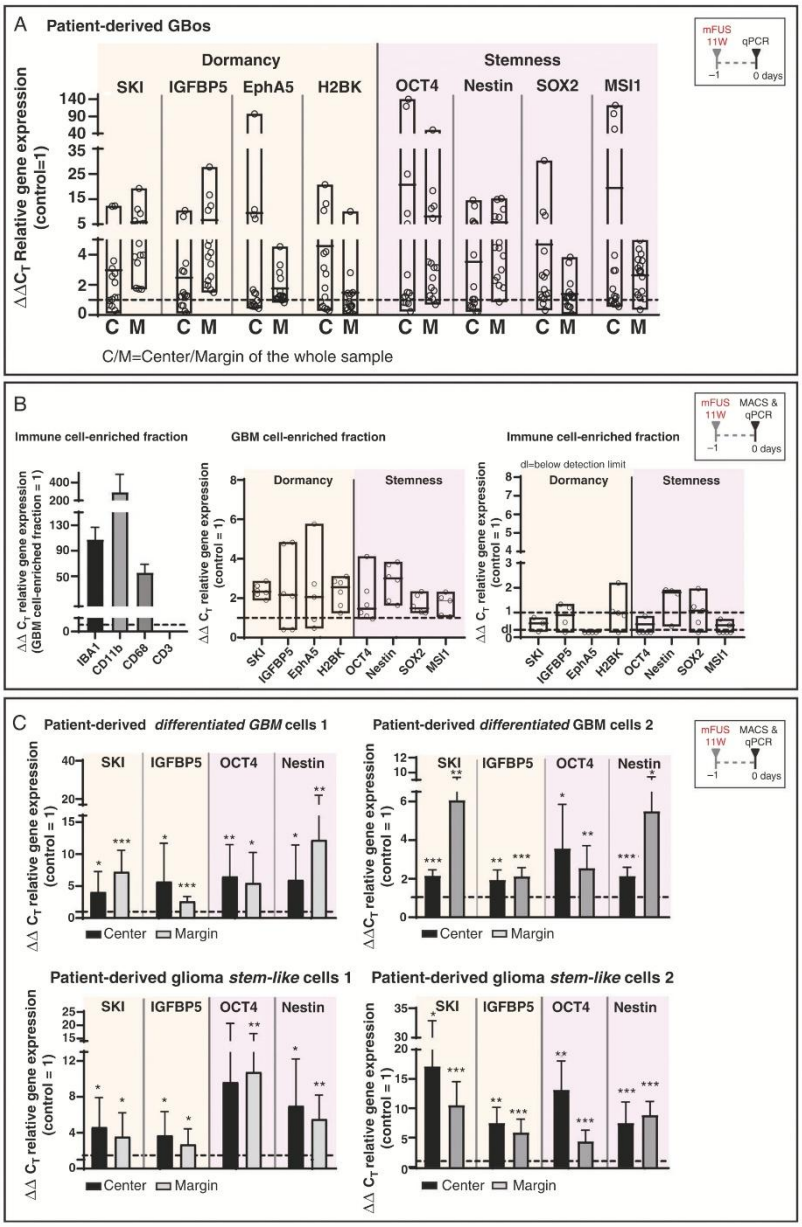


Figure 4. (A) GBOs treated with mFUS (average incident power 11 W, further cultured for 24 h) showed an induction of the mRNA expression of exemplary dormancy- and stemness-associated markers in the residual/peri-focal cells in a complex marker- and region-dependent manner (center/margin of whole samples) compared to average unstimulated controls (control = 1); $n = 8$ biological replicates with $n = 1$-2 technical replicates each. EphA5, ephrin receptor A5. (B) mFUS-treated (average incidence power 11 W) GBOs-containing samples were further cultured for another 24 h, and CD11b/CD3 MACS-based depletion of immune cells was performed. Left: Exemplary data on the success of MACS-based immune cell depletion is shown. Middle: The GBM cell-enriched fraction showed increased mRNA expression of dormancy- and

stemness-associated markers. Right: The immune cell-enriched fraction showed significantly lower inductions or no detection of dormancy- and stemness-associated markers. Control = 1: average unstimulated controls; $n = 3$ biological replicates with $n = 1$-2 technical replicates each. (C) Pure cultures of patient-derived GSCs and more differentiated GBM cells were treated with mFUS (average incident power 15 W, 24 h after mFUS treatment; 2 different cell preparations each). Induction of the mRNA expression of exemplary dormancy (SKI, IGFBP5) and stemness markers (OCT4, Nestin) could be determined in residual/peri-focal cells in a complex marker- and region-dependent manner (center/margin of whole samples) compared to average unstimulated controls (control = 1); $n = 3$ biological replicates with $n = 1$-2 technical replicates each. Significant differences compared to the untreated control were determined by a nonpaired *t*-test and are indicated directly above the bars (* $P < 0.05$; ** $P < 0.01$; *** $P < 0.001$). Error bars correspond to the standard deviation. Please also refer to Supplementary Fig. 1 for expression of dormancy-/stemness-associated molecules with increasing mFUS power in GSCs. For abbreviations, please refer to the previous figures.

the markers, samples, and regions examined (Figure 4C). Exemplified for GSCs, these effects were also detectable at lower mFUS settings (AIP 1, 5, and 11 W; Supplementary Fig. 1).

Thus, the mFUS treatment not only enhanced stemness- and dormancy-associated molecules in GSCs but also induced phenotypic changes in more differentiated GBM cells.

mFUS Pretreatment Promotes Sphere Formation Ability and Chemoresistance in Different GBM Cell Subpopulations

To test the biological consequence of the increased expression of dormancy- and stemness-associated markers, pure preparations of more differentiated patient-derived primary GBM cells (2 independent preparations) cultured in 3D hydrogels were treated without or with mFUS (AIP 5 and 11 W), seeded in neurosphere medium after an additional 48 h, and further cultured for 7 days to analyze survivability and sphere formation under these conditions. The ability of residual/peri-focal, patient-derived, formerly differentiated GBM cells to form stem-like cell-typical spheres increased with intensified average incidence mFUS power (Figure 5A), even if the individual preparations responded to the mFUS treatment to varying degrees (example of an unstimulated control shown in Supplementary Fig. 2). Additionally, the observed increased ability to form spheres was supported by the mRNA expression profile of the GBM cells, exemplified for the GBM cells treated with AIP 11 W. Depending on the preparation, the mRNA expression of SKI, H2BK, Nestin, MSI1, and SOX2 (first GBM cell preparation), as well as OCT4, MSI1, and IGFBP5 (second preparation), was particularly well regulated in this experimental setting (no separate analysis of the focal and peri-focal region, as methodologically not possible). All these molecules showed induction by mFUS pretreatment, which was further supported by cultivation in a neurosphere medium (Figure 5B).

Since increased resistance to chemotherapy is also an essential hallmark of stem-like GBM cells, both pure cultures of patient-derived GSCs and more differentiated GBM cells (both with a methylated MGMT-promotor) were treated with 50 µM Temozolomide (TMZ; concentration nearly equivalent to that observed in human cerebrospinal fluid after oral administration[34]) 48 h after mFUS pretreatment (AIP 5 and 11 W) for a total of 10 additional days, and the cytotoxic effect of TMZ with or without mFUS pretreatment was tested. A significantly lower cytotoxic potential of TMZ (lower numbers of dead cells) was observed in the different GBM subpopulations pretreated with mFUS compared to GBM subpopulations without mFUS pretreatment (Figure 5C). However, in GSCs, this was not as pronounced as in the differentiated GBM subpopulation. Moreover, TMZ did not show a cytotoxic effect on the GSCs until after 10 days due to their stem cell nature. With increasing mFUS intensity, a slight increase in the protective effect of the mFUS pretreatment on the subsequent TMZ treatment was observed in both preparations examined, but this was not significant compared to the corresponding controls. Interestingly, GBOs treated with mFUS (AIP 11 W) and stimulated with TMZ for a further 3 days, 48 h after mFUS, also showed increased protein expression of MSI1, IGFBP5, and EphA5 compared to GBOs without mFUS pretreatment. Following the previous data, the sole effect of mFUS on the increased expression of the markers mentioned above was again observed here (Figure 5D; refer to Supplementary Fig. 3 for full blots).

PI3-kinase Signaling Seems to be Involved in mFUS-mediated Phenotypic Changes

To gain a first insight into the signaling cascades involved in the mFUS-mediated effect of inducing the stemness and dormancy properties of residual/peri-focal GBM cells, we performed inhibition experiments in pure, more differentiated GBM cell cultures using the PI3-kinase inhibitor LY294002, followed by Western blot analysis of Akt (Thr308) and GSK3β (Ser9) phosphorylation, along with mRNA expression analysis of dormancy- and stemness-associated genes. Notably, the PI3-kinase/Akt pathway is frequently hyperactivated in GBM, supporting the maintenance and self-renewal of GSCs, contributing to tumor initiation and resistance to therapy.[35] Further, previous studies, including our own, have further demonstrated that the PI3-kinase/Akt signaling pathway regulates the stemness and dormancy properties of GBM cells.[27,36] Notably, the PI3-kinase (and Akt) activity is also known to be modulated by ROS.[37]

We demonstrated an effect of mFUS on the phosphorylation of Akt and GSK3β, which was partially prevented by LY294002 (Figure 6A; refer to Supplementary Fig. 4 for full blots). Importantly, mFUS-mediated Akt phosphorylation at Thr308 is an activating phosphorylation, while GSK3β phosphorylation at Ser9 inhibits GSK3β. Both ultimately lead to increased expression of molecules associated with dormancy and stemness (Figure 6B). Consequently, LY294002-mediated reduction of Akt and induction of GSK3β activation by inhibiting PI3-kinase resulted in a partial decrease in mFUS-induced expression of SKI and Nestin, especially, as dormancy- and stemness-associated

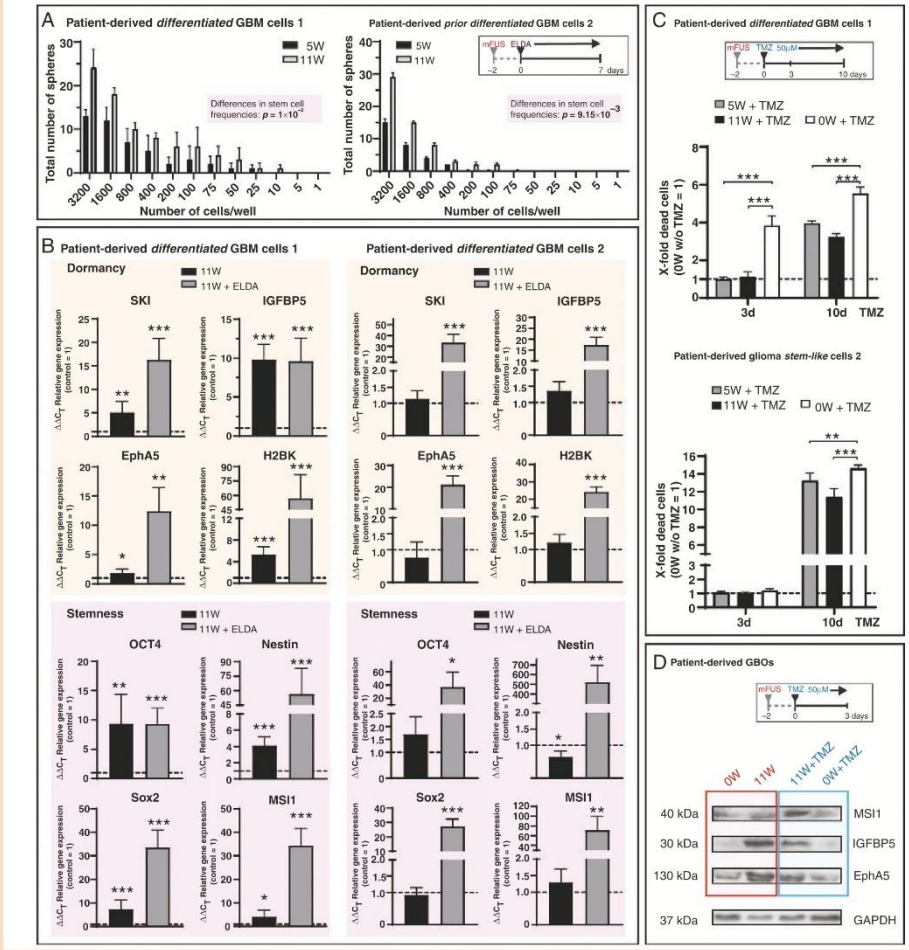


Figure 5. (A) mFUS (average incident power 5 and 11 W, 48 h after mFUS treatment) increased the ability of residual/peri-focal, formerly more differentiated GBM cells from patients to form cell-typical spheres when cultured under stem cell conditions as determined by the ELDA (2 different cell preparations with $n = 2$ biological replicates each). Briefly, cells were seeded at progressively lower densities, ranging from 3,200 cells per well to a single cell per well. Cultures were maintained until day 7 in neurosphere medium 48 h after mFUS treatment. At this point, the number of spheres per well and the number of wells containing spheres at each seeding density (number of positive cultures) were documented. Significance was tested using the online ELDA program 25 (https://bioinf.wehi.edu.au/software/elda/) with $P = 0.01$ for preparation 1 and $P = 0.00915$ for preparation 2. Refer to Supplementary Fig. 2 for the neurosphere formation assay of an example of an untreated control. (B) Determination of the mRNA expression of dormancy- and stemness-associated molecules 48 h after the mFUS treatment and continued cultivation for an additional 7 days in neurosphere medium compared to average unstimulated controls (control = 1). A separate analysis of the focal and peri-focal regions was not performed due to methodological constraints. Primary culture 1: $n = 5$ biological with $n = 1$-3 technical replicates each, primary culture 2: $n = 4$ biological with $n = 1$-3 technical replicates each. Significant differences compared to the untreated control were determined by a nonpaired *t*-test and are indicated directly above the bars (* $P < 0.05$; ** $P < 0.01$; *** $P < 0.001$). For abbreviations, please refer to the previous figures. (C) Pure cultures of patient-derived differentiated GBM cells and GSCs treated with mFUS (average incident power 5 and 11 W, 48 h after mFUS treatment stimulation with TMZ) showed higher resistance to TMZ (50 µM, treatment for 10 days), as evidenced by a lower number of dead cells compared to TMZ treatment alone ($n = 2$-3 biological replicates with $n = 1$-3 technical replicates each for differentiated GBM cells and GSCs, respectively; compared to average unstimulated controls (control = 1)). The significances between different stimulations were determined using a two-way ANOVA test followed by a Tukey's multiple comparison test (** $P < 0.01$; *** $P < 0.001$). Error bars correspond to the standard deviation. (D) GBOs treated with mFUS (average incident power 11 W, 48 h after mFUS treatment, stimulation with 50 µM TMZ for 3 days) showed increased protein expression of MSI1 (stemness marker), IGFBP5 (dormancy marker), and EphA5 (dormancy marker) compared to untreated control. GAPDH served as a loading control. Refer to Supplementary Fig. 3 for full blots. For abbreviations, please refer to the previous figures.

We determined an increased expression of dormancy and stemness markers after mFUS in a complex region- and marker-dependent way, suggesting an effect of mFUS beyond the focal region. Accordingly, ELDA resulted in an increased ability of residual/peri-focal, formerly differentiated patient-derived GBM cells to form stem-like cell-typical spheres. This was accompanied by an increased expression of dormancy- and stemness-associated markers. Moreover, residual/peri-focal GBM cells were characterized by a higher resistance to TMZ, resulting in fewer dead cells than those treated solely with TMZ. At this, the mFUS-induced phenotypic changes appeared to be mediated by the PI3-kinase/Akt/GSK3β signaling pathway.

Dormancy describes a reversible cellular resting stage that plays a fundamental role in tumor evolution. Leaving this dormant state can lead to proliferation and tumor growth in primary tumor cells and metastases.[44] In cellular dormancy, individual tumor cells can enter a cellular resting phase characterized by a reversible cell cycle arrest.[44] Dormant and tumor stem-like cells share some similarities.[16,17] Indeed, depending on the environmental stress (eg treatment), GBM cells can switch to a more dormant/stem cell-associated phenotype to survive unfavorable environmental conditions.[11,13] We showed that residual/peri-focally localized GBM cells responded to mFUS treatment with increased dormant/stem-like cell properties. This observation regarding the influence of mFUS on dormancy/stemness properties beyond the focal region is novel and particularly important.

A probably peri-focal effect of FUS has already been demonstrated. For example, Qu et al.[45] showed that cavitation-based focal ablation could stimulate local tumor infiltration by immune cells and promote inflammation at tumor sites that were not directly affected.[19,45] This shows the reactivity of the peri-focal area after mFUS, which, in addition to the intensity of the sonication, is of decisive importance for the (long-term) consequences of mechanical ablation.

Regarding the influence of FUS on stem cells or stem-like cell properties, the most common previous findings refer to the so-called phenomenon of stem cell homing. Here, the mechanical effects of FUS increase the ability of stem cells to extravasate into the tissue,[46] helping these cells to migrate more efficiently into damaged tissues. However, a few studies also refer to the direct influence of FUS on stem cell or stem-like cell properties. Seo et al.[47] showed that endogenous neural stem cells were activated after low-intensity FUS-induced blood–brain barrier modulation. The expression of SOX2 and Nestin was significantly upregulated, and the stem cell activity was higher 1 week after low-intensity FUS. Further, FUS-mediated hyperthermia could sensitize GSCs to radiation.[19,48] Hyperthermia also sensitizes GSCs to radiation therapy by downregulating the Akt signaling pathway, a key mediator of stemness and self-renewal.[19,49] Song et al.[50] observed that low-intensity pFUS attenuated GSC biomarkers' expression, promoted GSCs escape from G0 quiescence, and significantly weakened the Wnt and Hh pathways. Accordingly, the sonication's frequency and intensity appear decisive for the resulting biological effects.

In summary, we showed that mFUS exerts complex effects on residual GBM cells regarding their dormancy and stemness properties. Given that these properties may play a crucial role in the progression of GBMs, the observed effects of mFUS might be of great interest, especially concerning combined mFUS and chemotherapy concepts. Due to the complexity of the effects, further studies need to be conducted to develop efficient mFUS-based therapy options.

Limitation of the Study

The lack of in vivo validation restricts the broader translational interpretation of the findings. However, given the limited applicability of current rodent in vivo mFUS systems and the debated relevance of rodent models in recapitulating human GBM heterogeneity, we chose to concentrate on complex patient-derived, human-based 3D models. Moreover, further inhibition experiments targeting various points within signaling cascades must be conducted for a more precise elucidation, especially regarding the role of ROS (and mechanoreceptors) as a relevant factor in mFUS-mediated phenotypic changes.

Supplementary material

Supplementary material is available online at *Neuro-Oncology Advances* (https://academic.oup.com/noa).

Keywords:

mechanical focused ultrasound | glioblastoma | dormancy | stemness

Funding

This work was supported by the German Research Foundation as part of the Research Training Group "Materials4Brain" (RTG2154; P8) and by sponsorships from the University Medical Center Schleswig-Holstein, UKSH (start-up supports 2021, 2025).

Acknowledgments

We thank Corinna Keller for her expert technical assistance.

Conflict of interest statement. All authors declare no conflicts of interest.

Ethics

The study was conducted according to the Declaration of Helsinki and approved by the Ethics Committee of the University of Kiel, Germany (file reference: D524/17). Informed consent was obtained from all subjects involved in the study.

Authorship

Conceptualization: JH-F; methodology: DH, LJ, JC, NOS; software: DH, LJ, JC; validation: DH, LJ, JC; formal analysis: DH, LJ, JC, JH, FB; investigation: DH, LJ, JC, JH, NOS, FB; resources: NOS, CK-K, SW, HA, A-KH, MS; data curation: DH, LJ, JC, JH, FB, JH-F; writing - original draft preparation: JH-F; writing - review and editing: all authors; visualization: DH, LJ, JC, JH, FB; supervision: JH-F; project administration: JH-F; funding acquisition: JH-F, A-KH, CK-K. All authors have read and agreed to the final version of the manuscript.

Data availability

All data on which the paper's conclusions are based are available to readers in the manuscript.

Affiliations

Department of Neurosurgery, University Medical Center Schleswig-Holstein (UKSH), 24105 Kiel, Germany (D.H., L.J., J.C., J.H., N.O.S., F.B., H.A., C.K., S.W., A.-K.H., M.S., J.H.-F.)

References

1. Giammalva GR, Gagliardo C, Marrone S, et al. Focused ultrasound in neuroscience. state of the art and future perspectives. *Brain Sci.* 2021;11(1):84.
2. Hersh DS, Kim AJ, Winkles JA, et al. Emerging applications of therapeutic ultrasound in neuro-oncology: moving beyond tumor ablation. *Neurosurgery.* 2016;79(5):643–654.
3. Ashokkumar M. The characterization of acoustic cavitation bubbles - an overview. *Ultrason Sonochem.* 2011;18(4):864–872.
4. Xu Z, Hall TL, Vlaisavljevich E, Lee FT. Histotripsy: the first noninvasive, non-ionizing, non-thermal ablation technique based on ultrasound. *Int J Hyperthermia.* 2021;38(1):561–575.
5. Li S, Wei Y, Zhang B, Li X. Research progress and clinical evaluation of histotripsy: a narrative review. *Ann Transl Med.* 2023;11(6):263.
6. Roberts WW. Development and translation of histotripsy: current status and future directions. *Curr Opin Urol.* 2014;24(1):104–110.
7. Roberts JW, Powlovich L, Sheybani N, LeBlang S. Focused ultrasound for the treatment of glioblastoma. *J Neurooncol.* 2022;157(2):237–247.
8. Meng Y, Pople CB, Budiansky D, et al. Current state of therapeutic focused ultrasound applications in neuro-oncology. *J Neurooncol.* 2022;156(1):49–59.
9. Stupp R, Mason WP, van den Bent MJ, et al; European Organisation for Research and Treatment of Cancer Brain Tumor and Radiotherapy Groups. Radiotherapy plus concomitant and adjuvant temozolomide for glioblastoma. *N Engl J Med.* 2005;352(10):987–996.
10. Liang J, Lv X, Lu C, et al. Prognostic factors of patients with Gliomas - an analysis on 335 patients with Glioblastoma and other forms of Gliomas. *BMC Cancer.* 2020;20(1):35.
11. Kubelt C, Hellmold D, Esser D, et al. Insights into gene regulation under temozolomide-promoted cellular dormancy and its connection to stemness in human glioblastoma. *Cells.* 2023;12(11):1491.
12. Dirkse A, Golebiewska A, Buder T, et al. Stem cell-associated heterogeneity in Glioblastoma results from intrinsic tumor plasticity shaped by the microenvironment. *Nat Commun.* 2019;10(1):1787.
13. Adamski V, Hempelmann A, Flüh C, et al. Dormant glioblastoma cells acquire stem cell characteristics and are differentially affected by Temozolomide and AT101 treatment. *Oncotarget.* 2017;8(64):108064–108078.
14. Mitchell K, Troike K, Silver DJ, Lathia JD. The evolution of the cancer stem cell state in glioblastoma: emerging insights into the next generation of functional interactions. *Neuro Oncol.* 2021;23(2):199–213.
15. Almog N. Molecular mechanisms underlying tumor dormancy. *Cancer Lett.* 2010;294(2):139–146.
16. Endaya BB, Lam PYP, Meedeniya ACB, Neuzil J. Transcriptional profiling of dividing tumor cells detects intratumor heterogeneity linked to cell proliferation in a brain tumor model. *Mol Oncol.* 2016;10(1):126–137.
17. Zeng L, Zhao Y, Ouyang T, et al. Label-retaining assay enriches tumor-initiating cells in glioblastoma spheres cultivated in serum-free medium. *Oncol Lett.* 2016;12(2):815–824.
18. Bao S, Wu Q, McLendon RE, et al. Glioma stem cells promote radioresistance by preferential activation of the DNA damage response. *Nature.* 2006;444(7120):756–760.
19. Hersh AM, Bhimreddy M, Weber-Levine C, et al. Applications of focused ultrasound for the treatment of glioblastoma: a new frontier. *Cancers.* 2022;14(19):4920.
20. MacDonell J, Patel N, Rubino S, et al. Magnetic resonance-guided interstitial high-intensity focused ultrasound for brain tumor ablation. *Neurosurg Focus.* 2018;44(2):E11.
21. Bunevicius A, Pikis S, Padilla F, Prada F, Sheehan J. Sonodynamic therapy for gliomas. *J Neurooncol.* 2022;156(1):1–10.
22. Sukovich JR, Cain CA, Pandey AS, et al. In vivo histotripsy brain treatment. *J Neurosurg.* 2019;131(4):1331–1338.
23. Lu N, Hall TL, Choi D, et al. Transcranial MR-guided histotripsy system. *IEEE Trans Ultrason Ferroelectr Freq Control.* 2021;68(9):2917–2929.
24. Duclos S, Golin A, Fox A, et al. Transcranial histotripsy parameter study in primary and metastatic murine brain tumor models. *Int J Hyperthermia.* 2023;40(1):2237218.
25. Choi SW, Duclos S, Camelo-Piragua S, et al. Histotripsy treatment of murine brain and glioma: temporal profile of magnetic resonance imaging and histological characteristics post-treatment. *Ultrasound Med Biol.* 2023;49(8):1882–1891.
26. Jacob F, Salinas RD, Zhang DY, et al. A patient-derived glioblastoma organoid model and biobank recapitulates inter- and intra-tumoral heterogeneity. *Cell.* 2020;180(1):188–204.e22.
27. Hellmold D, Kubelt C, Daunke T, et al. Sequential treatment with temozolomide plus naturally derived AT101 as an alternative therapeutic strategy: insights into chemoresistance mechanisms of surviving glioblastoma cells. *Int J Mol Sci.* 2023;24(10):9075.
28. Flüh C, Chitadze G, Adamski V, et al. NKG2D ligands in glioma stem-like cells: expression in situ and in vitro. *Histochem Cell Biol.* 2018;149(3):219–233.
29. Kubelt C, Gilles L, Hellmold D, et al. Temporal and regional expression changes and co-staining patterns of metabolic and stemness-related markers during glioblastoma progression. *Eur J Neurosci.* 2024;60(1):3572–3596.
30. Budday S, Nay R, Rooij R de, et al. Mechanical properties of gray and white matter brain tissue by indentation. *J Mech Behav Biomed Mater.* 2015;46(June):318–330.
31. Gallelli CA, Calcagnini S, Romano A, et al. Modulation of the oxidative stress and lipid peroxidation by endocannabinoids and their lipid analogues. *Antioxidants (Basel).* 2018;7(7):93.

32. Quarato CMI, Lacedonia D, Salvemini M, et al. A review on biological effects of ultrasounds: key messages for clinicians. *Diagnostics (Basel).* 2023;13(5):855.
33. Adamski V, Schmitt AD, Flüh C, et al. Isolation and characterization of fast-migrating human glioma cells in the progression of malignant gliomas. *Oncol Res.* 2017;25(3):341–353.
34. Ostermann S, Csajka C, Buclin T, et al. Plasma and cerebrospinal fluid population pharmacokinetics of temozolomide in malignant glioma patients. *Clin Cancer Res.* 2004;10(11):3728–3736.
35. Li X, Wu C, Chen N, et al. PI3K/Akt/mTOR signaling pathway and targeted therapy for glioblastoma. *Oncotarget.* 2016;7(22):33440–33450.
36. Gulaia V, Kumeiko V, Shved N, et al. Molecular mechanisms governing the stem cell's fate in brain cancer: factors of stemness and quiescence. *Front Cell Neurosci.* 2018;12(Nov 19):388.
37. Chatterjee R, Chatterjee J. ROS and oncogenesis with special reference to EMT and stemness. *Eur J Cell Biol.* 2020;99(2-3):151073.
38. Alkins RD, Mainprize TG. High-intensity focused ultrasound ablation therapy of gliomas. *Prog Neurol Surg.* 2018;32:39–47.
39. Medel R, Monteith SJ, Elias WJ, et al. Magnetic resonance-guided focused ultrasound surgery: Part 2: a review of current and future applications. *Neurosurgery.* 2012;71(4):755–763.
40. Datta P, Moolayadukkam S, Chowdhury D, et al. Recent advances and future directions in sonodynamic therapy for cancer treatment. *BME Front.* 2024;5(Dec 27):80.
41. Ćwiklińska A, Przewodowska D, Koziorowski D, Szlufik S. Innovative approaches to brain cancer: the use of magnetic resonance-guided focused ultrasound in glioma therapy. *Cancers.* 2024;16(24):4235.
42. Nwafor DC, Obiri-Yeboah D, Fazad F, Blanks W, Mut M. Focused ultrasound as a treatment modality for gliomas. *Front Neurol.* 2024;15(May 15):1387986.
43. Young JS, Semonche A, Morshed RA, et al. Focused ultrasound therapy as a strategy for improving glioma treatment. *J Neurosurg.* 2025;142(6):1635–1644.
44. Liu R, Zhao Y, Su S, et al. Unveiling cancer dormancy: intrinsic mechanisms and extrinsic forces. *Cancer Lett.* 2024;591(Jun 1):216899.
45. Qu S, Worlikar T, Felsted AE, et al. Non-thermal histotripsy tumor ablation promotes abscopal immune responses that enhance cancer immunotherapy. *J ImmunoTher Cancer.* 2020;8(1):e000200.
46. Lorsung RM, Rosenblatt RB, Cohen G, Frank JA, Burks SR. Acoustic radiation or cavitation forces from therapeutic ultrasound generate prostaglandins and increase mesenchymal stromal cell homing to murine muscle. *Front Bioeng Biotechnol.* 2020;8(Jul 28):870.
47. Seo Y, Han S, Song B-W, et al. Endogenous neural stem cell activation after low-intensity focused ultrasound-induced blood-brain barrier modulation. *Int J Mol Sci.* 2023;24(6):1–10.
48. Zhu L, Altman MB, Laszlo A, et al. Ultrasound hyperthermia technology for radiosensitization. *Ultrasound Med Biol.* 2019;45(5):1025–1043.
49. Man J, Shoemake JD, Ma T, et al. Hyperthermia sensitizes glioma stem-like cells to radiation by inhibiting AKT signaling. *Cancer Res.* 2015;75(8):1760–1769.
50. Song S, Ma D, Xu L, et al. Low-intensity pulsed ultrasound-generated singlet oxygen induces telomere damage leading to glioma stem cell awakening from quiescence. *iScience.* 2022;25(1):103558.

Child's Nervous System (2025) 41:358
https://doi.org/10.1007/s00381-025-07032-8

RESEARCH

Neuroprotective properties of erythropoietin (Epo) and its receptor (EpoR) in open spinal dysraphism (OSD): an investigation of EpoR expression in a rat OSD model, along with *in vitro* studies on the neuroprotective effects of Epo on rat spinal cord-derived neural progenitor cells

Friederike Knerlich-Lukoschus[1] · Jacqueline Clüver[2] · Inez Manczuk[2] · Frieda Bayler[2] · Dana Hellmold[2] · Michael Synowitz[2] · Janka Held-Feindt[2]

Received: 24 June 2025 / Accepted: 9 November 2025 / Published online: 17 November 2025
© The Author(s) 2025

Abstract

Purpose Research into treatment options that complement surgery for open spinal dysraphism (OSD) is necessary to further improve outcomes following prenatal or postnatal surgery. We investigated erythropoietin (Epo) and its receptor (EpoR) as a potential neuroprotective agent and target in OSD.

Methods Epo- and EpoR-expression was examined on mRNA and immunohistochemical level in neuroplacodes obtained from a rat retinoic acid-induced OSD model at E16, E18, E22. Neural progenitor cells (NPCs) derived from spinal cords of adult Long Evans rats were exposed to varying concentrations of human artificial amniotic fluid (aAF). Cytotoxicity assays were conducted to assess the impact of aAF exposure, with and without Epo. The influence of Epo on NPC's cellular marker expression was analyzed using qRT-PCR.

Results EpoR mRNA expression was elevated significantly on E18 and E22 in OSD- compared to control tissue. EpoR immunoreactivity exhibited consistent expression in ventral and dorsal horns, central canal, and ganglia. It co-stained with Hif-2α, β-III-tubulin, NeuN, and Musashi1. Exposure of NPCs to aAF reduced proliferation and increased death rates dose-dependently. Adding Epo significantly counteracted antiproliferative and cytotoxic aAF effects on NPCs, resulting in similar or lower death rates than those observed in untreated controls. Exposure of NPCs to aAF reduced their expression of neuronal markers. Adding Epo restored their differentiation capacities.

Conclusion Induction of EpoR in neuroplacodes, its co-staining with neuronal and NPC markers, and the neuroprotective effects of Epo on aAF-treated NPCs in vitro establish Epo as a promising candidate for neuroprotective therapies that can supplement surgical measures for OSD.

Keywords Myelomeningocele · Neuroprotection · Animal model · Amniotic fluid · Neural progenitor cell culture

Abbreviations

aAF	Artificial amnionic fluid
Epo	Erythropoietin
EpoR	Erythropoietin receptor
Hif	Hypoxia inducible factor
IF	Immunofluorescence
IR	Immunoreactivity
OSD	Open spinal dysraphism (summarizes myelomeningocele and myeloshisis)
MMC	Myelomeningocele
NPC	Neural progenitor cells
SC	Spinal cord

Friederike Knerlich-Lukoschus and Jacqueline Clüver contributed equally to this work.

Trial registration numbers Protocols and procedures were approved by the Institutional Animal Care and Use Committee of the University of Schleswig–Holstein, Campus Kiel, Germany. (Ministerium für Landwirtschaft, Umwelt und ländliche Räume des Landes Schleswig–Holstein). Reference numbers: V242-22,800/2016 (39–3/16) and V 312–72241.121–35(34–4/05) (2005–2008), and [V 312–72241.121–35(77–6/09)] (2009).

Extended author information available on the last page of the article

RA	Retinoic acid
RA-OSD model	Retinoic acid-induced OSD model
qRT-PCR	Quantitative reverse transcription-polymerase chain reaction

Purpose

Open spinal dysraphism (OSD) is one of the leading causes of disability and mortality in children worldwide [1]. Significant advances have been made in the surgical and medical care of OSD patients, including developing fetal surgical approaches that preserve motor function [2]. However, long-term problems remain [3]. As surgical improvement cannot solve all OSD-associated problems [4], further treatment options must be explored to improve outcomes of pre- or postnatal surgeries.

According to the "two-hit hypothesis" [1, 2], toxic substances in the amniotic fluid and mechanical impacts activate similar signaling pathways in [4, 5] neuroprotective strategies may be suitable for OSD. Recombinant human erythropoietin (Epo) protects against neurodegenerative processes in neurological disorders [6]. Its "robust neuroprotective properties" [7], its clinical applicability in neonates [8–11], and the fact that its receptor (EpoR) is induced after SC injury in anatomical regions associated with neurorestorative processes [12], make Epo interesting for OSD. Since the neuroprotective potential of Epo in OSD has not yet been investigated, these studies focus on this molecule.

We investigated EpoR induction and expression patterns in neuroplacodes obtained from our retinoic acid (RA)-induced OSD rat model at different fetal times, along with EpoR-regulating molecules, hypoxia-inducible factors (Hifs). After identifying EpoR as a potential neuroprotective target in OSD, we investigated the neuroprotective effects of its ligand on rat SC-derived neural progenitor cells (NPCs) in vitro: NPCs exposed to artificial amniotic fluid (aAF) with or without Epo were analyzed for proliferation, cell death rates, and gene expression profiles (see Supplementary Fig. 1 for Graphical Abstract).

Materials and methods

RA-OSD rat model

The RA-OSD rat model, introduced by Danzer et al. [13], was used. 15 pregnant rats received RA, and 5 received olive oil only. Littermates were randomized across experimental groups. For further details on the rat paradigm, we refer to [14].

For mRNA isolation, dysraphic OSD defects were separated from intact SC sections, snap-frozen in liquid nitrogen, and stored at −80 °C. Corresponding SC segments of control animals were handled in the same way. For histological studies, fetuses were fixed in 4% paraformaldehyde/phosphate-buffered saline (pH 7.4) for ten days, embedded in paraffin wax, and sectioned (0.5 µm thickness).

Protocols were approved by the Institutional Animal Care and Use Committee of the University of Schleswig–Holstein, Campus Kiel, Germany (reference number: V242-22,800/2016 (39–3/16). Animal experiments were carried out in compliance with the European Union directive on animal protection used for scientific purposes.

Immunohistochemistry

Details on immunohistochemical procedures have been published previously [15, 16]. Cellular profiles of EpoR immunoreactivity (IR) were investigated by double-labeling with standard antibodies against neuronal and glial cells. Details on antibodies are summarized in Table 1. Controls included: Omitting the primary antibody and staining with monoclonal rabbit IgG (R&D Systems, Wiesbaden-Nordenstadt, Germany, #AB-105-C). Secondary antibodies were labeled with Alexa Fluor 488 (1:1,000) or Alexa Fluor 555 (1:1,000). Nuclei were stained with 4',6-diamidino-2-phenylindole (DAPI) (Molecular Probes/Invitrogen, Life Technologies, Karlsruhe, Germany; 1:30,000). Fluorescence was visualized using a Zeiss microscope Observer.Z1 + ApoTome.2, with an AxioCam MRm camera (Software: ZEN Pro [2012], Carl Zeiss GmbH, Jena, Germany). Qualitative Immunohistochemical analyses were conducted double blinded.

Cultivation of NPCs

NPCs were generated from adult male Long Evans rats' SC (details have been published previously [16]). All protocols and procedures were approved by the University of Schleswig–Holstein's Institutional Animal Care and Use Committee (Ministerium für Landwirtschaft, Umwelt und ländliche Räume des Landes Schleswig–Holstein; 2005, 2007, 2008 [V 312–72,241.121–35(34–4/05)], and 2009 [V 312–72,241.121–35(77–6/09)]). The obtained neurosphere-like cells were cultured as described before [17]. NPCs were identified by their ability to form neurospheres, survive and proliferate under stem cell conditions, and differentiate into mature cell types [17].

Preparation of artificial in vivo-adapted amniotic fluid (aAF)

aAF was prepared based on the mean concentrations reported in the literature to closely replicate the physiological composition of human AF at 22 weeks of

Table 1 **A:** Identifiers of TaqMan assays with gene-specific primers and probes, **B:** Applied antibodies in immunohistochemical procedures, **C:** Applied antibodies in Western Blot analysis

(A) TaqMan primer probes used for real-time RT-PCR (Applied Biosystems, Foster City, CA)

Gene	*Specificity*	*Sequence*
GAPDH	Glycerinaldehyd-3-phosphat-Dehydrogenase (housekeeping gene)	Rn99999916_s1
Epo	Erythropoietin	Rn01481376_m1
EpoR	Erythropoietin receptor	Rn00566533_m1
HIF1a	Hypoxia inducible factor 1	Rn01472831_m1
HIF2a	Hypoxia inducible factor 2	Rn00576515_m1
beta-III-tubulin	Marker for early neuronal differentiation	Rn01431594_m1
MAP	Microtubule-associated protein 2	Rn00565046_m1
Musashi1	Neural RNA-binding protein, strongly expressed in fetal and adult neural stem cells	Rn00596059_m1
Ki67	Proliferation marker	Rn01451446_m1

(B) Antibodies used for Immunohistochemistry

Marker	*Specificity*	*Dilution*	*Source*	*RRID*
Epo	Erythropoietin (intracellular, cell surface, extracellular localization)	Polyclonal rabbit IgG, 1:250	Abcam Cambridge, UK; #ab226956	n.a
EpoR	Erythropoietin Receptor (intracellular, cell surface localization)	Polyclonal rabbit IgG polyclonal, 1:50,	Abcam Cambridge, UK; #ab244202	n.a
HIF1a	Hypoxia-inducible factor 1 (cytoplasm, cell nuclei)	Polyclonal rabbit IgG, 1:100	Novus Biologicals Abingdon, UK; #nb100-134	AB_350071
HIF2a	Hypoxia-inducible factor 1 (cytoplasm, cell nuclei)	Polyclonal rabbit IgG, 1:100	Novus Biologicals Abingdon, UK; #nb100-122	AB_10002593
b-III-tubulin	Marker for early neuronal differentiation (cytoplasm)	Polyclonal rabbit IgG, 1:800	Sigma-Aldrich, Schnelldorf, Germany #T2200	AB_262133
NeuN	Neuron specific nuclear protein (neuronal nuclei)	Monoclonal mouse IgG, 1:500	Milipore, Schwalbach, Germany/#MAB377	AB_2298772
Musashi1	Marker for fetal and adult neural stem cells (cytoplasm, nuclei)	Monoclonal mouse IgG, 1:1000	R&D Systems, Wiesbaden-Nordenstadt, Germany #MAB2628	AB_2235632

(C) Antibodies used for Western Blot

Marker	*Dilution*	*Source*	*RRID*
PCNA (Proliferating-Cell-Nuclear-Antigen)	Monoclonal mouse IgG, 1:1000	Cell Signaling, Massachusetts, USA #2586	AB_2160343
pSTAT5 Tyr694 (Signal transducer and activator of transcription 5)	Polyclonal rabbit IgG, 1:250	Cell Signaling, Massachusetts, USA #9351	AB_2315225
p-Akt Thr308 (Protein kinase B)	Polyclonal rabbit IgG, 1:200	Cell Signaling, Massachusetts, USA #9275	AB_329828
Hsp90 α/β (Heat shock protein 90)	Polyclonal rabbit IgG, 1:1000	Santa Cruz, Dallas, Texas, USA, #sc-7947	AB_2121235
Donkey anti mouse (HRP-coupled Secondary antibody)	1:10.000	Invitrogen ThermoFisher, Massachusetts, USA A16011	AB_2534685
Donkey anti rabbit (HRP-coupled Secondary antibody)	1:12.500	Invitrogen ThermoFisher, Massachusetts, USA A16035	AB_2534709

gestation [18–22]. EMEM (#M0325, ThermoFisher Scientific) and F12 (#31,765, ThermoFisher Scientific) were selected as base media in equal proportions (1:1). The concentrations of added components were adjusted to align with the reported values to ensure physiological relevance. The final concentration, details of the supplemented components, pH, and osmolarity are listed in Table 2.

The solution's pH was adjusted to 7.8–7.5 using a maximum of 6 mL/1L of 1 N HCl to avoid excessive chloride ion concentrations. After ensuring the solution was free of precipitates and pH-stable, it was sterilized through 0.2 µm filters and aliquoted into single-use tubes for storage at −30°C for up to 1 month, ensuring aAF stability and preventing the need for freeze–thaw events. The pH was revalidated before use.

Stimulation of NPCs

NPCs were seeded in 6 well-plates with 50,000 cells/well in stem cell media supplemented with different ratios of aAF (e.g., 30% artificial amniotic fluid and 70% cell media) and cultivated at 37 °C and 5% CO_2 for up to 8 days. In a first step, rat NPCs were stimulated with aAF at concentrations of 0%, 30%, 55%, 80% and 100% (diluted with the remaining portion of cell culture medium) to assess the influence on

Table 1 **A:** Identifiers of TaqMan assays with gene-specific primers and probes, **B:** Applied antibodies in immunohistochemical procedures, **C:** Applied antibodies in Western Blot analysis

(A) TaqMan primer probes used for real-time RT-PCR (Applied Biosystems, Foster City, CA)

Gene	*Specificity*	*Sequence*
GAPDH	Glycerinaldehyd-3-phosphat-Dehydrogenase (housekeeping gene)	Rn99999916_s1
Epo	Erythropoietin	Rn01481376_m1
EpoR	Erythropoietin receptor	Rn00566533_m1
HIF1a	Hypoxia inducible factor 1	Rn01472831_m1
HIF2a	Hypoxia inducible factor 2	Rn00576515_m1
beta-III-tubulin	Marker for early neuronal differentiation	Rn01431594_m1
MAP	Microtubule-associated protein 2	Rn00565046_m1
Musashi1	Neural RNA-binding protein, strongly expressed in fetal and adult neural stem cells	Rn00596059_m1
Ki67	Proliferation marker	Rn01451446_m1

(B) Antibodies used for Immunohistochemistry

Marker	*Specificity*	*Dilution*	*Source*	*RRID*
Epo	Erythropoietin (intracellular, cell surface, extracellular localization)	Polyclonal rabbit IgG, 1:250	Abcam Cambridge, UK; #ab226956	n.a
EpoR	Erythropoietin Receptor (intracellular, cell surface localization)	Polyclonal rabbit IgG polyclonal, 1:50,	Abcam Cambridge, UK; #ab244202	n.a
HIF1a	Hypoxia-inducible factor 1 (cytoplasm, cell nuclei)	Polyclonal rabbit IgG, 1:100	Novus Biologicals Abingdon, UK; #nb100-134	AB_350071
HIF2a	Hypoxia-inducible factor 1 (cytoplasm, cell nuclei)	Polyclonal rabbit IgG, 1:100	Novus Biologicals Abingdon, UK; #nb100-122	AB_10002593
b-III-tubulin	Marker for early neuronal differentiation (cytoplasm)	Polyclonal rabbit IgG, 1:800	Sigma-Aldrich, Schnelldorf, Germany #T2200	AB_262133
NeuN	Neuron specific nuclear protein (neuronal nuclei)	Monoclonal mouse IgG, 1:500	Milipore, Schwalbach, Germany/#MAB377	AB_2298772
Musashi1	Marker for fetal and adult neural stem cells (cytoplasm, nuclei)	Monoclonal mouse IgG, 1:1000	R&D Systems, Wiesbaden-Nordenstadt, Germany #MAB2628	AB_2235632

(C) Antibodies used for Western Blot

Marker	*Dilution*	*Source*	*RRID*
PCNA (Proliferating-Cell-Nuclear-Antigen)	Monoclonal mouse IgG, 1:1000	Cell Signaling, Massachusetts, USA #2586	AB_2160343
pSTAT5 Tyr694 (Signal transducer and activator of transcription 5)	Polyclonal rabbit IgG, 1:250	Cell Signaling, Massachusetts, USA #9351	AB_2315225
p-Akt Thr308 (Protein kinase B)	Polyclonal rabbit IgG, 1:200	Cell Signaling, Massachusetts, USA #9275	AB_329828
Hsp90 α/β (Heat shock protein 90)	Polyclonal rabbit IgG, 1:1000	Santa Cruz, Dallas, Texas, USA, #sc-7947	AB_2121235
Donkey anti mouse (HRP-coupled Secondary antibody)	1:10.000	Invitrogen ThermoFisher, Massachusetts, USA A16011	AB_2534685
Donkey anti rabbit (HRP-coupled Secondary antibody)	1:12.500	Invitrogen ThermoFisher, Massachusetts, USA A16035	AB_2534709

gestation [18–22]. EMEM (#M0325, ThermoFisher Scientific) and F12 (#31,765, ThermoFisher Scientific) were selected as base media in equal proportions (1:1). The concentrations of added components were adjusted to align with the reported values to ensure physiological relevance. The final concentration, details of the supplemented components, pH, and osmolarity are listed in Table 2.

The solution's pH was adjusted to 7.8–7.5 using a maximum of 6 mL/1L of 1 N HCl to avoid excessive chloride ion concentrations. After ensuring the solution was free of precipitates and pH-stable, it was sterilized through 0.2 µm filters and aliquoted into single-use tubes for storage at −30°C for up to 1 month, ensuring aAF stability and preventing the need for freeze–thaw events. The pH was revalidated before use.

Stimulation of NPCs

NPCs were seeded in 6 well-plates with 50,000 cells/well in stem cell media supplemented with different ratios of aAF (e.g., 30% artificial amniotic fluid and 70% cell media) and cultivated at 37 °C and 5% CO_2 for up to 8 days. In a first step, rat NPCs were stimulated with aAF at concentrations of 0%, 30%, 55%, 80% and 100% (diluted with the remaining portion of cell culture medium) to assess the influence on

proliferation by determining cell numbers after 4 and 7 days of stimulation.

To evaluate the neuroprotective properties of Epo, 20 ng/ml Epo (rat; Sigma-Aldrich; #E8905; concentration within the established effective range for neural precursors [23–26] was added in the presence or absence of aAF in additional samples for up to 8 days. Cytotoxicity assays, Western Blots, and analysis of gene regulation (see below) were performed at different time points throughout the stimulation period. Based on our preliminary tests with aAF treatment of NPCs, aAF was added at concentrations of 55% to ensure sufficient cells remained for longitudinal analysis (too few cells remained under 100% stimulation).

Basal EpoR expression was verified by qRT-PCR in rat NPCs ($\Delta CT = 18.05$, $n = 4$). We measured proliferation by determining cell numbers after 2, 4, and 7 days of stimulation to investigate whether Epo exerts a protective effect.

To evaluate the involved signaling pathways affected by Epo, cells were stimulated with a JAK2/STAT5/Akt signaling pathway inhibitor (AG490, 10 µM; InSolutionTM, Calbiochem #658,411) for 30 min prior stimulation with Epo. Epo-stimulation was performed for a further 15 min under inhibitor influence, in the presence or absence of aAF.

Cytotoxicity assay

The cytotoxic effects were evaluated using the CytoTox-Fluor™ Cytotoxicity Assay (Promega, Walldorf, Germany; #G9260) following the manufacturer's instructions as described before [27]. Cell viability and proliferation were assessed by counting viable cells at the designated time points. The percentage of dead cells was calculated as described before [27]. Growth rates were determined as the fold increase in viable cells relative to day zero of the treatment.

aAF cytotoxicity was assessed over 8 days, with measurements taken on days 1, 2, 3, 4, and 8. Cells were treated daily with 0% (vehicle control; cell media, referred to as "control"), 30%, 55%, or 80% aAF 24 h before performing cytotoxicity, and the results were expressed as the x-fold increase in dead cells relative to the unstimulated control.

qRT-PCR

RNA was extracted from cells and tissues using either TRIzol® reagent (#15,596,026; Invitrogen, Carlsbad, CA, USA) or the ARCTURUS® PicoPure® RNA Isolation Kit (#15,295,033; Applied Biosystems, Foster City, CA, USA), following the manufacturers' protocols. DNase digestion, cDNA synthesis, and qRT-PCR were performed as described previously [26], using TaqMan primer probes (Applied Biosystems). Details of the gene-specific primers and probes are provided in Table 1. Threshold cycle (C_T)

Table 2 Supplementation of salts and amino acids to create artificial Amniotic fluid

Component	F12/EMEM (1:1) [mM]	Literature Mean ± SD [mM]	Supplementation [mM]
Sodium	52,360	135,4 ± 2,19	44,53
Potassium	2,18	3,8 ± 0,18	1,62
Chloride	78,18	106,9 ± 4,90	27,75
Calcium	0,38	1,5 ± 0,22	0,43
Magnesium			0,187
Glucose	7,78	44,1 ± 5,51	33,6
Urea		23,5 ± 0,49	23,5
Glycine	0,05	0,19 ± 0,001	0,13
L-Alanine	0,05	0,31 ± 0,014	0,25
Glutamine	0,19	0,22 ± 0,001	0,03
Arginine	0,56	0,03 ± 0,007	
Asparagine	0,51	0,00	
Aspartic acid	0,057	0,02	
Cysteine	0,066	0,06 ± 0,013	
L-Glutamic Acid	0,11	0,07 ± 0,033	
Glutamine	0,20	0,22 ± 0,001	
Histidine	0,07	0,05 ± 0,001	
Isoleucine	0,04	0,03 ± 0,011	
Leucine	0,08	0,07 ± 0,027	
Lysine	0,13	0,13 ± 0,021	
Methionine	0,02	0,01 ± 0,003	
Phenylalanine	0,03	0,04 ± 0,011	
Proline	0,15	0,12 ± 0,012	
Serine	0,05	0,08 ± 0,035	
Threonine	0,07	0,13 ± 0,011	
Trypthophan	0,01	0,00	
Tyrosine	0,04	0,04 ± 0,011	
Valine	0,07	0,09 ± 0,031	
Ornithine	0,00	0,05 ± 0,009	
Taurine	0,000	0,12 ± 0,009	
pH	7.5–7.8		
Osmolarity	300.66 mOsm/kg		

SD Standard Deviation, *mM* millimole. Distributor information: Sodium bicarbonate (Sigma Aldrich, Germany; S5761-500 g), sodium citrate (Carl Roth GmbH & Co. Karlsruhe, Germany; ≥ 99% p.a. ACS #3580.1), calcium chloride (Carl Roth; ≥ 95% water-free; #A119.1), magnesium chloride (Carl Roth; ≥ 99% water-free; #KK36.1), potassium chloride (Merck KGaA, Darmstadt, Germany; EMSURE® for analysis; #1.04936.0500), sodium chloride (Carl Roth; ≥ 99,5% p.a. ACS, ISO; #3957.1), Urea (Carl Roth; ≥ 99,5% Ph. Eur.Crist.; #X999.2), D-(+)-Glucose (Carl Roth; p.a. ACS; #X997.2), Glycine (Carl Roth; Pufferan® ≥ 99% p.a.; #3908.2), L-Alanine (Carl Roth; ≥ 98,5% for Biochemistry; #3076.1), and Glutamine (Carl Roth; Cellpure® ≥ 99%; HN08.1)

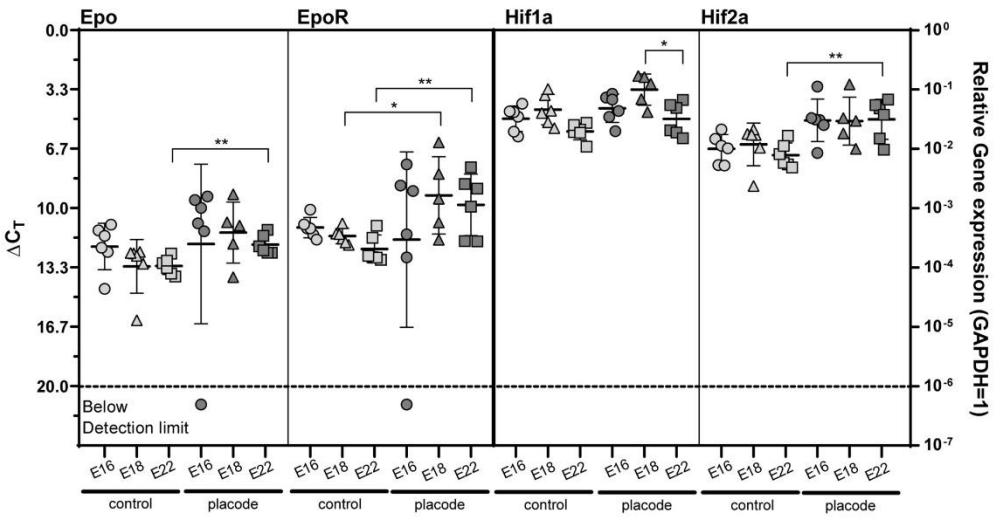


Fig. 1 mRNA expression of Epo and EpoR and their regulators Hif-1α and Hif-2α in neuroplacodes obtained from the rat RA-OCD Model. (**A**) Epo, EpoR mRNA expression was detected at significantly elevated levels in the neuroplacodes at E18 (EpoR; * $p<0.05$) and E22 (Epo/EpoR; ** $p<0.01$) compared to the respective controls. (**B**) Unlike Hif-1α, Hif-2α mRNA was detectable at increased levels at E16, E18, and E22 compared to the control samples. At E22, these differences were statistically significant (** $p<0.01$); n = 4–5 biological replicates; the significances were determined using a non-paired two-tailed *t*-test (* $p<0.05$; ** $p<0.01$; Epo Ctrl E22 vs. P E22 mean difference: −1.193, 95% CI: −1.847 – −0.539; EpoR Ctrl E18 vs. P E18 mean difference: −2.287, 95% CI: −4.319 – −0.257; EpoR Ctrl E22 vs. P E22 mean difference: −2.480, 95% CI: −4.206 – −0.753; Hif-1α P E18 vs. P E22 mean difference: 1.647, 95% CI: 0.409–2.884; Hif-2α Ctrl E22 vs. P E22 mean difference: −2.007, 95% CI: −3.209 – −0.805). Error bars correspond to the standard deviations. Abbreviations: RA-OCD = retinoic acid-induced open spinal dysraphism rat model; Epo = erythropoietin, EpoR = erythropoietin receptor, Hif = hypoxia inducible factor

values were determined, and ΔC_T values were calculated for each sample using the formula $\Delta C_T = C_T$ (gene of interest) $- C_T$ (GAPDH). Samples with undetectable expression levels were excluded from mean expression calculations. Data are presented as either ΔC_T values or linearized ΔC_T values ($2\text{-}C_T$). Gene expression regulation following stimulation (with aAF + /Epo) is shown as relative gene expression, which is calculated as a fold change in expression using the formula: n-fold expression $= 2\Delta C_T$ (control) $- \Delta C_T$ (stimulus).

Western blot

Western Blot analysis was performed as described before [28]. Briefly, treated cells were harvested in lysis buffer [28], and 15–20 µg protein per sample was used for Western blotting experiments [28]. Details on primary and secondary antibodies are summarized in Table 1. Equal protein loading was confirmed using Hsp90, as described previously [28].

Statistical analysis

Statistical analyses were conducted using GraphPad Prism 8.4® software (GraphPad Software, San Diego, California, USA). Depending on the experimental design, a two-tailed Student's t-test or a two-way ANOVA was performed. Statistical significance is indicated with asterisks based on p-values: * $p<0.05$, ** $p<0.01$, and *** $p<0.001$.

Results

EpoR expression and anatomical localization in OSD rat model-derived neuroplacodes

Epo and EpoR mRNA were detectable in control and OSD placode tissue at E16, E18, and E22. EpoR mRNA was significantly higher in neuroplacodes at E18 and E22 compared to controls (Fig. 1). No differences were

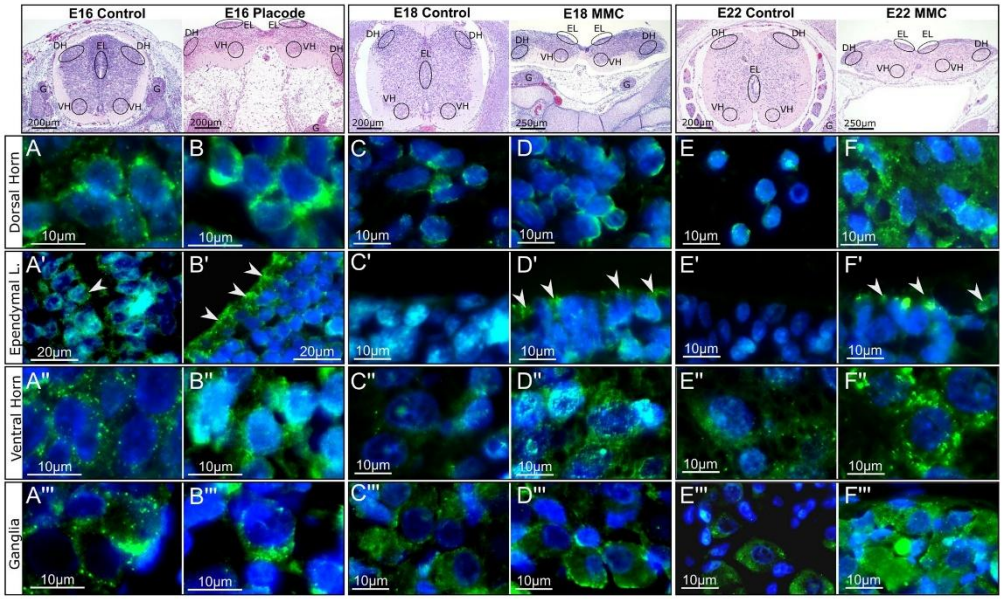


Fig. 2 Anatomical expression patterns of EpoR immunoreactivity in spinal cord segments of control animals and neuroplacodes obtained from the OSD model. In the first row, the anatomical localizations in the respective spinal cord or neuroplacode hematoxylin/eosin-stained tissue sections are marked (DH = dorsal horn; EL = ependymal layer—central canal in control animals; matrix zone in neuroplacodes; VH = ventral horn, G = ganglia). The columns below each overview section show the EpoR immunoreactivity (green) in the respective anatomical region of control and neuroplacode tissues at E16 (A to A''' = control and B to B''' = neuroplacode), E18 (C to C''' = control and D to D''' = neuroplacode), E22 (E to E''' = control and F to F''' = neuroplacode). Arrowheads depict EpoR staining in the ependymal layer. Scale bars are provided in each figure. n = 3 biological replicates (animals) with n = 6 technical replicates (serial sections)

found in Epo mRNA detection between OSD and control groups. Since hypoxia-induced factors regulate Epo and EpoR expression [29, 30], we investigated whether similar EpoR induction factors might play a role in OSD by examining hypoxia-inducible factors Hif-1α and Hif-2α as indirect indicators of hypoxia-related mechanisms. Unlike Hif-1α, Hif-2α mRNA was detectable at increased levels at E16, E18, and E22 compared to controls. At E22, these differences were statistically significant ($p < 0.01$) (Fig. 1).

In control tissues, EpoR-immunoreactive cells were consistently detected in the dorsal and ventral horns and ganglia at all examined time points, and in the central canal ependymal layer on E16 (Fig. 2). In OSD placodes, EpoR was also detected in these regions. Additional EpoR expression was observed on E18 and E22 in the outer layer of the dysraphic placode (matrix zone), which corresponds to the central canal ependymal layer (Fig. 2B', D', F').

Epo staining patterns were similar to those of its receptor (data not shown). In the anatomical regions described, EpoR-immunoreactive cells mainly exhibited morphological characteristics of neuronal cells. Double-labeling confirmed EpoR co-staining with markers for early (β-III-tubulin) (Fig. 3A to D) and mature neuronal cells (NeuN) (Fig. 3E to H). EpoR also co-stained with Musashi1, a marker for NPCs (Fig. 3I to L). Other cell markers, such as nestin, BLBP, GFAP, and NG2, were also detectable in the described anatomical regions. However, as these markers were not co-stained with EpoR-immunoreactivity, they were not pursued in the present study.

Qualitative double staining of EpoR and Hif-2α confirmed co-staining of cells in the aforementioned anatomical areas (Fig. 4).

Influence of aAF on NPCs' proliferation and cell death rates

30% and 55% aAF inhibited NPCs proliferation, while 80% and 100% aAF significantly reduced it (Fig. 5, left panel). The apparent antiproliferative effect of aAF suggested simultaneous cell death. Subsequent cytotoxicity

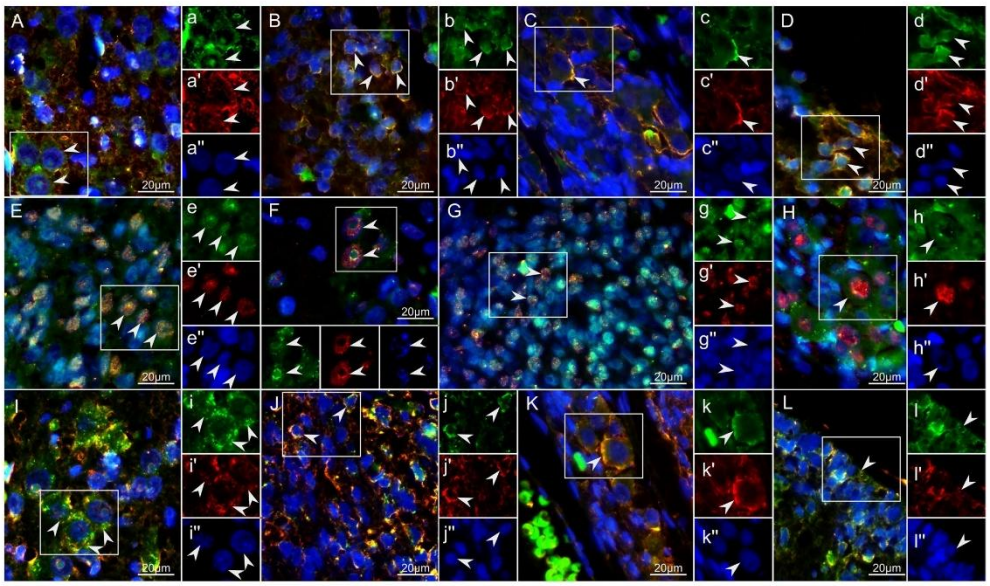


Fig. 3 EpoR co-staining with neuronal and progenitor markers in neuroplacode tissue obtained from the rat RA-OSD model. In all figures, EpoR is shown in green, the cellular markers in red, and DAPI for labeling the cellular nuclei in the blue channel. White rectangles in the merged images depict the areas for which separated channels are provided (labeled with lowercase letters). A – D: EpoR co-staining with β-III-tubulin in the placode at E22 in the ventral Horn (**A**), dorsal horn (**B**), spinal cord ganglia (**C**), and ependymal layer (**D**). E–H: EpoR co-staining with NeuN in the ventral horn at E18 (**E**), in the ventral horn at E22 (**F**), dorsal horn (**G**), and dorsal ganglia (**H**). I – L: EpoR co-staining with Musashi 1 at E22 in the ventral horn (**I**), dorsal horn (**J**), ganglia (**K**), and ependymal layer (**L**). Scale bar in all figures = 20 µm. n = 3 biological replicates (animals) with n = 6 technical replicates (serial sections)

assays confirmed this. The following experiments were performed with 30%, 55% and 80% aAF to ensure enough cells for longitudinal analysis (with 100% aAF stimulation, too many cells died). Cytotoxicity increased significantly from day 1 at 55% and 80% aAF, becoming more pronounced over time. By day 8, 80% aAF caused around six times more dead cells than the control. 55% aAF caused three and a half times more. Cytotoxicity at 30% aAF began on day 3 and increased gradually (Fig. 5, right panel).

Influence of Epo on aAF-induced effects on NPCs

Stimulation with aAF (55%) resulted primarily in a pronounced antiproliferative effect compared to unstimulated control (Fig. 6A). The antiproliferative effects of 55% aAF stimulation were less pronounced in the presence of Epo (Fig. 6A, 55% aAF + Epo). Cytotoxicity Assay results showed that Epo application alone did not influence non-aAF-treated NPC cell death rates at any of the examined time points (Fig. 6B, Epo). The addition of Epo to 55% aAF maintained the levels of cell death below or comparable to those of the non-aAF-treated controls (Fig. 6B).

Influence of Epo and aAF on NPC's cell marker mRNA expression profiles

Figure 6C, panel 1, shows NPC's mRNA expression level of Musashi1, b-III-tubulin, and MAP2 under basal conditions (1 = Ctrl = control). After two days of stimulation with 55% aAF, NPCs exhibited different expression patterns compared to untreated controls, with downregulation of precursor (e.g., Musashi1) and neuronal (e.g., β-III-tubulin, MAP2) markers (Fig. 6C, panels 2). Adding Epo to 55% aAF showed a tendency to restore the unstimulated control state (Fig. 6C, panel 3). Western blot analysis confirmed robust phosphorylation of STAT5, and Akt in

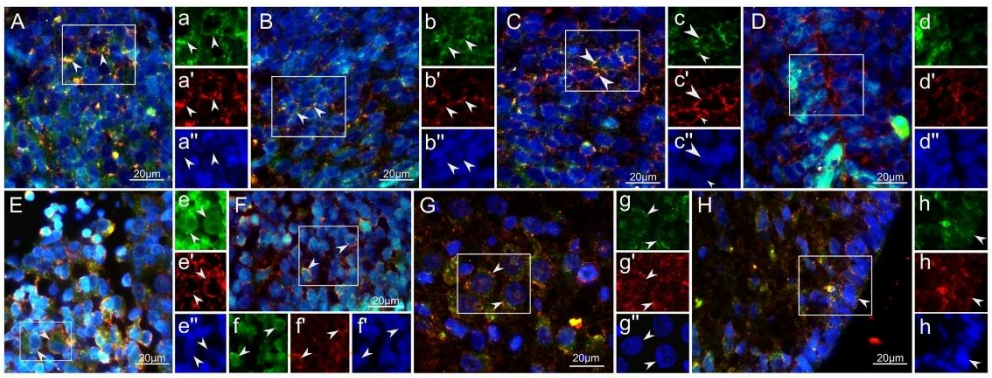


Fig. 4 EpoR co-staining with HIF-2α in neuroplacode tissue obtained from the rat RA-OSD model. In all figures, the following color channels were applied: EpoR green, Hif-2α red, and DAPI (labeling the cellular nuclei) blue. White rectangles in the merged images depict the areas for which separate channels are provided (labeled with lower case letters); Yellow/orange indicates co-staining of EpoR- and Hif-2α-immunoreactivity. (**A**) EpoR co-staining with Hif-2α in dorsal ganglia of control spinal cord (SC) specimen at E16. (**B**) EpoR co-staining with Hif-2α in the dorsal horn of the control SC specimen at E16. (**C**) EpoR co-staining with Hif-2α in the ventral horn of a control SC specimen at E16. (**D**) EpoR co-staining with Hif-2α in the central canal of the control SC specimen at E16. (**E**) EpoR co-staining with Hif-2α in dorsal ganglia at the level of the neuroplacode of RA-OSD derived specimen at E16. (F) EpoR co-staining with Hif-2α in the dorsal horn of the neuroplacode of RA-OSD-derived specimens at E16. (**G**) EpoR co-staining with Hif-2α in the ventral horn of the neuroplacode of RA-OSD-derived specimens at E22. (**H**) EpoR co-staining with Hif-2α in the ependymal layer of the neuroplacode of RA-OSD-derived specimens at E22. Scale bar in all figures = 20 µm. $n = 3$ biological replicates (animals) with n = 6 technical replicates (serial sections)

response to Epo stimulation under aAF condition, which was markedly attenuated under JAK2/STAT5/Akt pathway inhibition via AG490 (10 µM). Furthermore, cell growth analysis revealed the lowest cell growth under aAF treatment, an effect that could be counteracted to a certain extent by Epo, which in turn was inhibited by the application of AG490 (Fig. 6D).

Discussion

We investigated Epo as a potential candidate for neuroprotection in OSD. The prerequisite for this is given in principle with our detection of significantly increased EpoR mRNA expression in the neuroplacodes of our OSD model. This finding and the detectable EpoR immunoreactivity in ventral horns, which co-stained with neuronal and neural progenitor markers, encouraged us to investigate Epo's effect on rat SC-derived NPCs, treated with aAF. This in vitro approach is based on the assumption that neurotoxic substances in the aAF, alongside mechanical effects, contribute to progressive damage to the exposed neuroplacode in OSD [1, 31]. It has been demonstrated that human AF exhibits cytotoxic effects on cells obtained from dissected rat SC [31, 32]. In surgically induced OSD, exchange of AF led to higher neural cell counts in MMC placodes obtained from chick embryos, compared to those in which the AF was not exchanged [33]. Our study confirmed similar, dose-dependent effects of aAF on rat SC NPCs, which exhibited significantly lower proliferation and higher cellular death rates when exposed to aAF. Our findings that adding Epo to aAF-treated NPC cultures significantly increased cell growth and decreased cell death rates via JAK2/STAT5/Akt-signaling suggest that Epo may play a protective role in mitigating the harmful effects of AF stimulation. This observation may be explained by Epo's possible antiapoptotic effects, which have recently been demonstrated [34]. Given the increased apoptosis in OSD neuroplacodes, which contributes to the progressive loss of neural function in the late fetal period [35, 36], the antiapoptotic properties of EPO are interesting.

Our in vitro studies found that Epo showed the tendency to restore the expression pattern and, thus, the differentiation properties of NPCs: NPC cultures treated with aAF exhibited decreased mRNA expression levels of neuronal and neural progenitor cell markers. Adding Epo to these cultures tend to reverse this effect. Future studies will address the underlying molecular mechanisms of Epo's potential influence on NPC differentiation capacities.

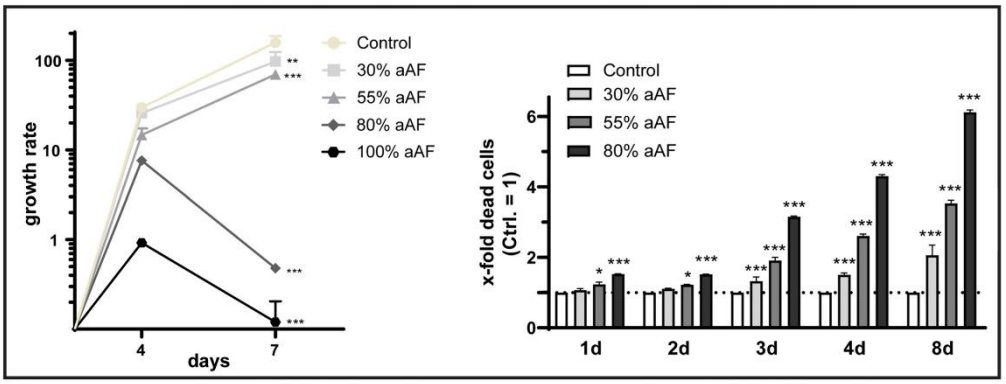


Fig. 5 Effect of artificial amniotic fluid (aAF) on neural progenitor cells (NPCs). Left: Stimulation with aAF resulted in an antiproliferative effect, which increased progressively with higher aAF concentrations; $n=4$ biological replicates. Right: aAF resulted in higher numbers of dead cells in a concentration-dependent manner; $n=2$ biological replicates with $n=2$ technical replicates each; the significances were determined using an ordinary two-way ANOVA test followed by a Tukey's multiple comparison test (* $p<0.05$; *** $p<0.001$; Left: Ctrl vs. 30% aAF mean difference: 60.800, 95% CI: 19.370–102.200; Ctrl vs. 55% aAF mean difference: 88.470, 95% CI: 47.040–129.900; Ctrl vs. 80% aAF mean difference: 157.9, 95% CI: 111.600–204.200; Right: 1 d Ctrl vs. 55% aAF mean difference: −0.235, 95% CI: −0.447 – −0.023; 1 d Ctrl vs. 80% aAF mean difference: −0.525, 95% CI: −0.737 – −0.3126; 2 d Ctrl vs. 55% aAF mean difference: −0.220, 95% CI: −0.432 – −0.008; 2 d Ctrl vs. 80% aAF mean difference: −0.518, 95% CI: −0.729 – −0.305; 3 d Ctrl vs. 30% aAF mean difference: −0.325, 95% CI: −0.537 – −0.113; 3 d Ctrl vs. 55% aAF mean difference: −0.910, 95% CI: −1.122 – −0.698; 3 d Ctrl vs. 80% aAF mean difference: −2.153, 95% CI: −2.365 – −1.940; 4 d Ctrl vs. 30% aAF mean difference: −0.503, 95% CI: −0.715 – −0.290; 4 d Ctrl vs. 55% aAF mean difference: −1.610, 95% CI: −1.822 – −1.398; 4 d Ctrl vs. 80% aAF mean difference: −3.305, 95% CI: −3.517 – −3.093; 8 d Ctrl vs. 30% aAF mean difference: −1.063, 95% CI: −1.275 – −0.850; 8 d Ctrl vs. 55% aAF mean difference: −2.533, 95% CI: −2.745 – −2.320; 8 d Ctrl vs. 80% aAF mean difference: −5.118, 95% CI: −5.330 – −4.905). Error bars correspond to the standard deviation

Epo has been used in clinical trials to address various neuropathological conditions (see review [6]). In the pediatric clinical practice, Epo has been used in phase I studies of hypoxia-related neurological incidents in neonates [9–11]. Intravenously administering high doses of recombinant Epo achieved neuroprotective serum levels that were well tolerated by extremely low birth weight infants and did not cause excess morbidity or mortality [8]. These findings encourage the design of therapeutic trials using Epo as a neuroprotective molecule in other pathological conditions, such as OSD. Regarding the direct accessibility of the defect zone (i.e., exposed neuroepithelium) in OSD, one could consider applying Epo directly to the tissue during surgery. This could circumvent the problem of its short half-life and rapid clearance from the delivery site [37, 38]. Techniques for modifying tissue engineering scaffolds or hydrogels with Epo-loaded nanoparticles have been described in the literature [38–40]. When designing tissue-engineered scaffolds for OSD, it will be important to consider the interplay of different molecular mediators of the cascades induced by the second hit. Based on our previous findings regarding expression of proinflammatory cytokines in OSD neuroplacodes [14], tissue-engineered constructs that deliver a combination of immunomodulating and neuroprotective factors to the open dysraphic site could be a promising adjunct to existing fetal and early postnatal surgical techniques.

Limitations

We used aAF with a concentration similar to 22 weeks of human gestation and neither considered the varying compositions of AF throughout the fetal period nor investigated the potential influence of individual AF substances on neural cells. Exposure to different concentrations of certain AF components, such as meconium, can have detrimental effects on the neuroepithelium in OSD [32]. Furthermore, we have prioritized maintaining the physiological Cl^- value over a pH adjustment to physiological ranges below pH 7.5, given the

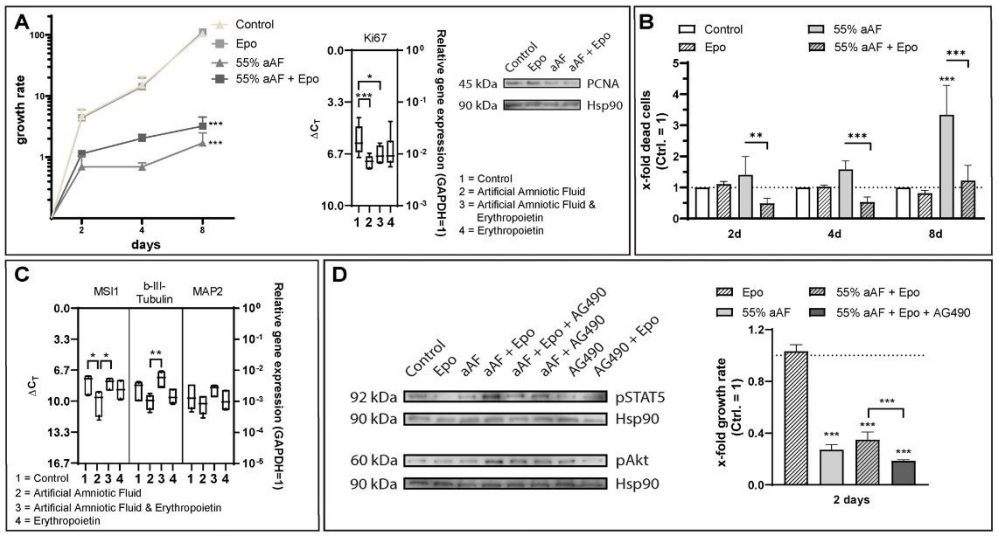


Fig. 6 Effect of erythropoietin (Epo) on artificial amniotic fluid (aAF)-treated neural progenitor cells (NPCs). Results were expressed as the x-fold increase in dead cells relative to the unstimulated control. (**A**) Stimulation with aAF (55%) resulted in a pronounced antiproliferative effect compared to unstimulated control. Stimulation with aAF (55%) combined with Epo (20 ng/mL) resulted in less pronounced antiproliferative effects by aAF; growth rate: n = 6 biological replicates, Western Blot: n = 2 biological replicates, qPCR analysis: n = 3 biological replicates. (**B**) The cytotoxicity of aAF was counteracted by Epo stimulation; n = 6 biological replicates. (**C**) Rat progenitor cells stimulated with aAF showed a reduced expression of neuronal cell markers. Stimulation with aAF and Epo showed a tendency to restore gene expression to control levels; n = 3 biological replicates with n = 2 technical replicates each. (**D**) Western blotting confirmed robust phosphorylation of STAT5 and Akt mainly in response to Epo stimulation under aAF conditions, which was markedly attenuated with application of the inhibitor AG490 (10 µM); n = 2 biological replicates. The cell growth was lowest under aAF treatment, an effect that could be counteracted to a certain extent by Epo, which in turn was inhibited by the application of AG 490 (10 µM); n = 6 biological replicates. The significances (A + B + C) were determined using an ordinary two-way ANOVA test followed by a Tukey's multiple comparison test (* $p < 0.05$; ** $p < 0.01$; *** $p < 0.001$; (**A**) Growth rate: Ctrl vs. 55% aAF mean difference: 102.9, 95% CI: 92.06–113.7; Ctrl. vs. 55% aAF + Epo mean difference: 101.4, 95% CI: 90.55–112.2 (**B**) 2 d 55% aAF vs 55% aAF + Epo mean difference: 0.9233, 95% CI: 0.204–1.643; 4 d 55% aAF vs 55% aAF + Epo mean difference: 1.043, 95% CI: 0.424–1.763; 8 d 55% aAF vs 55% aAF + Epo mean difference: 2.115, 95% CI: 1.396–2.834; 8 d Ctrl. vs 55% aAF mean difference: −2.340, 95% CI: −3.059 – −1.621 (C) MSI1 Ctrl vs. aAF mean difference: 2.042, 95%CI: 0.019–4.066; MSI1 aAF vs. aAF + Epo mean difference: −2.046, 95% CI: −4.070 – −0.023; b-III-Tubulin aAF vs. aAF + Epo mean difference: 2.490, 95% CI: 0.467–4.514). Furthermore, the significances (A + D) were determined using a non-paired two-tailed *t*-test (*** $p < 0.001$; (A) qPCR: Ki67 Ctrl. vs. 55% aAF mean difference: 1.425, 95% CI: 0.708–2.141; Ki67 Ctrl. vs. 55% aAF + Epo mean difference: 1.006, 95% CI: 0.250–1.761 (D) Ctrl. vs. 55% aAF mean difference: 0.728, 95% CI: 0.6913–0.7654; Ctrl. vs. 55% aAF + Epo mean difference: 0.650, 95% CI: 0.5963–0.704; Ctrl. vs. 55% aAF + Epo + AG 490 mean difference: 0.815, 95% CI: 0.806–0.825; 55% aAF + Epo vs. 55% aAF + Epo + AG490 mean difference: −0.160, 95% CI: −0.220—−0.111). Error bars correspond to the standard deviation

influence of Cl^- in nervous tissue and the critical effects of hyperchloremia. Therefore, the pH is slightly above physiological ranges. Another point is how EpoR expression is regulated in neuroplacodes, which remains unclear for now. The EpoR and Hif-2α mRNA expression levels alongside the co-staining of the molecules in neuroplacodes suggest that hypoxia-related mechanisms may also be involved in EpoR regulation in OSD, like in other conditions. Further comprehensive inhibition studies, including targeting downstream signaling cascades or the use of Epo analogues such as carbamylated Epo will be required to fully elucidate the pathways involved. The in vitro experiments were performed with adult rat NPCs rather than embryonic NPCs, ensuring a standardized, reproducible model system. Since EpoR expressions tended to be reduced in adult NPCs, the Epo-effect in embryonic NPCs may show stronger mitogenic responses to Epo due to higher EpoR expression levels. Confirmatory experiments with fetal rat NPCs are likely to support our data.

Conclusion

We demonstrated, for the first time, an upregulation of EpoR expression in neuroplacodes of OSD, and the neuroprotective effects of Epo when added to aAF-treated NPC cultures. These results suggest that Epo is a promising mediator and its receptor is a suitable target for surgery accompanying neuroprotective therapies in OSD.

Supplementary Information The online version contains supplementary material available at https://doi.org/10.1007/s00381-025-07032-8.

Author contribution Conceptualization: [FKL, JC, JHF]; Methodology: [all authors]; Formal analysis and investigation: [FKL, JC, IM, DH, JHF]; Writing—original draft preparation: [FKL, JC, JHF]; Writing—review and editing: [all authors]; Resources: [JHF, MS]; Supervision: [FKL, JC, JHF].

Funding Open Access funding enabled and organized by Projekt DEAL. No funds, grants, or other support were received. The authors declare no relevant financial or non-financial interests. The Graphical Abstract (Supplementary Fig. 1) was created in BioRender (Held-Feindt, J. (2025),https://BioRender.com/c46tsxd).

Data availability No datasets were generated or analysed during the current study.

Declarations

Competing interests The authors declare no competing interests.

Open Access This article is licensed under a Creative Commons Attribution 4.0 International License, which permits use, sharing, adaptation, distribution and reproduction in any medium or format, as long as you give appropriate credit to the original author(s) and the source, provide a link to the Creative Commons licence, and indicate if changes were made. The images or other third party material in this article are included in the article's Creative Commons licence, unless indicated otherwise in a credit line to the material. If material is not included in the article's Creative Commons licence and your intended use is not permitted by statutory regulation or exceeds the permitted use, you will need to obtain permission directly from the copyright holder. To view a copy of this licence, visit http://creativecommons.org/licenses/by/4.0/.

References

1. Heffez DS, Aryanpur J, Hutchins GM, Freeman JM (1990) The paralysis associated with myelomeningocele: clinical and experimental data implicating a preventable spinal cord injury. Neurosurgery 26:987–992
2. Stiefel D, Copp AJ, Meuli M (2007) Fetal spina bifida in a mouse model: loss of neural function in utero. J Neurosurg 106:213–221
3. Knerlich-Lukoschus F, Held-Feindt J (2015) Chemokine-ligands/receptors: multiplayers in traumatic spinal cord injury. Mediators Inflamm 2015:486758
4. Hilton BJ, Moulson AJ, Tetzlaff W (2017) Neuroprotection and secondary damage following spinal cord injury: concepts and methods. Neurosci Lett 652:3–10
5. Knerlich-Lukoschus F (2015) Chemokines and their receptors: important mediators to be aware of in neuroregenerative approaches for spinal cord injury. Neural Regen Res 10:562–564
6. Hemani S, Lane O, Agarwal S, Yu SP, Woodbury A (2021) Systematic review of erythropoietin (EPO) for neuroprotection in human studies. Neurochem Res 46:732–739
7. Nguyen AQ, Cherry BH, Scott GF, Ryou MG, Mallet RT (2014) Erythropoietin: powerful protection of ischemic and post-ischemic brain. Exp Biol Med (Maywood) 239:1461–1475
8. Juul SE, McPherson RJ, Bauer LA, Ledbetter KJ, Gleason CA, Mayock DE (2008) A phase I/II trial of high-dose erythropoietin in extremely low birth weight infants: pharmacokinetics and safety. Pediatrics 122:383–391
9. Rangarajan V, Juul SE (2014) Erythropoietin: emerging role of erythropoietin in neonatal neuroprotection. Pediatr Neurol 51:481–488
10. Rogers EE, Bonifacio SL, Glass HC, Juul SE, Chang T, Mayock DE, Durand DJ, Song D, Barkovich AJ, Ballard RA, Wu YW (2014) Erythropoietin and hypothermia for hypoxic-ischemic encephalopathy. Pediatr Neurol 51:657–662
11. Wu YW, Bauer LA, Ballard RA, Ferriero DM, Glidden DV, Mayock DE, Chang T, Durand DJ, Song D, Bonifacio SL, Gonzalez FF, Glass HC, Juul SE (2012) Erythropoietin for neuroprotection in neonatal encephalopathy: safety and pharmacokinetics. Pediatrics 130:683–691
12. Cohrs G, Goerden S, Lucius R, Synowitz M, Mehdorn HM, Held-Feindt J, Knerlich-Lukoschus F (2018) Spatial and cellular expression patterns of erythropoietin-receptor and erythropoietin during a 42-day post-lesional time course after graded thoracic spinal cord impact lesions in the rat. J Neurotrauma 35:593–607
13. Danzer E, Schwarz U, Wehrli S, Radu A, Adzick NS, Flake AW (2005) Retinoic acid induced myelomeningocele in fetal rats: characterization by histopathological analysis and magnetic resonance imaging. Exp Neurol 194:467–475
14. Cohrs G, Blumenrother AK, Surie JP, Synowitz M, Held-Feindt J, Knerlich-Lukoschus F (2021) Fetal and perinatal expression profiles of proinflammatory cytokines in the neuroplacodes of rats with myelomeningoceles: a contribution to the understanding of secondary spinal cord injury in open spinal dysraphism. J Neurotrauma 38:3376–3392
15. Cohrs G, Drucks B, Surie JP, Vokuhl C, Synowitz M, Held-Feindt J, Knerlich-Lukoschus F (2019) Expression profiles of pro-inflammatory and pro-apoptotic mediators in secondary tethered cord syndrome after myelomeningocele repair surgery. Childs Nerv Syst 35:315–328
16. Kowitzke B, Cohrs G, Leuschner I, Koch A, Synowitz M, Mehdorn HM, Held-Feindt J, Knerlich-Lukoschus F (2016) Cellular profiles and molecular mediators of lesion cascades in the placode in human open spinal neural tube defects. J Neuropathol Exp Neurol 75:827–842
17. Knerlich-Lukoschus F, Krossa S, Krause J, Mehdorn HM, Scheidig A, Held-Feindt J (2015) Impact of chemokines on the properties of spinal cord-derived neural progenitor cells in a rat spinal cord lesion model. J Neurosci Res 93:562–571
18. Benzie RJ, Doran TA, Harkins JL, Owen VM, Porter CJ (1974) Composition of the amniotic fluid and maternal serum in pregnancy. Am J Obstet Gynecol 119:798–810
19. Gillibrand PN (1969) Changes in amniotic fluid volume with advancing pregnancy. J Obstet Gynaecol Br Commonw 76:527–529
20. Naila D, Sadanand S, Sussman D (2022) Artificial amniotic fluid for nuclear magnetic resonance spectroscopy studies. Anal Sci Adv 3:174–187
21. Oliveira FR, Barros EG, Magalhães JA (2002) Biochemical profile of amniotic fluid for the assessment of fetal and renal development. Braz J Med Biol Res 35:215–222
22. Pettit BR, Baker SP, King GS (1979) The composition of amniotic fluid in pregnancies complicated by fetal anencephaly or spina bifida. Br J Obstet Gynaecol 86:637–641

23. Niemann T, Greiner JFW, Kaltschmidt C, Kaltschmidt B (2023) EPO regulates neuronal differentiation of adult human neural-crest derived stem cells in a sex-specific manner. BMC Neurosci 24:19
24. Sims B, Clarke M, Njah W, Hopkins ES, Sontheimer H (2010) Erythropoietin-induced neuroprotection requires cystine glutamate exchanger activity. Brain Res 1321:88–95
25. Wang Y, Yao M, Zhou C, Dong D, Jiang Y, Wei G, Cui X (2010) Erythropoietin promotes spinal cord-derived neural progenitor cell proliferation by regulating cell cycle. Neuroscience 167:750–757
26. Zhang H, Fang X, Huang D, Luo Q, Zheng M, Wang K, Cao L, Yin Z (2018) Erythropoietin signaling increases neurogenesis and oligodendrogenesis of endogenous neural stem cells following spinal cord injury both in vivo and in vitro. Mol Med Rep 17:264–272
27. Hellmold D, Arnaldi P, Synowitz M, Held-Feindt J, Akbari M (2023) A biopolymeric mesh enriched with PLGA microparticles loaded with AT101 for localized glioblastoma treatment. Biomed Mater. https://doi.org/10.1088/1748-605X/acccc4
28. Knerlich-Lukoschus F, von der Ropp-Brenner B, Lucius R, Mehdorn HM, Held-Feindt J (2010) Chemokine expression in the white matter spinal cord precursor niche after force-defined spinal cord contusion injuries in adult rats. Glia 58:916–931
29. Chavez JC, Baranova O, Lin J, Pichiule P (2006) The transcriptional activator hypoxia inducible factor 2 (HIF-2/EPAS-1) regulates the oxygen-dependent expression of erythropoietin in cortical astrocytes. J Neurosci 26:9471–9481
30. Sanchez PE, Fares RP, Risso JJ, Bonnet C, Bouvard S, Le-Cavorsin M, Georges B, Moulin C, Belmeguenai A, Bodennec J, Morales A, Pequignot JM, Baulieu EE, Levine RA, Bezin L (2009) Optimal neuroprotection by erythropoietin requires elevated expression of its receptor in neurons. Proc Natl Acad Sci U S A 106:9848–9853
31. Athiel Y, Jouannic JM, Lépine M, Maillet C, de Saint DT, Larghero J, Guilbaud L (2024) Role of amniotic fluid toxicity in the pathophysiology of myelomeningocele: a narrative literature review. Prenat Diagn 44:1530–1535
32. Drewek MJ, Bruner JP, Whetsell WO, Tulipan N (1997) Quantitative analysis of the toxicity of human amniotic fluid to cultured rat spinal cord. Pediatr Neurosurg 27:190–193
33. Olguner M, Akgür FM, Ozdemir T, Aktuğ T, Ozer E (2000) Amniotic fluid exchange for the prevention of neural tissue damage in myelomeningocele: an alternative minimally invasive method to open in utero surgery. Pediatr Neurosurg 33:252–256
34. Si W, Wang J, Li M, Qu H, Gu R, Liu R, Wang L, Li S, Hu X (2019) Erythropoietin protects neurons from apoptosis via activating PI3K/AKT and inhibiting Erk1/2 signaling pathway. 3 Biotech 9:131
35. Avagliano L, Doi P, Tosi D, Scagliotti V, Gualtieri A, Gaston-Massuet C, Pistocchi A, Gallina A, Marconi AM, Bulfamante G, Massa V (2016) Cell death and cell proliferation in human spina bifida. Birth Defects Res A Clin Mol Teratol 106:104–113
36. Reis JL, Correia-Pinto J, Monteiro MP, Costa M, Hutchins GM (2008) Vascular and apoptotic changes in the placode of myelomeningocele mice during the final stages of in utero development. J Neurosurg Pediatr 2:150–157
37. Murua A, Orive G, Hernández RM, Pedraz JL (2011) Emerging technologies in the delivery of erythropoietin for therapeutics. Med Res Rev 31:284–309
38. Wu XY, Zhu YM, Qi Y, Xu WW, Jing Z (2021) Erythropoietin, as a biological macromolecule in modification of tissue engineered constructs: a review. Int J Biol Macromol 193:2332–2342
39. Gholami M, Gilanpour H, Sadeghinezhad J, Asghari A (2021) Facile fabrication of an erythropoietin-alginate/chitosan hydrogel and evaluation of its local therapeutic effects on spinal cord injury in rats. Daru 29:255–265
40. Ji R, Hao Z, Wang H, Li X, Duan L, Guan F, Ma S (2023) Application of injectable hydrogels as delivery systems in spinal cord injury. Gels. https://doi.org/10.3390/gels9110907

Publisher's Note Springer Nature remains neutral with regard to jurisdictional claims in published maps and institutional affiliations.

Authors and Affiliations

Friederike Knerlich-Lukoschus[1] · Jacqueline Clüver[2] · Inez Manczuk[2] · Frieda Bayler[2] · Dana Hellmold[2] · Michael Synowitz[2] · Janka Held-Feindt[2]

✉ Friederike Knerlich-Lukoschus
Friederike.knerlich-lukoschus@med.uni-goettingen.de

[1] Division of Pediatric Neurosurgery, Department of Neurosurgery, University Medical Center Göttingen, Robert-Koch-Str. 40, 37075 Göttingen, Germany

[2] Department of Neurosurgery, University Hospital of Schleswig-Holstein Campus Kiel, Arnold-Heller-Str. 3, House D, 24105 Kiel, Germany

A.3 Danksagung

An dieser Stelle möchte ich mich bei allen meinen Wegbegleitern bedanken, die mir während meines Studiums und meiner Dissertation zur Seite standen und ohne die ich heute nicht dort stehen würde, wo ich mittlerweile bin.

An erster Stelle möchte ich meinem Ehemann danken. Du warst während der gesamten Zeit mein wichtigster Rückhalt. Danke, dass du immer für mich da warst – in den produktiven Phasen ebenso wie in den Momenten, in denen Zweifel, Erschöpfung oder Frustration überwogen haben. Du hast mir zugehört, mich aufgefangen, mich ermutigt und mir immer wieder gezeigt, dass ich meinen Weg nicht allein gehe – Danke!

Mein ganz besonderer Dank gilt zudem meiner Doktormutter Prof. Dr. Dr. Janka Held-Feindt. Du hast mich während der gesamten Zeit mit großem Engagement begleitet und unterstützt. Ich bin dir sehr dankbar für das Vertrauen, das du mir entgegengebracht hast, die wissenschaftliche Anleitung und die beruflichen Möglichkeiten, die du mir eröffnet hast. Ich schätze unsere Zusammenarbeit, an die ich mich mit Freude zurückerinnern werde.

Darüber hinaus danke ich allen Kolleginnen und Kollegen, die mich im Laboralltag begleitet, Experimente unterstützt, Diskussionen bereicht und diese Zeit zu einer ganz besonderen gemacht haben. Mein ganz besonderer Dank gilt Frau Corinna Keller, welche mich mit ihrer optimistischen Art und Fröhlichkeit durch die Arbeit begleitet hat - ohne dich wäre der Laboralltag nur halb so schön gewesen!

Ich danke Prof. Dr. Axel Scheidig für die Übernahme des Zweitgutachtens und Unterstützung während des Studiums. Sicherlich wäre der Biochemie-Studiengang ohne Sie nur halb so schön gewesen, und die Zusammenarbeit während meiner Fachschaftszeit habe ich sehr geschätzt.

Zuletzt bedanke ich mich bei meinen Eltern und Großeltern, die mir das Studium erst ermöglicht haben und mir während der gesamten Zeit stets liebevoll zur Seite standen. Ich danke euch für eure Geduld, euer Verständnis und die Unterstützung während dieser intensiven Zeit.

A.4 Eidesstattliche Erklärung

Hiermit erkläre ich an Eides Statt, dass ich die vorliegende Dissertation nach Inhalt und Form selbstständig unter der Beratung durch meine Betreuerin und ohne fremde Hilfe oder nicht aufgeführter Quellen angefertigt habe. Wörtlich oder inhaltlich zitierte Stellen sind als solche kenntlich gemacht. Außerdem versichere ich, dass weder ich noch ein anderer diese Arbeit an einer anderen Stelle im Rahmen eines Promotionsprüfungsverfahrens vorgelegt haben. Teile dieser Arbeit wurden bereits in wissenschaftlichen Fachmagazinen publiziert. Weiterhin wurde die Arbeit unter Einhaltung der Regeln über gute wissenschaftliche Praxis der Deutschen Forschungsgemeinschaft erstellt. Zusätzlich bekräftige ich, dass mir noch kein akademischer Grad entzogen wurde.

Kiel, den _____



Jacqueline Clüver